University of Southampton
Faculty of Engineering and the Environment

THESIS FOR THE DEGREE OF DOCTOR OF PHILOSOPHY

Stability and Transition of the Flow behind Isolated Roughness Elements in Hypersonic Boundary Layers

by

Jeroen Van den Eynde

July 2015

University of Southampton
Faculty of Engineering and the Environment

Doctor of Philosophy

Stability and Transition of the Flow behind Isolated Roughness Elements in Hypersonic Boundary Layers

Jeroen Van den Eynde

Abstract

In this work the effect of isolated surface roughness on the behaviour of a hypersonic boundary layer is investigated, with a particular focus on the effect of the three-dimensional roughness shape on the instability of the roughness wake and the subsequent transition process. The analysis is performed computationally using direct numerical simulations, which solve the compressible Navier-Stokes equations, and a new code, developed in the scope of the current work, to analyse the linear stability of these equations. The full three-stage roughness-induced transition process has been investigated: firstly, the receptivity process and generation of boundary layer instabilities from freestream disturbances; secondly, the generation of a roughness wake and its initial linear instability; and finally the non-linear breakdown to turbulence of the roughness wake. In particular the effect of the three-dimensional roughness shape on these processes has been studied, looking at the roughness height, frontal profile, planform shape and upward/downward ramps. Also the effect of freestream disturbance amplitude and wall cooling has been investigated. It has been found that the roughness height and frontal profile have a large influence on the stability characteristics of the resulting wake and the subsequent transition. The roughness planform shape has a marginal effect, although cylindrical and diamond-shaped elements yield more unstable wakes than a square roughness element. Bi-local stability analysis can be used in most cases to predict the most unstable wake mode, but it under-predicts the instability growth rates due to non-parallel effects. The roughness shape has been observed to affect the transition onset location. The criteria commonly used to predict roughness-induced transition, do not take into account the three-dimensional shape, and an alternative transition prediction, based on the amplitude of the roughness-induced streamwise streak, is considered.

Contents

List of Figures

List of Tables

List of Symbols

Greek symbols

α	streamwise wavenumber
β	spanwise wavenumber
δ_0	displacement thickness
δ_{99}	boundary layer thickness
δ_{ij}	Kronecker delta function
γ	specific heat ratio
λ	thermal conductivity
μ	dynamic viscosity
ω	circular frequency
ϕ	phase
ρ	density
σ	growth rate from DNS
τ	viscous stress tensor
θ	azimuthal coordinate

Roman symbols

a	disturbance amplitude
A_{st}	streak amplitude
b_y	stretching factor
c_f	skin friction coefficient
C_p	specific heat at constant pressure
C_v	specific heat at constant volume
$c_{1,2,3,4}$	constants

c_{ph}	phase speed
D	roughness diameter
E	total energy
e	disturbance energy
F	non-dimensional frequency
f	frequency
$\Im$	imaginary part
$\mathcal{I}_e$	integrated disturbance energy
k	roughness height
k_z	spanwise wavenumber
L	length
L_{sep}	separation length
M	Mach number
N	number of grid points; N-factor
p	pressure
Pr	Prandtl number
$\mathbf{q}$	flow variable vector
Q	second invariant; momentum deficit
q	heat flux vector
R	universal gas constant
r	radius
Re	Reynolds number
S	Sutherland's temperature; speed-up
S_{yz}	roughness projected frontal area
T	temperature
t	time
u, v, w	streamwise, wall-normal and spanwise velocity
u_s	shear magnitude
U_∞	freestream velocity
u_τ	friction velocity
W	roughness width
w	local roughness width

x, y, z	streamwise, wall-normal and spanwise coordinate

Subscripts & superscripts

$\hat{\bullet}$	Fourier transformed variable
$\bullet^*$	dimensional variable
$\bullet'$	fluctuation
$\tilde{\bullet}$	coordinate relative to roughness centre; unsteady flow variable
$\bar{\bullet}$	steady base flow variable
$\bullet_i$	imaginary part
$\bullet_r$	real part
$\bullet_r$	reference value
$\bullet_w$	value taken at the wall
$\bullet_{x,y,z}$	streamwise, wall-normal and spanwise component

List of Acronyms

ACM Artificial Compression Method
BLS bi-local stability
CGL Chebyshev-Gauss-Lobatto
COMPASS Compressible Analysis-of-Stability Suite
DFT discrete Fourier transform
DNS direct numerical simulation
EVP eigenvalue problem
FD finite difference
GEVP generalised eigenvalue problem
LES large eddy simulation
LNSE linearised Navier-Stokes equations
LST linear stability theory
MPI Message Passing Interface
MUMPS MUltifrontal Massively Parallel sparse direct Solver
ODE ordinary differential equation
OS Orr-Sommerfeld
PSE parabolic stability equations
QEVP quadratic eigenvalue problem
SL sinuous-lateral
SLEPc Scalable Library for Eigenvalue Problem Computations
TVD total variation diminishing
VC varicose-centre
VL varicose-lateral

Declaration of Authorship

I, Jeroen Van den Eynde, declare that the thesis entitled *Stability and Transition of the Flow behind Isolated Roughness Elements in Hypersonic Boundary Layers* and the work presented in the thesis are both my own, and have been generated by me as the result of my own original research. I confirm that:

- this work was done wholly or mainly while in candidature for a research degree at this University;
- where any part of this thesis has previously been submitted for a degree or any other qualification at this University or any other institution, this has been clearly stated;
- where I have consulted the published work of others, this is always clearly attributed;
- where I have quoted from the work of others, the source is always given. With the exception of such quotations, this thesis is entirely my own work;
- I have acknowledged all main sources of help;
- where the thesis is based on work done by myself jointly with others, I have made clear exactly what was done by others and what I have contributed myself;
- parts of this work have been published as:
  - Journal Papers

    J. P. J. P. Van den Eynde & N. D. Sandham, 'Numerical Simulations of Transition due to Isolated Roughness Elements at Mach 6', *AIAA Journal*, 2015 (accepted), `doi:10.2514/1.J054139`

  - Conference Proceedings

    J. P. J. P. Van den Eynde & N. D. Sandham, 'Numerical Simulation of Roughness-Induced Instability Growth and Transition at Mach 6', *7th AIAA Theoretical Fluid Mechanics Conference*, June 2014

J. P. J. P. Van den Eynde & N. D. Sandham, ' Numerical Investigation of Roughness-Induced Transition at Mach 6 in the European ATLLAS-2 Programme', *8th European Symposium on Aerothermodynamics for Space Vehicles*, March 2015

- Project Deliverables

  J. P. J. P. Van den Eynde & N. D. Sandham, 'Transition to turbulence', *ATLLAS-II Deliverable D5.3.2*, 2014

  N. De Tullio, J. P. J. P. Van den Eynde & N. D. Sandham, 'Receptivity of smooth and sharp-edged roughness elements to free stream disturbances', *ATLLAS-II Deliverable D5.3.5*, 2015

_____

Signature

_____

Date

Acknowledgements

I would like to thank Prof. Neil Sandham for giving me the opportunity to pursue my PhD at the Aerodynamics & Flight Mechanics research group of the University of Southampton, and for providing me with his invaluable advice, guidance and support throughout my degree. I have also had several fruitful discussions with Dr. Nico De Tullio, Andrea Sansica, Patrick Bechlars and Richard Pichler, among others, who have helped me a great deal in these years.

I would like to acknowledge the financial support of the European Union through the ATLLAS II project (Contract no. ACP0-GA-2010-263913) of the Seventh Framework Program and the UK Turbulence Consortium for providing the required computational time on HECToR and ARCHER, the UK's national supercomputing service. I would also like to thank the University of Southampton for providing access to its high-performance computing service, Iridis.

I am extremely grateful for my family, who have supported me unconditionally, even in large periods of absence and during times when I should have been there for them. Finally, I would like to thank Francesca for her love, support and encouragement throughout this long and sometimes difficult journey. She has been more important to me than she realises.

Jeroen Van den Eynde
Southampton
May 2015

Chapter 1

Introduction

1.1 Motivation

The motion of fluids has been a topic of interest for hundreds of years. The drafting of the governing equations of motion in the early nineteenth century, which we now call the Navier-Stokes equations, gave rise to a new field of research. By careful investigation of the equations governing an inviscid flow, Stokes (1843) was one of the first to point out that fluid motion can become unstable under certain circumstances, allowing for a small disturbance to change the nature of the flow to become sinusoidal. Reynolds (1883) showed this experimentally in his famous pipe flow experiment. What they observed is what we now call *turbulence*.

Turbulent flows have some beneficial properties such as improved mixing – useful in, for example, chemical processes – and delayed flow separation, which reduces pressure drag and can thus sometimes be desirable in certain applications such as cars, airplanes, etc. Turbulence is however often undesirable because it increases friction drag and heat loads, and can decrease the performance of control surfaces when caught in a turbulent wake. Because these effects are often crucial in fluid flows, understanding turbulence is of great importance.

How exactly the transition from a laminar flow to turbulence occurs is still not fully understood, despite the great deal of work that has been done on this topic. Researchers have tried to gain more insight into the laminar-turbulent transition process by studying the effects of geometry, surface roughness, compressibility, shock interaction, etc. Some reviews of these topics can be found in Tani (1969), Reshotko (1976), Adamson and Messiter (1980), Lele (1994), Schneider (2008) and Fedorov

(2011) among others. However a single theory of transition to turbulence is still to be found and laminar-turbulent transition is one of the great outstanding problems in modern day aerodynamics.

With recent and ongoing hypersonic flight vehicle development projects, such as Boeing's X-51[1], SKYLON[2], ZHEST[3] and European Space Agency's ATLLAS[4], the need to understand turbulence and the transition process in the high Mach number regime is greater than ever. Although stability and transition of supersonic and hypersonic boundary layers has been studied for more than 50 years (Schneider, 2004), the computational advances in the last decade have made it possible to study these phenomena numerically, allowing for a more in-depth analysis of the mechanisms behind them. An important consideration to be taken into account in hypersonic vehicle design is the presence of surface roughness. Surface roughness can come in the form of distributed surface irregularities, originating from e.g. machining processes, material oxidation or ablation, or in the form of discrete isolated protuberances. Both surface roughness types are known to be able to promote boundary layer transition. A practical example of the latter roughness type is the gap filler that was found protruding from in between the thermal protection tiles of the Space Shuttle orbiter (Berry and Hamilton, 2002; Horvath et al., 2012), acting as a discrete roughness element and inducing transition at a higher Mach number than anticipated.

The mechanisms governing roughness-induced transition are not yet fully understood, and the prediction of transition due to surface roughness is still mainly based on engineering correlations and transition criteria originating from wind tunnel testing and in-flight experiments. The current work aims to add to the body of knowledge by analysing some of the processes involved.

1.2 Theory of boundary layer instability and transition

Even though the transition from a laminar boundary layer to a turbulent one is a much studied topic, it is still not completely understood as it is a complicated

[1] Boeing X-51, http://www.boeing.com/boeing/defense-space/military/waverider/index.page

[2] Reaction Engines Ltd., http://www.reactionengines.co.uk/

[3] EADS, http://www.eads.com/eads/int/en/our-innovation/our-technologies/Advanced-Concepts/ZEHST-concept.html

[4] ATLLAS II, http://www.esa.int/Our_Activities/Space_Engineering/ATLLAS_II_-_Project_summary

process that is dependent on many factors. The noise level in the freestream, the presence of roughness or shocks and other external perturbations can significantly change the way boundary layer instabilities originate, grow and eventually lead to the breakdown to turbulence.

Boundary layer transition is in essence a stability problem. If perturbations introduced in a laminar flow increase in amplitude, the boundary layer is unstable and may eventually transition to turbulence if a critical disturbance amplitude is reached. If the perturbations die out before reaching this critical amplitude, the boundary layer will remain laminar. The topic concerned with studying this behaviour is called *stability analysis*.

1.2.1 Instability

In the early 20th century Orr (1907) and Sommerfeld (1908) had a big influence in this subject. They investigated the stability of two-dimensional harmonic perturbations superimposed on a parallel laminar flow and derived a fourth order ordinary differential equation governing the amplitude of a perturbation mode. This equation – which is now called the Orr-Sommerfeld equation in their honour – is one of the corner stones of linear stability theory (LST). Squire (1933) performed a similar analysis based on the growth of small perturbations, but looked at the evolution of three-dimensional disturbances in a steady incompressible flow between parallel walls. He concluded that the development of a three-dimensional disturbance is similar to that of a two-dimensional one and that any instability for the three-dimensional case is also present for two-dimensional disturbances at a lower Reynolds number. Therefore (for incompressible parallel flows) *"it is sufficient to confine attention to disturbances of two-dimensional type"*.

Many authors have used linear stability theory to look at the linear growth of disturbances and no attempt is made here to give a complete overview of this topic. A detailed review of linear stability theory of boundary layers can be found in Reed et al. (1996) and Schmid and Henningson (2001). Linear stability theory is concerned with the growth of small disturbances in a flow. Although this linear growth stage is important in laminar-turbulent transition, it is far from being the complete picture. The mechanism of how these small initial disturbances enter the boundary layer — called *receptivity* — and the various ways how transition can occur are explained next.

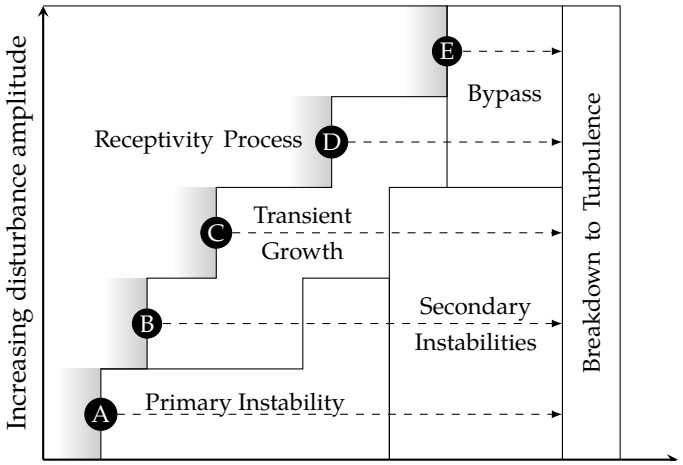

Figure 1.1. Paths to boundary layer transition depending on disturbance amplitude.

1.2.2 Receptivity & Transition Mechanisms

External disturbances enter the boundary layer through a process called receptivity (Morkovin, 1969) where they are transformed into instability waves (Kerschen, 1993; Ma and Zhong, 2003). These disturbances can originate from the freestream environment, such as sound, vorticity and entropy waves (Kovasznay, 1953), or from localised features such as surface imperfections (Choudhari, 1993; Gaponenko et al., 2002) and other wall perturbations (Fedorov and Khokhlov, 2002). The different mechanisms that lead to transition after the instabilities have entered the boundary layer are highly dependent on the character of the disturbance environment (Kachanov, 1994). A schematic showing the potential paths to transition as proposed by Morkovin (1994) and Reshotko (2008a) is given in Figure 1.1.

In a very low disturbance environment, transition follows the traditional three-stage path Ⓐ . Primary boundary layer eigenmodes, i.e. two-dimensional Tollmien-Schlichting waves, are generated by the receptivity process and grow linearly. After this initial growth, described by linear stability theory, secondary three-dimensional non-linear instabilities will form, grow rapidly and eventually break down into turbulence. As disturbance amplitude increases, transient growth becomes important. Transient growth is essentially algebraic growth followed by an exponential decay and arises from the non-orthogonality of Orr-Sommerfeld and Squire eigenfunctions. It has been described in detail by Landahl (1980) and Hultgren and Gustavsson (1981). Weak transient growth can occur for two-dimensional and axi-symmetric modes leading to path Ⓑ (Reshotko, 2001). Stronger transient growth can skip the

eigenmodes stage and lead directly to the non-linear instabilities (Ⓒ) or bypass these instabilities completely and break down to turbulence right away as depicted by path Ⓓ . Path Ⓔ describes the transition mechanism where no linear regime is present. This occurs in the case of very large amplitude forcing (Reshotko, 2001).

These paths are essentially the same for low and high speed boundary layers, however the basic features can be quite different (Fedorov, 2011). For example, the primary instabilities might be of a different nature, i.e. viscid or inviscid. The transition mechanisms for supersonic and hypersonic flows are also more complex and less well understood than those for incompressible boundary layers (Zhong and Wang, 2012). Most of the early work on receptivity and transition was done for subsonic or low supersonic flows. Since the focus of the present work will be on high speed boundary layers (high supersonic to hypersonic), we will keep the focus of this literature review on this topic. An extended overview of the work done on low speed receptivity and transition can be found in Reshotko (1976), Kachanov (1994) and Reed et al. (1996) among others. It should be noted that the term *hypersonic* is used in the current work for flows with a Mach number greater than or equal to 6, irrespective of the occurrence of high-enthalpy effects like dissociation.

Mack (1975) was the first to investigate the linear stability characteristics of a compressible boundary layer. He studied the linear growth or decay of boundary layer modes in high supersonic and hypersonic flow using linear stability theory. He showed that the stability characteristics of a boundary layer in high supersonic and hypersonic flows are very different from their subsonic counterparts (Mack, 1984). Mack discovered the existence of higher acoustic instability modes, called Mack modes, and found that at Mach numbers higher than 4, the second mode is the dominant one and thus very likely to cause transition.

Fedorov and Khokhlov (1991, 1992) used asymptotic theory to show the excitation of boundary layer modes in the leading-edge region by acoustic waves. Their results agreed very well with the experimental work of Maslov et al. (2001) as later shown by Fedorov (2003). The mechanisms responsible for this were identified as being diffraction and/or scattering of these acoustic waves. From this it follows that the excitation of the boundary layer modes is dependent on the angle of the incident waves. Gaponov (1995) reached a similar conclusion by studying the receptivity of a boundary layer by acoustic plane waves. He concluded that the intensity of the boundary layer disturbance is highly dependent on the spatial orientation of external acoustic waves.

Not a lot of experimental supersonic and hypersonic receptivity work has been reported because of the inherent difficulties of such studies. The high background noise level of conventional wind tunnels promotes bypass transition, circumventing the linear receptivity stage. Kendall (1975) studied the evolution of fluctuations in a zero pressure gradient boundary layer and reported a strong correlation between the freestream acoustic disturbances and the boundary layer fluctuations. It was also found that significant growth occurs already before the region of instability predicted by linear stability theory for Mach numbers between 3.0 and 5.6. Stetson et al. (1991) showed the same for a Mach number of 8. Also Maslov et al. (2001) investigated the receptivity at hypersonic flow velocities and used concentrated two-dimensional and three-dimensional acoustic sources. All these studies confirm that acoustic disturbances in the freestream generate boundary layer modes and the boundary layer receptivity coefficient, defined as the ratio of the amplitude of the Tollmien-Schlichting wave in the leading-edge region to the freestream disturbance amplitude, is highly dependent on the incident wave angle.

1.2.3 Effect of the free-stream disturbance type

All receptivity studies mentioned until now used acoustic waves as freestream disturbances. McKenzie and Westphal (1968) showed that a single-type wave – either acoustic, vorticity or entropy – upstream of a leading-edge shock will produce disturbances of all three types after the shock. One might therefore argue that it is necessary to investigate receptivity to all types of freestream disturbances. Choudhari and Streett (1990) examined the generation of instability waves near local wall inhomogeneities and found that receptivity to acoustic disturbances is much stronger than receptivity to vorticity or entropy disturbances. Ma and Zhong (2005) investigated the receptivity to slow and fast acoustic waves, entropy waves and vorticity waves. They found that slow acoustic waves can excite Mack modes in the boundary layer directly, while the other three disturbance types follow a completely different path. Fast acoustic waves can generate stable mode I waves in the leading-edge region because of their resonant interaction. These modes are then converted into second Mack modes at their synchronisation point. They found that the receptivity to entropy and vorticity waves follows the same two-step resonant interaction path because of the fast acoustic waves generated behind the shock as predicted by the theory of McKenzie and Westphal (1968). Quantitatively the amplitude of disturbances behind the shock in the case of entropy and vorticity waves is several orders of magnitude smaller than for fast acoustic waves.

1.2.4 Roughness-induced transition

Already early on in transition research it was known that surface roughness (either distributed or isolated) can lead to early boundary layer transition. Some of the important work on roughness-induced transition in the low speed regime is summarised in Tani (1969) and Saric et al. (2003) among others, and is not considered here. More recently the effects of roughness on supersonic transition were addressed by Reshotko (2008b) while hypersonic transition was reviewed very extensively by Schneider (2008), who in particular summarised the physical effects of roughness, the parameters affecting transition and some of the commonly used correlations. Schneider concluded that there are essentially three ways roughness can affect transition: instabilities might grow in the wake behind the roughness element, streamwise vortices generated by the surface roughness may grow or boundary layer modes might be generated by interaction of freestream disturbances with the roughness element.

Almost all of the work cited by Schneider (2008) is experimental or based on flight data. Because of the high computational cost, direct numerical simulations (DNS) have not made a great contribution in studies concerning roughness-induced transition in high speed flows. Only recently DNS has been used to simulate the effect of roughness elements on high speed boundary layer transition. Marxen and Iaccarino (2008) investigated the effect of two-dimensional localised roughness on boundary layer instability in a Mach 4.8 flow. They observed a strong alteration of disturbance amplitudes in the vicinity of the roughness element. Near the separation zones upstream and downstream of the roughness, the second-mode disturbance was found to be amplified; along the roughness element the disturbance was strongly damped. They proposed the hypothesis that *"two-dimensional roughness elements behave as disturbance amplifiers with limited bandwidth, capable of filtering a range of frequencies and strongly amplify only a selected range"*.

Direct numerical simulations and bi-global stability analysis of the flow behind a three-dimensional roughness element at Mach 4.8 were performed by Groskopf et al. (2008), who found that absolute instabilities can occur in the recirculation zones around the roughness elements and that the trailing vortices generate streaks that sustain strongly growing convective instabilities. Different types of wake instabilities can occur: sinuous (sometimes called odd or anti-symmetric) and varicose (or even/symmetric). It is still not entirely understood how the dominant mode depends on the flow conditions and the roughness geometry, but it has been found

that varicose modes are generally more unstable (Choudhari et al., 2013). Choudhari et al. (2010) found that the sinuous mode was dominant for a roughness element with lower height, while the varicose mode was more unstable for larger roughness heights.

Redford et al. (2010) studied transition due to an isolated smooth bump at Mach 3.0 and 6.0 and found a strong effect of compressibility on the detached shear layer behind the roughness element. They also found a correlation based on roughness height Reynolds number, Mach number and wall temperature that separated the cases that went through transition from those that remained laminar. Bernardini et al. (2012a) did comparable simulations and extended the range of flow conditions. They found a similar correlation as Redford et al. (2010), thereby validating this transition criterion. Bernardini et al. (2014) proposed an alternative transition criterion based on the momentum deficit induced by a roughness element, thereby incorporating the effect of the projected frontal shape and aspect ratio of the roughness element.

Most of these studies on roughness wake instability modes are based on numerical simulations. The high structural loads on measurement probes makes it inherently difficult to perform experimental measurements of wake instability at hypersonic speeds. The first experimental detection of the instability of the wake behind a cylindrical roughness element at Mach 6.0 was performed by Wheaton and Schneider (2012, 2014), who found that the instability was largest away from the wake centreline. These experimental results were successfully cross-validated using direct numerical simulations by Subbareddy et al. (2014).

De Tullio and Sandham (2012, 2015) performed a receptivity study of a Mach 6.0 boundary layer with a sharp-edged localised roughness element. They looked at the effect of roughness height, type of imposed disturbance and wall temperature. Their results showed that roughness height has a significant effect on instability growth. For a roughness height approaching the local displacement thickness, the detached shear layer becomes receptive to a broad range of frequencies, increasing the growth rate of instabilities. A roughness element half as high had only a small effect on mode growth. De Tullio and Sandham also found that different types of disturbances lead to differences in amplitude functions and mode growth rates, and that wall cooling tends to reduce the growth rate of instabilities.

The wake behind a Mach 2.5 sharp-edged roughness element was comprehensively analysed using direct numerical simulations, bi-global stability analysis and analysis of the three-dimensional parabolic stability equations (PSE) by De Tullio et al. (2013).

A large number of potential instability modes were found to be sustained by the shear layers of the wake, with varicose modes being more unstable than the sinuous ones. Bi-global stability was found to accurately predict the mode shapes but not the instability growth rates, while the three-dimensional PSE analysis could be used to accurately compute the growth rate of these modes.

1.3 Current study

In the current work, roughness-induced wake instability and transition behaviour at Mach 6.0 is studied for a large number of different roughness elements. It aims to extend the work of De Tullio (2013), who performed a similar study for a sharp-edged rectangular box roughness element, to roughness elements with three-dimensional geometries of various types.

The current work tries to analyse and quantify the effect of the three-dimensional roughness shape on the instabilities in the resulting wake and the subsequent transition process. In particular, the roughness frontal profile, planform shape, and the presence of upward or downward ramps have been investigated. This extensive study has been performed using direct numerical simulations and linear stability analysis. For this purpose, a new code was developed and validated that is able to perform linear stability analysis of compressible flows.

Some of the specific research questions that have been addressed in this work are:

(i) How does the three-dimensional shape of an isolated roughness element affect the growth of boundary layer and roughness wake instability modes?

(ii) Does the three-dimensional roughness shape influence the onset location and behaviour of the turbulence transition process?

(iii) Can roughness-induced transition be predicted more accurately using an approach based on features of the roughness near-wake?

(iv) Is linear stability analysis capable of accurately predicting the roughness wake instability modes and/or the overall growth of wake instabilities?

The outline of the current work is as follows: the direct numerical simulation methodology and implementation of the code is discussed in Chapter 2 *(Direct Numerical Simulation Code)*. Linear stability theory is discussed and the newly developed linear stability analysis code `COMPASS` is introduced and validated in Chapter 3 *(COMPASS: Compressible Stability Analysis)*. The computational set-up of the different direct numerical simulations performed in this work is explained in Chapter 4 *(Problem*

Definition & Numerical Set-up), followed by discussion of the results. The results from the direct numerical simulations concerned with the boundary layer receptivity and linear wake instability behind various roughness elements is discussed in Chapter 5 *(Roughness Receptivity & Wake Instability)*, while the linear stability analysis of these roughness wakes is performed in Chapter 6 *(Stability Analysis of Roughness Wakes)*. The full non-linear transition process and the effect of roughness elements on the onset of transition is studied in Chapter 7 *(Roughness-induced Transition)*. Finally, the results are summarised, conclusions are drawn and suggestions for future studies are given in Chapter 8 *(Conclusions & Future Work)*.

Chapter 2

Direct Numerical Simulation Code

In this chapter the governing equations, the three-dimensional compressible Navier-Stokes equations, and the non-dimensionalisation of these equations used in this work are described. Also the implementation of the direct numerical simulation (DNS) code `SBLI` to numerically solve these equations is briefly explained. Although the in-house developed `SBLI` code has been used in the Aerodynamics and Flight Mechanics research group of the University of Southampton for the last few years and has been validated extensively (Redford et al. (2010) and Touber and Sandham (2011) among others), an additional validation test case is discussed that will give more fidelity in some of the more recent code developments and the applicability of `SBLI` to the problems in this work.

2.1 Governing equations

The compressible Navier-Stokes equations for a Newtonian fluid with viscosity μ are obtained by imposing conservation of mass, momentum and energy on a fluid element. The result is a system of non-linear partial differential equations, which in dimensionless form and in a Cartesian reference system can be written as

$$\frac{\partial \rho}{\partial t} + \frac{\partial \rho u_j}{\partial x_j} = 0 \tag{2.1a}$$

$$\frac{\partial \rho u_i}{\partial t} + \frac{\partial \rho u_i u_j}{\partial x_j} + \frac{\partial p}{\partial x_i} = \frac{\partial \tau_{ij}}{\partial x_j} \tag{2.1b}$$

$$\frac{\partial \rho E}{\partial t} + \frac{\partial \left(\rho E + p\right) u_i}{\partial x_i} = -\frac{\partial q_i}{\partial x_i} + \frac{\partial u_i \tau_{ij}}{\partial x_j}. \tag{2.1c}$$

The symmetric viscous stress tensor, τ_{ij}, is defined as

$$\tau_{ij} = \frac{\mu}{Re}\left(\frac{\partial u_j}{\partial x_i} + \frac{\partial u_i}{\partial x_j} - \frac{2}{3}\frac{\partial u_k}{\partial x_k}\delta_{ij}\right), \tag{2.2}$$

where δ_{ij} is the Kronecker delta function defined as

$$\delta_{ij} = \begin{cases} 1 & \text{for } i = j \\ 0 & \text{for } i \neq j. \end{cases} \tag{2.3}$$

The properties of the fluid and the components of the heat flux vector (q_j) are calculated considering the equation of state and the Fourier's law of heat conduction, given respectively by:-

$$p = (\gamma - 1)\left(\rho E - \frac{1}{2}\rho u_i u_i\right) = \frac{1}{\gamma M^2}\rho T \tag{2.4}$$

and

$$q_j = -\frac{\mu}{(\gamma - 1)M^2 Pr Re}\frac{\partial T}{\partial x_j}. \tag{2.5}$$

The non-dimensional parameters involved in the calculations are Reynolds number (Re), Prandtl number (Pr), Mach number (M) and ratio of specific heats (γ), defined as:

$$Re = \frac{\rho_r^* u_r^* l_r^*}{\mu_r^*}, \quad Pr = \frac{C_p^* \mu^*}{\lambda^*}, \quad M = \frac{u_r^*}{\sqrt{\gamma R^* T_r^*}} \quad and \quad \gamma = \frac{C_p^*}{C_v^*}, \tag{2.6}$$

where C_p^* and C_v^* are the specific heats at constant pressure and constant volume, R^* is the specific gas constant and λ^* is the thermal conductivity. Note that the subscript *r* refers to reference values whereas the asterisks (*) denote dimensional variables. The reference values for velocity (u_r^*), density (ρ_r^*), temperature (T_r^*) and dynamic viscosity (μ_r^*) are taken at the free stream. The reference length (l_r^*) is specific to the problem under investigation. Unless stated otherwise, it is taken as the displacement thickness δ_0^* of the laminar similarity profile at the inlet of the numerical domain. The principal non-dimensional variables are defined as follows,

$$\begin{aligned} t &= \frac{t^* u_r^*}{l_r^*}, & x_i &= \frac{x_i^*}{l_r^*}, & \rho &= \frac{\rho^*}{\rho_r^*}, & u_i &= \frac{u_i^*}{u_r^*}, \\ p &= \frac{p^*}{\rho_r^* u_r^{*2}}, & E &= \frac{E^*}{u_r^{*2}}, & T &= \frac{T^*}{T_r^*}, & \mu &= \frac{\mu^*}{\mu_r^*}. \end{aligned} \tag{2.7}$$

The molecular viscosity of a Newtonian fluid is, by definition, only dependent upon temperature and pressure. Here, only its variation with temperature is taken into

account and is calculated by applying Sutherland's law,

$$\mu = T^{\frac{3}{2}} \frac{1 + S^*/T_r^*}{T + S^*/T_r^*}, \tag{2.8}$$

where $S^* = 110.4$ K is the Sutherland reference temperature. The reference temperature T_r^*, taken in the freestream as mentioned earlier, is set to $T_r^* = 273.15$ K unless otherwise stated. It should be noted that this reference value has been chosen to match the set-up of earlier numerical simulations, as will be discussed in Chapter 4 *(Problem Definition & Numerical Set-up)*, and does not correspond to any wind tunnel experiments.

2.2 Numerical methodology

2.2.1 Core of `SBLI`

The core of the `SBLI` DNS code is a collection of Fortran routines to solve the Navier-Stokes equations numerically and advance the solution in time. The calculations are carried out on a structured single-block or multi-block grid discretising the computational domain. An explicit 4^{th}-order central difference scheme is used to compute spatial derivatives at the internal points of the domain, while at the boundaries a stable boundary treatment by Carpenter et al. (1999) is applied, giving an overall 4^{th}-order accuracy. Time integration is based on an explicit third-order compact Runge-Kutta method (Wray, 1986). `SBLI` was made parallel in all spatial directions using the Message Passing Interface (MPI) library.

In order to improve the stability of the non-dissipative central scheme, an entropy splitting approach by Sandham et al. (2002) is used to split the inviscid flux derivatives into conservative and non-conservative parts. The viscous and heat conduction terms in the Navier-Stokes equations are formulated in their Laplacian form to avoid odd-even decoupling commonly associated with central schemes. Odd-even decoupling could occur when a second-derivative is computed by two first-derivative central-difference operations. A total variation diminishing (TVD) shock capturing scheme of Yee et al. (1999) coupled with the Ducros sensor (Ducros et al., 1999) and the Artificial Compression Method (ACM) of Harten (1979) are implemented to handle shocks and contact discontinuities, while minimising introduced numerical dissipation. More features, such as high-order filtering, large eddy simulation (LES) models and passive scalar transport, are available in `SBLI` but have not been used for the work in this report.

2.2.2 Boundary conditions

A variety of different boundary conditions are implemented in SBLI. A very short description is given of the boundary conditions that were used in the simulations of this report.

Wall boundary condition The boundary condition used at walls is isothermal and no-slip (i.e. $u_i = 0$). The wall temperature is set to the wall temperature of the laminar boundary layer imposed at the domain inflow.

(Integrated) characteristic boundary condition At boundaries where unwanted reflections need to be minimised, such as the top and outflow boundary, characteristic boundary conditions are used. At the top boundary, where certain mean freestream conditions are imposed, an integrated characteristic boundary condition (Sandhu and Sandham, 1994) is applied.

Periodic boundary condition At spanwise boundaries of the domain, periodic boundary conditions are always employed. Halo points at the outside of the domain are updated at every time step so that the fourth order central scheme can be used at the periodic boundaries and the use of a one-sided scheme is avoided at these points.

Inflow boundary condition The boundary condition imposed at the inflow is case-specific. A fixed, extrapolated or other inlet condition might be used, and the boundary conditions used for the various cases will be presented in Chapter 4 *(Problem Definition & Numerical Set-up)*.

2.2.3 Linearised version of SBLI

The SBLI code can also be run in a *linearised* mode. This linearised version solves the fluctuating flow variables of the compressible three-dimensional linearised Navier-Stokes equations in its primitive form (and thus for primitive variables $(\rho, u, v, w, T)^\top$) around a steady imposed base flow, instead of the full non-linear Navier-Stokes equations of Equation (2.1). This version has been used to support the validation of the stability analysis code COMPASS, presented in Chapter 3 *(COMPASS: Compressible Stability Analysis)*.

2.3 Validation of SBLI

New major features have been implemented in SBLI in recent years, notably the possibility of having a numerical grid defined fully in three-dimensional generalised coordinates. An earlier version of the code was only able to have extruded grids in the third spatial direction, i.e. $\frac{\partial \xi}{\partial \zeta} = \frac{\partial \eta}{\partial \zeta} = 0$. This new feature allows for the simulation of fully three-dimensional geometries with body-fitted grids, such as wavy walls or bumps. Another new feature is the possibility of defining sector-like grids in cylindrical coordinates. This makes it possible to simulate the flow around bodies of revolution, such as cylindrical cones, with a reduced cost.

2.3.1 Taylor-Couette flow

Taylor-Couette flow is the flow that exists between two cylinders which have a difference in angular velocity between them, i.e. either one cylinder is rotating with the other stationary or both are rotating at different angular velocities. The former case has been chosen here. The curved geometry and the existence of an analytical solution for incompressible Taylor-Couette flow makes it an ideal test case to verify the previously discussed new features of SBLI.

2.3.1.1 Numerical set-up

The numerical grid for this test case has been generated between two cylinders; the inner cylinder of radius $r_1 = 1$ and outer cylinder of radius $r_2 = 2$. The grid does not encompass the full 360° in azimuthal direction, but uses a sectorial grid with an azimuthal angle of $\theta_L = 28°$ with periodic boundary conditions. A diagram of the Taylor-Couette domain is shown in Figure 2.1. Note that not all grid lines are drawn.

The inner boundary (r_1) has been defined as an isothermal wall at which the velocity components have been set to have an azimuthal velocity of unity $(u_\theta = 1)$ while the outer boundary (r_2) has been defined as an isothermal wall at which all velocity components are zero. In radial direction 75 grid points were used and the grid was stretched to cluster more points near the walls. In the azimuthal direction the domain was divided into sectors of 2°, i.e. 15 points ranging from $\theta = 0 - 28°$. In the axial direction (x-direction) the domain length has been set to $L_x = 0.2$ with only 10 grid points since no variation in the axial direction was expected. Periodic boundary conditions are defined to essentially simulate infinite cylinders.

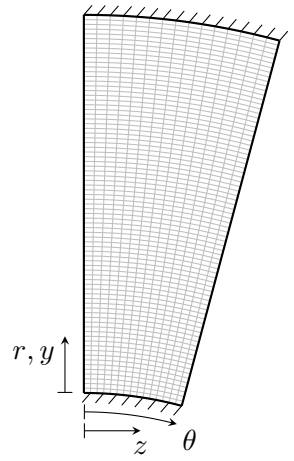

Figure 2.1. Diagram of the Taylor-Couette numerical domain

The Mach number of the flow, i.e. at the rotating inner cylinder, is set to $M = 0.1$ so the result can be compared to the incompressible analytical solution of Taylor-Couette flow. Running the code at a lower Mach number requires very small time steps for stability reasons and was not performed for this validation study. The Reynolds number in this simulation is $Re = 100.0$. The analytical solution of Taylor-Couette flow is independent of Reynolds number however.

2.3.1.2 Analytical solution

In this section the analytical solution of incompressible Taylor-Couette flow is derived from the non-dimensionalised incompressible mass and momentum conservation equations in cylindrical coordinates. A steady-state solution is assumed with no variation in azimuthal and along the length of the cylinder (z-direction). The velocity in the latter direction is set to zero. Therefore

$$\frac{\partial}{\partial t} = 0, \quad u_z = 0, \quad \frac{\partial}{\partial \theta} = \frac{\partial}{\partial z} = 0\,. \tag{2.9}$$

Applying these assumptions to the mass conservation equation yields

$$\frac{1}{r}\frac{\partial\left(r u_r\right)}{\partial r} + \frac{1}{r}\cancel{\frac{\partial u_\theta}{\partial \theta}} + \cancel{\frac{\partial u_z}{\partial z}} = 0$$

$$u_r = 0\,, \tag{2.10}$$

since $u_r(r_1) = u_r(r_2) = 0$.

The radial and azimuthal momentum equations then yield

$$\cancel{u_r\frac{\partial u_r}{\partial r}}+\frac{u_\theta}{r}\cancel{\frac{\partial u_r}{\partial \theta}}-\frac{u_\theta^2}{r}+\cancel{u_z\frac{\partial u_r}{\partial z}} = -\frac{\partial p}{\partial r}+\frac{1}{Re}\left(\frac{1}{r}\frac{\partial}{\partial r}\cancel{\left(r\frac{\partial u_r}{\partial r}\right)}-\cancel{\frac{u_r}{r^2}}+\cancel{\frac{1}{r^2}\frac{\partial^2 u_r}{\partial \theta^2}}-\cancel{\frac{2}{r^2}\frac{\partial u_\theta}{\partial \theta}}+\cancel{\frac{\partial^2 u_r}{\partial z^2}}\right) \tag{2.11}$$

$$\cancel{u_r\frac{\partial u_\theta}{\partial r}}+\frac{u_\theta}{r}\cancel{\frac{\partial u_\theta}{\partial \theta}}+\cancel{\frac{u_r u_\theta}{r}}+\cancel{u_z\frac{\partial u_\theta}{\partial z}} = -\frac{1}{r}\cancel{\frac{\partial p}{\partial \theta}}+\frac{1}{Re}\left(\frac{1}{r}\frac{\partial}{\partial r}\left(r\frac{\partial u_\theta}{\partial r}\right)-\frac{u_\theta}{r^2}+\cancel{\frac{1}{r^2}\frac{\partial^2 u_\theta}{\partial \theta^2}}+\cancel{\frac{2}{r^2}\frac{\partial u_r}{\partial \theta}}+\cancel{\frac{\partial^2 u_\theta}{\partial z^2}}\right) \tag{2.12}$$

$$\begin{cases} \dfrac{u_\theta^2}{r} & = \dfrac{\partial p}{\partial r} \\ \dfrac{1}{r}\dfrac{\partial}{\partial r}\left(r\dfrac{\partial u_\theta}{\partial r}\right) & = \dfrac{u_\theta}{r^2} \end{cases} \tag{2.13}$$

Solving the system in Equation (2.13) for the azimuthal velocity u_θ when applying boundary conditions $u_\theta(r_1) = u_{\theta 1}$ and $u_\theta(r_2) = 0$ results in the analytical solution for the azimuthal velocity in function of the radial coordinate

$$u_\theta(r) = \frac{r_1}{r_1^2 - r_2^2}\, u_{\theta 1}\left(r - \frac{r_2^2}{r}\right) . \tag{2.14}$$

From this equation it is clear that the solution is only dependent on the azimuthal velocity of the inner cylinder $u_{\theta 1}$ and cylinder radii.

2.3.1.3 Validation results

The simulation has been initialised using a linear azimuthal velocity profile in the radial direction and then run until convergence was reached. A contour plot of azimuthal velocity u_θ after convergence is shown in Figure 2.2. It shows perfect concentric circles as expected.

A better comparison between the results can be seen in Figure 2.3, which shows the computed velocity profile at $\theta = 10^\circ$ compared to the analytical profile. The largest relative error between the analytical velocity profile and the DNS results has been found to be approximately 0.006%. Two additional simulations have been performed for which the coordinate system is rotated to ensure that there are no implementation errors that are coordinate-dependent. Excellent agreement has been reached between the different simulations, and it has been found that results are completely independent of the coordinate system.

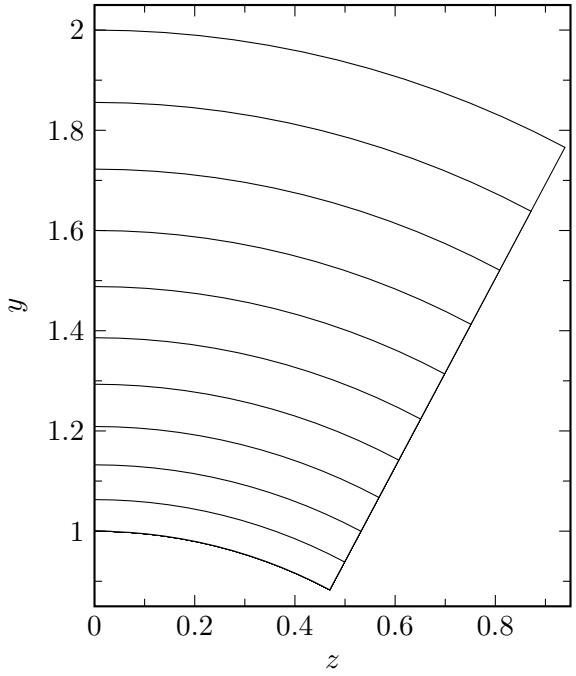

Figure 2.2. Contour plot of azimuthal velocity u_θ. Contours are drawn for $\Delta u_\theta = 0.1$.

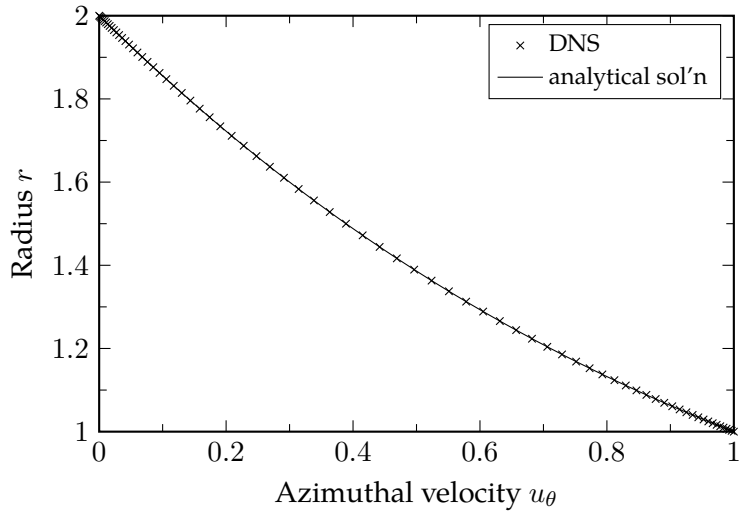

Figure 2.3. Comparison between the numerical result (DNS) and the analytical solution.

Chapter 3

COMPASS: Compressible Stability Analysis

A suite of tools has been developed to perform linear stability analysis of fluid flows, both in the incompressible and compressible regime. It has been named `COMPASS` (***Comp**ressible **A**nalysis-of-**S**tability **S**uite*) and can perform temporal or spatial stability analysis of one-dimensional, two-dimensional or three-dimensional base flows. It has been validated using a large number of reference cases, from the subsonic to the hypersonic flow regime. In this chapter the concept of linear stability theory is briefly explained, the implementation of the code is discussed and the result of the validation campaign are given.

3.1 Linear stability theory

3.1.1 Linearised Navier-Stokes equations

Linear stability theory is concerned with the growth or decay of small unsteady perturbations in a steady base flow. Assuming these perturbations have a much smaller amplitude than the base flow, the primitive flow variables $\mathbf{q} = (\rho, u, v, w, T)^\top$ in the Navier-Stokes equations can be decomposed into a steady part $\bar{\mathbf{q}} = (\bar{\rho}, \bar{u}, \bar{v}, \bar{w}, \bar{T})^\top$ and unsteady part $\tilde{\mathbf{q}} = (\tilde{\rho}, \tilde{u}, \tilde{v}, \tilde{w}, \tilde{T})^\top$, i.e.

$$\mathbf{q}(\mathbf{x}, t) = \bar{\mathbf{q}}(\mathbf{x}) + \epsilon\, \tilde{\mathbf{q}}(\mathbf{x}, t) \tag{3.1}$$

with the small amplitude ansatz

$$\mathcal{O}(\epsilon) \ll 1\,. \tag{3.2}$$

Note that the Navier-Stokes equations in the context of stability analysis are expressed in a primitive variable form, different from the equations in the DNS code discussed in the previous chapter. The primitive form of the compressible Navier-Stokes equations are:

$$\frac{\partial \rho}{\partial t} + \frac{\partial \rho u_j}{\partial x_j} = 0 \tag{3.3a}$$

$$\rho \frac{\partial u_i}{\partial t} + \rho u_j \frac{\partial u_i}{\partial x_j} + \frac{1}{\gamma M^2} \frac{\partial \rho T}{\partial x_i} = \frac{\partial \tau_{ij}}{\partial x_j} \tag{3.3b}$$

$$\rho \frac{\partial T}{\partial t} + \rho u_j \frac{\partial T}{\partial x_j} + (\gamma - 1)\, \rho T \frac{\partial u_j}{\partial x_j} = \frac{\gamma}{Re\, Pr}\, \frac{\partial}{\partial x_j}\left(\mu \frac{\partial T}{\partial x_j}\right) + \gamma(\gamma - 1) M^2 \left(\tau_{ij} \frac{\partial u_i}{\partial x_j}\right) . \tag{3.3c}$$

The Navier-Stokes equations can be linearised around the steady base flow by substitution of the Reynolds decomposition and discarding the higher-order terms of ϵ using the small amplitude ansatz. After subtracting the original Navier-Stokes terms from these equations, the linearised Navier-Stokes equations (LNSE) are obtained. These equations govern the behaviour of the unsteady perturbations and are valid as long as the assumption in Equation (3.2) is not violated. In incompressible form the linearised Navier-Stokes equations can be written as

$$\nabla \cdot \tilde{\mathbf{u}} = 0 \tag{3.4a}$$

$$\frac{\partial \tilde{\mathbf{u}}}{\partial t} + \bar{\mathbf{u}} \cdot \nabla \tilde{\mathbf{u}} + \tilde{\mathbf{u}} \cdot \nabla \bar{\mathbf{u}} = -\nabla \tilde{p} + \frac{1}{Re} \nabla^2 \tilde{\mathbf{u}} \tag{3.4b}$$

The compressible form of the linearised Navier-Stokes equations is given in Appendix A. From here onwards the compressible linearised Navier-Stokes equations are always used.

Note that also in the primitive form of the Navier-Stokes equations, Sutherland's law of viscosity is assumed. Special care should be taken of the linearisation and differentiation of the terms consisting viscosity, because the linearisation of Sutherland's law is non-trivial. Spatial derivatives of the mean viscosity $\bar{\mu}$ follow the usual definition:

$$\frac{\partial \bar{\mu}}{\partial x} = \frac{\mathrm{d}\bar{\mu}}{\mathrm{d}\bar{T}} \frac{\partial \bar{T}}{\partial x} \tag{3.5}$$

During the linearisation, terms consisting of the fluctuating viscosity $\tilde{\mu}$ are introduced. This variable is a new unknown, and a relation between $\tilde{\mu}$ and other (mean)

flow quantities should be defined explicitly. Using a Taylor expansion of the fluctuating viscosity, it can be written as (Lees and Reshotko, 1962)

$$\tilde{\mu} = \frac{\mathrm{d}\bar{\mu}}{\mathrm{d}\bar{T}}\tilde{T} \tag{3.6}$$

for which $\frac{\mathrm{d}\bar{\mu}}{\mathrm{d}\bar{T}}$ arises directly from Sutherland's law and $\tilde{T}$ is part of the solution vector. Derivatives of this term are then expressed as

$$\frac{\partial\tilde{\mu}}{\partial x} = \frac{\mathrm{d}\bar{\mu}}{\mathrm{d}\bar{T}}\frac{\partial\tilde{T}}{\partial x} + \frac{\partial}{\partial x}\left(\frac{\mathrm{d}\bar{\mu}}{\mathrm{d}\bar{T}}\right)\tilde{T}\,. \tag{3.7}$$

3.1.2 Modal stability analysis

Using the linearised Navier-Stokes equations, both the stability of modal and non-modal perturbations can be investigated. In the current work only modal stability analysis is performed.

3.1.2.1 Tri-global stability analysis

If temporally growing (or decaying) modal disturbances with circular frequency ω are assumed one can write the unsteady fluctuations as

$$\tilde{\mathbf{q}}(\mathbf{x}, t) = \hat{\mathbf{q}}(\mathbf{x})\, e^{-i\omega t} \tag{3.8}$$

and the linearised Navier-Stokes equations can be rewritten and expressed as the following generalised eigenvalue problem:

$$\mathbf{A}\hat{\mathbf{q}} = \omega\,\mathbf{B}\hat{\mathbf{q}}\,. \tag{3.9}$$

The matrices $\mathbf{A}$ and $\mathbf{B}$ in this system are square and have dimensions $(5\,N_x N_y N_z)^2$. They multiply the solution vector

$$\hat{\mathbf{q}} = (\rho_{1,1,1}, \mathbf{u}_{1,1,1}, T_{1,1,1}, \rho_{1,1,2}, \ldots, T_{N_x,N_y,N_z})^\top \tag{3.10}$$

and contain the linear operators of the linearised Navier-Stokes equations.

These operators consist of terms originating from the base flow, derivative operators $\mathcal{D}$ working on the base flow, and derivative operators working on the solution vector $\hat{\mathbf{q}}$. The derivative matrices $\mathcal{D}$ are dependent on the chosen method of discretisation, as will be discussed further in this chapter.

In this most general form, no further assumptions are made about the disturbances and the solution of Equation (3.9) yields three-dimensional eigenmodes $\hat{\mathbf{q}}$ with eigenvalue ω. This type of analysis is called *tri-global* stability analysis because it resolves the three non-homogeneous spatial directions.

3.1.2.2 Bi-local/bi-global stability analysis

A simplification of the general tri-global analysis can be made by assuming a parallel base flow and modal disturbances with wavenumber α in the streamwise direction, i.e.

$$\tilde{\mathbf{q}}(\mathbf{x}, t) = \hat{\mathbf{q}}(y, z)\, e^{i(\alpha x - \omega t)}\,. \tag{3.11}$$

The base flow and eigenmodes of the resulting eigenvalue problem will have two non-homogeneous spatial directions, i.e. y and z, and this analysis is therefore called *bi-local* stability analysis. Note that one could also assume modal disturbances in the spanwise direction z with wavenumber β and keep the streamwise direction non-homogeneous. This would allow for the analysis of e.g. two-dimensional growing boundary layers, but is not considered in the current work. Note that in literature *bi-local* stability analysis is usually called *bi-global* analysis. However, this term does not seem appropriate here, since the instability analysis is not concerned with global instabilities but convective instabilities. Therefore, the term *bi-local* will be used from here onwards.

Both temporally and spatially growing (or decaying) instabilities can be investigated using the bi-local stability framework of Equation (3.11). Temporally growing disturbances can be computed by defining a real wavenumber α and solving the resulting eigenvalue problem for the complex eigenvalue $\omega = \omega_r + i\omega_i$ in which ω_r is the wavenumber and ω_i the growth rate of the corresponding eigenmode. Spatially growing disturbances can be computed by defining a real frequency ω and solving for a complex $\alpha = \alpha_r + i\alpha_i$. In this case, the resulting eigenvalue problem will be a quadratic eigenvalue problem (QEVP) due to the higher spatial derivatives in the LNSE. The resulting QEVP has the following form:

$$\alpha^2\, \mathbf{M}\hat{\mathbf{q}} + \alpha\, \mathbf{C}\hat{\mathbf{q}} + \mathbf{K}\hat{\mathbf{q}} = 0\,. \tag{3.12}$$

Direct quadratic eigenvalue solvers exist but are a fairly recent development, such that this quadratic eigenvalue problem is often linearised so that traditional eigenvalue solvers can be used. More details on the used eigenvalue solvers and their implementation into `COMPASS` will be discussed in the next section.

Table 3.1. Summary of different stability analysis types and the related assumptions, base flow, disturbance and phase functions

Analysis	Assumption	Base Flow	Disturbance	Phase Func.
Tri-global	-	$\bar{\mathbf{q}}(x,y,z)$	$\tilde{\mathbf{q}}(x,y,z,t)$	$e^{-i\omega t}$
Bi-local	$\frac{\partial \bar{\mathbf{q}}}{\partial x} = 0$	$\bar{\mathbf{q}}(y,z)$	$\tilde{\mathbf{q}}(y,z,t)$	$e^{i(\alpha x - \omega t)}$
Local	$\frac{\partial \bar{\mathbf{q}}}{\partial x} = \frac{\partial \bar{\mathbf{q}}}{\partial z} = 0$	$\bar{\mathbf{q}}(y)$	$\tilde{\mathbf{q}}(y,t)$	$e^{i(\alpha x + \beta z - \omega t)}$

3.1.2.3 Local stability analysis

A further simplification can be made by assuming a single non-homogeneous direction, in this case the wall-normal direction y, and perturbations of the form

$$\tilde{\mathbf{q}}(\mathbf{x},t) = \hat{\mathbf{q}}(y)\, e^{i(\alpha x + \beta z - \omega t)}\,. \tag{3.13}$$

This type of analysis is called *local* stability analysis. After substituting the assumption of Equation (3.13) in the incompressible form of the linearised Navier-Stokes equations, the classic Orr-Sommerfeld (OS) equation can be retrieved. The compressible form of the resulting equations can be found in Malik (1990). Similarly to bi-local stability, both temporal and spatial local stability analysis can be performed by solving for complex frequency ω or wavenumber α respectively. A summary of the different types of analysis, the assumptions, and the form of the base flow and disturbances is given in Table 3.1.

3.2 Implementation of the stability code COMPASS

COMPASS consists of a number of tools, written in MATLAB and Fortran, to perform modal linear stability analysis, both temporal and spatial, in a local or bi-local framework. In the code all matrices and structures are inherently three-dimensional, so that performing tri-global analysis of three-dimensional base flows would be trivial, except for the computational cost.

Figure 3.1 is a diagram that shows the core of the COMPASS code. Further in this section some of the building blocks in this diagram will be discussed in more detail, but essentially it consists of four main pillars:

Initialisation The flow variables (M, Re, C_{suth}, etc) and the analysis variables (type of analysis, grid size, ω, α, etc) are set, matrices are allocated in memory and a numerical grid is constructed.

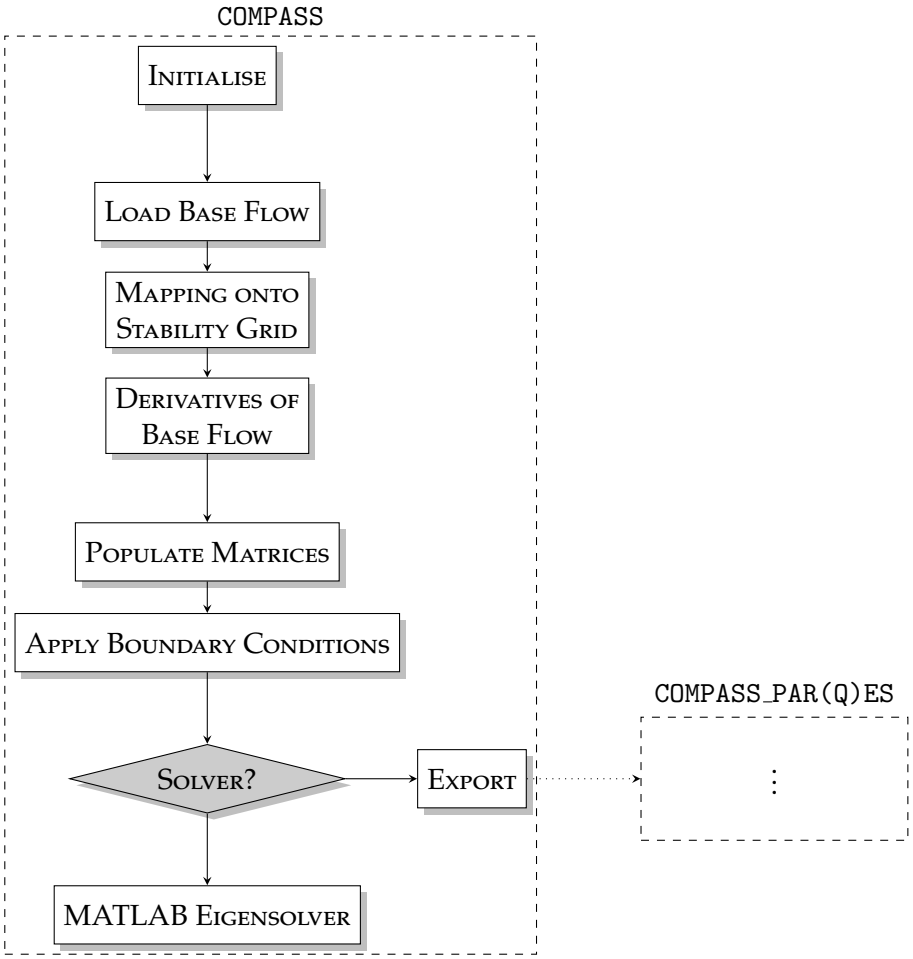

Figure 3.1. Flowchart of the core of `COMPASS` and solver `COMPASS_PAR(Q)ES`

Loading base flow The base flow is read from an external file (or computed in case of simple flows like a Blasius boundary layer), mapped onto the numerical grid and its spatial derivatives are computed.

Matrix generation The matrices $\mathbf{A}$ and $\mathbf{B}$ (or $\mathbf{M}$, $\mathbf{C}$, $\mathbf{K}$ for spatial analysis) of the relevant eigenvalue problem are constructed and populated. Appropriate boundary conditions are also applied.

Solving The relevant eigenvalue problem can be solved by two different solvers: the internal MATLAB eigensolvers or the fully parallelised `COMPASS_PAR(Q)ES`.

The main routine of `COMPASS` expects the following input arguments: Mach number M, Reynolds number Re, streamwise wavenumber α, spanwise wavenumber β, frequency ω, number of grid points of the numerical grid in all three directions

$(N_x, N_y, N_z)^\top$, size of the numerical domain $(L_x, L_y, L_z)^\top$ and Sutherland's law constant C_{suth}. Note that not all arguments are required for all types of analysis, e.g. for temporal stability analysis the frequency ω is the sought after variable and therefore does not need to be given as input, whereas for bi-local stability the spanwise wavenumber β is not required since no modal solution is assumed in the spanwise direction.

3.2.1 Numerical grid and differentiation methods

During initialisation, a numerical grid is constructed based on the input arguments. The grid coordinates in a certain direction not only depend on the length of the domain and the number of grid points, but also on the differentiation method that will be used in that direction.

3.2.1.1 Fourier spectral differentiation

In the spanwise direction, a spectral differentiation method based on the (inverse) discrete Fourier transform (DFT) is used in the current work. On an equispaced grid with coordinates $x_n = 2\pi n/N$, the discrete Fourier transform of a continuous periodic function $f(x)$ is defined as

$$F_k = \frac{1}{N} \sum_{n=0}^{N-1} f_n \, e^{-ikx_n}, \quad \text{for } k = 0, 1, \ldots, N-1 \tag{3.14}$$

with N the number of Fourier modes, always taken to be even in this work. The inverse DFT is then

$$f(x_n) \equiv f_n = \sum_{k=0}^{N-1} F_k \, e^{ikx_n} \, . \tag{3.15}$$

If a function $f(x)$ can be approximated at a coordinate x_n as $f(x_n) \equiv f_n$, then the first derivative $f'(x)$ of this function can then be approximated as

$$f'(x_n) = \sum_{k=0}^{N-1} i \, k \, F_k \, e^{ikx_n} \, . \tag{3.16}$$

This operation can be expressed explicitly as a matrix multiplication

$$\mathbf{f}' = \mathbf{D}_N^{(1),\text{Fourier}} \cdot \mathbf{f} \tag{3.17}$$

with $\mathbf{D}_N^{(1),\text{Fourier}}$ the Fourier differentiation matrix for the first derivative. The elements $d_{i,j}^{(1)}$ of this matrix can be computed a priori:

$$d_{i,j}^{(1)} = \begin{cases} 0 & \text{if } i = j \\ \frac{1}{2}(-1)^{(i+j)} \cot((i-j)h/2) & \text{if } i \neq j \end{cases} \tag{3.18}$$

so that the Fourier differentiation matrix has the form

$$\mathbf{D}_N^{(1),\text{Fourier}} = \begin{bmatrix} 0 & \dots & -\frac{1}{2}\cot\frac{1}{2}h \\ -\frac{1}{2}\cot\frac{1}{2}h & \ddots & \frac{1}{2}\cot\frac{2}{2}h \\ \frac{1}{2}\cot\frac{2}{2}h & \ddots & -\frac{1}{2}\cot\frac{3}{2}h \\ \vdots & \ddots & \vdots \\ \frac{1}{2}\cot\frac{1}{2}h & \dots & 0 \end{bmatrix} \tag{3.19}$$

with $h = 2\pi/N$.

Matrix multiplication with matrix $\mathbf{D}^{(1),\text{Fourier}}$ yields a first derivative. Higher-order derivatives, e.g. the second derivative, can then be obtained by recursion, i.e.

$$\mathbf{D}_N^{(p),\text{Fourier}} = \underbrace{\mathbf{D}_N^{(1),\text{Fourier}} \cdot \mathbf{D}_N^{(1),\text{Fourier}} \cdot \dots}_{p \text{ times}} \tag{3.20}$$

Recall that this method requires an equispaced grid, such that the coordinates of the numerical grid in z-direction are set to

$$z_k = \frac{k-1}{N_z} L_z\,, \qquad \text{where } k = 1, \dots, N_z\,. \tag{3.21}$$

Note that, since the differentiation matrices introduced before assume a grid on the interval $z \in [0, 2\pi)$ instead of $z \in [0, L_z)$, the elements of matrices $\mathbf{D}_N^{(p),\text{Fourier}}$ need to be multiplied by $(L_z/(2\pi))^p$.

In the wall-normal direction no periodicity can be assumed and two different differentiation methods are implemented: the Chebyshev pseudo-spectral method and the high-order finite-difference method (FD-q) of Hermanns and Hernández (2008).

3.2.1.2 Chebyshev pseudo-spectral method

In case no periodicity can be assumed but one would like to exploit the advantage that spectral methods have regarding convergence behaviour, a differentiation method

based on Chebyshev polynomials can be applied (Don and Solomonoff, 1997). On interval $\xi \in [-1, 1]$, a continuous function $f(\xi)$ can be be approximated as a Chebyshev series at N discrete Chebyshev-Gauss-Lobatto (CGL) points $\xi_n = \cos(\frac{n\pi}{N})$:

$$f(\xi_n) \equiv f_n = \sum_{k=0}^{N} a_k T_k(\xi_n) \tag{3.22}$$

with Chebyshev coefficients a_k and Chebyshev polynomial of degree k

$$T_k(\xi) = \cos(k \cos^{-1}(\xi)) \,. \tag{3.23}$$

The first derivative $f'(\xi)$ can then be approximated by

$$f'(\xi_n) = \sum_{k=0}^{N} a_k T'_k(\xi_n) \,. \tag{3.24}$$

Using Equation (3.22), a discrete Fourier transform can be applied to express the Chebyshev coefficients a_k as a function of the function values at the CGL points x_n:

$$a_k = \frac{2}{c_k N} \sum_{n=0}^{N} \frac{1}{c_n} f(\xi_n) \cos(\frac{nk\pi}{N}) \tag{3.25}$$

in which $c_1 = c_N = 2$ and $c_n = 1$ for $n = 1, 2, \ldots, N-1$.

Also the operation in Equation (3.24) can then be expressed as a matrix multiplication, for which the resulting differentiation matrix $\mathbf{D}_N^{(1),\text{Chebyshev}}$ will have elements

$$d_{i,j}^{(1)} = \begin{cases} \frac{c_i}{c_j} \frac{(-1)^{i+j}}{\xi_i - \xi_j} & \text{for } i \neq j, 0 \leq i, j \leq N \\ -\frac{\xi_i}{2(1-\xi_i^2)} & \text{for } i = j, 1 \leq i, j \leq N-1 \\ \frac{1N^2+1}{6} & \text{for } i = j = 1 \text{ or } i = j = N \end{cases} \tag{3.26}$$

Higher-order differentiation matrices can be easily computed using recursion, i.e.

$$\mathbf{D}_N^{(p),\text{Chebyshev}} = \underbrace{\mathbf{D}_N^{(1),\text{Chebyshev}} \cdot \mathbf{D}_N^{(1),\text{Chebyshev}} \cdot \ldots}_{p \text{ times}} \tag{3.27}$$

3.2.1.3 FD-q method

The disadvantage of the spectral methods introduced in this chapter is that the resulting matrix multiplication will yield full matrices. When a large number of grid points (and thus matrix elements) is required, for example in the case of bi-local

or tri-global stability analysis, full matrices will result in very high computational memory usage. Therefore methods that result in sparse or banded matrices, such as finite difference (FD) methods, are desired, since they are computationally much cheaper and can reduce the computational requirements significantly.

For this reason, Hermanns and Hernández (2008) developed a high-order finite difference method FD-q, that uses the sparsity advantage of finite difference methods and allows for the construction of FD stencils of arbitrary order q, which minimises interpolation errors and for which spectral-like convergence behaviour is reached as $q \to N$. A very brief explanation of the method is given here. For the full details of the method, the reader is advised to consult the original work of Hermanns and Hernández.

The FD-q method approximates the derivative of a continuous function $f(\xi)$ by constructing a piecewise polynomial interpolant, consisting of individual interpolants $I_n(\xi)$ of polynomial degree q, that match the function values $f(\xi_n)$ at a series of discrete grid points ξ_n in the interval $\xi \in [-1, 1]$. The derivative of this function $f'(\xi_n)$ is then found by computing the derivative of the interpolants I_n at these points. A typical value of q used in this work is $q = 8$.

The individual polynomial interpolants $I_n(x)$ are defined using Lagrange interpolation as

$$I_n(x) = \sum_{m=s_n}^{s_n+q} \ell_{n,m}(\xi) f_m \,, \qquad \ell_{n,m} = \prod_{\substack{j=0 \\ s_n+j \neq m}}^{q} \frac{\xi - \xi_{s_n+j}}{\xi_m - \xi_{s_n+j}} \tag{3.28}$$

where the seed s_n denotes the index of the lower limit grid point ξ_n of the stencil used for the construction of the interpolant, defined as

$$s = \{\underbrace{0, \ldots, 0}_{q/2 \text{ times}}, 0, 1, \ldots, N-q, \underbrace{N-q, \ldots, N-q}_{q/2 \text{ times}}\} \,. \tag{3.29}$$

This approach results in a centred FD stencil away from the domain boundaries and stencils biased towards the inner grid points near the domain boundaries.

A key characteristic of the FD-q method is that it uses Chebyshev roots (or Chebyshev-Gauss quadrature points) as grid points ξ_n in the limit of $q \to N$ in order to suppress the Runge phenomenon, characterised by oscillations near the ends of the interpolation interval, that accompanies high-order polynomial interpolation on equispaced grids (Platte et al., 2011). For $q < N$ the grid points will be non-uniformly distributed and are obtained by a non-linear optimisation problem that minimises the pointwise interpolation error on the resulting grid.

3.2.1.4 Mapping to physical coordinates

Both Chebyshev's pseudo-spectral method and the FD-q method are defined on bounded interval $\xi \in [-1, 1]$. In order to map the computational coordinates ξ to physical coordinates in interval $y \in [0, y_{\text{max}}]$, the algebraic mapping proposed by Malik (1990) is used:

$$y = a\frac{1+\xi}{b+\xi} \tag{3.30}$$

with

$$a = y_i \frac{y_{\text{max}}}{y_{\text{max}} - 2\,y_i}\,, \quad b = 1 + 2\frac{a}{y_{\text{max}}}\,. \tag{3.31}$$

In these equations the constant y_i can be chosen freely to cluster points together, such that half of the grid points are located in interval $[0, y_i]$.

3.2.2 Base flow

After the initialisation, a steady base flow is loaded into memory. This can either be done from an external data file, e.g. computed from a precursor LES or DNS, or by calling a function that computes the base flow directly. The latter method is used to obtain simple base flows like a Blasius boundary layer, for which the theoretical solution can easily be computed. The base flow is then mapped onto the numerical grid, and the spatial derivatives of the base flow are computed using the differentiation matrices resulting from one of the methods discussed previously.

3.2.3 Populating of matrices

Once the base flow and its derivatives are computed, the matrices $\mathbf{A}$ and $\mathbf{B}$ (or $\mathbf{M}$, $\mathbf{C}$, $\mathbf{K}$) of the relevant eigenvalue problem are populated. For each grid point (i, j, k) a call is made to a function that returns the linearised Navier-Stokes operators, based on the base flow at that point and the chosen differentiation method.

3.2.4 Boundary Conditions

Appropriate conditions for the perturbations need to be prescribed at the domain boundaries. In general, various types of boundary conditions can be applied, but in the current work only two different conditions are prescribed.

At the domain boundaries in the y-direction, it is assumed that perturbations vanish, since the current work is only concerned with flows that are wall-bounded and/or

bound by an undisturbed freestream far away. Therefore, fluctuating quantities $\tilde{\mathbf{u}}$ and $\tilde{T}$ are set to zero at these boundaries, while the density $\tilde{\rho}$ is allowed to vary, i.e.

$$\tilde{u}_{i,1,k} = \tilde{u}_{i,N_y,k} = 0 \tag{3.32a}$$

$$\tilde{v}_{i,1,k} = \tilde{v}_{i,N_y,k} = 0 \tag{3.32b}$$

$$\tilde{w}_{i,1,k} = \tilde{w}_{i,N_y,k} = 0 \tag{3.32c}$$

$$\tilde{T}_{i,1,k} = \tilde{T}_{i,N_y,k} = 0 \tag{3.32d}$$

with $i = 1, \ldots, N_x$ and $k = 1, \ldots, N_z$.

Whenever the spanwise direction is not taken to be homogeneous, e.g. for bi-local or tri-global stability analysis, periodicity is always assumed in this direction. Because a Fourier differentiation method is used in this direction, as discussed previously in this chapter, boundary conditions do not need to be explicitly applied at the spanwise boundaries ($k = 1, k = N_z$).

3.2.5 Solver

After applying the boundary conditions, the matrices of the eigenvalue system are complete, and the system can be solved. Two different solvers can be used.

3.2.5.1 MATLAB eigensolver

For cases where not a lot of computational memory and power is required, such as local or small bi-local cases, the eigenvalue problem can be solved directly by the internal MATLAB eigensolver `eigs` or `polyeig`.

3.2.5.2 `COMPASS_PAR(Q)ES`

For larger problems where the memory requirements are too high to solve the system on a single workstation, the generated matrices of the eigenvalue problem can be exported and solved by `COMPASS_PAR(Q)ES` or ***Par**allel (**Q**uadratic) **E**igenvalue **S**olver*. This solver is programmed in Fortran and is built around the high-performance libraries SLEPc [1], PETSc [2] and MUMPS[3]. The solver is fully parallelised and can run on computational clusters.

[1] SLEPc - `http://www.grycap.upv.es/slepc/`
[2] PETSc - `http://www.mcs.anl.gov/petsc/`
[3] MUMPS - `http://mumps.enseeiht.fr/`

COMPASS_PAR(Q)ES uses a Krylov-Schur technique, implemented in SLEPc, to iteratively solve the eigenvalue system. This method is essentially a modified Arnoldi iteration with an improved restarting technique, which overcomes some of the problems of the traditional implicitly restarted Arnoldi algorithm (Stewart, 2002). Full details on this technique and its implementation in SLEPc can be found in Hernandez et al. (2005). Note that COMPASS_PAR(Q)ES reads in either matrices $\mathbf{A}$ and $\mathbf{B}$ or $\mathbf{M}$, $\mathbf{C}$ and $\mathbf{K}$, depending on whether the matrices originate from a temporal or spatial stability problem respectively. In the case where the matrices $\mathbf{M}$, $\mathbf{C}$ and $\mathbf{K}$ of the quadratic eigenvalue problem are given, the problem is linearised internally by SLEPc.

The Krylov-Schur method (and related methods) is very effective at finding eigenvalues near the extremes of the spectrum, i.e. largest/smallest eigenvalues. In order to efficiently compute eigenvalues that are not located near the extremes of the spectrum, a shift-and-invert spectral transformation technique is used to improve the convergence of eigenvalues near a certain region of interest. Essentially, the generalised eigenvalue problem of Equation (3.9) is transformed into

$$(\mathbf{A} - \sigma\mathbf{B})^{-1}\,\mathbf{B}\,\hat{\mathbf{q}} = \theta\hat{\mathbf{q}} \tag{3.33}$$

such that the largest eigenvalues θ of the transformed system correspond to the eigenvalues ω of the original system that are closest to a certain shift σ. After using the Krylov-Schur method to find the eigenvalues of the transformed system, the original eigenvalues can be retrieved by

$$\omega = \sigma + 1/\theta\,. \tag{3.34}$$

The shift σ can be a complex number such that the target eigenvalues, i.e. the region of interest, can lie in the whole complex plane, as long as the resulting matrix $(\mathbf{A} - \sigma\mathbf{B})$ is not singular.

3.2.5.3 Parallel scaling of COMPASS_PAR(Q)ES

The ability of COMPASS to run very large problems can be assessed by the effectiveness of the parallel scaling. If the code has good scalability characteristics, larger problems can be run on a larger number of processors to reduce the overall runtime and the memory requirements per computational processor. The code speed-up is defined as the ratio of the serial runtime, run on a single processor, to the runtime of the

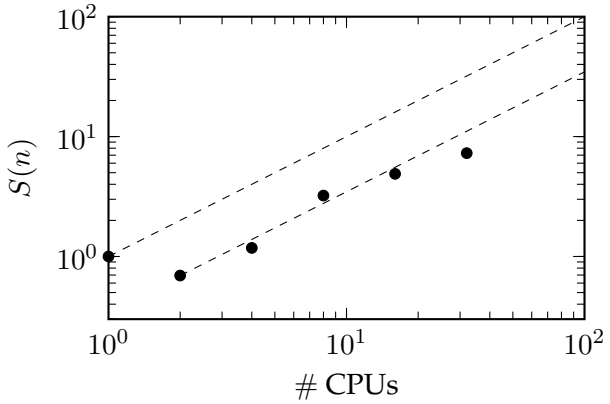

Figure 3.2. Strong scaling of `COMPASS_PAR(Q)ES`.

code run on a specific number of processors:

$$S(n) = \frac{t(n=1)}{t(n)} \tag{3.35}$$

Two different types of scaling can be considered: weak and strong. Weak scaling is concerned with the speed-up when the number of processors and the size of the problem increases such that the problem size per processor remains the same. For strong scaling, the number of processors increases while the total size of the problem remains the same. Analysis of the strong scaling characteristics essentially yields the number of processors that can be used to efficiently solve a problem with a specific size. The optimal strong scaling is linear speed-up, i.e. the computational time halves for a doubling of the number of processors ($S_{\text{opt}}(n) = n$).

The strong scaling behaviour of `COMPASS_PAR(Q)ES` is shown in Figure 3.2. The speed-up curve in this figure is for a typical bi-local stability computation of a roughness wake, as will be discussed in Chapter 6 *(Stability Analysis of Roughness Wakes)*. This case has $N_y = 301$ grid points in the wall-normal direction, discretised using the FD-q method of order $q = 8$, and $N_z = 140$ grid points in the spanwise direction, using Fourier spectral differentiation. The case was run for 30 Arnoldi iterations on the Iridis 4[4] high performance computing facility from the University of Southampton, after which approximately 30-35 eigenvalues are found.

From Figure 3.2 it can be seen that there is an initial penalty to running the code in parallel, and the runtime on 2 processors is actually longer than running the

[4]Iridis, University of Southampton, `http://cmg.soton.ac.uk/iridis`

code in a serial way. This is due to the necessary internal communication between the different processors, which adds to the runtime. After this initial penalty the scaling behaviour is relatively linear. It should be noted that the parallel scaling capability and its associated behaviour should be completely attributed to the high performance library MUMPS.

However, the scaling behaviour is far from being optimal. For example, the computation on 32 processors took approximately 4.4 longer than the optimal runtime based on the serial code and 1.5 times longer than the optimal time if the initial penalty is neglected. This might be due to the fact that Fourier discretisation is used in the spanwise direction, which yields dense differentiation matrices and thus not a fully sparse eigenvalue problem. The Krylov-Schur technique used to solve the eigenvalue problem is optimised for sparse matrices, such that better scaling might be achieved if the FD-q method is also used in the spanwise direction.

3.3 Validation of COMPASS

COMPASS has been extensively validated for subsonic to hypersonic flows, both for temporal/spatial and local/bi-local stability analysis. In this section some of the validation cases are discussed.

3.3.1 Blasius boundary layers

The first validation cases that are investigated are temporally and spatially growing disturbances in Blasius boundary layers at a variety of Mach numbers. The results computed by COMPASS are compared with the original published results and/or cross-validated with the local stability analysis and PSE code NoSTRANA, developed completely independently from COMPASS by Andrea Sansica at the University of Southampton. The flow parameters of the investigated cases are listed in Table 3.2 and Table 3.3 for respectively the temporal and spatial stability analyses.

Since the base flows of these cases are one-dimensional boundary layer profiles, COMPASS was run in local stability mode. The code was run with Chebyshev differentiation in the wall-normal direction and an increasing number of grid points to ensure a grid-converged solution.

The sensitivity of the full spectrum to the number of grid points for case MAL-2.5 can be seen in Figure 3.3. From this figure it is clear that the most unstable mode and the discrete modes for $c_{ph} < 0.5$, which are the actual modes of interest, agree

Table 3.2. Parameters of the Blasius boundary layer validation cases for temporal stability analysis. References specified in the table are Malik (1990), Macaraeg (1988) and Sandham and Lüdeke (2009).

Case	Reference	M	Re	α	β	C_{suth}
MAL-0	Malik	0	580	0.179	0.0	198.6/500
MAL-0.5	Malik	0.5	2000	0.1	0.0	198.6/476.19
MAL-2.5	Malik	2.5	3000	0.06	0.01	198.6/266.67
MAC-0	Macaraeg	0	2200	0.2	0.0	198.6/520
MAC-4.5	Macaraeg	4.5	10 000	0.6	1.0392	198.6/520
SAN-6	S & L	6.0	20 000	$2/3\pi$	0.0	110.4/216.65

Table 3.3. Parameters of the Blasius boundary layer validation case for spatial stability analysis, based on Danabasoglu and Biringen (1990).

Case	Reference	M	Re	ω	β	C_{suth}
DAN-0	Danabasoglu & Biringen	0	580	0.0652	0.0	198.6/600

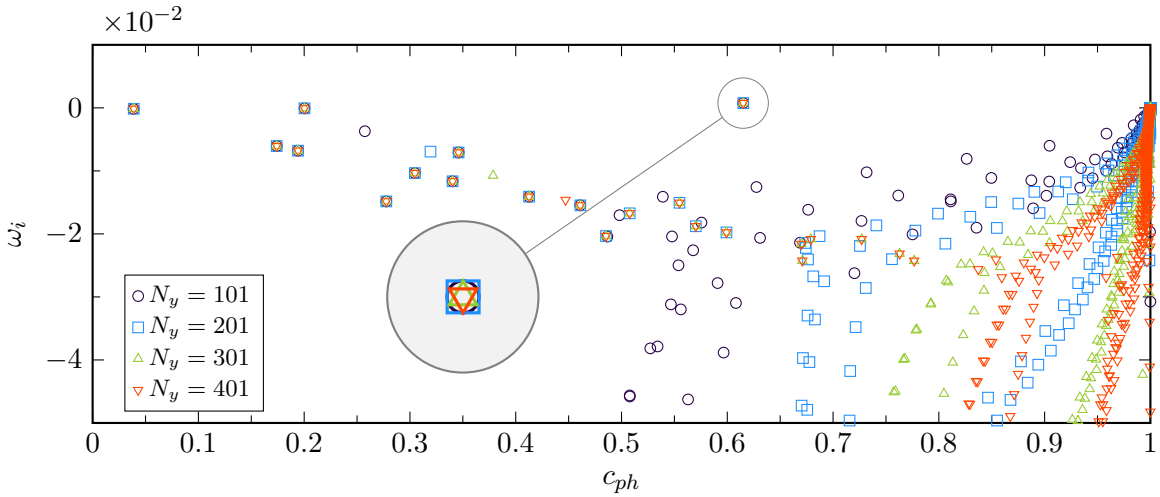

Figure 3.3. Grid sensitivity of the COMPASS results for the Mach 2.5 temporal stability case MAL-2.5.

perfectly for grid sizes above $N_y > 100$. The branches on the right ($c_{ph} > 0.5$) are discrete representations of a continuous branch, a characteristic resulting from the truncated semi-infinite domain.

A more quantitative representation of the grid sensitivity and convergence behaviour

Table 3.4. Eigenvalue of the most unstable mode of the Mach 2.5 Blasius boundary layer validation case MAL-2.5 for different grid sizes.

N_y	ω_r	ω_i
41	0.038 152 117 548 121	0.002 770 150 953 887
61	0.036 481 149 482 166	0.000 604 402 715 123
81	0.036 734 273 813 152	0.000 591 163 112 862
101	0.036 733 849 945 214	0.000 584 595 468 103
121	0.036 733 747 334 344	0.000 584 468 170 743
141	0.036 733 746 024 881	0.000 584 464 471 315
161	0.036 733 746 083 224	0.000 584 464 402 815
181	0.036 733 746 087 597	0.000 584 464 403 179
201	0.036 733 746 089 944	0.000 584 464 402 666

of case MAL-2.5 is given in Table 3.4, which shows the eigenvalue of the most unstable mode computed for different grids. From this table, it is evident that the first six significant digits are converged already at $N_y = 141$. This explains the excellent agreement between the results on the different grids in Figure 3.3, which had many more grid points.

Table 3.5 (temporal) and Table 3.6 (spatial) show the grid-converged values of the computed most unstable (or least stable) eigenvalues for the Blasius boundary layer validation cases. In these tables the results computed with COMPASS and NoSTRANA are listed and a comparison is made between COMPASS, NoSTRANA and the original reference (or original code in case of SAN-6.0). The difference between COMPASS and the other results, listed in these tables, is computed as

$$\phi_{\text{Diff.}} = \frac{\phi_{\texttt{COMPASS}} - \phi_r}{\phi_r} \tag{3.36}$$

with $\phi_{\texttt{COMPASS}}$ and ϕ_r respectively the eigenvalue computed by COMPASS and the reference value.

It can be seen that the agreement between the results from COMPASS and the original reference (or the independent code NoSTRANA) is excellent. For the temporal stability analyses, the only difference occurs for the growth rate (the imaginary part of the eigenvalue) of case MAL-0 ($\Im(\phi_{\text{Diff.}}) = 0.77\%$) and case SAN-6.0 ($\Im(\phi_{\text{Diff.}}) = 0.11\%$). For all other temporal stability cases, there is no difference between the results, up to six significant digits. For the spatial case DAN-0, the difference with the original results is slightly larger for the growth rate, i.e. $\Im(\phi_{\text{Diff.}}) = 1.18\%$, but the comparison between COMPASS and NoSTRANA reduces to $\Im(\phi_{\text{Diff.}}) = 0.09\%$.

Table 3.5. Comparison of computed most unstable eigenvalues $\omega = \omega_r + i\omega_i$ of the Blasius boundary layer cases.

Case	COMPASS	Reference	Diff. (%)	NoSTRANA	Diff. (%)
MAL-0	$0.065178 + i0.001425$	$0.065174 + i0.001414$	$0.00 + i0.77$	$0.065178 + i0.001425$	$0.00 + i0.00$
MAL-0.5	$0.029082 + i0.002244$	$0.029082 + i0.002244$	$0.00 + i0.00$	$0.029082 + i0.002244$	$0.00 + i0.00$
MAL-2.5	$0.036751 + i0.000581$	$0.036734 + i0.000584$	$0.00 + i0.00$	$0.036734 + i0.000584$	$0.00 + i0.00$
MAC-0	$0.059836 + i0.004023$	$0.059836 + i0.004023$	$0.00 + i0.00$	$0.059836 + i0.004023$	$0.00 + i0.00$
MAC-4.5	$0.496105 + i0.003765$	$0.496105 + i0.003765$	$0.00 + i0.00$	$0.496105 + i0.003765$	$0.00 + i0.00$
SAN-6.0	$1.964614 + i0.015733$	$1.964614 + i0.015751$	$0.00 + i0.11$	$1.964614 + i0.015733$	$0.00 + i0.00$

Table 3.6. Comparison of computed least stable eigenvalue $\alpha = \alpha_r + i\alpha_i$ of the Blasius boundary layer case.

Case	COMPASS	Reference	Diff. (%)	NoSTRANA	Diff. (%)
DAN-0	$0.17930 + i0.003317$	$0.17939 + i0.003278$	$0.01 + i1.18$	$0.17932 + i0.003320$	$-0.01 - i0.09$

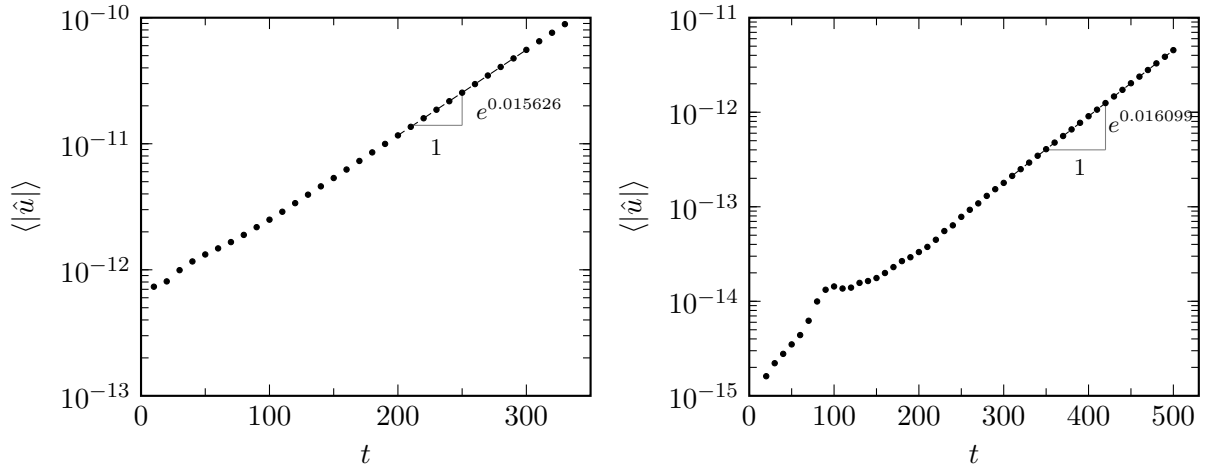

(a) Lin. SBLI **(b)** SBLI

Figure 3.4. Temporal evolution of the streamwise velocity fluctuations for case SAN-6.0, computed by Lin. SBLI and SBLI.

Table 3.7. Comparison of the largest growth rate of case SAN-6.0.

Case	COMPASS	**Lin.** SBLI	**Diff. (%)**	SBLI	**Diff. (%)**
SAN-6.0	0.015733	0.015626	−0.68	0.016099	2.33

The instability of case SAN-6.0 has also been computed using the non-linear and linearised version of SBLI, as introduced in Chapter 2 *(Direct Numerical Simulation Code)*. In the non-linear computation, the base flow is kept constant by an appropriate forcing in the Navier-Stokes equations. A streamwise periodic domain with a streamwise parallel base flow is used in the SBLI computations. The streamwise extent is taken to be the wavelength of the most unstable mode computed by COMPASS, and the flow fields are sampled at regular time intervals such that the temporal growth of this mode can be computed. The growth rate is computed from the streamwise velocity fluctuation integrated over the numerical domain, as shown by Figure 3.4. The resulting growth rates are summarised in Table 3.7, which shows a good agreement (less than 1%) between COMPASS and the linearised version of SBLI. The non-linear version of SBLI shows a slightly larger difference, i.e. 2.3%.

From the comparisons between COMPASS, the original references, NoSTRANA and SBLI, summarised in Tables 3.5 to 3.7, it can be concluded that the linear stability of Blasius boundary layers at a variety of Mach numbers is accurately computed by COMPASS.

Table 3.8. Parameters of the incompressible streaky Couette flow validation case of Reddy et al. (1998).

Case	Reference	M	Re	α	β
REDDY	Reddy et al.	0	500	1.0	2.0

3.3.2 Streaky Couette flow

The validation cases in the previous section were performed using local stability analysis, i.e. the flow in the spanwise direction was taken to be homogeneous and not resolved by the analysis. In order to validate the bi-local analysis, a two-dimensional base flow and disturbances with two non-homogeneous directions needs to be considered. Bi-local analysis has been performed of the Blasius boundary layer cases of the previous section, for which no significant difference was observed between the local and bi-local results. However, since these boundary layer flows are constant in the spanwise direction, the spanwise differencing portion of `COMPASS` cannot be fully tested by these cases. A well-prescribed base flow is thus required which varies both in the wall-normal and spanwise direction. The case that was used to validate the bi-local stability analysis is the streaky Couette flow of Reddy et al. (1998), termed REDDY from here onwards.

An incompressible Couette flow is assumed between two walls at $y = -1$ and $y = 1$. The walls are assumed infinite, so periodic boundary conditions can be applied at the spanwise boundaries (i.e. the z-direction). The Reynolds number of the flow is set to $Re = 500$ and the base flow has only a streamwise velocity component, and is prescribed by

$$\bar{u}(y, z) = Sy + 2A_{st}\cos(\beta z) \tag{3.37}$$

with shear S. In this equation, A_{st} is the amplitude of a prescribed streak that has spanwise wavenumber β. The case that will be used for comparison has $\beta = 2.0$. The disturbances that will be analysed will have streamwise wavenumber $\alpha = 1.0$. A summary of the parameters of the REDDY validation case is given in Table 3.8.

The stability characteristics of a wide range of base flows have been computed by varying shear S and streak amplitude A_{st}. A visualisation of the base flows with and without the presence of a streak is shown in Figure 3.5.

A map showing the growth rate (the imaginary part of the eigenvalue) of the most unstable (or least stable) modes for a range of S and A_{st} is given in Figure 3.6. In

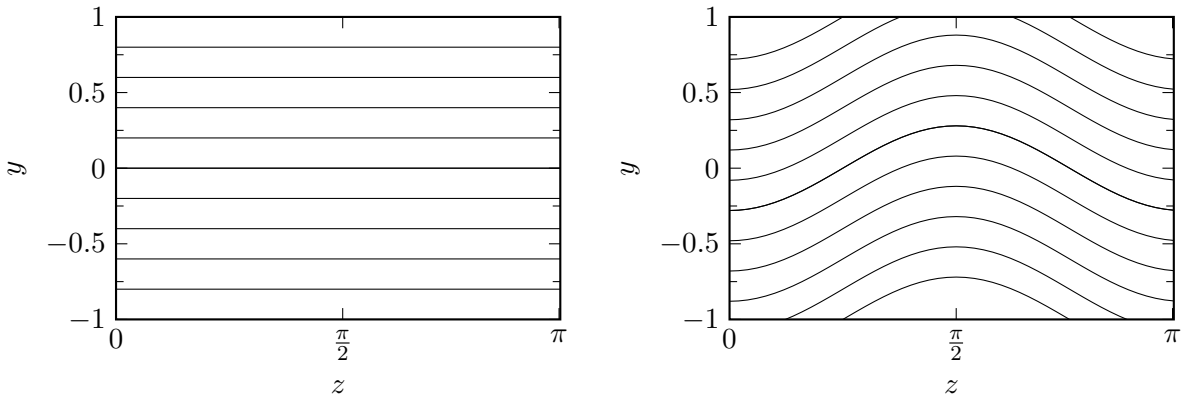

(a) $A = 0.0$ **(b)** $A = 0.14$

Figure 3.5. Contours of streamwise velocity of the Couette base flow with shear $S = 1.0$, and without and with streaks of amplitude A_{st}. The contour levels range from -1 to 1 in increments of 0.2.

this map the black contours represent the results of Reddy et al. (1998), while the solid red contours show the results obtained by COMPASS. Note that the apparent discrepancy for $A_{st} > 0.12$ and $S < 0.2$ is due to the lack of resolution in the original map of Reddy et al. (1998), who used only 11 data points for each parameter. The dashed red contours in Figure 3.6 indicate results by COMPASS if only those points are used. An excellent agreement is evident between the results. A quantitative comparison is shown in Table 3.9 for a selected number of base flows: $S = [0, 0.5, 1.0]$ and $A_{st} = [0.00, 0.07, 0.14]$. Note that the reference values reported in this table are taken from Pook (2013), who also performed bi-local stability analysis of the REDDY case as validation.

From the eigenvalue map in Figure 3.6 and the comparison of eigenvalues in Table 3.9, it can be concluded that the agreement with the original results is excellent and the (temporal) bi-local stability analysis by COMPASS yields correct results for incompressible flow. In the next section, spatial bi-local stability of a compressible flow will be performed to complete the validation campaign of COMPASS.

3.3.3 Supersonic roughness wake (M=2.5)

In order to validate the (spatial) bi-local stability analysis of flows where compressibility is important, the wake behind a sharp-edged roughness element at Mach 2.5 is investigated. The base flow was obtained from DNS performed by De Tullio et al. (2013). The analysis was performed at a streamwise location of $x = 93.66$

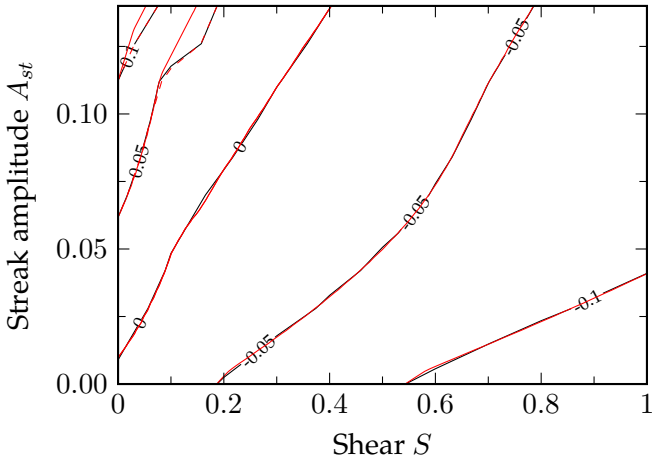

Figure 3.6. Map showing the growth rate of the most unstable (or least stable) modes of case REDDY with shear S and streak amplitude A_{st}. Black contours show the original results of Reddy et al. (1998); red contours indicate results computed by `COMPASS`.

Table 3.9. Comparison of computed most unstable eigenvalues $\omega = \omega_r + i\omega_i$ of some of the Reddy et al. (1998) cases. Note that the values have been taken from Pook (2013).

S	A_{st}	`COMPASS`	**Reference**	**Diff. (%)**
0	**0.00**	$0.000000 - i0.006935$	$0.000000 - i0.006935$	$0.00 + i0.00$
	0.07	$0.000000 + i0.058070$	$0.000000 + i0.058070$	$0.00 + i0.00$
	0.14	$0.000000 + i0.127541$	$0.000000 + i0.127542$	$0.00 + i0.00$
0.5	**0.00**	$0.339288 - i0.094793$	$0.339287 - i0.094788$	$0.00 + i0.00$
	0.07	$0.362114 - i0.043439$	$0.362109 - i0.043454$	$0.00 + i0.00$
	0.14	$0.342285 - i0.016698$	$0.342280 - i0.016690$	$0.00 + i0.00$
1.0	**0.00**	$0.744887 - i0.149290$	$0.744884 - i0.149292$	$0.00 + i0.00$
	0.07	$0.775942 - i0.079444$	$0.775942 - i0.079436$	$0.00 + i0.00$
	0.14	$0.788792 - i0.065234$	$0.788793 - i0.065234$	$0.00 + i0.00$

and for a disturbance with frequency $\omega = 0.08 \times 2\pi$, so that a comparison with the bi-local stability results computed by De Tullio et al. is possible. A summary of the parameters of this validation case, termed DT-2.5, is given in Table 3.10.

The base flow under investigation is visualised in Figure 3.7 using contours of streamwise velocity. It clearly shows the mushroom-shaped low-velocity streak induced by the roughness element, which is located at the centreline of the domain and has width $W = 6.0$ and height $h = 1.0$, and a relatively undisturbed boundary

Table 3.10. Parameters of the supersonic roughness wake validation case of De Tullio et al. (2013).

Case	Reference	M	Re	ω	C_{suth}
DT-2.5	De Tullio et al.	2.5	3300	$0.08 \times 2\pi$	110.4/273.15

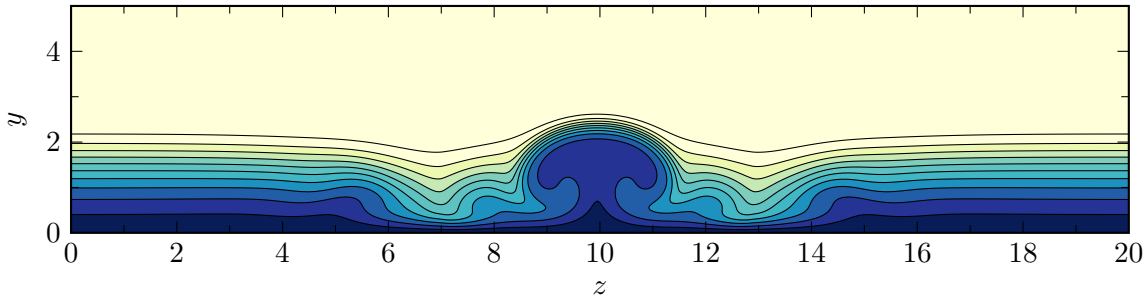

Figure 3.7. Contours of streamwise velocity of the base flow De Tullio et al. (2013) at $x = 93.66$.

layer further away from the roughness. The domain size is $L_z = 20$ in the spanwise direction, in which periodic boundary conditions are assumed, and $L_y = 16$ in the wall-normal direction, bounded by a solid wall at $y = 0$ and a quiet freestream at $y = 16$. Note that the full wall-normal extent is not shown in Figure 3.7. The analysis was performed with $N_z = 140$ grid points in the spanwise direction and $N_y = 121$ points in the wall-normal direction. The high-order FD method FD-q was used with order $q = 8$ in the wall-normal direction, similar to De Tullio et al. (2013), to reproduce their set-up as accurately as possible.

The spatial stability spectrum for $\omega = 0.08 \times 2\pi$ computed by COMPASS is shown in Figure 3.8. In this figure also the digitised results reported in De Tullio et al. (2013) are shown. Note that COMPASS finds a number of eigenvalues in a certain (specified) region of interest and that only a single run was performed, with the region of interest set near the most unstable eigenvalue. Therefore, the eigenvalues close to the neutral line $\alpha_i = 0$ found by De Tullio et al. (2013) were not looked for, because for the purpose of this validation only the most unstable eigenvalues are of interest.

It can be seen from Figure 3.8 that the two most unstable eigenvalues found by COMPASS agree very well with the results of De Tullio et al. (2013). In fact, the most unstable eigenvalue is found to have $-\alpha_i^{\texttt{COMPASS}} = 0.148$, compared to $-\alpha_i^{\text{DT-2.5}} = 0.149$ reported in the reference. This gives a relative difference of about 0.67%. Also the two wake modes near $(\alpha_r, -\alpha_i) \approx (0.6, 0.06)$ that were reported by De

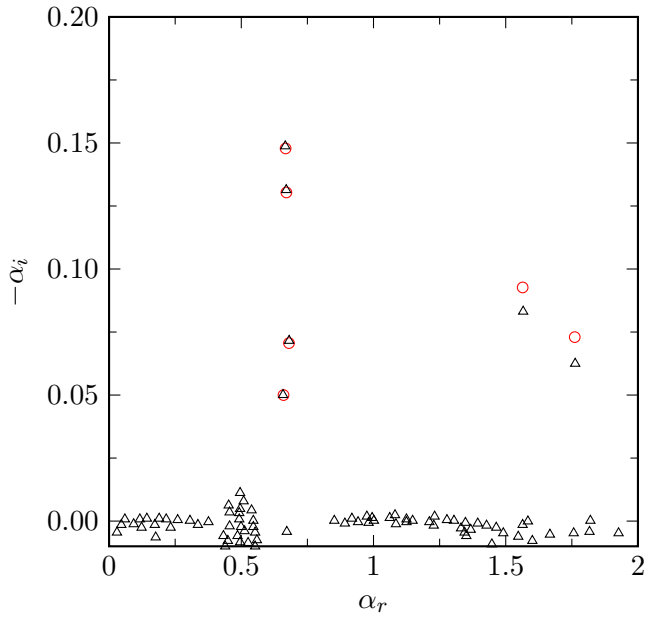

Figure 3.8. Spectrum at $x = 93.66$ for $F = 0.08$. Black triangles are the digitised results of De Tullio et al. (2013); red circles show the eigenvalues computed by COMPASS.

Tullio et al. (2013) are found and accurately predicted by COMPASS. However, the two modes near $(\alpha_r, -\alpha_i) \approx (1.6, 0.07)$, which were found to be Mack modes active in the undisturbed boundary layer away from the roughness wake, seem to have a relatively large difference between the computed growth rates. Why exactly the growth rate of these two modes do not match between COMPASS and De Tullio et al. (2013) is not known. Since the results presented here are grid-converged, this gives an indication that there is a difference between the codes.

A comparison of the most unstable mode shapes shown in Figure 3.9, which shows the velocity component mode shapes computed by COMPASS (Figures 3.9a, 3.9c and 3.9e) and the original work (Figures 3.9b, 3.9d and 3.9f). Note that the latter figures show the mode shapes obtained using bi-local stability analysis as shaded contours and mode shapes from DNS as black contour lines. It can be seen that the comparison between the results from COMPASS and De Tullio et al. (2013) (the shaded contours) is excellent.

From the comparison of the computed spectrum in Figure 3.8 and the mode shapes in Figure 3.9, it can be concluded that COMPASS can accurately predict the bi-local stability of the Mach 2.5 roughness wake of case DT-2.5.

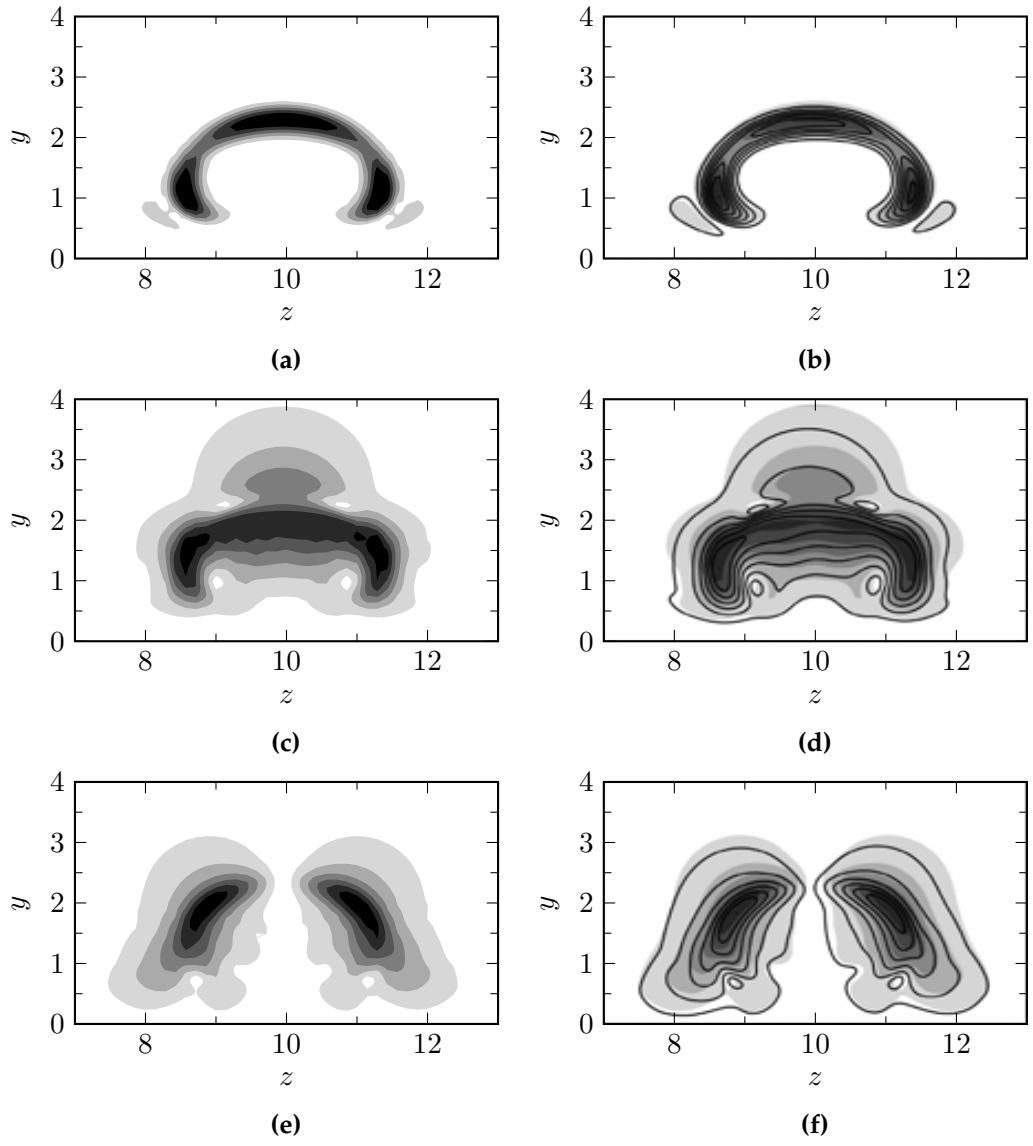

Figure 3.9. Mode shapes of the three velocity components at $x = 93.66$ for $F = 0.08$ **(a,c,e)**, compared with the results of De Tullio et al. (2013, Fig. 12) **(b,d,f)**.

Table 3.11. Parameters of the hypersonic roughness wake validation case of De Tullio and Sandham (2015).

Case	Reference	M	Re	ω	C_{suth}
DT-6.0-F0.06	De Tullio (2015)	6.0	8200	$0.06 \times 2\pi$	110.4/273.15
DT-6.0-F0.14	De Tullio (2015)	6.0	8200	$0.14 \times 2\pi$	110.4/273.15

Table 3.12. Comparison of the temporal growth rate of the most unstable mode, computed by COMPASS and the linearised version of SBLI.

Case	COMPASS	Lin. SBLI	Diff. (%)
DT-6.0-F0.06	0.01017	0.01021	-0.39
DT-6.0-F0.14	0.01349	0.01341	-0.60

3.3.4 Hypersonic roughness wake (M=6.0)

Another validation case of a compressible roughness wake case is performed to increase the confidence in the code to accurately compute the stability of a highly compressible flow. The base flow was obtained from DNS performed by De Tullio and Sandham (2015). The analysis was performed at a streamwise location of $x = 142.55$ and for disturbances with frequencies $\omega = 0.06 \times 2\pi$ and $\omega = 0.14 \times 2\pi$. A summary of the parameters of this validation case, termed DT-6.0-F0.06 and DT-6.0-F0.14, is given in Table 3.11. Besides the flow parameters, the set-up of the stability analysis for cases DT-6.0-F0.06 and DT-6.0-F0.14, e.g. the domain size and differentiation method, is the same as DT-2.5.

Comparisons are made between the results computed by COMPASS and computed by the linearised version of SBLI, as mentioned earlier. The temporal evolution of the streamwise velocity fluctuations and the associated growth rate for case DT-6.0-F0.06 is shown by Figure 3.10. Table 3.12 gives the temporal growth rate of the most unstable mode for the two cases (DT-6.0-F0.06 and DT-6.0-F0.14) obtained with COMPASS and the linearised version of SBLI. These results shows that the difference between the growth rates computed with the two methods is well below 1% for both cases.

The mode shapes of the streamwise velocity disturbances are shown in Figures 3.11 and 3.12, for which a good agreement can be observed. The excellent comparison between the stability code COMPASS and the linearised version of SBLI, both for the growth rate and the mode shapes, shows that COMPASS can be used to accurately

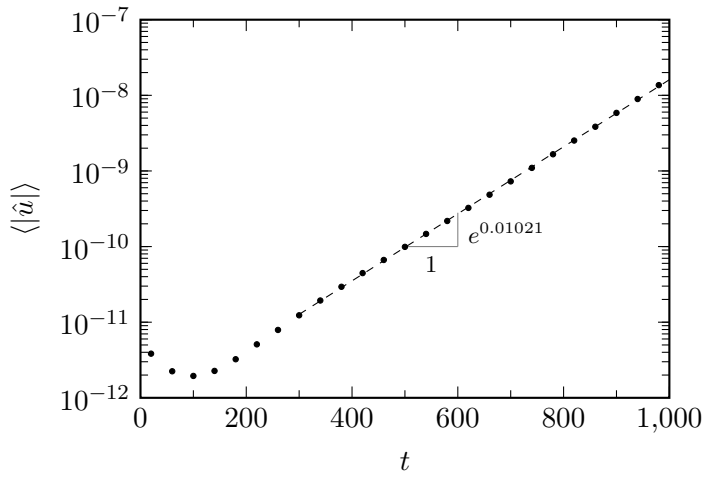

Figure 3.10. Temporal evolution of the streamwise velocity fluctuations in the domain for case DT-6.0-F0.06.

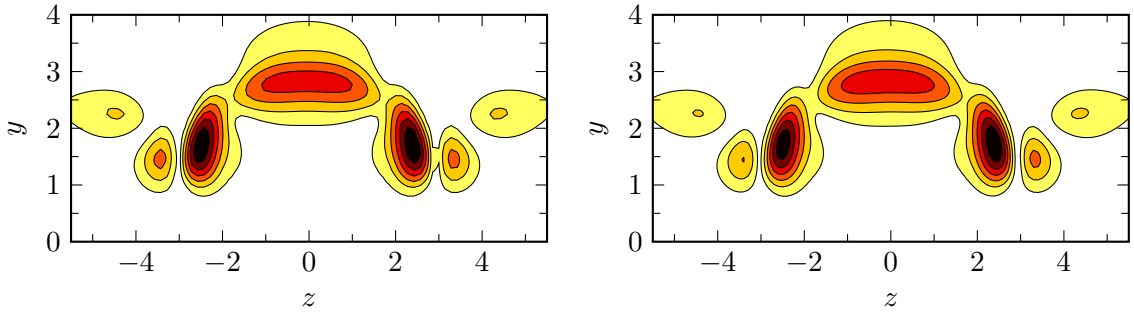

(a) COMPASS **(b)** Lin. SBLI

Figure 3.11. Mode shapes of the streamwise velocity component at $x = 142.55$ for $F = 0.06$, compared with the results computed by the linearised version of SBLI.

predict the linear instability at Mach numbers in the hypersonic regime.

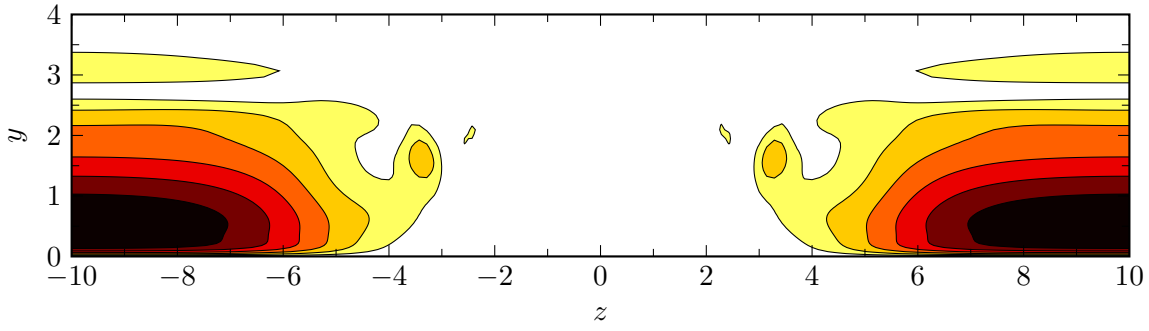

(a) COMPASS

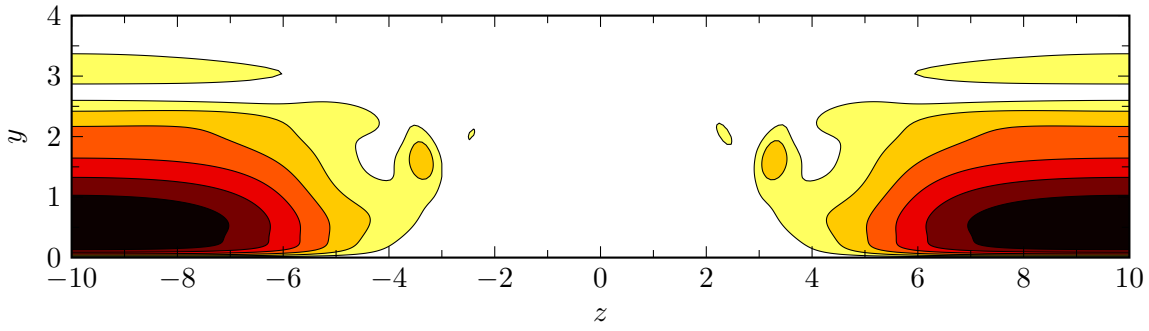

(b) Lin. SBLI

Figure 3.12. Mode shapes of the streamwise velocity component at $x = 142.55$ for $F = 0.14$, compared with the results computed by the linearised version of SBLI.

Chapter 4

Problem Definition & Numerical Set-up

In this chapter the problem and numerical set-up of the following three chapters will be discussed in detail. These three chapters — Chapter 5 *(Roughness Receptivity & Wake Instability)*, Chapter 6 *(Stability Analysis of Roughness Wakes)* and Chapter 7 *(Roughness-induced Transition)* — essentially share the same problem set-up, i.e. an isolated roughness element at a certain distance from the leading edge of a flat plate in a Mach 6 flow.

4.1 Geometry of the problem

A diagram of the geometry under consideration is shown in Figure 4.1. This figure presents the (sharp) flat plate with an isolated roughness element, and shows the extent of the two numerical domains that are used in the next chapters. Note that this sketch is not to scale.

4.1.1 Numerical domain

Two different domains are used because of the nature of the simulations that have been performed. In Chapter 5 *(Roughness Receptivity & Wake Instability)*, boundary layer receptivity and the initial linear growth of instabilities in the wake behind a roughness element are investigated. Since these investigations are performed in the near-field of the roughness element, a relatively small numerical domain (domain B) around the element can be used. Chapter 6 *(Stability Analysis of Roughness*

Wakes) is also concerned with the linear growth of instabilities in the wake near the roughness element and will make use of the results computed in Chapter 5. It will therefore also use domain B. Chapter 7 *(Roughness-induced Transition)* will deal with the non-linear interactions and the eventual breakdown to turbulence of the wake behind a roughness element. Because the full transition process is computed, a longer numerical domain and a finer grid is required. This chapter will therefore use domain A.

Domain A is the largest domain and has dimensions $L_x \times L_y \times L_z = 300 \times 20 \times 50$. It is placed downstream of the leading edge of the plate, and does not encompass the leading edge shock. The normalisation is such that the laminar boundary layer profile at the inflow of this domain has a non-dimensional displacement thickness δ_0 of unity. Recall that the inflow displacement thickness is used as reference length in the non-dimensionalisation. Domain B is much smaller and is essentially a subset of domain A. Its dimensions are $L_x \times L_y \times L_z = 150 \times 16 \times 20$ and it is placed at a streamwise distance of $16\delta_0^*$ from the inflow of domain A. The resulting boundary layer profile at the inlet of domain B has a displacement thickness of $\delta_0^* = 9.07$. It is noted that the numerical set-up of the current work is the same as the set-up of De Tullio and Sandham (2012). They chose the wall-normal dimensions of the two domains such that any reflection from the top boundary would hit the outflow boundary without affecting the boundary layer inside the domain, and the spanwise dimensions to allow for the development of a number of unstable smooth flat plate first and second mode instabilities (De Tullio and Sandham, 2012).

4.1.2 Roughness element

An isolated roughness element is placed at the domain centreline at a streamwise distance $x_r = x_r^*/\delta_0^* = 53.0$ from the inflow of domain A or $x_r = 37.0$ from the inflow of domain B. The roughness elements investigated are continuous, i.e. described by a smooth analytical function, such that a single-block body-fitted grid can be used, and a variety of different roughness element shapes are considered.

Two elemental roughness shapes are considered: the smooth bump used in the work of Redford et al. (2010) and a roughness shape with a more flattened top, using a definition very similar to the roughness of Marxen and Iaccarino (2008). The former roughness element is defined as

$$y_0(\tilde{x}, \tilde{z}) = c_1 \left(\tanh\left(\frac{\tilde{r}}{c_2} + 1 \right) - \tanh\left(\frac{\tilde{r}}{c_2} - 1 \right) \right), \tag{4.1}$$

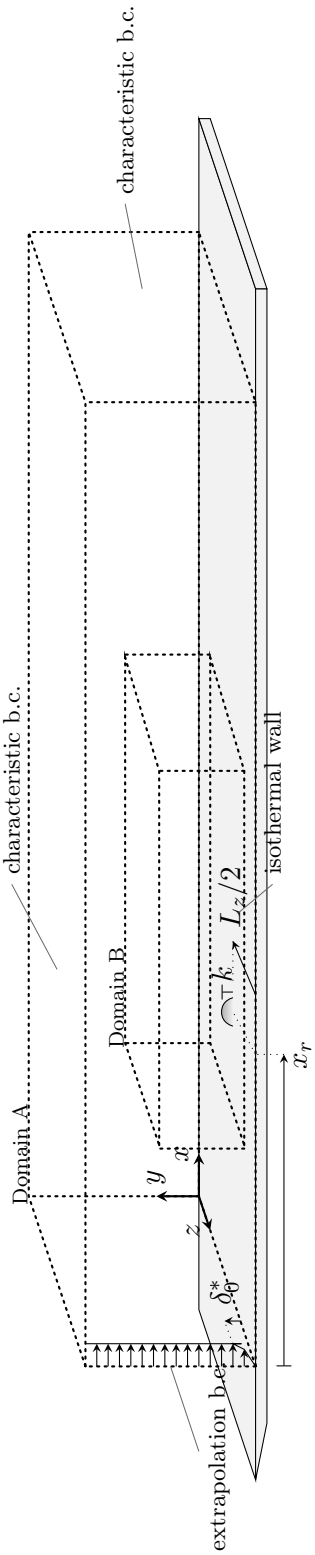

Figure 4.1. Problem set-up and computational domains used in the current work.

where y_0 is the y-coordinate of the grid point at the wall. In this equation $\tilde{r} = \sqrt{\tilde{x}^2 + \tilde{z}^2}$, and $\tilde{x}$ and $\tilde{z}$ are the coordinates relative to the roughness centre. In these equations c_1 and c_2 are defined as

$$c_1 = \frac{c_3}{2}\left(1 + \cos\left(\frac{j}{N_y}\,\pi\right)\right) \tag{4.2a}$$

$$c_2 = c_4\left(1 + c_5\,\frac{j-1}{N_y - 1}\right), \tag{4.2b}$$

with N_y the number of grid points in the wall-normal direction, $j = 1, 2, ..., N_y$ and the constants $c_3 = 0.6565$, $c_4 = 2.28478$ and $c_5 = 6$. The constants are defined so as to have a roughness height $k = 1.0$ and a frontal area $S_{yz} = 6.0$.

The other roughness element shape is defined using a different function, that gives direct control on the slope of the roughness element's sides, its width and maximum height. This function is:

$$y_0(\tilde{x}) = \frac{-k}{2\tanh(S\frac{W}{k})}\left[\tanh\left(\frac{S}{k}\,(2\tilde{x} - W)\right) + \tanh\left(\frac{S}{k}\,(-2\tilde{x} - W)\right)\right], \tag{4.3}$$

where k is the roughness height at $\tilde{x} = 0$ and W is defined as the distance between the spanwise locations with the maximum slope. S is defined as $S = \cot(S^*)$ with S^* in the range $0 < S^* < \pi/2$. The variable S^* can be seen as a *smoothness* factor, which controls the slope of the roughness sides. In the limit of $S^* \to 0$ the roughness will become a sharp-edged element with 90° sides, such as the "pizza-box" roughness element of De Tullio (2013), while for increasingly large values of S^* the roughness will become more *smooth* and bump-like. In the current work the smoothness factor is set to $S^* = \pi/4$ and $W = 6.0$, except where mentioned otherwise. Note that the roughness type that follows from this formula will be called a *flat-top* roughness element hereafter.

The effect of the parameters k, S and W in the flat-top roughness definition on the shape of the roughness is evident in Figure 4.2. From this figure it is evident that the three parameters have an almost independent effect on the roughness profile: parameter k has an effect on the maximum height of the roughness, but does not significantly change the angle of the roughness sides; parameter S^* changes the smoothness, i.e. the angle of the roughness sides, but not the maximum height or width; parameter W changes the width of the roughness element without affecting the height or smoothness.

Flat-top roughness elements with different planform shapes can be obtained by combination or modification of this roughness function. For example, $y_0(\tilde{r})$ with the

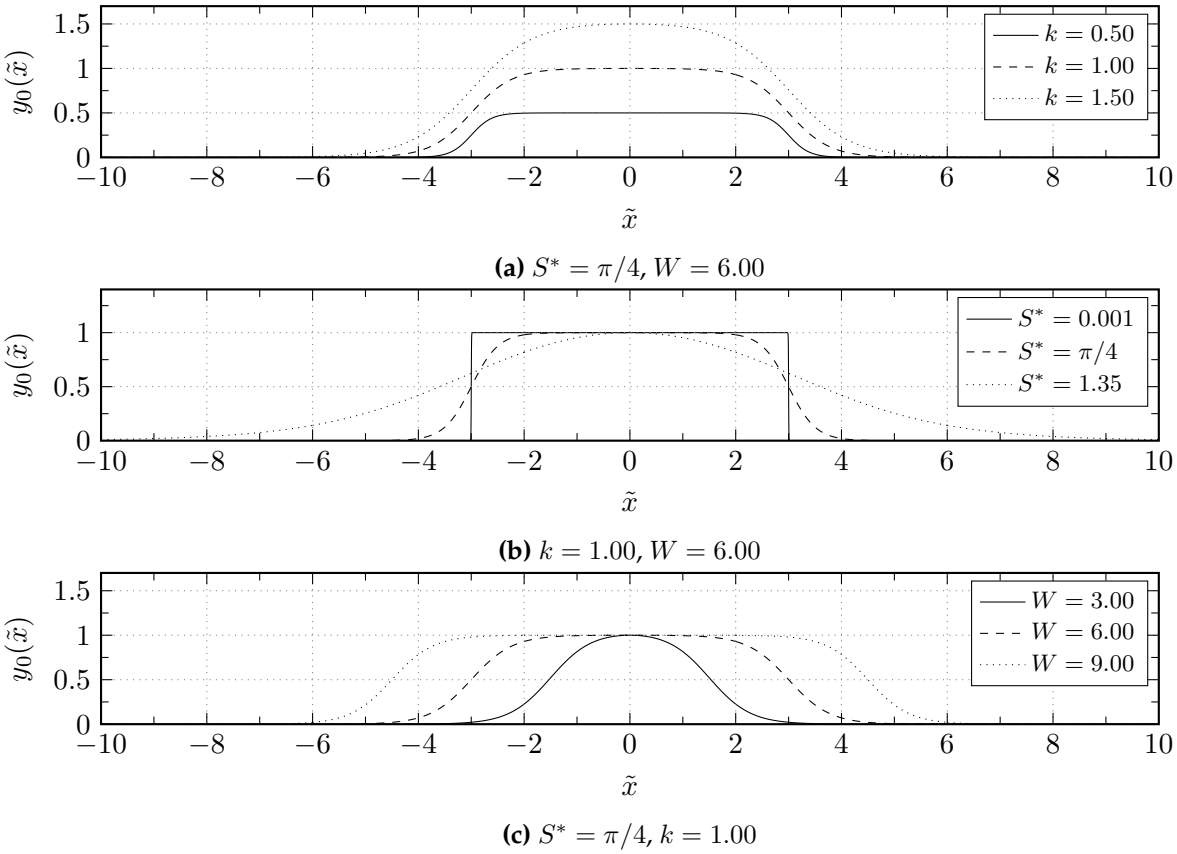

(a) $S^* = \pi/4$, $W = 6.00$

(b) $k = 1.00$, $W = 6.00$

(c) $S^* = \pi/4$, $k = 1.00$

Figure 4.2. Effect of parameters k, S and W in the flat-top roughness definition on roughness shape.

radius from the roughness centre $\tilde{r} = \sqrt{\tilde{x}^2 + \tilde{y}^2}$ will result in a cylindrical roughness element. The product of $y_0(\tilde{x})$ and $y_0(\tilde{z})$, with $\tilde{x}$ and $\tilde{z}$ being the streamwise and spanwise coordinates relative to the roughness centre, will yield a roughness element with a square planform. Rotating the flat-top square $45°$ and scaling its width by a factor of $\sqrt{2}$ yields the flat-top roughness element with a diamond-shaped planform. Cylindrical flat-top roughness elements with height $k = 1.0$ and $k = 0.5$ are visualised in Figure 4.3.

An additional type of roughness element, namely ramped up or ramped down, has also been investigated. These roughness elements are a combination of the smooth bump and flat-top definition in the streamwise direction, while the flat-top definition is used in the spanwise direction. The ramp-up case is defined as a smooth bump element (with $c_4 = 6.85434$) for $\tilde{x} \leq 0$ and flat-top element for $\tilde{x} > 0$, and vice versa for the ramp-down case.

Three-dimensional visualisations of the different roughness elements introduced in this section are shown in Figure 4.3.

4.2 Numerical set-up

4.2.1 Boundary conditions

The boundary conditions that are used in the current work are indicated in the sketch in Figure 4.1. Isothermal no-slip boundary conditions are set at the wall in domain A and B. The temperature is fixed to the adiabatic wall temperature T_{ad} unless stated otherwise. In the spanwise direction periodic boundary conditions are applied. At the top and outflow boundaries, characteristic boundary conditions (Sandhu and Sandham, 1994) are applied to minimise unwanted reflections into the domain.

At the inlet of domain A, the flow is initialised with a compressible laminar boundary layer similarity solution and a pressure extrapolation boundary condition is applied. In the subsonic region of the boundary layer, this boundary condition computes the conservative flow variables by linearly extrapolating the pressure from within the domain, while in the supersonic region the inflow is fixed. The inflow boundary condition of domain B is the same as the inlet of domain A, but the initial compressible boundary layer profile is different, since boundary layer growth is accounted for.

The growth of the laminar displacement thickness (δ^*) and the boundary layer thickness (δ_{99}) in the streamwise direction is derived using the Illingworth transformation in White (1991):

$$\frac{\delta^*(x^*)}{\delta_0^*} = \Delta\sqrt{\frac{2}{Re_{\bar{x}^*}}}\left(\frac{Re_{\delta_0^*}}{2\Delta^2} + \frac{x^*}{\delta_0^*}\right), \tag{4.4a}$$

$$\frac{\delta_{99}(x^*)}{\delta^*(x^*)} = \frac{\Delta_{99}}{\Delta}, \tag{4.4b}$$

where

$$Re_{\bar{x}^*} = \frac{1}{2}\left(\frac{Re_{\delta_0^*}}{\Delta}\right)^2 + Re_{\delta_0^*}\frac{x^*}{\delta_0^*}. \tag{4.5}$$

Note that $\bar{x}^*$ is the dimensional streamwise coordinate in a reference frame positioned at the flat plate leading edge. The scaling factors Δ and Δ_{99} vary with Mach number and wall temperature, and are set to $\Delta = 9.071$ and $\Delta_{99} = 11.858$ for the hot-wall cases (with adiabiatic wall temperature $T_w = 7.02$), and $\Delta = 6.183$ and $\Delta_{99} = 9.037$ for the cooled-wall ($T_w = 3.50$) case in the current work.

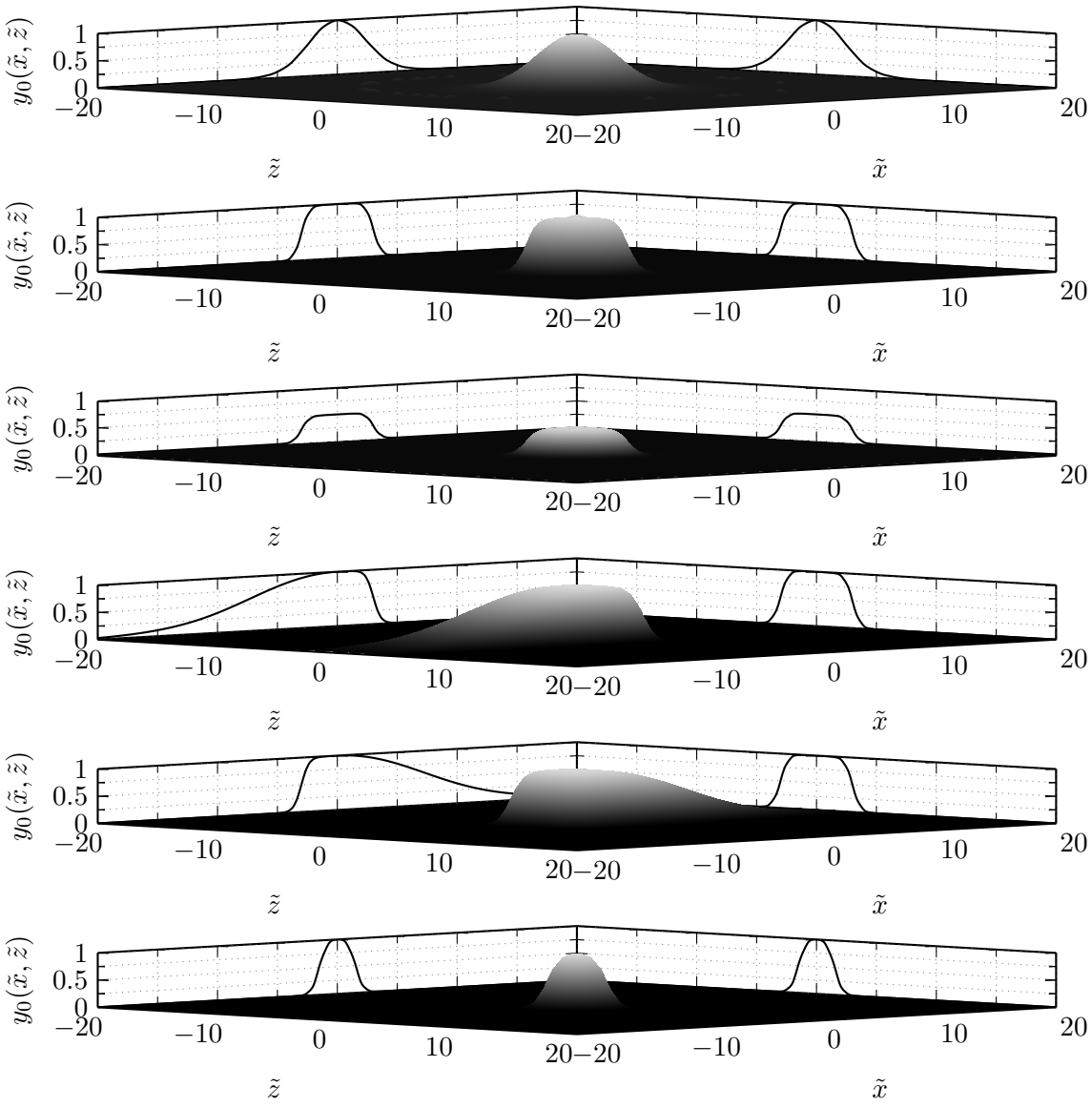

Figure 4.3. Three-dimensional visualisations of the roughness elements in the numerical simulations: **(a)** smooth bump; **(b)** flat-top; **(c)** flat-top with $k = 0.5$; **(d)** ramp-up; **(e)** ramp-down; **(f)** flat-top with width $W = 3.0$.

4.2.2 Freestream and boundary layer disturbances

In Chapter 5 *(Roughness Receptivity & Wake Instability)* the receptivity of the boundary layer near a roughness element is investigated. To analyse how different upstream perturbations influence the receptivity process, three different types of inflow disturbances are considered: acoustic (type A), vortical (type V) and entropy (type Æ) disturbances.

The different types of disturbances are defined as variations of the following generic function:

$$\psi(\mathbf{x},t) = a\left(1 - e^{(-y^p/g^l)}\right)\sum_{m=0}^{M}\sum_{n=1}^{N}\cos\left(\beta_m z + \phi_m\right)\cos\left(\omega_n t + \phi_n\right)\ , \tag{4.6}$$

where a is the amplitude of the perturbation, and $M = 6$ and $N = 16$ are the number of spanwise modes and temporal frequencies respectively. Random phases ϕ are introduced to avoid spurious high amplitude peaks in the forcing signal which might trigger undesired local non-linearities. The term $f_d \coloneqq 1 - \exp\left(-y^p/g^l\right)$, with coefficients g, p and l, is a damping function to control the location where the disturbances are introduced. The coefficients in the damping function are set to $g = 1.0$, $p = 3.0$ and $l = 1.0$ such that disturbances are imposed inside the boundary layer. Note that an additional damping function is employed near the top boundary of the domain to drive the forcing function to zero.

The three types of disturbances are then formed obtained from the forcing function ψ as follows:

Type A $\rho'(\mathbf{x},t) = \psi(\mathbf{x},t)$; $\quad u' = v' = w' = T' = 0$
Type V $v'(\mathbf{x},t) = -\partial\psi(\mathbf{x},t)/\partial z$; $\quad w'(\mathbf{x},t) = \partial\psi(\mathbf{x},t)/\partial y$; $\quad u' = \rho' = T' = 0$
Type Æ $T'(\mathbf{x},t) = \psi(\mathbf{x},t)$; $\quad u' = v' = w' = \rho' = 0$

Note that disturbance type V results in a divergence free velocity disturbance field at the inflow boundary. In Chapter 5 *(Roughness Receptivity & Wake Instability)* these disturbances are applied at the inlet boundary of domain B by superimposing them onto the specified inflow profile.

In Chapter 7 *(Roughness-induced Transition)* the effect of the roughness element on the transition behaviour is investigated. For these cases a different upstream forcing is used in the freestream that mimics freestream acoustic noise. Acoustic disturbances are placed far outside of the boundary layer, upstream of the roughness element,

and have the following form:

$$\rho'(\mathbf{x},t) = \psi(\mathbf{x},t) = a\, e^{-r_f^2} \sum_{m=0}^{M} \sum_{n=1}^{N} \cos\left(\beta_m\, z + \phi_m\right) \sin\left(\omega_n\, t + \phi_n\right) \tag{4.7}$$

with amplitude a and $r_f = \sqrt{(x - x_f)^2 + (y - y_f)^2}$. The forcing function is essentially a line source with forcing radius r_f, placed at a streamwise and wall-normal position $x_f = 12.0$ and $y_f = 6.0$. The acoustic source is of broadband nature with $M = 20$ spanwise modes and $N = 20$ temporal modes. Contrary to the type A, V, Æ disturbances used in Chapter 5 *(Roughness Receptivity & Wake Instability)*, that are applied as boundary conditions at the domain inflow, the acoustic disturbances in Chapter 7 *(Roughness-induced Transition)* are generated by adding the forcing term ρ' to the continuity equation in the DNS code.

Note that in the forcing functions given by Equation (4.6) and Equation (4.7), the spanwise wavelength is defined as $\beta_m = 2\pi\, m/L_z$ and frequency $\omega_n = 2\pi\, n\, F_0$ with $F_0 = 0.02$.

4.2.3 Computational grid

In order to ensure sufficient grid points at specific regions of the flow, e.g. near the roughness element or the point of transition, while keeping the computational expense at a minimum, the numerical grids in the current work are stretched in the streamwise and spanwise directions. The stretched grids consist of regions of constant grid spacing that are connected by ninth-order polynomials, such that the overall stretching function is at least C^4 continuous and the fourth-order differencing routine in the DNS code does not encounter any difficulties with discontinuities. This polynomial stretching approach is illustrated in Figure 4.4.

To ensure that the boundary layer is sufficiently resolved, the grid is also stretched in the wall-normal direction. The stretching function between the computational uniform grid ($0 < \eta < 1$) and the physical non-uniform grid ($y_0 < y < L_y$) is given by

$$y = y_0 + (L_y - y_0)\, \frac{\sinh\left(b_y \eta\right)}{\sinh\left(b_y\right)}\,, \tag{4.8}$$

where b_y is a stretching factor. In this equation, y_0 is the coordinate of the first grid point at the wall.

The grid stretching in the streamwise and wall-normal direction employed for the transition study can be seen Figure 4.5, which shows a portion of the numerical grid

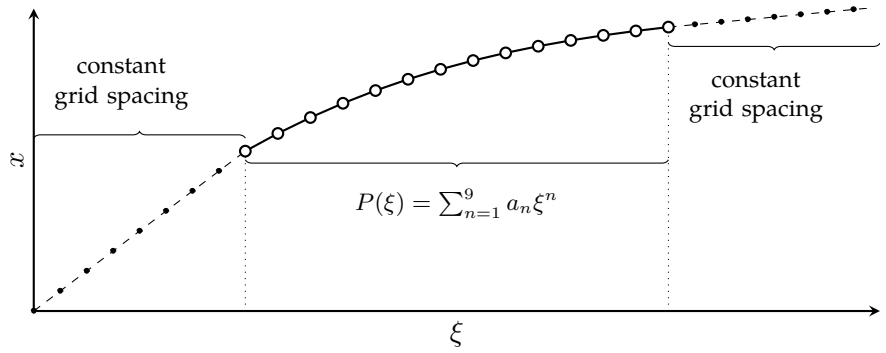

Figure 4.4. High-order polynomial grid stretching between regions of constant grid spacing. (Diagram reproduced from De Tullio (2013))

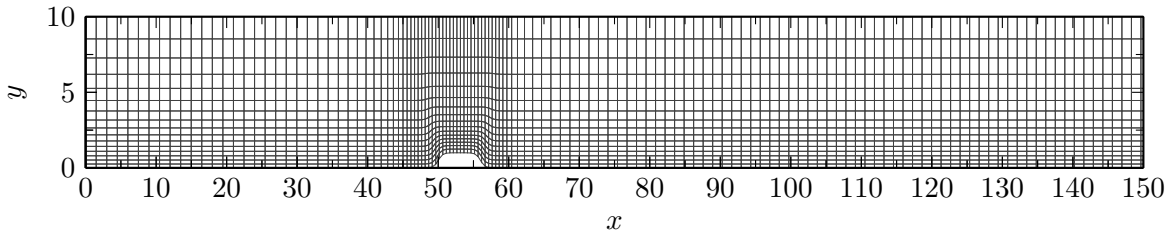

Figure 4.5. Numerical grid used in the transition study (shown every 10^{th} grid line), indicating the streamwise and wall-normal grid stretching.

of domain A. It demonstrates that the grid in the vicinity of the roughness element is considerably finer. Note that only every 10^{th} grid line is shown in this figure.

Because body-fitted grids are used in the current work, grid lines around the roughness elements will not be perpendicular to each other and will introduce skewed *cells*. These skewed grid lines can introduce a locally non-physical solution or numerical grid-to-grid point oscillations that can affect the rest of the flow and invalidate the computed results. It is therefore important that the roughness elements, introduced earlier in this chapter, are smooth and have a relatively slow-varying geometry, i.e. the slopes of the roughness elements are not too steep. It has been found that the DNS code used in the current work can correctly handle grids with angles at least down to $30\,\text{deg}$[1], with $90\,\text{deg}$ being a standard Cartesian grid. The slopes of the roughness elements have been limited to maximum $45\,\text{deg}$ by the choice of an appropriate smoothness factor S^* in Equation (4.3). A close-up of a typical body-fitted grid near a flat-top roughness element is shown in Figure 4.6.

[1]Chris Tyson, *University of Southampton* (private communication, 2013)

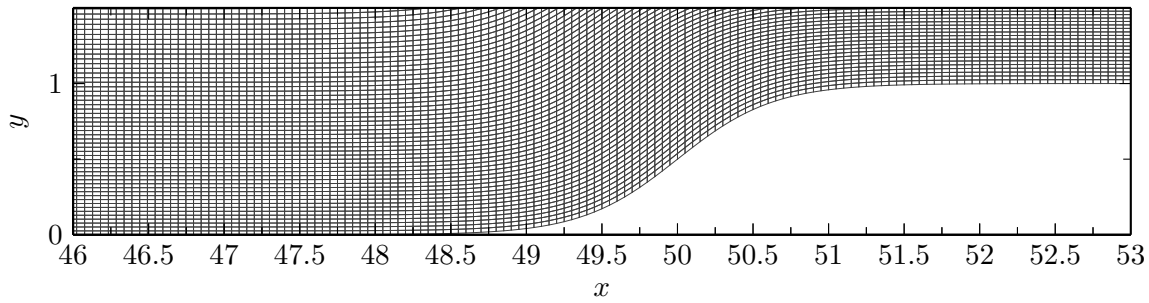

Figure 4.6. Close-up of the centreline body-fitted grid around a flat-top roughness element used in the transition study.

Table 4.1. Details of the computational grids. The values of Δx for the cases with roughness indicate the grid spacing upstream, near the roughness and downstream. The values of Δz indicate the grid spacing near the roughness centreline and the domain edges.

Case	N_x	N_y	N_z	b_y	Δx	Δz
Domain A	2415	205	468	3.40	[0.15, 0.05, 0.135]	[0.04, 0.15]
Domain B	949	205	209	3.19	[0.20, 0.06, 0.20]	[0.05, 0.20]

Domains A and B in Figure 4.1 are used for investigating different phenomena, respectively transition to turbulence and receptivity of a laminar boundary layer, and therefore are discretised using different grids. The study of transition and the eventual breakdown to turbulence in Chapter 7 is performed at a higher Reynolds number than the receptivity study in Chapter 5 and thus requires a much finer grid. The details on the grid spacing and resulting number of grid points in domain A and B are given in Table 4.1

The grid spacing used in the current work, and given in Table 4.1, is taken to be at least as fine as the simulations of De Tullio (2013), who used a very similar numerical set-up (except the roughness element shape) and performed an extensive grid convergence study. In order to increase the confidence in the current set of simulations, another grid convergence study has been performed to confirm that the results are grid-independent.

The flow around the cylindrical flat-top element is simulated in Domain B, i.e. case Cyl in Chapter 5 *(Roughness Receptivity & Wake Instability)*, on the reference grid given in Table 4.1 and on a finer grid with

$$(\Delta x)^{\text{fine}} = 75\% \ (\Delta x)^{\text{ref.}} = [0.15, 0.045, 0.15] \tag{4.9a}$$

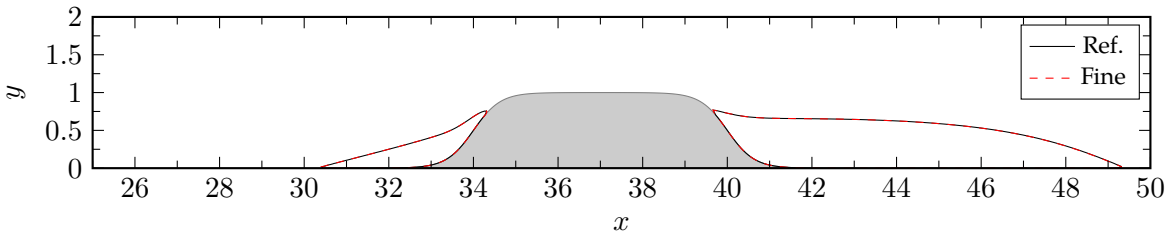

Figure 4.7. Comparison of the recirculation regions computed on the reference and fine grid.

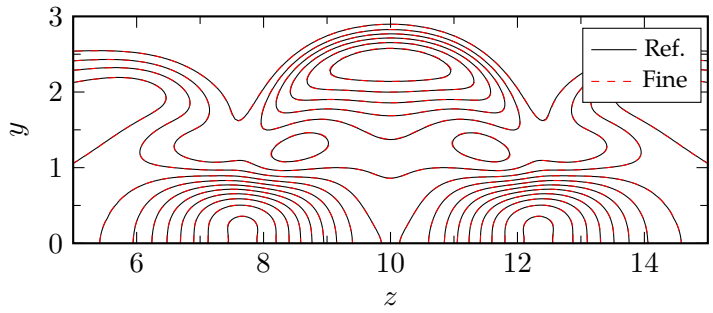

Figure 4.8. Comparison of the roughness wake structure at $x = 120.0$, visualised by contours of wall-normal shear stress, computed on the reference and fine grid.

$$(\Delta z)^{\text{fine}} = 75\% \ (\Delta z)^{\text{ref.}} = [0.0375, 0.15]\,. \tag{4.9b}$$

Also the number of wall-normal grid points was increased from 205 to 240, resulting in a fine grid with $[N_x, N_y, N_z] = [1264, 240, 278]$ grid points.

Figure 4.7 shows the recirculation regions near the cylindrical flat-top roughness element for both the reference and fine cases. This figure shows the excellent agreement of the flow near the roughness element. Also further downstream the agreement is excellent between the results on the reference and fine grid, as demonstrated by Figure 4.8 which shows contours of wall-normal shear stress at $x = 120.0$. These two figures prove that the reference grid can accurately resolve the flow and yield grid-independent results.

4.2.4 Flow parameters

The flow parameters, like Mach number M and Reynolds number Re, for the different simulations in Chapter 5 *(Roughness Receptivity & Wake Instability)* and Chapter 7 *(Roughness-induced Transition)* will be defined at the beginning of those chapters.

4.2.5 Sensitivity to the viscosity law

Throughout this work, Sutherland's law (see Equation (2.8)) is used to compute the dynamic viscosity. By this definition, the viscosity of the fluid is assumed to be solely dependent on the local temperature and Sutherland's law constant S^*, in the form of a temperature. This reference temperature is taken to be $S^* = 110.4\,\mathrm{K}$ and is non-dimensionalised using the reference temperature in the freestream (in this work taken to be $T_r^* = 273.15\,\mathrm{K}$). The reference values used in the current work are taken to match previous numerical simulations, but do not correspond to any wind tunnel experiment, for which the freestream temperature would generally be much lower. Since Kimmel and Poggie (2000) noted that the stability of a compressible boundary layer is dependent on the absolute (total) temperature, the computations and results in this work might be expected to be dependent on the particular choice of T_r^*. The sensitivity of numerical computations of high-speed boundary layer instability and transition to the non-dimensional Sutherland's law constant $S = S^*/T_r^*$ has not yet been quantified to the author's knowledge.

The sensitivity of the instability growth of the two-dimensional Mack mode in a Mach 6.0 boundary layer with $Re_{\delta_0^*} = 20000$ and hot-wall conditions has been studied using `COMPASS` for a range of values of the non-dimensional Sutherland's law constant S by keeping $S^* = 110.4\,\mathrm{K}$ constant and varying the freestream reference temperature T_r^*. Note that this case is similar to case SAN-6 in Chapter 3 *(COMPASS: Compressible Stability Analysis)*, but not the same due to a differently chosen adiabatic wall-temperature, and should thus not be compared to each other.

Figure 4.9 shows the resulting boundary layer mean profiles of streamwise velocity and temperature, and clearly shows that they are not very sensitive to the reference temperature. Figure 4.9 also shows the streamwise velocity profile of the resulting Mack mode, which is the most unstable two-dimensional instability mode. From this figure it can be clearly seen that the resulting Mack mode profile is highly dependent on the freestream reference temperature. For lower temperatures the near-wall peak becomes fuller and the secondary peaks near $y \approx 1.0$ and $y \approx 1.3$ become stronger.

The change in reference temperature also has a significant effect on the growth rate of the Mack mode, as indicated by Figure 4.10. For temperatures $T_r^* > 200\,\mathrm{K}$ the difference in growth rate is limited to a few percent. However, for colder reference temperatures, the growth rate rapidly increases with decreasing temperature. For example, the Mack mode growth rate at a freestream temperature of $55.2\,\mathrm{K}$, which is a realistic value for hypersonic wind tunnel experiments, is approximately 43%

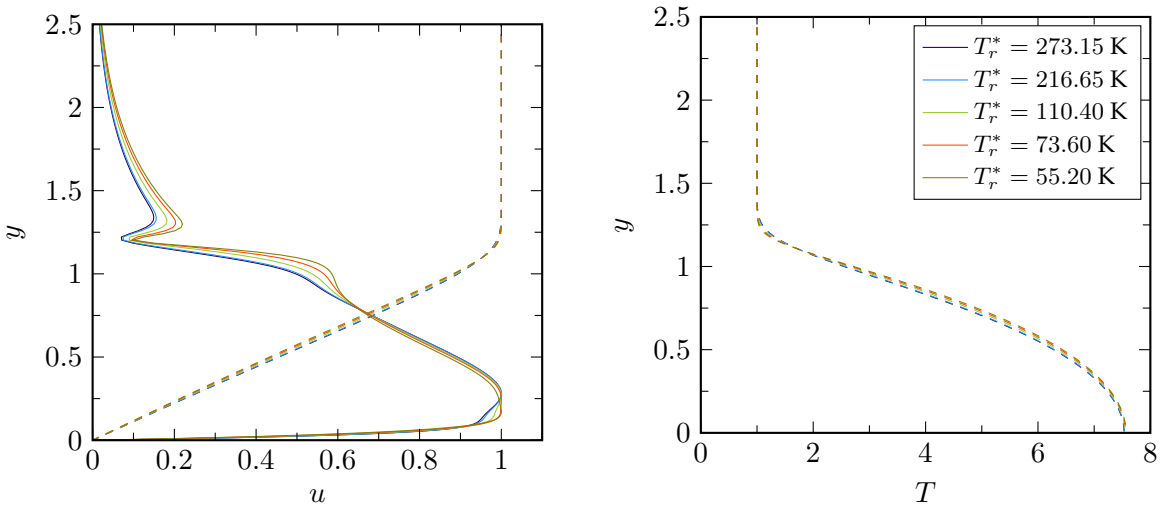

Figure 4.9. Sensitivity of the Mach 6.0 boundary layer profile *(dashed)* of streamwise velocity *(left)* and temperature *(right)*, and the Mack mode streamwise velocity profile *(solid; left)* to the absolute reference temperature T_r^*.

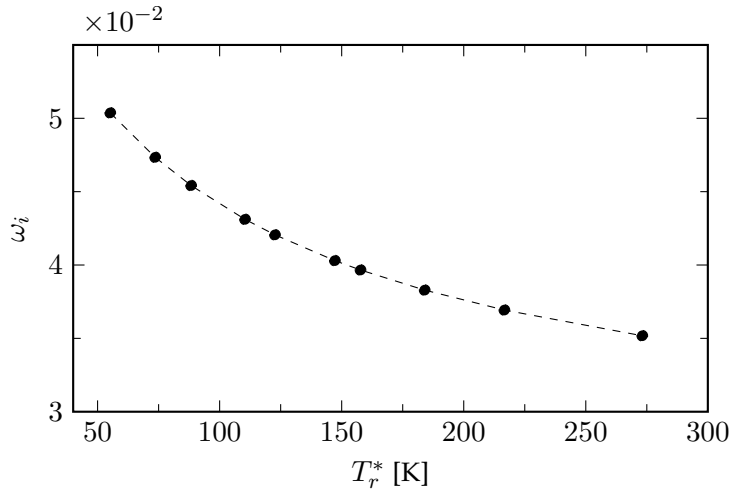

Figure 4.10. Sensitivity of the Mack mode temporal growth rate to the absolute reference temperature T_r^*.

higher than at the reference temperature used in the current work, i.e. 273.15 K. Therefore, one should be careful in comparing results from wind tunnel experiments with data extracted from the current work.

4.3 Provision of DNS data

The data obtained from the DNS, used for the analysis of the results in the current work, has been made publicly available. The access procedure, the complete description of the structure of the database and the specifications of the data formats are discussed in Appendix B *(DNS Database)*.

Chapter 5

Roughness Receptivity & Wake Instability

In this chapter the receptivity of a boundary layer near roughness elements and the linear instability of the resulting roughness wake is investigated. The effect of different freestream disturbance types, roughness shape and wall temperature is studied. A similar study was performed by De Tullio and Sandham (2012) using a single sharp-edged roughness element. In this work a large number of different roughness element shapes are used.

5.1 Case details

The details of the different cases carried out for the current study on roughness receptivity and wake instability are provided in Table 5.1. A single naming convention is used in both the current chapter and Chapter 6 *(Stability Analysis of Roughness Wakes)* since they deal with the same simulations. The naming convention is centred around the type of roughness element, as it is the primary aspect that distinguishes the different cases. Six different roughness elements, characterised in Chapter 4 *(Problem Definition & Numerical Set-up)*, are investigated: a smooth bump (Bump), three flat-top elements with cylindrical (Cyl), square (Square) and diamond-shaped (Diam) planform shapes, and roughness elements with an upward (R-Up) and downward (R-Down) ramp. A flat plate case without roughness element (Plate) is used as a baseline case for comparisons.

The effect of the freestream disturbance type on the roughness receptivity is investi-

Table 5.1. Cases details of the simulations in the roughness receptivity and wake instability study.

Case	M	Re	Re_k	T_w	Disturbance	Geometry
Bump	6.0	8200	331	7.02	type A	smooth bump
Cyl (-A)	6.0	8200	331	7.02	type A	flat-top (cyl.)
Cyl-V	6.0	8200	331	7.02	type V	flat-top (cyl.)
Cyl-Æ	6.0	8200	331	7.02	type Æ	flat-top (cyl.)
Cyl-T0.5	6.0	4135	331	3.50	type A	flat-top (cyl.)
Square	6.0	8200	331	7.02	type A	flat-top (square)
Diam	6.0	8200	331	7.02	type A	flat-top (diamond)
R-Up	6.0	8200	331	7.02	type A	ramp-up
R-Down	6.0	8200	331	7.02	type A	ramp-down
Plate	6.0	8200	–	7.02	type A	flat plate

gated by comparing the results of the cylindrical flat-top cases with disturbances of type A (Cyl-A), type V (Cyl-V) and type Æ(Cyl-Æ). Note that in all other cases type A disturbances were introduced. As explained in Chapter 4 *(Problem Definition & Numerical Set-up)*, the disturbances are imposed at the inflow boundary and have an amplitude of $a = 2 \times 10^{-6}$ in the current chapter, which is small enough to yield linear disturbance growth. The baseline wall temperature is set to a hot wall, i.e. adiabatic wall temperature $T_w = T_{ad}$. A cylindrical flat-top roughness case with a reduced wall temperature ($T_w = 0.5\,T_{ad} = 3.5$) is included (Cyl-T0.5) to study the effect of a cold wall condition on the receptivity and wake instability.

For all of the hot-wall simulations, the Mach number is $M = 6.0$ and the Reynolds number, based on the displacement thickness of the laminar boundary layer at the inflow, is $Re = 8200$. For the cold-wall case the Reynolds number based on inflow displacement thickness is set to $Re = 4135$, such that the roughness Reynolds number Re_k, based on the roughness height and computed using the flow parameters in the surrounding laminar boundary layer at this height, is the same for the hot-wall and cold-wall cases. The height of the roughness elements in the current chapter is set to $k = 1.0$. Since the height of all roughness elements is the same, also the roughness Reynolds numbers are identical ($Re_k = 331$). The details of the grid used in the simulations of the current chapter is given in Table 4.1 (Domain B).

5.2 Analysis of the roughness-modified base flow

To study the effect of the roughness element on boundary layer receptivity and the instability of its wake, the differences between the flat plate boundary layer and roughness-induced modifications of the base flow should be understood. In order to highlight the modifications induced by the roughness element, which will determine the stability characteristics of the laminar flow, the steady-state laminar base flow around the roughness elements is analysed and compared with the flow over a smooth flat plate without roughness.

5.2.1 Effect of roughness shape

One of the primary effects of an obstacle, like a roughness element, encountering a supersonic flow is the formation of shock waves, which are not present in the case of a flat plate boundary layer. Figure 5.1 shows the boundary layer, visualised by streamwise velocity at the roughness centreline, over the six different roughness elements (with hot wall conditions). Black contours of negative $\nabla \cdot \mathbf{u}$ show shock waves that are generated by the coalescence of compression waves originating from the roughness element. Except in the case of cases R-Up and R-Down, two oblique shock waves can be seen to be present: one originating from the front of the roughness and another originating from the aft section. The slowly-varying geometry of the upward and downward ramps prevent the generation of a rapid succession of compression waves and the subsequent coalescence into shocks. In cases R-Up and R-Down, a single shock is present originating from the aft and front section respectively. It can be seen that the angles of the shocks are similar for all cases. This is because the height of the roughness elements are the same and only the top part of the different roughness elements (which are quasi shape-independent) encounter supersonic flow, so that the planform shape of the roughness elements does not play a large role in the shock patterns. The Mach number at the roughness element height in the undisturbed boundary layer is $M_k = 1.78$.

A closer view of the flow around the different roughness elements, and in particular of the induced recirculation/separation regions, is shown in Figure 5.2 using contours of wall-normal velocity and of small negative velocity to indicate the flow recirculation. A table with the lengths of these regions is shown in Table 5.2, from which a more quantitative comparison can be drawn.

The generation of recirculation regions and their lengths can be seen to be highly

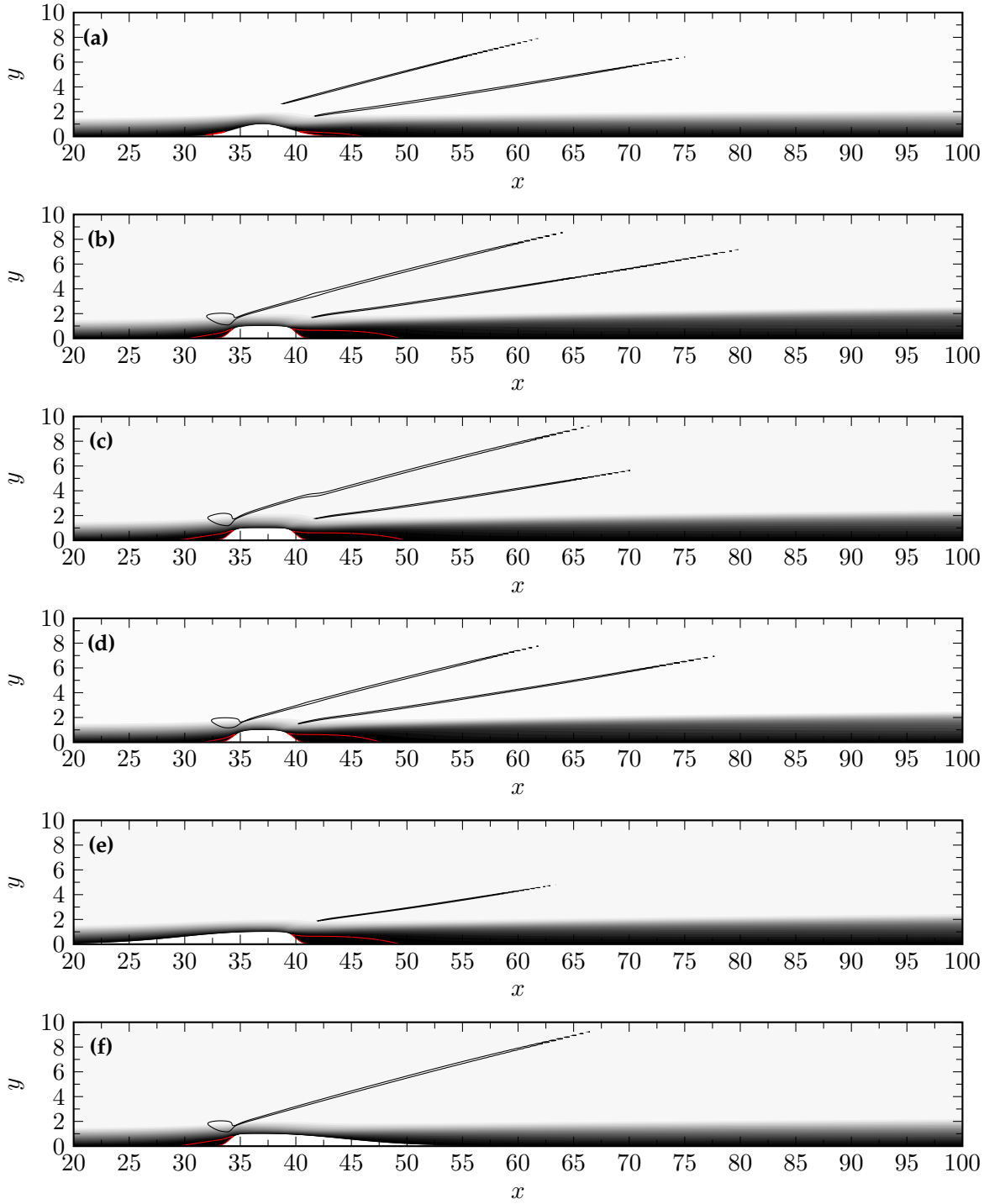

Figure 5.1. Contours of streamwise velocity u for the different roughness elements. Recirculation regions are shown as red contours of $u = -10^{-4}$ and and the separation and reattachment shocks are visualised using black contours of negative $\nabla \cdot \mathbf{u}$. **(a)** Bump; **(b)** Cyl; **(c)** Square; **(d)** Diam; **(d)** R-Up; **(f)** R-Down

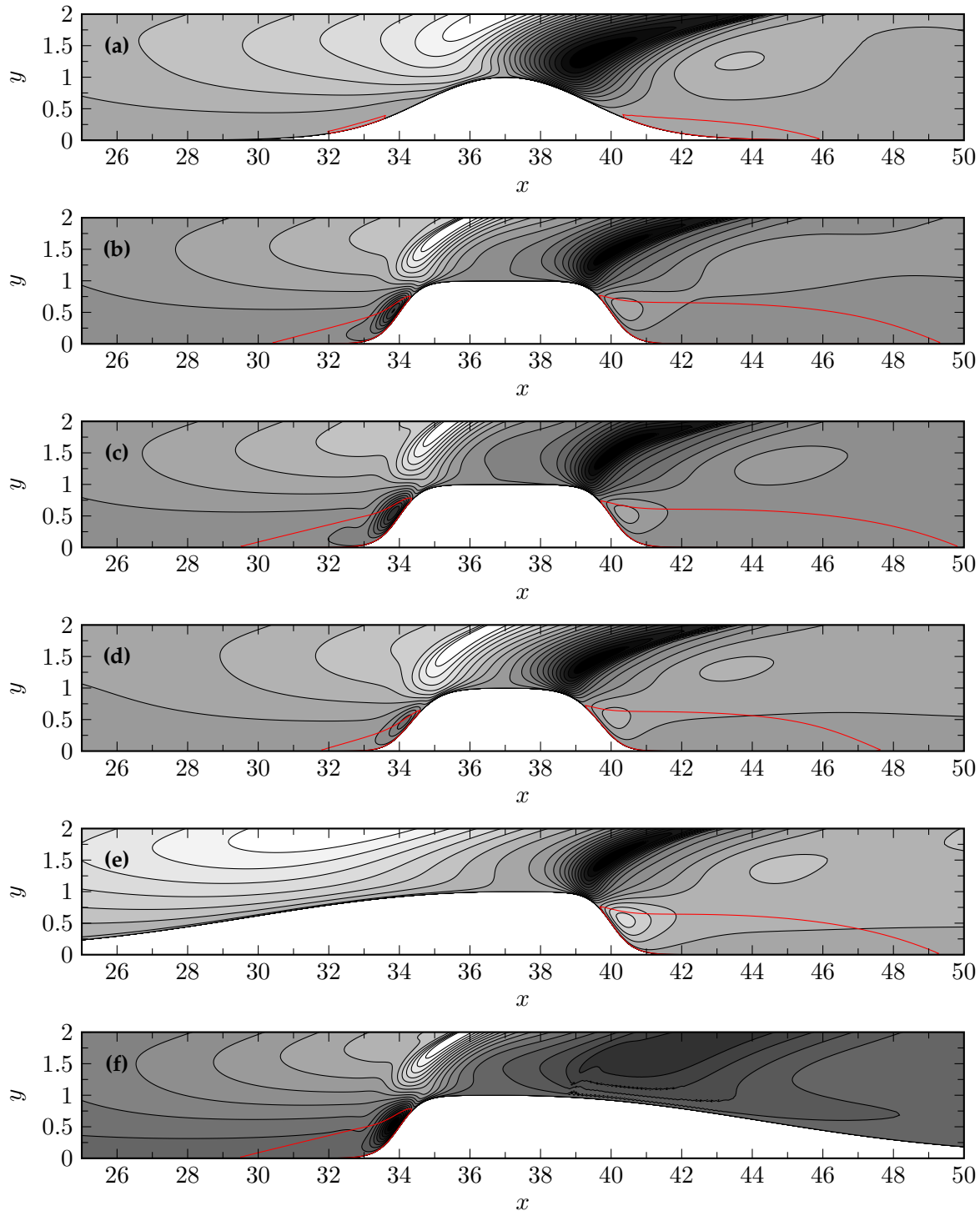

Figure 5.2. Contours of wall-normal velocity v around the different roughness elements. Recirculation regions are shown as red contours of $u = -10^{-4}$. **(a)** Bump; **(b)** Cyl; **(c)** Square; **(d)** Diam; **(d)** R-Up; **(f)** R-Down

Table 5.2. Length of the front and aft recirculation regions around the different roughness elements.

Case	$L_{\text{sep}}^{\text{front}}$	$L_{\text{sep}}^{\text{aft}}$
Bump	1.6	5.6
Cyl	3.9	9.7
Square	4.8	10.1
Diam	2.8	8.4
R-Up	–	9.6
R-Down	4.9	–
Cyl-T0.5	3.4	7.5

dependent on the roughness element shape. The recirculation regions around the smooth bump are considerably smaller than in the case of the flat-top roughness elements. The upstream region is approximately 59% smaller and the downstream region approximately 42% smaller than the regions around the cylindrical flat-top element. These regions are also much thinner than in the case of the flat-top element, as illustrated by Figure 5.2. This behaviour is expected, since the flow around the smooth bump does not encounter an abrupt change in geometry. The recirculation zones around the cylindrical, square and diamond-shaped flat-top roughness elements are qualitatively similar and have approximately the same thickness, but varying separation lengths. Between these three roughness elements, case Diam has the shortest recirculation zones, both upstream and downstream. The cylindrical element has regions of separation that are 39% (upstream) and 15% (downstream) larger, while case Square has the largest upstream and downstream separation lengths, i.e. respectively 71% and 20% larger than for case Diam. The ramps in cases R-Up and R-Down can be seen to completely prevent flow separation due to the slowly-varying ramp geometry. They do not have a significant impact on the recirculation lengths on the opposite side of the ramp, i.e. the separation length upstream of roughness element with downward ramp (case R-Down) is approximately the same as the no-ramp case Square and the recirculation region downstream of the ramped-up element (case R-Up) has roughly the same length as case Square.

Pairs of counter-rotating streamwise vortices are generated by the roughness elements, which generate a wake consisting of a low-speed streak at the centreline flanked by a pair of high-speed streaks due to the lift-up mechanism (Landahl, 1980). The vortices transport low-momentum fluid away from the wall and high-momentum fluid towards the wall, yielding the low-speed and high-speed streaks

respectively. Regions of high shear stress, both wall-normal and spanwise shear, are generated in the roughness wake. Figure 5.3 shows contours of wall-normal shear $\partial u/\partial y$ (*left*) and spanwise shear $\partial u/\partial z$ (*right*) at $x = 60$. It shows that the structure of the shear layers generated behind the different roughness elements is essentially the same in all cases. High levels of wall-normal shear are present away from the wall ($y \approx 1.5 - 2.0$) at the roughness centreline as a detached shear layer, and close to the wall away from the centreline (at approximately $z = z_r \pm 7.5 - 8.0$). High levels of spanwise shear can be observed away from the centreline. The spanwise position of these high-shear regions is dependent on the location of the generated streamwise vortices and therefore the shape of the roughness elements.

Besides the location of the high-shear regions, the strength is highly dependent on the roughness element. As can be seen in Figure 5.3, the smooth bump roughness element generates considerably weaker shear layers than the other roughness elements. The flat-top roughness elements with cylindrical, square and diamond planform shapes have very similar levels of shear stress, with only the spanwise position of the shear stress different: closest to the centreline for case Diam, and furthest away for case Square. The case with an upward ramp case R-Up has a very similar structure of the shear layers than the no-ramp case Square, both in position and shape of the high-shear regions. However, the level of the shear stress behind this ramped-up roughness element is lower than the element without ramp. It has been observed that the upward ramp yields considerably lower levels of streamwise vorticity, resulting in lower levels of shear and thus a weaker roughness wake. The roughness element of case R-Down generates considerably lower levels of wall-normal shear stress and the detached shear layer is weaker. The levels of spanwise shear are comparable to case R-Up however, although these high-shear regions are differently shaped and seem to be located further away from the roughness centreline.

This behaviour is also observed in more detail in Figure 5.4, which shows the maximum shear stress along the domain for all the hot-wall cases. For $x \geq 60$ the wall-normal shear stress, shown in Figure 5.4a, is similar for cases Cyl, Square and Diam, although the former has a value that is approximately 10% higher (computed at $x = 60.0$) than the latter two. Both the ramp-up and ramp-down cases reach much lower shear stress values, even though the differences between these cases decrease further downstream. The smooth bump generates significantly lower values of wall-normal shear stress. The spanwise shear stress, shown in Figure 5.4b, generally follows the same trend. However, the spanwise shear stress behind case Diam now

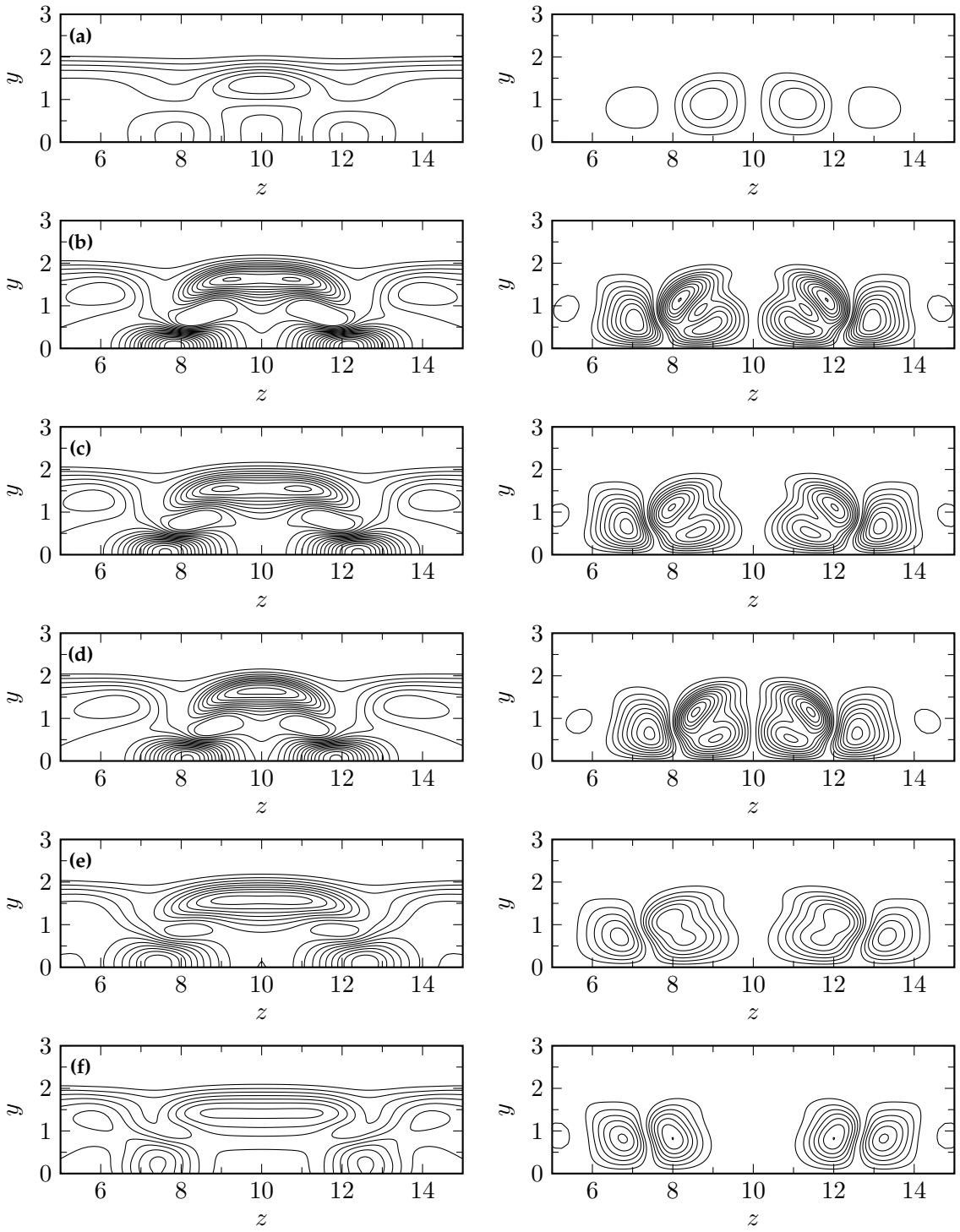

Figure 5.3. Contours of wall normal shear $\partial u/\partial y$ (*left*) and spanwise shear $\partial u/\partial z$ (*right*) at $x = 60$ for the hot-wall roughness cases. Contour levels are plotted every $\Delta\frac{\partial u}{\partial y} = 0.10$ and $\Delta\frac{\partial u}{\partial z} = 0.05$ starting from zero. **(a)** Bump; **(b)** Cyl; **(c)** Square; **(d)** Diam; **(d)** R-Up; **(f)** R-Down

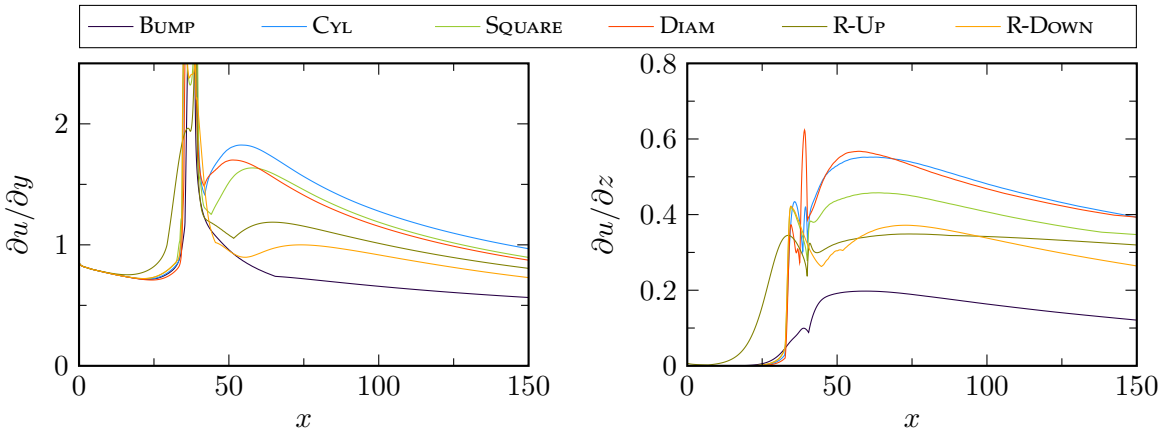

(a) Wall-normal shear $\partial u/\partial y$

(b) Spanwise shear $\partial u/\partial z$

Figure 5.4. Maximum shear stress along the domain for the hot-wall roughness cases.

follows case Cyl, while the square flat-top element has slightly lower values. Both the upward and downward ramps decrease the generated spanwise shear, and also the smooth bump has a considerably weaker wake.

In summary, the different flat-top roughness elements have fairly similar levels of (wall-normal) shear stress in the roughness wake, and the change in planform has mainly an influence of the spanwise location of the high-shear regions. The upward ramp slightly reduces the creation of streamwise vorticity and results in a slightly weaker roughness wake compared to the no-ramp case. The downward ramp allows the detached shear layer to weaken considerably, while minimally affecting the generated spanwise shear stress compared to the ramped-up case. Both the ramp-up and ramp-down cases result in lower levels of shear stress. The smooth bump does not yield a very strong roughness wake, and the levels of shear are considerably lower than for the other roughness elements.

5.2.2 Effect of wall cooling

The effect of wall cooling on receptivity near a roughness element is studied by considering case Cyl-T0.5 and comparing it to the corresponding hot wall baseline case Cyl. The effects of wall cooling on the laminar base flow need to be understood to correctly interpret its effect on the stability characteristics of the roughness wake.

Figure 5.5 shows the recirculation regions as red contour lines around the cold-wall cylindrical flat-top roughness element on top of contours of wall-normal velocity.

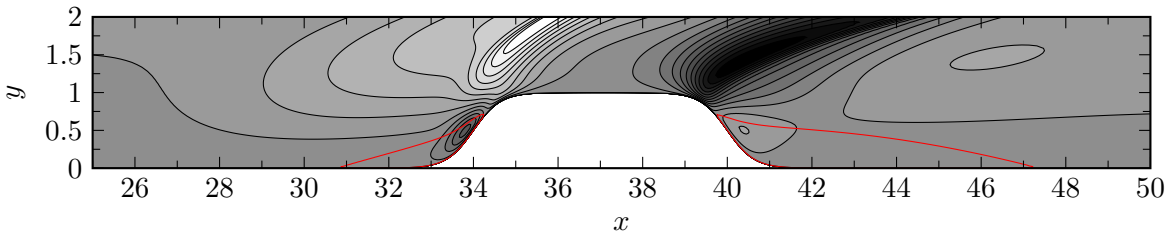

Figure 5.5. Contours of wall-normal velocity v around the cold-wall flat-top roughness case Cyl-T0.5. Recirculation regions are shown as red contours of $u = -10^{-4}$.

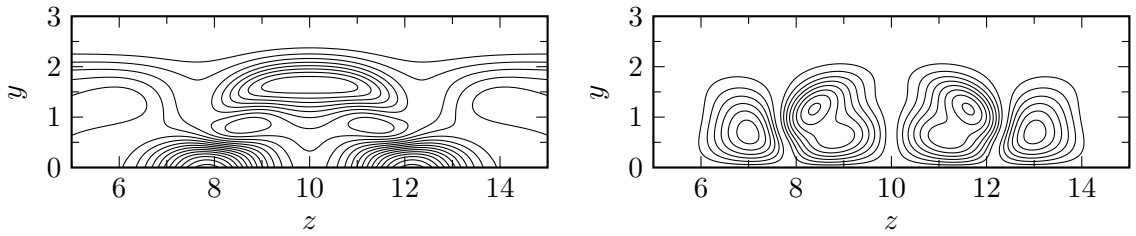

Figure 5.6. Contours of wall normal shear $\frac{\partial u}{\partial y}$ (*left*) and spanwise shear $\frac{\partial u}{\partial z}$ (*right*) at $x = 60$ for the cold-wall roughness case Cyl-T0.5. Contour levels are plotted every $\Delta\frac{\partial u}{\partial y} = 0.10$ and $\Delta\frac{\partial u}{\partial z} = 0.05$ starting from zero.

By comparing this figure with its hot-wall counterpart in Figure 5.2, it can be seen that the separation lengths are considerably smaller. The lengths of the front and aft recirculation lengths, computed at the roughness centreline and given in Table 5.2, are respectively 13% and 23% smaller for the cold-wall case. This can be understood as the increased resistance to separation of a boundary layer with increased shear stress.

Contours of wall-normal and spanwise shear stress behind cylindrical flat-top element with a cooled wall are shown Figure 5.6. By comparison to Figure 5.3, it can be seen that the structure of the high-shear regions is very similar, but that the levels of shear stress generated by the roughness element with wall cooling are lower than in the case with hot-wall conditions, in particular for the detached shear layer at the roughness centreline away from the wall. Wall cooling seems to have a stabilising effect on the shear layers of the roughness wake.

5.3 Boundary layer receptivity

In this section the growth of boundary layer instabilities in the vicinity of the roughness elements is investigated.

5.3.1 Characterisation of disturbances

The post-processing method used to characterise the boundary layer disturbances in this section is the same as De Tullio and Sandham (2012, 2015) and full details can be found in that reference. A very short summary is given here.

The behaviour of disturbances in the flow field is dependent on their frequency. The time-dependent flow fields, computed by the DNS, are therefore transformed from the temporal space into Fourier space using the discrete Fourier transform algorithm. The flow field is thus decomposed into its frequency components with non-dimensional frequencies $F = f^*\delta_0^*/U_\infty^*$. The flow is also Fourier transformed in the spanwise spatial direction, resulting in a collection of spanwise modes with spanwise wavenumbers k_z. The discrete Fourier transform equation that is used for the transformation from physical to Fourier space is:

$$\hat{s}_{\eta,\xi}(x,y) \coloneqq \frac{2}{LJ}\sum_{j=0}^{J-1}\sum_{l=0}^{L-1}\mathbf{s}(x,y,z_l,t_j)e^{-2\pi i\frac{\eta}{J}j}e^{-2\pi i\frac{\xi}{L}l}, \tag{5.1}$$
$$\eta = 0,1,\ldots,J-1 \;\text{ and }\; \xi = 0,1,\ldots,L-1,$$

where J and L are the total temporal and spatial samples and $\mathbf{s} = [\rho,u,v,w,T]$. The indices η and ξ represent respectively the discretised frequencies and spanwise wavenumbers.

The amplitude of a disturbance of a certain frequency in the boundary layer is obtained by summing the amplitude of the spanwise Fourier modes $|\hat{s}_{\eta,\xi}|(x,y)$, and the overall boundary layer response is given by integrating this amplitude over the wall-normal extent of the boundary layer, defined by the boundary layer thickness δ_{99}, i.e.

$$\langle|\hat{s}|\rangle(x) \coloneqq \int_0^{\delta_{99}}\sum_{\xi=-M}^{+M}|\hat{s}_{\eta,\xi}|(x,y)\,dy. \tag{5.2}$$

5.3.2 Flat plate stability

Before investigating the instability of the roughness wake cases, the linear stability of the flat-plate boundary layer is analysed using `COMPASS` and DNS. The base profiles

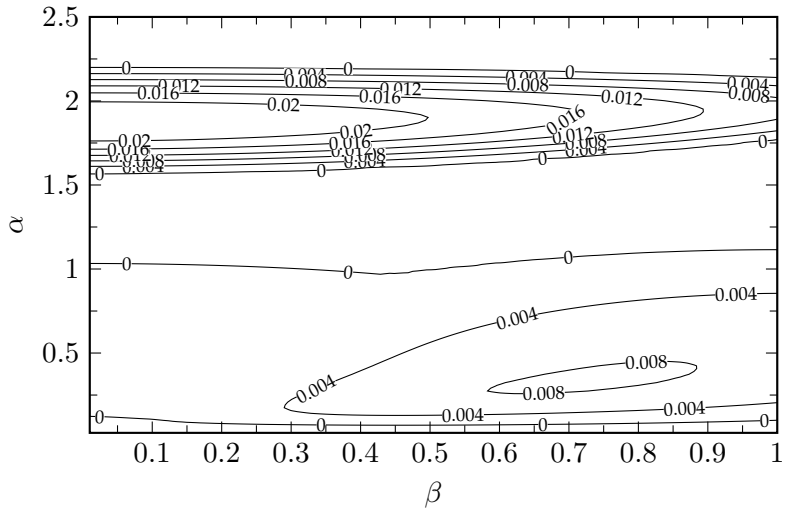

Figure 5.7. Temporal stability map of the flat plate at $x = 0.0$, depending on spanwise and streamwise wavenumber, shown by contours of temporal growth rate.

used for the linear stability analysis are taken from the DNS results of case Plate.

Figure 5.7 shows the temporal stability map of the Mach 6.0 flat plate boundary layer with Reynolds number $Re = 8200$, computed by COMPASS, and gives an indication of the most unstable boundary layer modes. Two distinct peaks in the temporal growth rate can be observed: a two-dimensional disturbance with a high streamwise wavenumber ($\alpha = 1.87$, $\beta = 0.0$) and a three-dimensional disturbance at a lower streamwise wavenumber ($\alpha = 0.36$, $\beta = 0.74$). The temporal growth rate of this two-dimensional mode is $\omega_i^{\text{2D}} = 0.0238$, while the three-dimensional oblique mode has a growth rate that is approximately three times lower, i.e. $\omega_i^{\text{3D}} = 0.0083$. The boundary layer can be seen to be stable for two-dimensional disturbances with streamwise wavenumbers of $1.0 \lessapprox \alpha \lessapprox 1.5$ and $\alpha \gtrapprox 2.2$.

The eigenfunctions of the streamwise velocity and temperature disturbance of these two most unstable modes are given in Figure 5.8. From Figure 5.8a, which shows the three-dimensional mode, it can be seen that the peak fluctuations occur near the edge of the boundary layer and a second lower-amplitude peak occurs close to the wall. This mode is an oblique first-mode. The phase speed of this mode is $c_{ph} = 0.84$, which is near the slow acoustic mode travelling at $c_{ph} = 1 - \frac{1}{M} = 0.8\bar{3}$. The eigenfunctions shown in Figure 5.8b demonstrate that the most unstable mode is a two-dimensional Mack mode, and has a phase speed of $c_{ph} = 0.93$. The frequency (or in this case the streamwise wavenumber) of the Mack mode is dependent on the

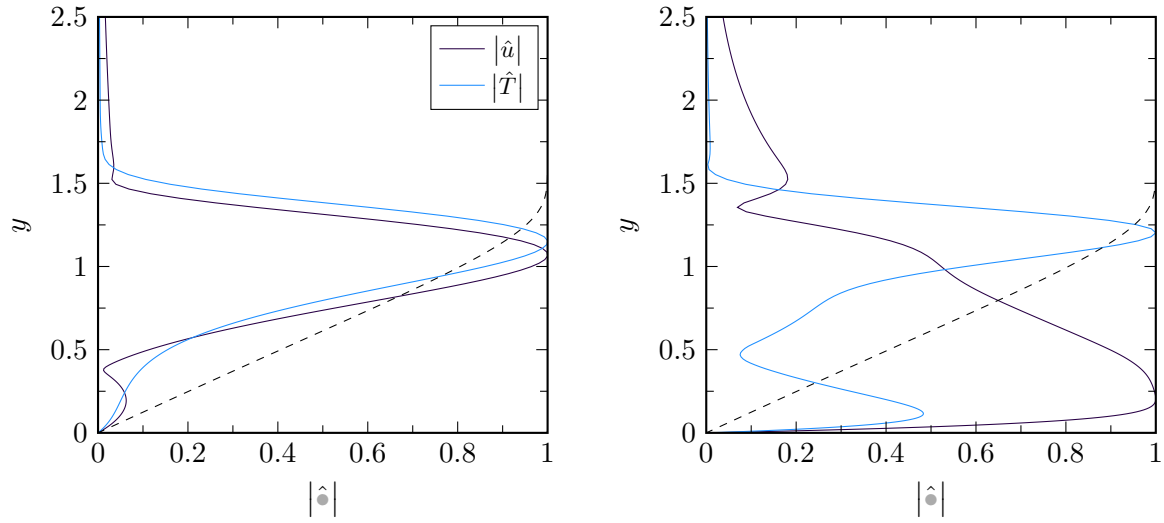

(a) Three-dimensional first mode ($\alpha = 0.36$, $\beta = 0.74$).

(b) Two-dimensional Mack mode ($\alpha = 1.87$, $\beta = 0.0$).

Figure 5.8. Eigenfunction of the most unstable flat-plate instability modes, normalised by its maximum value. Dashed lines show the streamwise velocity profile of the boundary layer.

boundary layer thickness, illustrated by Figure 5.9. This figure shows the stability map for two-dimensional modes (i.e. $\beta = 0.0$) along the flat plate. The streamwise wavenumber of the most unstable two-dimensional Mack mode ranges from $\alpha = 1.87$ near the beginning of the domain and $\alpha = 1.02$ near the end, while the neutral line for the first mode does not show such a strong decay.

Gaster's transform (Gaster, 1962) yields a relation between spatial and temporal instabilities in the limit of small growth rates, and can thus be used to compute the temporal frequency of the neutral curve, which gives information on the frequencies expected to be unstable in the spatial DNS. Gaster states that within the neutral curve, the real part of the spatial wavenumbers and temporal frequencies are approximately the same, i.e.

$$\omega_r^{\text{spatial}} \approx \omega_r^{\text{temporal}} \tag{5.3a}$$

$$\alpha_r^{\text{spatial}} \approx \alpha_r^{\text{temporal}} \tag{5.3b}$$

At $x = 0.0$ and for two-dimensional modes, this would result in the first mode having an unstable envelope up to $\omega_r \approx 0.77$ (or $F \approx 0.12$), while the two-dimensional Mack mode is unstable between $\omega_r \approx 1.40$ (or $F \approx 0.22$) and $\omega_r = 2.02$ (or $F \approx 0.32$).

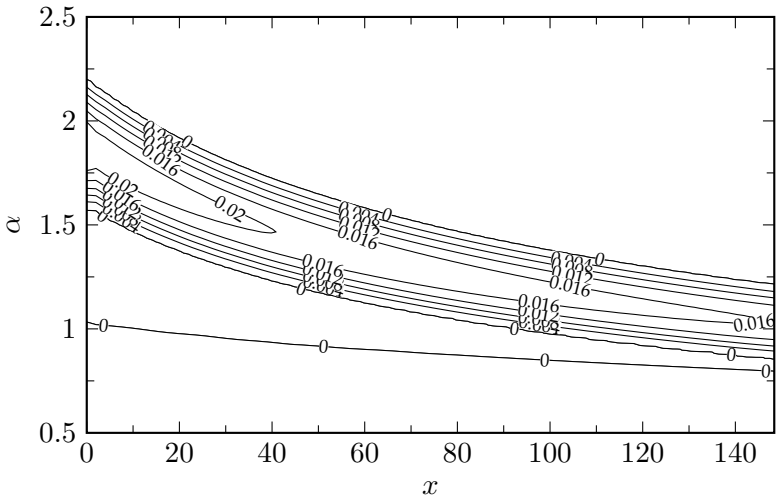

Figure 5.9. Temporal stability map, showing contours of ω_i, of two-dimensional modes along the flat plate.

The spatial growth of disturbances in the flat-plate boundary layer computed from the DNS, i.e. the results from case Plate, are shown in Figure 5.10. It shows that the disturbances with low frequencies have the largest disturbance amplitude in the boundary layer. Up to $x \approx 20$, the boundary layer instabilities are developing from the imposed inflow disturbances, and from that point onwards, exponential instability growth is obtained for most of the frequencies. At $x \approx 20$, the frequencies up to $F = 0.14$ are unstable, while the disturbances with $F = 0.16 - 0.20$ are stable and decay. This is in agreement with the linear stability predictions discussed in the previous paragraph. The small discrepancy between the envelope limit of the first mode instability is most likely due to non-parallel effects which are not taken into account by the linear stability analysis. While the disturbances with low frequencies remain stable throughout the domain, the instabilities with higher frequencies, i.e. $F = 0.16 - 0.20$, go through a region of strong instability grow and subsequent decay along the domain. This is consistent with the instabilities at these frequencies being Mack modes, which were shown in Figure 5.9 to have narrow unstable envelope that moves from high spatial wavenumbers to lower wavenumbers along the domain.

5.3.3 Receptivity near roughness elements

Interaction of different disturbance types Cases with different disturbance types have been run to see how the interaction of these disturbances with the roughness

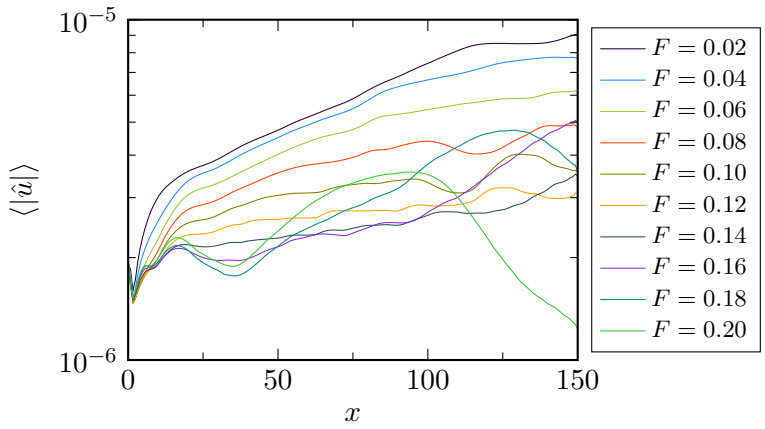

Figure 5.10. Amplitudes of the full spectrum of u' disturbances inside the boundary layer for the flat-plate case PLATE.

element and the resulting roughness wake differs from each other. Figure 5.11 shows the evolution of u' disturbances in the boundary layer of cases with type A (CYL-A), V (CYL-V) and Æ (CYL-Æ) disturbances for $F = 0.06$ and $F = 0.16$.

Upstream of the roughness element, slight disturbance growth occurs at both frequencies when type A disturbances are imposed. For type Æ disturbances, no disturbance growth occurs inside the boundary layer at $F = 0.06$, while the disturbances experience initial decay ($x \lessapprox 20$) and subsequent growth ($20 \lessapprox x \lessapprox x_r$) at $F = 0.16$. Downstream of the roughness element the behaviour of cases CYL-A and CYL-Æ is qualitatively the same, and the boundary layer disturbances grow at a similar rate at both frequencies. The amplitudes of the disturbances are one order of magnitude lower for type Æ disturbances however. When type V perturbations are imposed (case CYL-V) the behaviour is completely different, and another receptivity mechanism seems to be active. Initially, upstream of the roughness element, the boundary layer disturbances grow rapidly when type V perturbations are imposed. Downstream of the roughness element, this growth is weakened and disturbances are quasi-neutral (minor growth at $F = 0.06$ and minor decay at $F = 0.16$) up to $x \approx 80$. Further downstream, disturbance growth occurs again for $F = 0.06$, while disturbances at the higher frequency seem marginally unstable. Overall, the growth rate of the boundary layer disturbances is much smaller when type V disturbances are imposed, and type A perturbations seem the most efficient in exciting unstable boundary layer instabilities. Therefore type A perturbations are imposed in all the other cases of the current chapter. It should be noted that De Tullio and Sandham

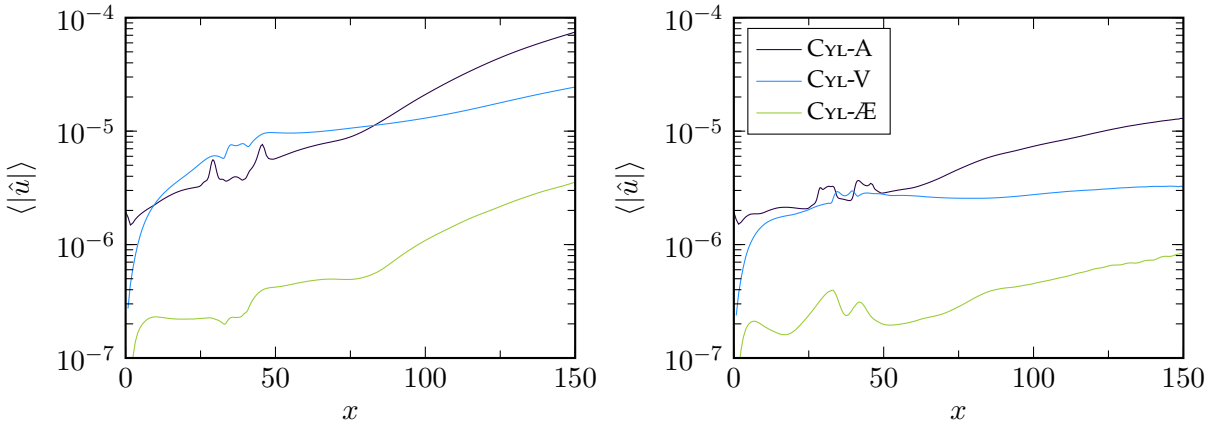

(a) $F = 0.06$ **(b)** $F = 0.16$

Figure 5.11. Amplitude of u' disturbances inside the boundary layer for cases Cyl-A, Cyl-V and Cyl-Æ, showing the effect of different disturbance types. **(a)** $F = 0.06$, **(b)** $F = 0.16$.

(2012) reported similar results for their sharp-edged roughness element, which indicates that the receptivity mechanisms and the interaction between the different disturbance types and the roughness wake is independent of the structure of the wake, and by extension the shape of the roughness element.

Effect of wall temperature The effect of wall temperature on the disturbances developing behind the cylindrical flat-top roughness element is analysed by comparing the hot wall and cold wall cases Cyl and Cyl-T0.5. The wall temperature in the former case is set to $T_w = 3.5$ and type A disturbances were introduced. In Figure 5.12 disturbances of both the hot and cold wall cases, respectively Cyl and Cyl-T0.5, are shown for frequencies $F = 0.02$, $F = 0.06$, $F = 0.14$ and $F = 0.18$.

Upstream of the roughness element the amplitude of the disturbances in the cold wall case is lower than those of the hot wall case for $F = 0.02$ and $F = 0.06$ and higher for $F = 0.14$ and $F = 0.18$. Exactly the same behaviour was seen for the cold wall sharp-edged roughness case of De Tullio and Sandham (2012). This is expected since the presence of the roughness element is not felt that far upstream, and this behaviour is thus not dependent on the type or shape of the roughness element.

Downstream of the roughness element, the behaviour between the hot wall and cold wall case of the disturbances is very different. It can be seen that wall cooling has a stabilising influence on the disturbances with a lower frequency, i.e. $F = 0.02$ and

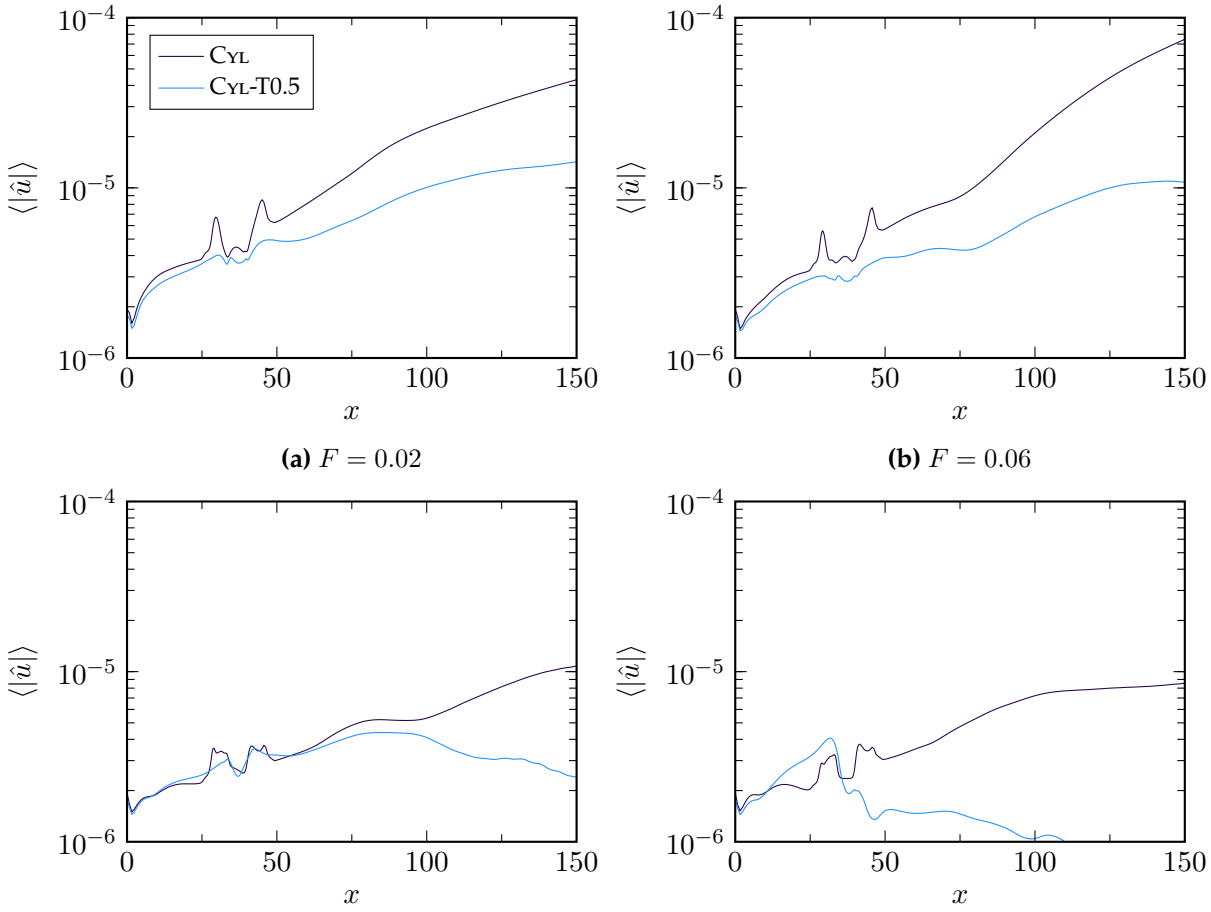

(a) $F = 0.02$ **(b)** $F = 0.06$

(c) $F = 0.14$ **(d)** $F = 0.18$

Figure 5.12. Amplitude of u' disturbances inside the boundary layer for cases Cyl and Cyl-T0.5, showing the effect of wall cooling. **(a)** $F = 0.02$, **(b)** $F = 0.06$, **(c)** $F = 0.14$, **(d)** $F = 0.18$.

$F = 0.06$. The disturbance with $F = 0.02$ is still unstable, but grows much more slowly than its hot wall counterpart. For $F = 0.06$ it can be seen that the disturbance is unstable initially, albeit less so than the hot wall case, but becomes neutrally stable near the end of the domain.

For $F = 0.14$ there is not a large qualitative difference between the two cases up to $x \approx 80$. The growth rate downstream of the roughness element is lower for the cold wall case, but the disturbance amplitude for the hot wall and cold wall cases is approximately the same at $x \approx 80$. After this point however, cooling leads to damping of the disturbances with $F = 0.14$, while the disturbances are unstable

throughout the domain for the case with a hot wall. Upstream of the roughness element, wall cooling leads to a strong increase in the instability growth rate for $F = 0.18$. After interaction with the roughness element, strong disturbance damping occurs however.

Effect of roughness shape It has been noted that there are some differences between the receptivity and wake instability behaviour of the cylindrical flat-top roughness element presented here and the sharp-edged roughness element of De Tullio and Sandham (2012). The roughness element shape can have a significant effect on the behaviour of instabilities downstream, owing to the distinct roughness wake structure and corresponding stability characteristics. The effect of the roughness element shape on the disturbance growth in the wake is discussed in more detail in the next section.

5.4 Effect of roughness shape on wake instability

In this section the influence of the shape of the roughness on the behaviour of disturbances growing in the wake is investigated by considering the wakes behind the various roughness elements, i.e. smooth bump (Bump), cylindrical flat-top (Cyl), square flat-top (Square), diamond-shaped flat-top (Diam), ramp-up (R-Up) and ramp-down (R-Down). Only the response to acoustic disturbances (type A) and cases with hot-wall conditions are considered in the study of the effect of roughness shape on wake instability. Note that the roughness height and the frontal projected area are the same for all roughness elements.

5.4.1 Disturbance growth in the roughness wake

The boundary layer response to disturbances of type A for the frequencies $F = 0.02 - 0.20$ is shown in Figure 5.13 for all the different roughness elements. This figure shows the streamwise evolution of fluctuating u' disturbances with frequencies F, and gives an immediate overview of the largest differences between the cases.

From Figure 5.13 it can be seen that the largest amplitudes of disturbances at the end of the domain are of similar order for case Square, Diam, R-Up and R-Down ($\langle|\hat{u}|\rangle \approx 3 - 5 \times 10^{-5}$), while case Bump has considerably lower amplitudes of disturbances in the wake and none of the modes show any large amplification. Case Cyl has the largest amplitudes at the end of the domain ($\langle|\hat{u}|\rangle \approx 8 \times 10^{-5}$), but qualitatively looks

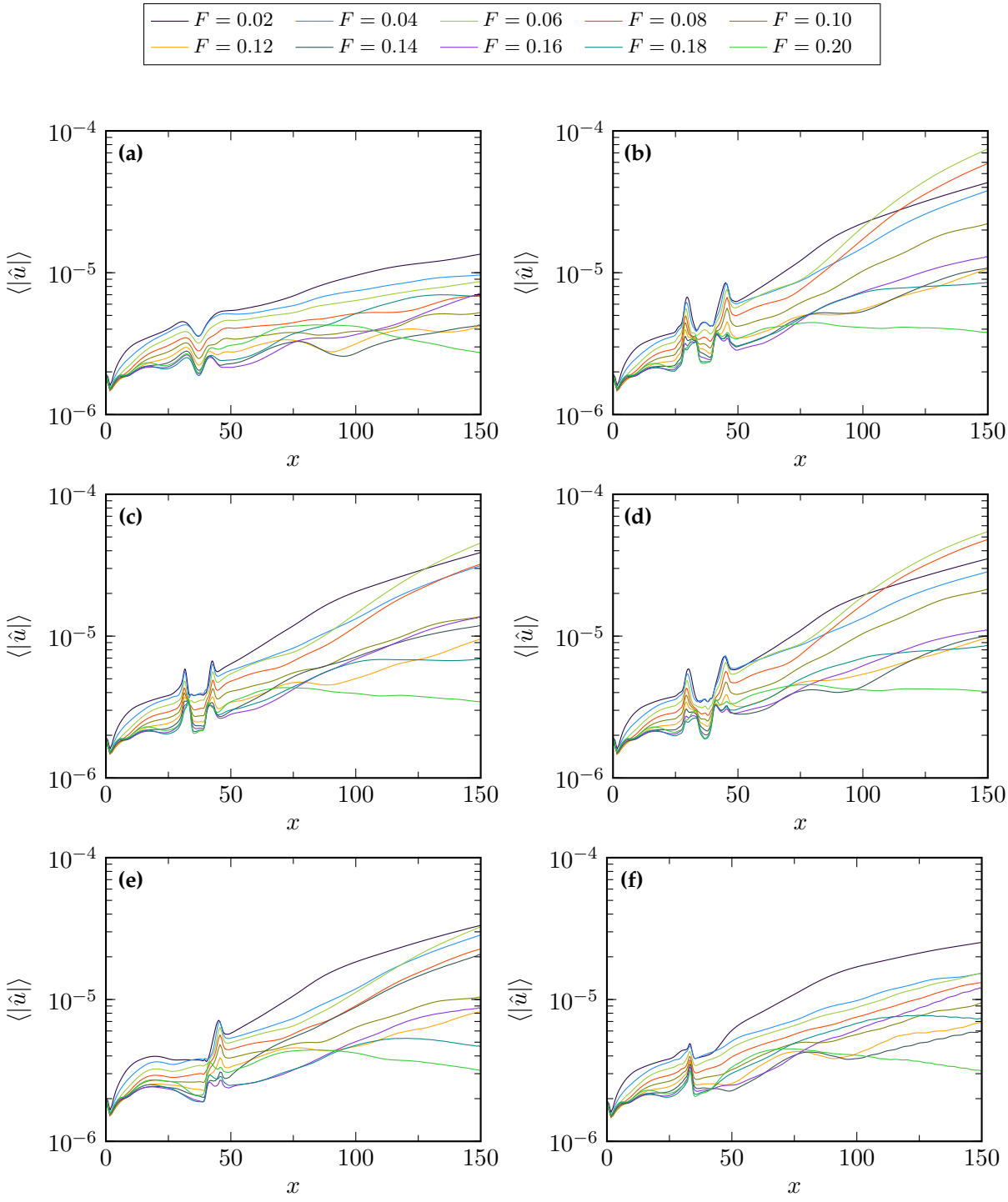

Figure 5.13. Amplitudes of the full spectrum of u' disturbances inside the boundary layer for all hot-wall cases. **(a)** Bump, **(b)** Cyl, **(c)** Square, **(d)** Diam, **(e)** R-Up, **(f)** R-Down.

very similar to cases Square and Diam, for which the modes with $F = 0.06$ are the most amplified. For the rest of the cases, it generally holds that the amplitude at the end of the domain reduces with increasing frequency F. The mode with $F = 0.20$ is stable after a short unstable region up to $x \approx 75$.

In the next sections, these results will be discussed in more detail.

Effect of roughness frontal profile Figure 5.14 shows the amplitude of u' disturbances with $F = 0.02$, $F = 0.06$, $F = 0.14$ and $F = 0.18$ inside the boundary layer for cases Cyl and Bump, and shows the effect of the roughness frontal shape on the disturbance behaviour in the wake. In this figure, also the flat plate case Plate is shown as grey dashed lines. From Figure 5.14 it is evident that the roughness frontal profile has a large impact on the behaviour of disturbances in the wake. This is as expected, since it has a large influence on the strength and structure of the roughness wake, as was shown earlier, and thus its stability characteristics.

The cylindrical flat-top roughness element induces a large disturbance amplification across the element relative to the smooth bump, as can be seen by comparing the disturbance amplitude at $x \approx 50$. At this location behind the smooth bump, the amplitude is only slightly larger than in the no-roughness flat-plate case (shown as dashed lines). This behaviour is independent of the disturbance frequency. Further downstream of the smooth bump, the rate at which the disturbances grow is comparable to the growth rate in the flat-plate case and the amplitude of disturbances near the end of the domain is only slightly larger than without a roughness element. This shows that the smooth bump in case Bump acts mainly as a disturbance amplifier instead of yielding a roughness wake that considerably increases the disturbance growth rate. The flat-top roughness element in case Cyl can be seen to generate a wake that does strongly alter the growth rate of instabilities, and the disturbance amplitude at the end of the domain is much larger than for the smooth bump or flat-plate case.

Figure 5.15 shows the growth rate of the u' disturbances, computed as

$$\sigma \coloneqq \frac{\mathrm{d}[\ln \langle |\hat{u}| \rangle (x)]}{\mathrm{d}x} \tag{5.4}$$

for these two cases. Note that the differentiation might introduce oscillations in this metric. In particular near the end of the domain, where a one-sided differencing scheme is used to compute the derivative, some oscillations have occasionally been

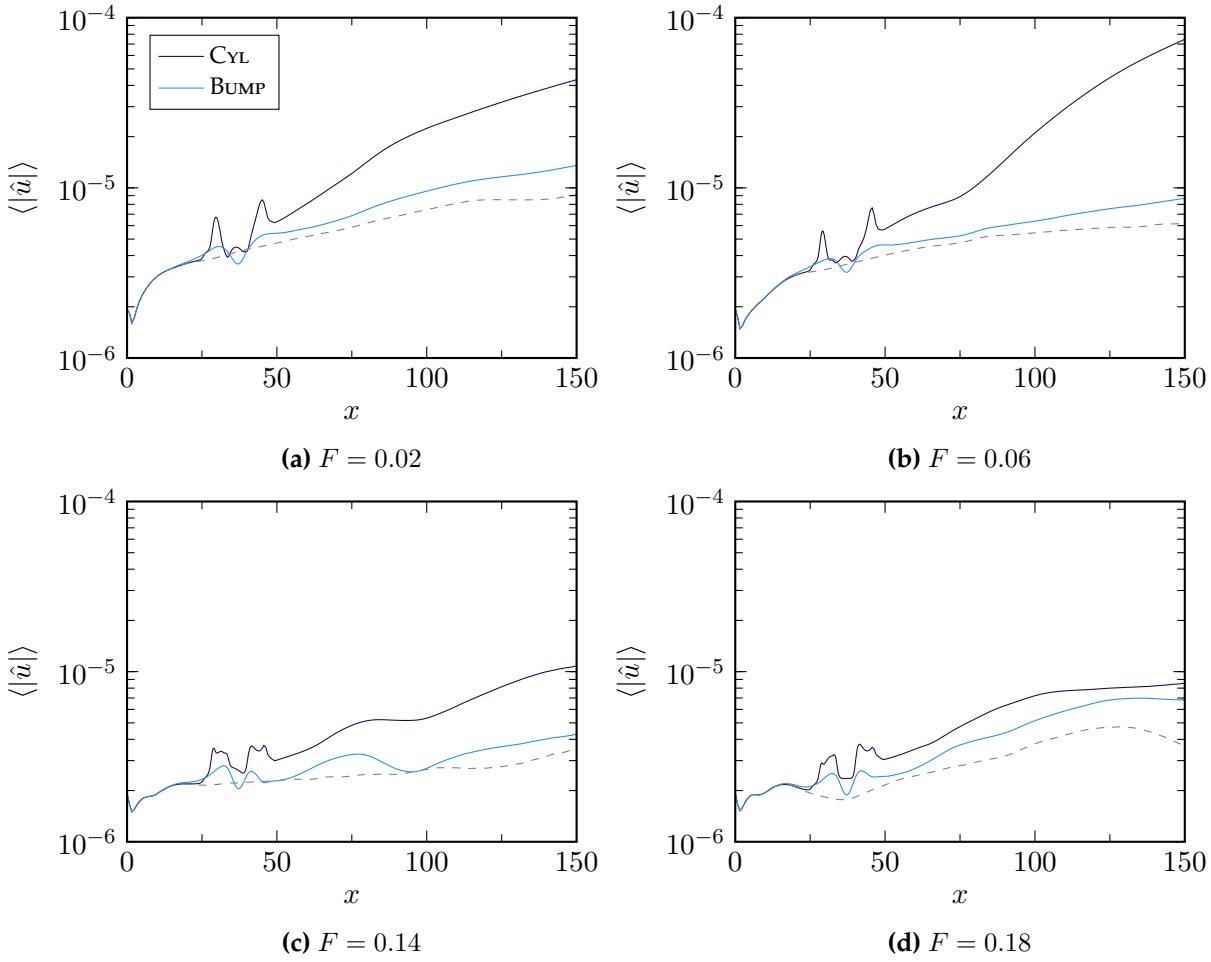

(a) $F = 0.02$ **(b)** $F = 0.06$

(c) $F = 0.14$ **(d)** $F = 0.18$

Figure 5.14. Amplitude of u' disturbances inside the boundary layer for cases Cyl and Bump, showing the effect of roughness frontal shape. **(a)** $F = 0.02$, **(b)** $F = 0.06$, **(c)** $F = 0.14$, **(d)** $F = 0.18$.

observed. It is important to make clear that these oscillations are not grid-to-grid-point oscillations that originate from under-resolved DNS data.

From Figure 5.15 it can be seen that at $F = 0.02$ the behaviour is qualitatively the same for both cases, i.e. an increasing growth rate up to $x \approx 80$, after which the growth rate decays and roughly stabilises. Initially Cyl is much more unstable than Bump, with a growth rate three times as high, but near the end of the domain that difference has reduced and the growth rate behind the cylindrical flat-top is about 70% higher than behind the smooth bump.

A completely different situation occurs at $F = 0.06$, for which case Bump has a

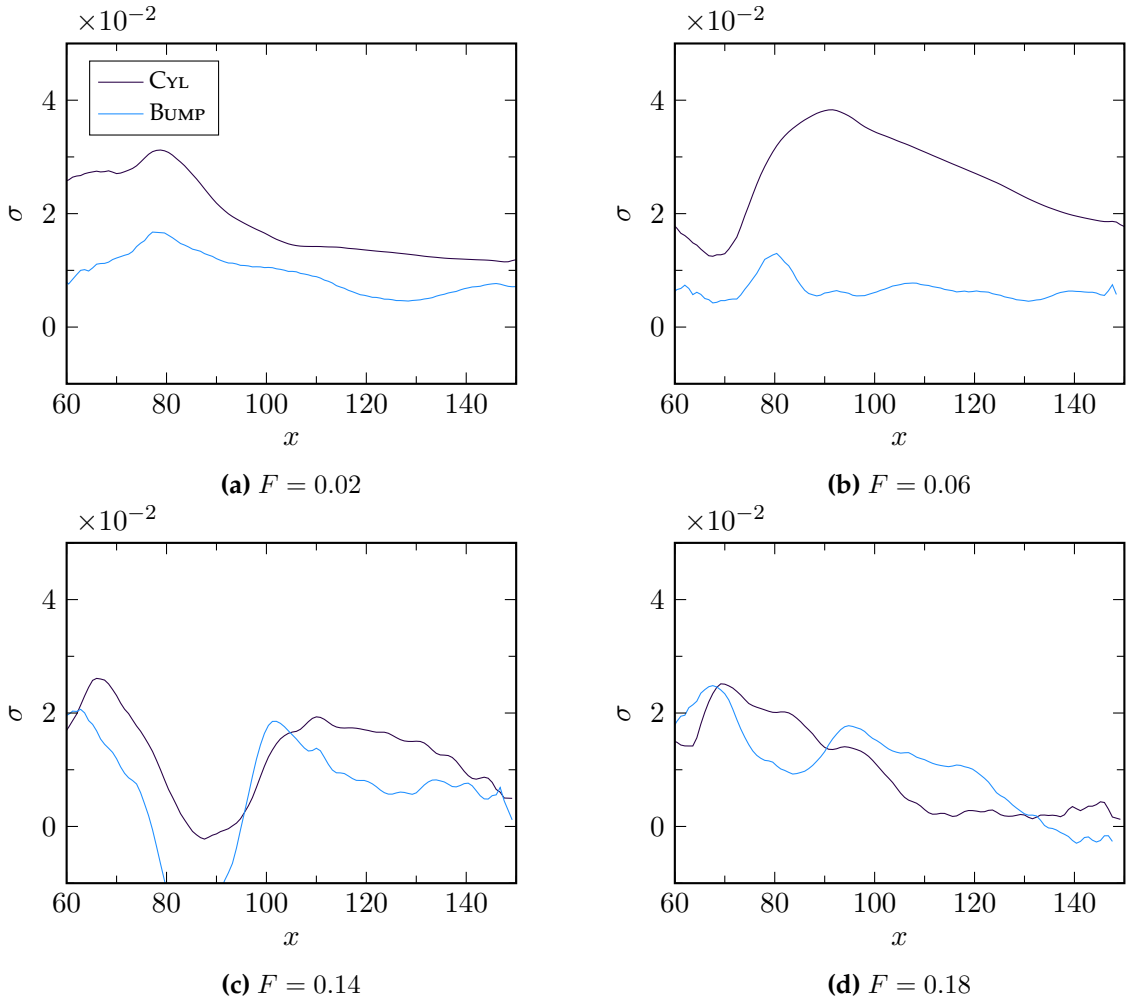

(a) $F = 0.02$ **(b)** $F = 0.06$

(c) $F = 0.14$ **(d)** $F = 0.18$

Figure 5.15. Growth rate of u' disturbances inside the boundary layer for cases Bump and Cyl, showing the effect of roughness frontal shape. **(a)** $F = 0.02$, **(b)** $F = 0.06$, **(c)** $F = 0.14$, **(d)** $F = 0.18$.

relatively constant and small growth rate while CYL is very unstable throughout. The growth rate for CYL experiences a large and abrupt increase between $x \approx 70$ and $x \approx 90$, with a peak instability growth rate that is more than four times larger than case BUMP, after which it slowly and monotonically decreases further downstream. The disturbance with this frequency has the largest growth rate.

At a frequency of $F = 0.14$, the behaviour between the two cases is qualitatively the same. Between $x \approx 60 - 70$ and $x \approx 90$ the wake is stabilising with a rapidly decreasing growth rate and even a short stable region for which the growth rate becomes negative. After $x \approx 100$, the disturbances with $F = 0.14$ are unstable again. The growth rate for case CYL is slightly larger than for case BUMP, although this difference strongly decreases near the end of the domain, where the disturbances seem to be stabilising. At $F = 0.18$ both cases have a growth rate peak at $x \approx 70$, after which the growth rate decays. Behind the flat-top in CYL this decay is monotonic and a constant, approximately neutral state, is reached at $x \approx 110$. Behind the smooth bump in BUMP the wake experiences a stabilising-destabilising pocket between $x \approx 70$ and $x \approx 95$, after which monotonic decay takes place and the growth rate stabilises at $x \approx 140$.

The different behaviour of the disturbances can be explained by investigating the modes that are active at the specific frequencies. Figures 5.16 and 5.17 show the different mode shapes behind the smooth bump of BUMP and flat-top roughness element of CYL at a streamwise location of $x = 96.4$, visualised by contours of $|u'|$-velocity and the real part of the u'-velocity respectively. In the case BUMP, the modes of $F = 0.02$, $F = 0.06$ and $F = 0.14$ are not clearly defined and have the largest amplitude away from the roughness wake in the undisturbed boundary layer. This shows that the roughness wake behind the smooth bump is not very unstable and explains why the behaviour of case BUMP seen in Figure 5.14 is very similar to the flat-plate behaviour.

In this work, the nomenclature introduced by De Tullio and Sandham (2015) will be used to classify the different wake mode types: sinuous-lateral (SL) for an asymmetric mode with the largest amplitude in the lateral shear layers; varicose-lateral (VL) for the symmetric mode with the largest amplitude in the top and lateral shear layers; varicose-centre (VC) for the symmetric mode active near the wall at the roughness centreline.

The modes (with $F = 0.02$, $F = 0.06$ and $F = 0.14$) behind the flat-top roughness element have the largest amplitude in the roughness wake. At $F = 0.02$ and $F = 0.06$

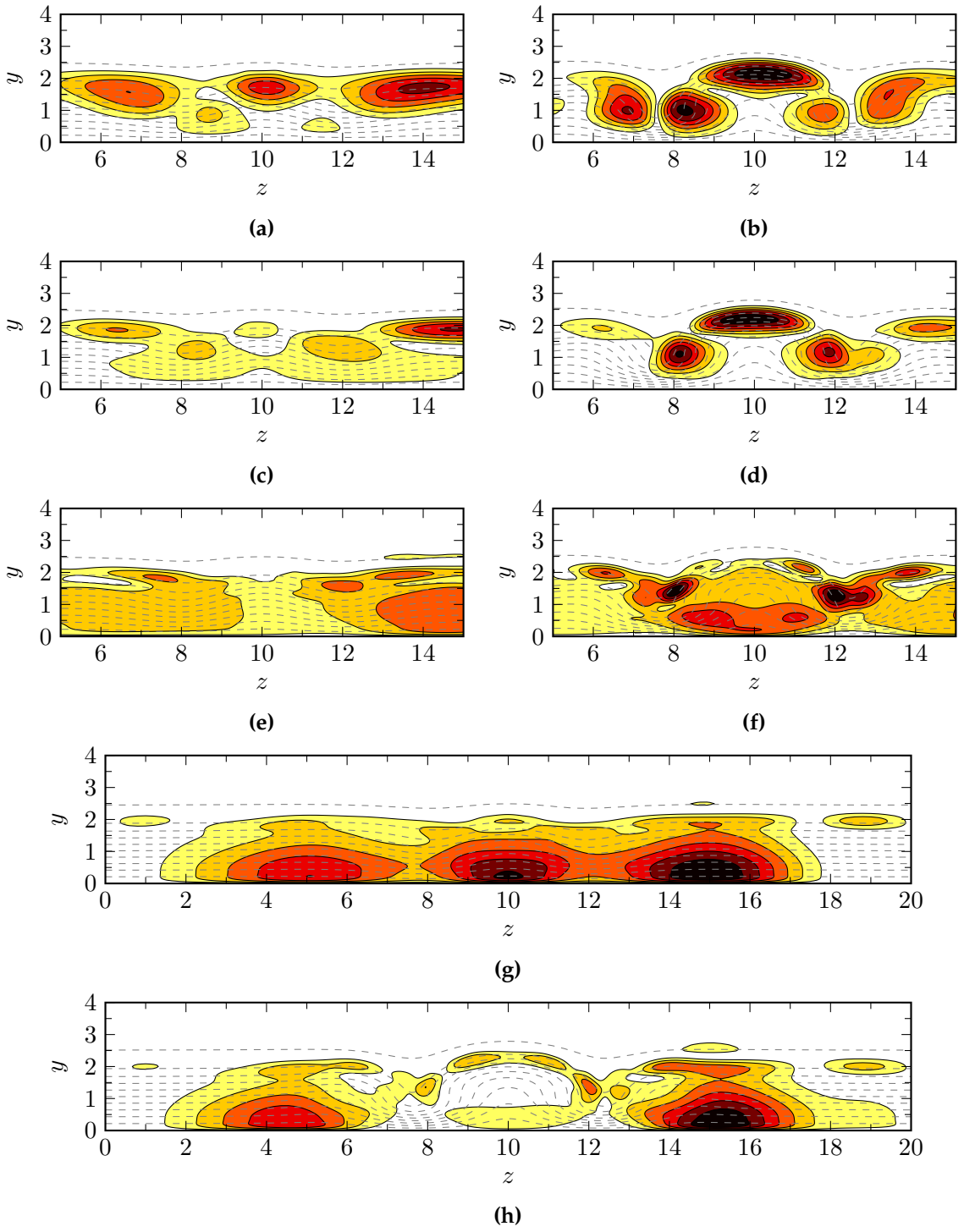

Figure 5.16. Mode shapes at $F = 0.02$ **(a-b)**, $F = 0.06$ **(c-d)**, $F = 0.14$ **(e-f)** and $F = 0.18$ **(g-h)** behind the smooth bump **(a,c,e,g)** and cylindrical flat-top **(b,d,f,h)** roughness element, visualised by contours of $|u'|$-velocity at $x = 96.4$. Dashed contour lines, drawn every $\Delta u = 0.1$, show the mean streamwise velocity.

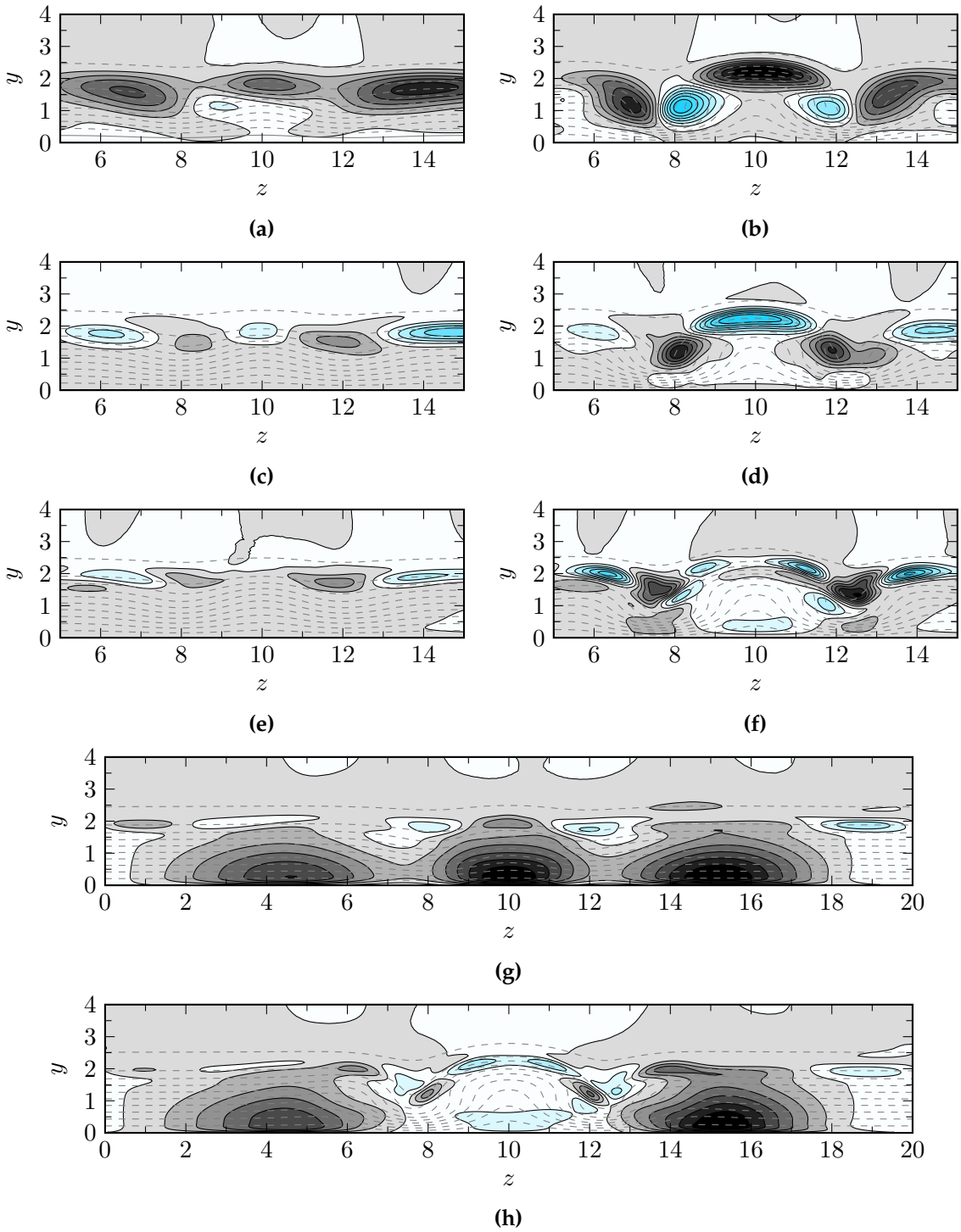

Figure 5.17. Mode shapes at $F = 0.02$ **(a-b)**, $F = 0.06$ **(c-d)**, $F = 0.14$ **(e-f)** and $F = 0.18$ **(g-h)** behind the smooth bump **(a,c,e,g)** and cylindrical flat-top **(b,d,f,h)** roughness element, visualised by contours (black *(negative)* - blue *(positive)*) of the real part of u'-velocity at $x = 96.4$.

the modes are varicose-lateral, with an amplitude largest in the top and lateral shear layers, while at $F = 0.14$ the mode is concentrated in the lateral shear layers, and close to the wall at the roughness centre, i.e. a varicose-centre mode. The latter mode also has a relatively large amplitude outside the roughness wake in the undisturbed boundary layer, i.e. a Mack mode, similar to case Bump. There are clearly two different modes, the varicose-centre and Mack mode, at work at this frequency. At $F = 0.18$ the modes can be seen to be Mack modes active in the undisturbed boundary layer behind both the smooth bump and flat-top element. This explains the qualitatively similar behaviour of the two cases, as shown in Figure 5.14. Since the roughness wake is very weak behind the smooth bump and the boundary layer profile at the roughness centreline is similar to the undisturbed boundary layer profile, the Mack mode is also active at this location. The wake of the flat-top roughness element is much stronger, resulting in the absence of the Mack mode at the roughness centreline.

Effect of planform shape In Figure 5.18 the amplitude of u' disturbances is shown for cases Cyl, Square and Diam to evaluate the effect of the roughness planform shape. This figure shows that the behaviour of disturbances in the wake is very similar for the roughness elements with cylindrical, square and diamond-shaped planform. At $F = 0.02$ and $F = 0.14$ the evolution of the amplitude is almost identical downstream of the different roughness elements. Only at $F = 0.06$ and $F = 0.14$ some minor quantitative differences in the growth rates can be observed.

Figure 5.19 shows the growth rate of the u' disturbances discussed before, and confirms that the growth rates at $F = 0.02$ and $F = 0.18$ are effectively independent of the roughness planform shape. This is as expected for $F = 0.18$, since it was shown in the previous section that the most unstable mode at this frequency is a Mack mode, active in the undisturbed boundary layer and therefore not associated with the strength or shape of the roughness wake.

At $F = 0.06$ the behaviour of the disturbances is qualitatively the same. The disturbance growth rate increases between $x \approx 70$ and $x \approx 90 - 95$, after which it reaches a peak and decays monotonically further downstream. Quantitatively the growth rates differ slightly, as noted before. The wake behind the cylindrical flat-top element of case Cyl has the largest growth rate at this frequency and is generally the most unstable. Up to $x \approx 100$ the growth rate of case Diam is the second largest with a peak growth rate that is approximately 10% lower than Cyl, while the case Square is the least unstable with a peak growth rate that is about 23% lower. Further

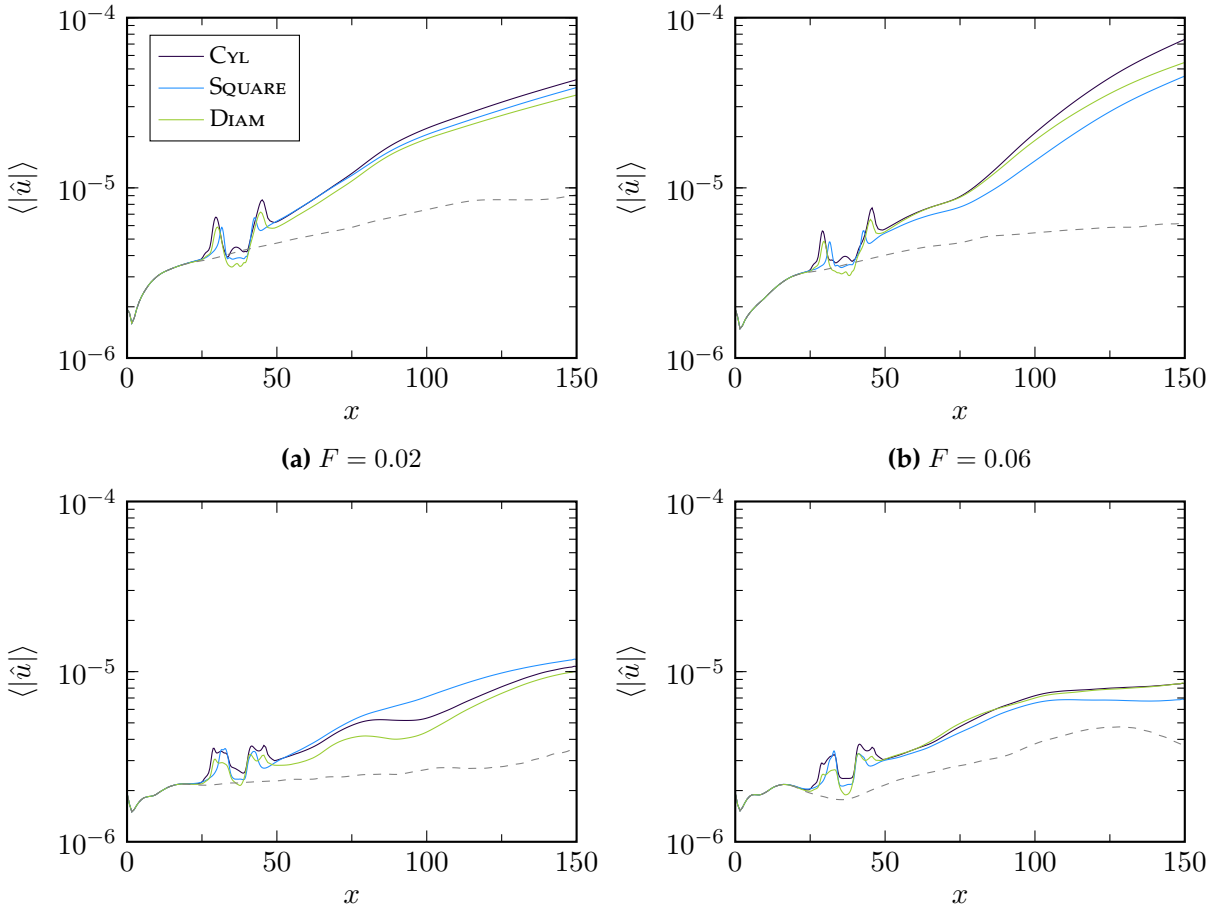

(a) $F = 0.02$ **(b)** $F = 0.06$

(c) $F = 0.14$ **(d)** $F = 0.18$

Figure 5.18. Amplitude of u' disturbances inside the boundary layer for cases Cyl, Square and Diam, showing the effect of roughness planform. **(a)** $F = 0.02$, **(b)** $F = 0.06$, **(c)** $F = 0.14$, **(d)** $F = 0.18$.

downstream, for $x > 100$, case Square is more unstable than case Diam and has a growth rate that is roughly the same as that of case Cyl.

At $F = 0.14$ there are also some quantitative differences between cases Cyl, Square and Diam, while the behaviour is qualitatively the same. Between $x \approx 70$ and $x \approx 100-110$ the growth rate strongly decays and increases again for all cases. Cases Cyl and Diam experience a small region where the growth rate is negative, i.e. a stable region, while the case Square is unstable throughout. Further downstream ($x > 110$) cases Cyl and Diam have approximately the same growth rate, which is considerably larger than the growth rate for Square. At $x = 130$, the growth rate for

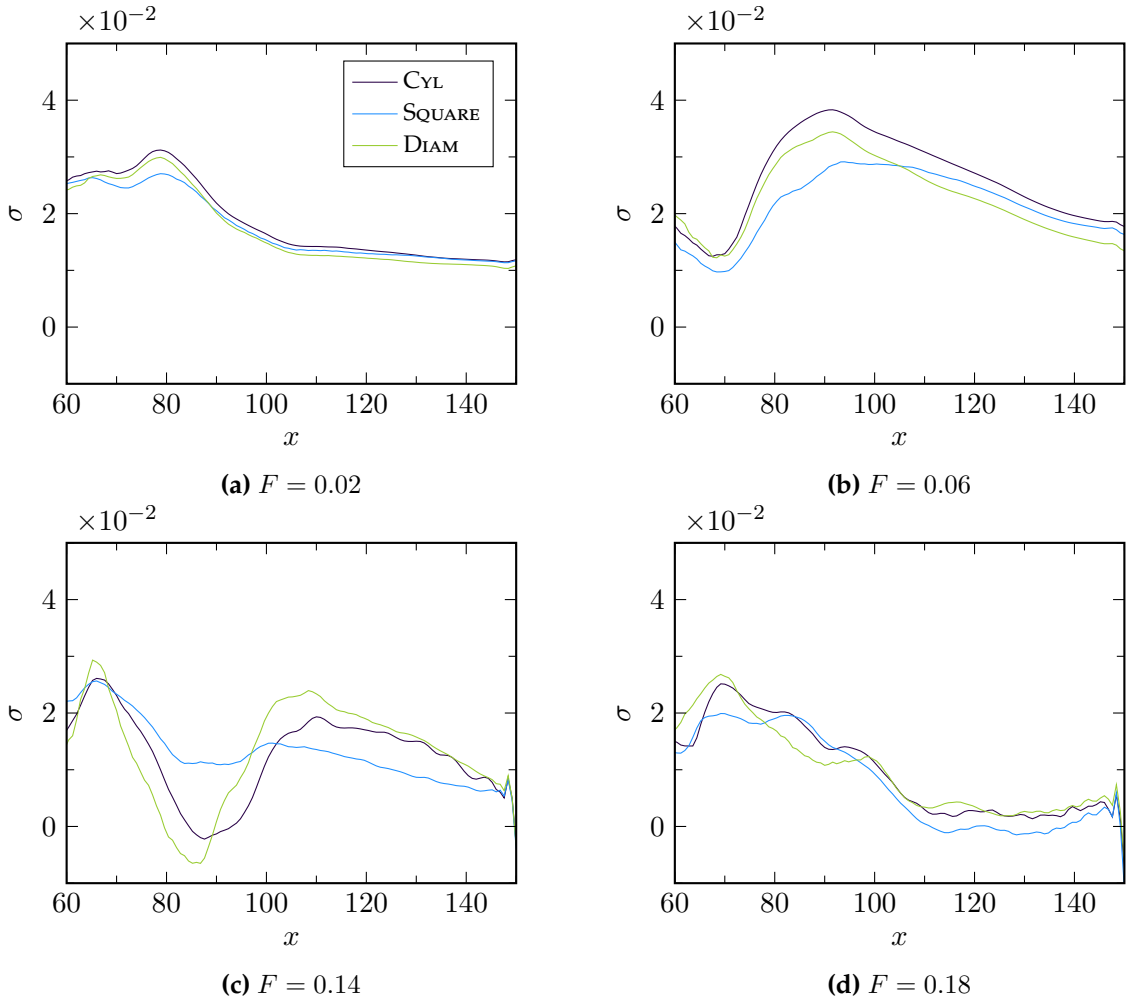

(a) $F = 0.02$ **(b)** $F = 0.06$

(c) $F = 0.14$ **(d)** $F = 0.18$

Figure 5.19. Growth rate of u' disturbances inside the boundary layer for cases Cyl, Square and Diam, showing the effect of roughness planform. **(a)** $F = 0.02$, **(b)** $F = 0.06$, **(c)** $F = 0.14$, **(d)** $F = 0.18$.

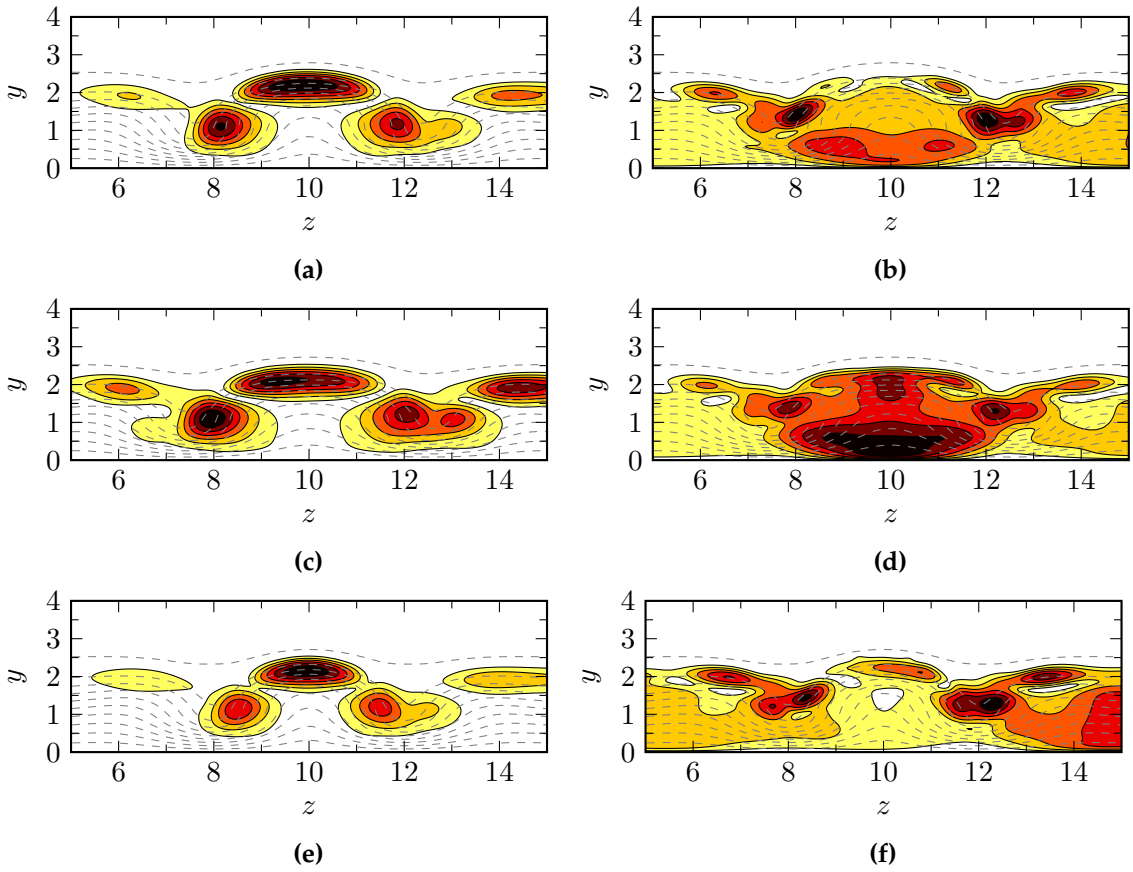

Figure 5.20. Mode shapes at $F = 0.06$ **(a,c,e)** and $F = 0.14$ **(b,d,f)** behind the cylindrical **(a-b)**, square **(c-d)** and diamond-shaped **(e-f)** flat-top roughness element, visualised by contours of $|u'|$-velocity at $x = 96.4$. Dashed contour lines, drawn every $\Delta u = 0.1$, show the mean streamwise velocity.

case SQUARE is about 47% smaller than for CYL and DIAM.

The similar behaviour between the roughness cases with different planform shapes can also be observed in the mode shapes. The mode shapes for $F = 0.02$ and $F = 0.18$ (not shown) are remarkably similar between the different cases, which explains the behaviour seen in Figure 5.18 and Figure 5.19.

Figures 5.20 and 5.21 show the mode shapes for $F = 0.06$ and $F = 0.14$. These figures shows that at $F = 0.06$ the modes are of a varicose-lateral type and are similar for all three roughness cases. At $F = 0.14$ there are large differences between the different cases however. As mentioned previously, multiple modes seem to be active at this frequency and evidence of both a varicose-centre and Mack mode has

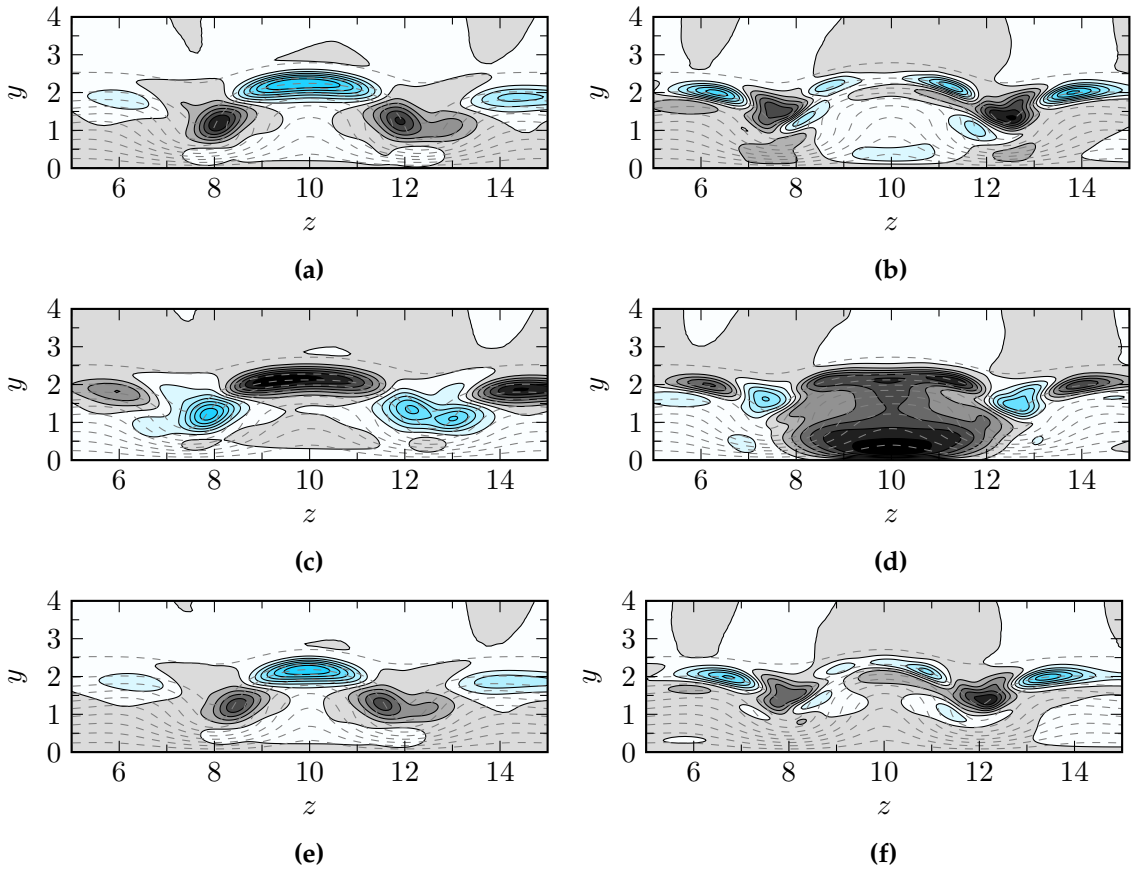

Figure 5.21. Mode shapes at $F = 0.06$ **(a,c,e)** and $F = 0.14$ **(b,d,f)** behind the cylindrical **(a-b)**, square **(c-d)** and diamond-shaped **(e-f)** flat-top roughness element, visualised by contours (black *(negative)* - blue *(positive)*) of the real part of u'-velocity at $x = 96.4$.

been seen behind the flat-top of case Cyl. Also for case Square these two modes can be observed in Figures 5.20 and 5.21, but the varicose-centre mode is much stronger and more clearly defined than for Cyl, for which the largest amplitude is actually concentrated in the lateral shear layer away from the wall. Case Diam does not show any evidence of the varicose-centre mode. The largest amplitude is mainly located in the lateral shear layer and further in the undisturbed boundary layer, i.e. a Mack mode. From these results, it can be concluded that the varicose-centre mode behind the square roughness element at $F = 0.14$ is responsible for the unstable disturbance growth observed for $70 < x < 110$, for which the other roughness elements showed a large decay in growth rate and even momentary stabilising behaviour.

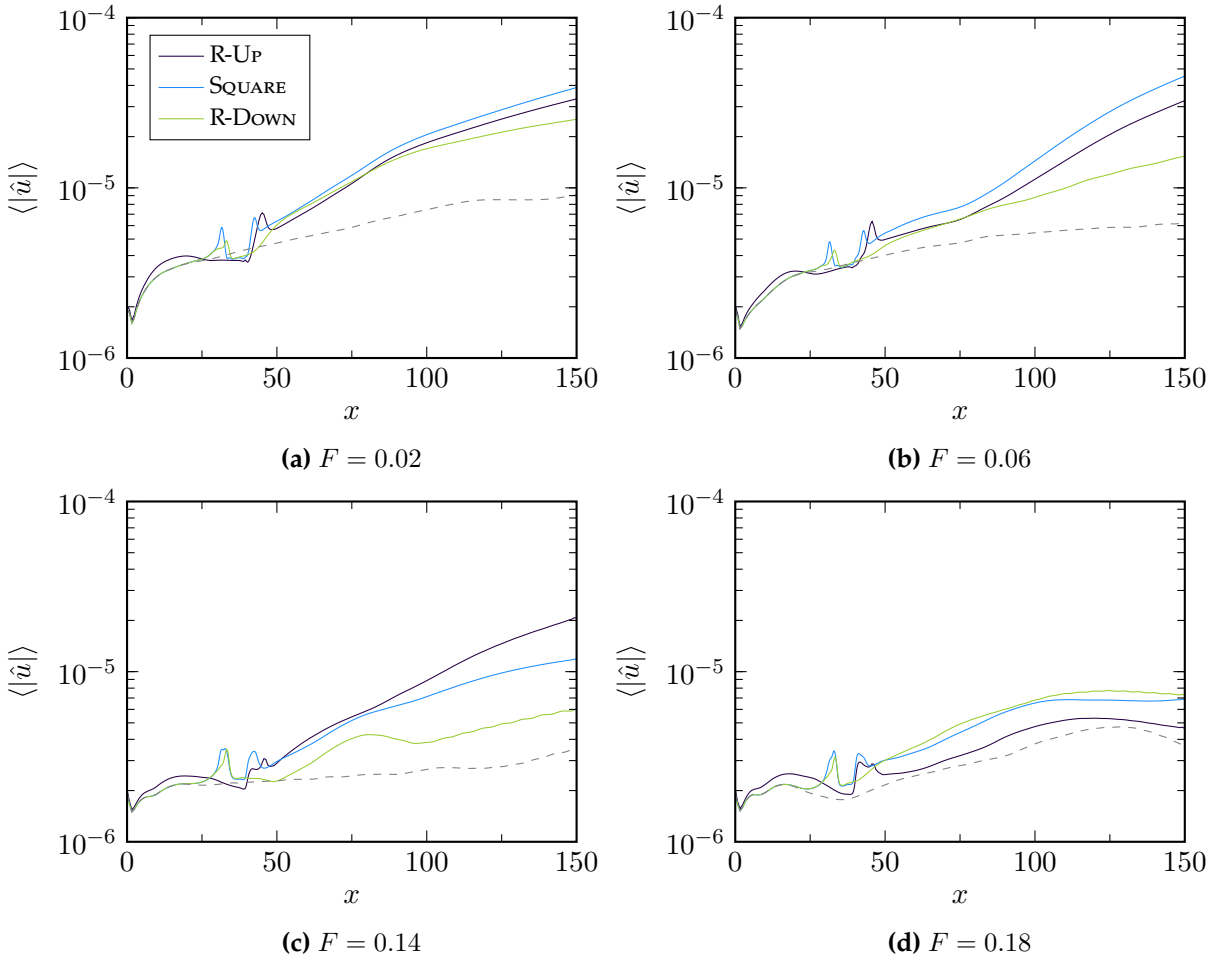

(a) $F = 0.02$ **(b)** $F = 0.06$

(c) $F = 0.14$ **(d)** $F = 0.18$

Figure 5.22. Amplitude of u' disturbances inside the boundary layer for cases R-Down, Square and R-Down, showing the effect of ramps. **(a)** $F = 0.02$, **(b)** $F = 0.06$, **(c)** $F = 0.14$, **(d)** $F = 0.18$.

Effect of ramps To study the effect of a ramp at the upstream (R-Up) or downstream (R-Down) side of the roughness element, these cases can be compared to a corresponding no-ramp roughness element, i.e. case Square. The amplitude of u' disturbances in the boundary layer for these cases is shown in Figure 5.22.

It can be observed the R-Up element has a noticeable influence on the flow upstream of the roughness element, while there is essentially no difference between the other roughness elements and the flat plate results up to $x \approx 25$. The disturbances grow faster far upstream of the roughness element for case R-Up, although they decay again and the amplitudes at the roughness centre ($x_r = 37.0$) are approximately the

same (at $F = 0.02$ and $F = 0.06$) or lower (at $F = 0.14$ and $F = 0.18$) than for cases Square and R-Down.

From Figure 5.22 it can be seen that the upstream ramp in case R-Up does not significantly alter the behaviour of the disturbances downstream compared to the roughness element without ramp (Square) at $F = 0.02$, $F = 0.06$ and $F = 0.18$. Both qualitatively and quantitatively the disturbances grow in a similar way for these two cases. The amplitudes for case R-Up are slightly smaller immediately downstream of the element, which persists further downstream. Only at $F = 0.14$ the wake behind the ramp-up element shows a significant difference with case Square. At this frequency, case R-Up has the most unstable wake and disturbances in its wake reach the highest amplitude. The behaviour for case R-Down is considerably different than for case Square at $F = 0.02$ and $F = 0.06$ and the downward ramp seems to have a large influence on the wake instabilities at these frequencies. At $F = 0.14$ and $F = 0.18$ there are large qualitative similarities between cases R-Down and Square. Only at $F = 0.18$ the disturbances in the wake of R-Down have a comparable amplitude than those behind Square. At all other frequencies, the amplitudes near the end of the numerical domain are considerably lower than the two other cases.

The growth rates of these disturbances are given in Figure 5.23. This figure confirms that at $F = 0.02$ there is almost no difference between the upward ramp case R-Up and the no-ramp square roughness case Square. The growth rate behind R-Down qualitatively follows the behaviour of cases R-Up and Square very closely, but is roughly 40% lower (computed at $x = 130$). Also at $F = 0.06$, the behaviour of cases R-Up and Square is qualitatively very similar. The growth rate of case Square is larger for $80 < x < 120$, after which the growth rate becomes comparable to case R-Up. The growth rate of the boundary layer disturbances behind the ramp-down element is considerably lower at this frequency and can be seen to be oscillating around a mean value. This oscillatory behaviour (*beating*) is also present in the disturbances with higher frequencies, i.e. $F = 0.14$ and $F = 0.18$, and is an indication that multiple distinct modes with the same frequency but different phase speeds are present. At $F = 0.14$ the behaviour of cases R-Up, Square and R-Down is considerably different from each other. While case Square has the largest growth rates at frequencies $F = 0.02$ and $F = 0.06$, the ramp-up case R-Up is considerably more unstable at $F = 0.14$. The strong momentary drop in growth rate between $70 < x < 100$ that has been seen for all the previous cases, and is clearly present for case R-Down (see Figure 5.23c), does not occur. Also further downstream, near the end of the

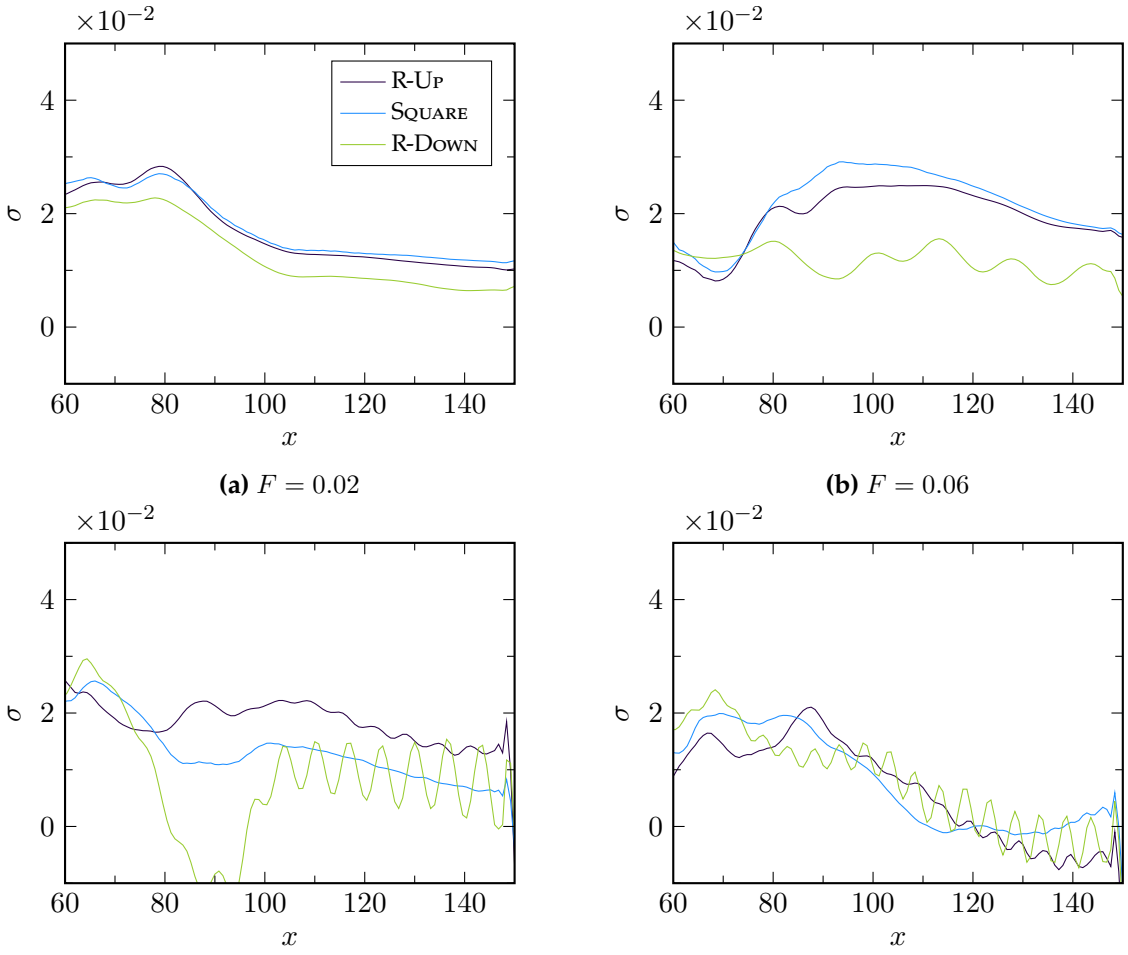

(a) $F = 0.02$ **(b)** $F = 0.06$

(c) $F = 0.14$ **(d)** $F = 0.18$

Figure 5.23. Growth rate of u' disturbances inside the boundary layer for cases R-Down, Square and R-Down, showing the effect of ramps. **(a)** $F = 0.02$, **(b)** $F = 0.06$, **(c)** $F = 0.14$, **(d)** $F = 0.18$.

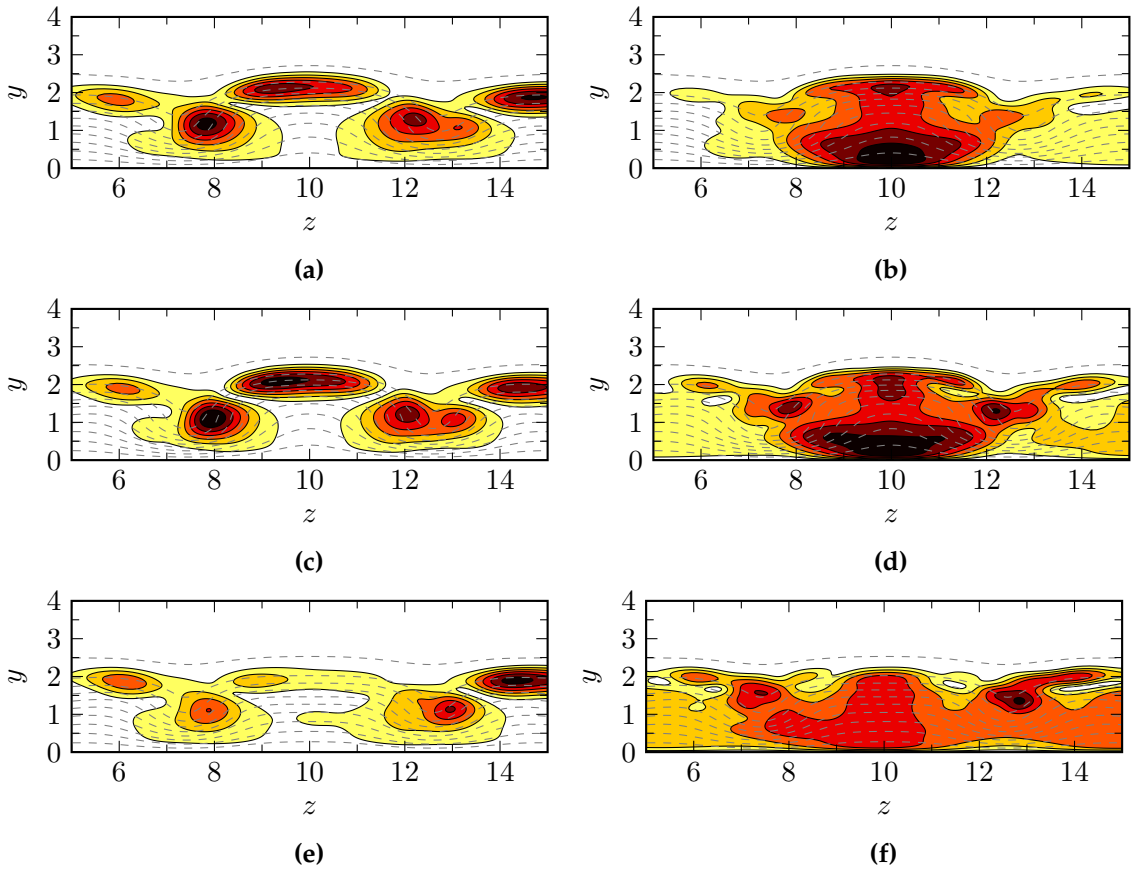

Figure 5.24. Mode shapes at $F = 0.06$ **(a,c,e)** and $F = 0.14$ **(b,d,f)** behind the ramp-up **(a-b)**, square **(c-d)** flat-top and ramp-down **(e-f)** roughness element, visualised by contours of $|u'|$-velocity at $x = 96.4$. Dashed contour lines, drawn every $\Delta u = 0.1$, show the mean streamwise velocity.

domain, the growth rate is significantly larger. At $x = 130$, the growth rate behind the ramp-up case is more than 50% larger than the growth rate behind the square roughness element without the upward ramp. The downward ramp does not have a large influence on the disturbance growth rate at this frequency. Downstream of the large growth rate dip ($x > 110$), the disturbances grow — in a mean sense — at a similar rate as the disturbances for case Square. Large oscillations in growth rate are present however. At $F = 0.18$ the behaviour is relatively independent on the roughness element and thus the presence of a ramp. It has already been shown that this is also true for the roughness elements with different planform shapes, as was seen in Figure 5.19d.

Figures 5.24 and 5.25 show the mode shapes for $F = 0.06$ and $F = 0.14$ at $x = 96.4$

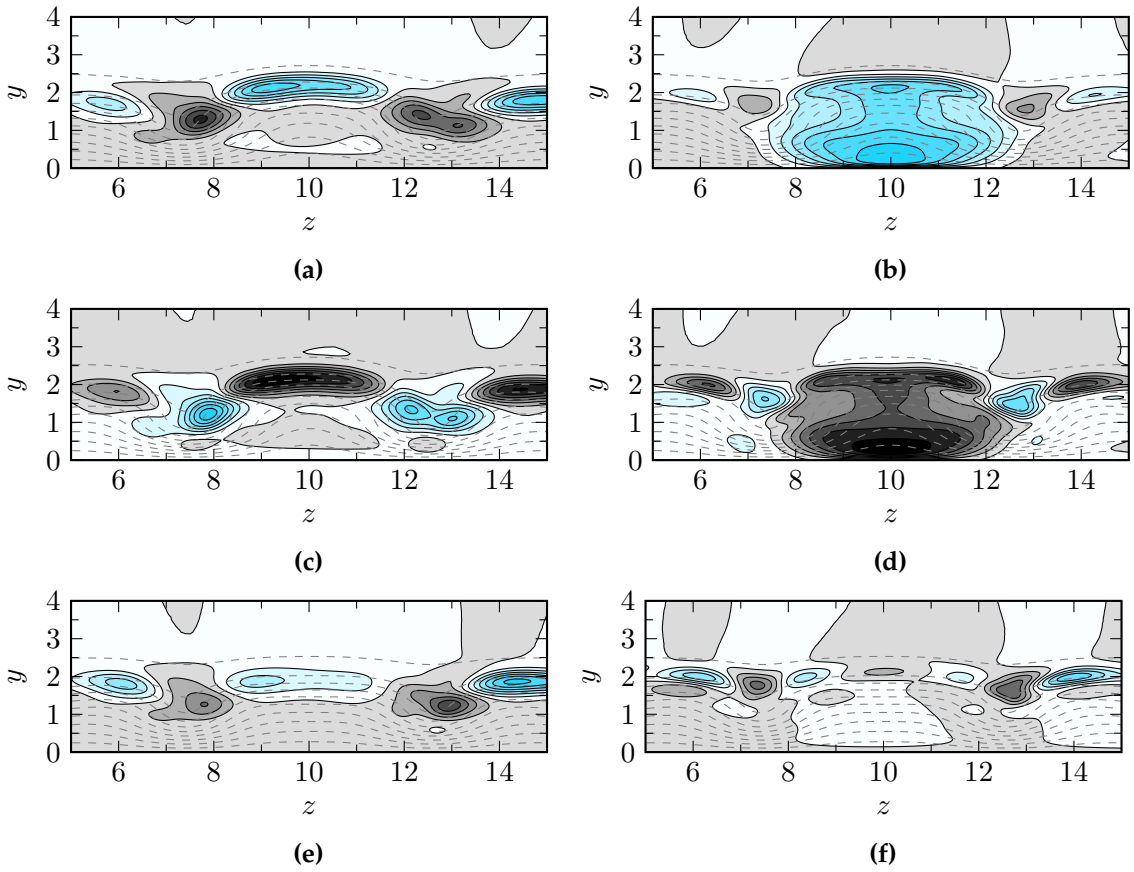

Figure 5.25. Mode shapes at $F = 0.06$ **(a,c,e)** and $F = 0.14$ **(b,d,f)** behind the ramp-up **(a-b)**, square **(c-d)** flat-top and ramp-down **(e-f)** roughness element, visualised by contours (black *(negative)* - blue *(positive)*) of the real part of u'-velocity at $x = 96.4$.

downstream of the cases R-Up, Square and R-Down, visualised by contours of $|u'|$-velocity and the real part of the u'-velocity. It shows that the mode shapes for cases R-Up and Square are very similar at both frequencies: a varicose-lateral mode is active at $F = 0.06$, while the mode at $F = 0.14$ is of a clearly-defined varicose-centred nature. This strengthens the assumption, proposed in the previous subsection, that the varicose-centre modes are responsible for the unstable region at $70 < x < 100$, where the other roughness elements showed stabilising behaviour. Behind the ramp-down roughness element, the largest disturbance amplitude at a frequency $F = 0.06$ is not located in the roughness wake, but in the shear layer away from the wake, i.e. in the undisturbed boundary layer. The most unstable mode at this frequency is thus not a wake mode, explaining the relatively low growth rate observed in Figure 5.23b. However, it can be seen that also in the lateral shear layers

of the roughness wake there is a slightly elevated disturbance amplitude, indicating the presence of multiple instability modes. For $F = 0.14$ the largest amplitude is found in the lateral shear layers of the wake, although a relatively high amplitude can also be found at the roughness centreline. Also at this frequency multiple modes are active and contribute to the overall disturbance amplitude shown in Figure 5.22.

An overview of the growth rates of the different disturbances is shown at three distinct locations downstream of the various roughness elements in Figure 5.26. It confirms the strong instability growth near $F = 0.06$ for all cases except Bump, for which a disturbance with $F = 0.02$ has a larger growth rate throughout the domain. A second peak of strong instability growth occurs at higher frequencies, i.e. $F = 0.14 - 0.18$, corresponding to the Mack mode (or Mack-like VC mode) instability.

5.4.2 Most amplified mode

A measure of the overall boundary layer response to exponentially growing instabilities is the N-factor, defined as the natural logarithm of the ratio of a disturbance amplitude at a specific streamwise position x to a reference amplitude at position x_{ref}, i.e.

$$N \coloneqq \ln\left(\frac{\langle|\hat{u}|\rangle(x)}{\langle|\hat{u}|\rangle_{x_{\text{ref}}}}\right) . \tag{5.5}$$

The N-factor is often used as a predictive tool for boundary layer transition and can give an indication of the most *dangerous* roughness element in the current work, i.e. the roughness element that induces the largest overall amplitude amplification and would be most likely to trigger transition the earliest.

The largest N-factor, and its associated frequency, obtained downstream of each roughness element is listed in Table 5.3. The maximum N-factor occurs behind the cylindrical flat-top element of case Cyl, closely followed by the diamond-shaped and square flat-top elements of cases Diam and Square. As was already earlier in this chapter, there is not a large difference between the roughness elements with different planform shapes. The frequency that leads to the highest growth behind these elements is $F = 0.06$. Slightly lower amplitudes are found downstream of case R-Up with the upstream ramp, and this case has an N-factor that is approximately 20% lower than the corresponding no-ramp case Square. Both the disturbances with $F = 0.06$ and $F = 0.14$ reach this maximum N-factor near the end of the domain, and therefore both the varicose-lateral mode at $F = 0.06$ and the varicose-centre mode

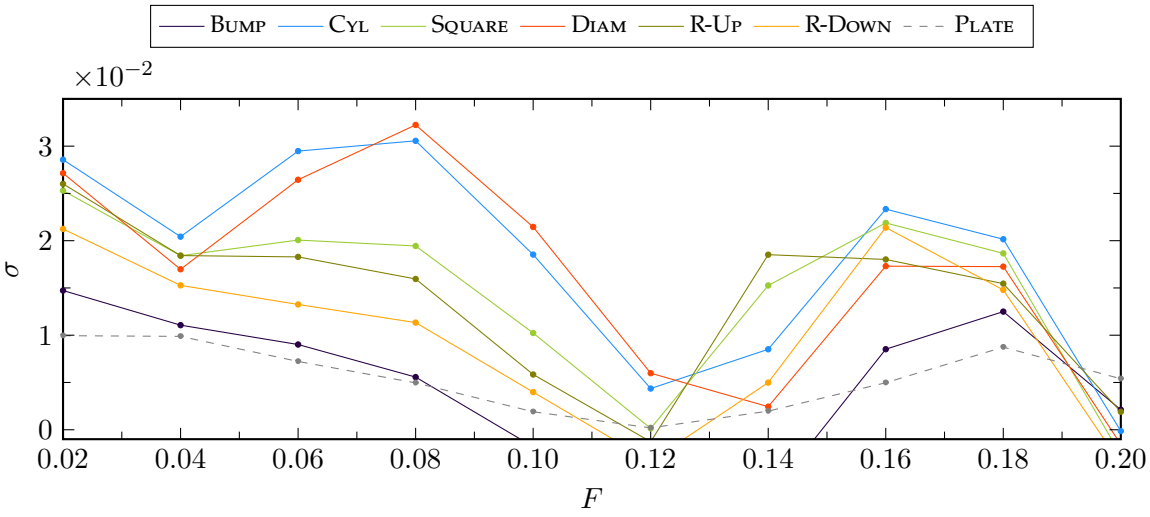

(a) $x = 79.6$

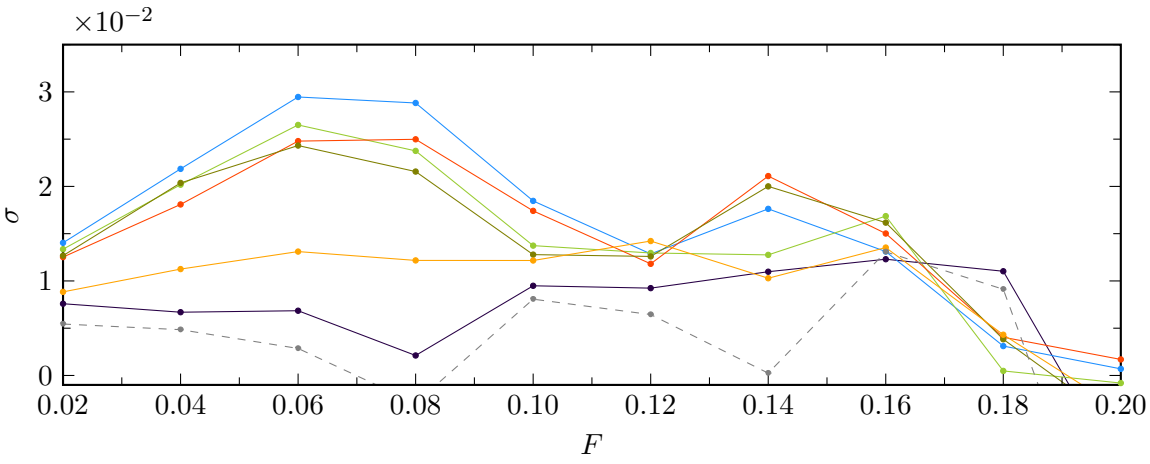

(b) $x = 113.2$

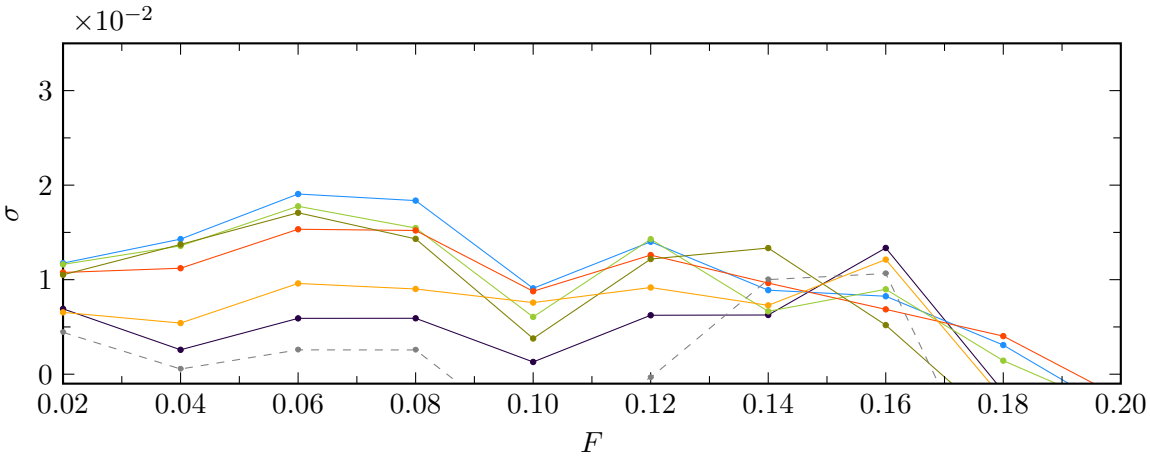

(c) $x = 142.6$

Figure 5.26. Disturbance growth rate of the disturbances in the roughness wakes at **(a)** $x = 79.6$, **(b)** $x = 113.2$ and **(c)** $x = 142.6$.

Table 5.3. Maximum N-factors, computed at the end of the numerical domain, and their corresponding frequency, using roughness centre ($x_{\text{ref}} = 37.0$) as reference location.

Case	$N_{\max}$	$F_{(N_{\max})}$
Bump	1.3	0.02
Cyl	2.9	0.06
Square	2.6	0.06
Diam	2.8	0.06
R-Up	2.3	0.06/0.14
R-Down	1.9	0.02
Plate	0.9	0.16

at $F = 0.14$ could play an important role in the eventual transition process further downstream. Both the smooth bump of case Bump and ramped-down element of R-Down behave differently: the N-factors at the end of the domain are considerably smaller and the frequency which yields the largest amplitudes is $F = 0.02$ instead of $F = 0.06$ for the other cases. The downward ramp or slowly-varying geometry at the aft section of the smooth bump seems to strongly stabilise the most unstable wake mode at $F = 0.06$. The case Plate without roughness element has the lowest N-factor at the end of the domain, which is as expected due to the absence of unstable wake modes. The frequency of the largest amplitude disturbance is $F = 0.16$, corresponding to a two-dimensional Mack mode.

5.5 Summary of results

In this chapter the Mach 6.0 boundary layer receptivity and linear instability growth of the wake behind various roughness elements has been studied using direct numerical simulations.

In the initial receptivity study, the effect of the external forcing type, i.e. acoustic (type-A), vortical (type-V) and entropy (type-Æ), was investigated. The disturbance growth in the wake of a cylindrical flat-top roughness element was found to be qualitatively the same for the type-A and type-Æ forcing. The disturbances in the case of the acoustic forcing are one order of magnitude larger, however, making it more effective at exciting unstable wake modes. The boundary layer and wake instabilities induced by the vortical forcing of type-V are much less unstable and a different receptivity mechanism seems to be active. Similar results were reported by De Tullio

and Sandham (2012) for a sharp-edged square roughness element, demonstrating that the interaction between the different disturbances and the roughness wake is independent of the structure of the wake, and in extension the shape of the roughness element.

The main interest of this chapter is the effect of the three-dimensional roughness shape on the wake instability behaviour. It was found that the frontal profile is a critical parameter in the generation of an unstable wake. While unstable wake modes are found in the wake of a flat-top element, a smooth bump (with the same maximum height) was found to act mainly as a disturbance amplifier and does not significantly increase the disturbance growth rate in the wake.

The planform shape was found to have only a weak effect on the wake instability. The cylindrical, square and diamond-shaped flat-top elements generate similar wakes in which the same instability modes grow. A varicose-lateral mode with frequency $F = 0.06$ was found to be the most unstable. The growth rates of the unstable wake modes are very similar for the roughness elements with different planform shapes, and also the overall disturbance growth, i.e. the N-factor obtained at the end of the domain, is of comparable magnitude. The cylindrical element has the most unstable wake, closely followed by the diamond-shaped element and finally the square element.

The presence of an upward ramp does not seem to generate a much more unstable wake than the corresponding roughness element without ramp, and in general the behaviour is similar. Although the varicose-centre mode, which has similarities with a Mack mode, is more unstable behind the ramp-up and has a larger unstable envelope along the domain, the most unstable varicose-lateral mode is slightly damped. This results in an N-factor at the end of the domain that is approximately 10% lower for the case with an upward ramp. A downward ramp at the aft section of the roughness element has been found to strongly damp the wake modes and the generated wake is much less unstable. The N-factor reached by the wake instabilities behind the ramp-down element is approximately 70% of the N-factor reached behind the corresponding no-ramp roughness element. A down-ward ramp or slowly-varying geometry at the aft section, such as for the smooth bump, seems to strongly stabilise the resulting roughness wake.

Chapter 6

Stability Analysis of Roughness Wakes

In this chapter the stability of the wake behind the various roughness elements are studied using linear stability analysis. The goal of this work is to investigate if linear stability analysis can accurately predict the stability characteristics of roughness wakes and the overall growth of wake and boundary layer instabilities.

6.1 Case details & set-up

The stability of the wake behind the isolated roughness elements, studied using DNS in Chapter 5 *(Roughness Receptivity & Wake Instability)*, is investigated using the linear stability code `COMPASS`. The same naming of the cases is used as in the previous chapter, e.g. Bump, Cyl, Square, Diam.

6.1.1 Base flows

Accurate and time-converged base flows of the roughness wakes are needed, from which the linear stability can be computed using bi-local stability analysis. These base flows are extracted as cross-flow slices at distinct streamwise positions from the direct numerical simulations presented in Chapter 5 *(Roughness Receptivity & Wake Instability)*. Since the bi-local stability analysis assumes parallel flow in the streamwise direction, the base flows should be extracted at locations far enough downstream of the roughness elements, where non-parallel effects are expected to be small, or at least smaller than in the near-wake region.

Table 6.1. Details of the numerical grids used in the grid study of the wake instability analysis.

Grid	N_z	N_y	q
Coarse	120	81	8
Ref.	160	121	8
Fine	220	161	8

In total five base flow slices are extracted from each of the different roughness simulations. The cross-flow slices are taken at $x = [79.6, 96.4, 113.2, 125.8, 142.6]$, so that they span the streamwise length of the domain, downstream of the roughness elements, without including the immediate near-wake region. At these locations the conservative flow variables are extracted from the DNS results, transformed into primitive flow variables and written out into a format that can be read by the linear stability code `COMPASS`.

The bi-local stability analysis in the current chapter is performed in the spatial instability framework, i.e. spatially developing instabilities of a specified temporal frequency are sought. The frequencies that are investigated using bi-local stability correspond to the frequencies that were resolved in the DNS results of Chapter 5 *(Roughness Receptivity & Wake Instability)*, so that a direct comparison between the results of the direct numerical simulations and the stability analysis is possible.

6.1.2 Grid study

A grid study is performed to ensure that the results of the stability analysis are converged and independent of the number of grid points. In the spanwise direction the Fourier spectral method is used for discretisation, while in the wall-normal direction the high-order finite-difference FD-q method of Hermanns and Hernández (2008) is applied, presented in Chapter 3 *(COMPASS: Compressible Stability Analysis)*. The order of the FD-q method is set to $q = 8$ in this chapter. The algebraic mapping of Malik (1990), introduced in Chapter 3, is used to cluster half of the wall-normal grid points below $y = 2.5$. The grid study is performed for a single roughness case and frequency, i.e. case Cyl with frequency $F = 0.14$. This case is run on three different grids, each with an increased level of grid refinement. The details of these grids are summarised in Table 6.1.

A portion of the computed spectrum for case Cyl with frequency $F = 0.14$ is shown

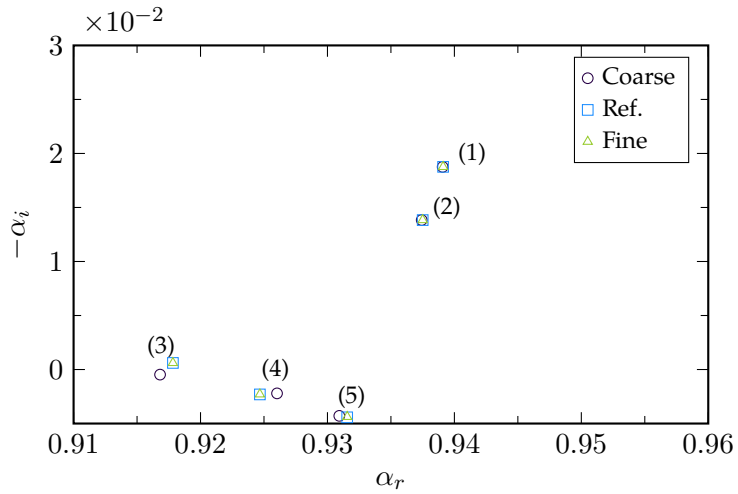

Figure 6.1. Part of the spectrum computed on three increasingly refined grids.

Table 6.2. Eigenvalues of two distinct modes computed on three increasingly refined grids.

	Mode (1)		**Mode (3)**	
Grid	α_r	α_i	α_r	α_i
Coarse	0.939 075 0	−0.018 756 6	0.916 812 7	0.000 471 7
Ref.	0.939 111 7	−0.018 760 0	0.917 825 3	−0.000 608 9
Fine	0.939 111 0	−0.018 762 7	0.917 824 1	−0.000 616 3

in Figure 6.1, computed on the three grids in Table 6.1. The five most unstable (or least stable) modes are shown and annotated. It can be seen from this figure that the two most unstable modes, modes (1) and (2), are resolved by the three grids to have very similar eigenvalues. The eigenvalue of the most unstable mode is given in Table 6.2 for the three different grids, which shows that the difference between the growth rate computed on the coarse and fine grid is about 0.03%.

There is a large difference between the coarse grid and the finer grids for modes (3)-(5) however. The eigenvalues of these modes are very similar for the reference grid and the fine grid, but the coarse grid does not yield the same eigenvalues. Mode (3) is even stable on the coarse grid, while it is slightly unstable on the other two grids. The eigenvalues for this mode are also given in Table 6.2, which shows that the relative difference between the growth rate computed on the reference grid and the fine grid is approximately 1%. This is sufficiently accurate such that the results on the reference grid can be considered grid-converged.

The eigenfunctions for modes (1) and (3) are shown in Figures 6.2 and 6.3, and indicate that they are respectively a two-dimensional Mack mode in the undisturbed boundary layer and a varicose-centre (VC) wake mode. The two-dimensional Mack mode has a very limited spanwise dependency and slowly-varying wall-normal structure, which explains why it is fairly well resolved on the coarse grid. The VC mode (mode (3)) is a wake mode with a complex structure, i.e. high wall-normal and spanwise gradients, of its eigenfunction. More grid points are required to adequately resolve this mode shape, which is why the coarse grid solution is poor compared to the reference grid solution.

6.2 Stability analysis of the wake

Of interest in the current chapter is the comparison between the results from the direct numerical simulations, presented in Chapter 5 *(Roughness Receptivity & Wake Instability)*, and bi-local stability analysis of the roughness wakes. The first question to be answered is whether or not bi-local stability analysis can accurately resolve the instability modes growing in the wake behind roughness elements. Both an accurate computation of the growth rate and the type of the instability mode, e.g. varicose or sinuous, is of interest. Due to the parallel flow assumption in the linear stability analysis, it is expected that the accuracy of the comparison is dependent on the structure of the wake, in particular the streamwise dependency of the wake, and thus the streamwise position. The second question that will be investigated is whether the streamwise evolution of the instability modes can be resolved using bi-local stability and if the main trends of growth and decay can be predicted.

6.2.1 Instability modes and mode growth rate

Figure 6.4 shows a map of the unstable and least stable modes found in the wake (at $x = 96.4$) behind the cylindrical flat-top roughness element in Cyl. For each frequency F, the growth rate of the computed modes is given and the type of mode (sinuous-lateral, varicose-lateral, varicose-centre or Mack mode) is indicated. The growth rates from the DNS results are also given in this figure as dashed lines, such that it gives a clear overview of the qualitative and quantitative accuracy of the bi-local stability analysis of the roughness wakes.

Multiple instability modes are found at different frequencies, as indicated by the stability results shown in Figure 6.4. For the frequency band $F = 0.02 - 0.14$,

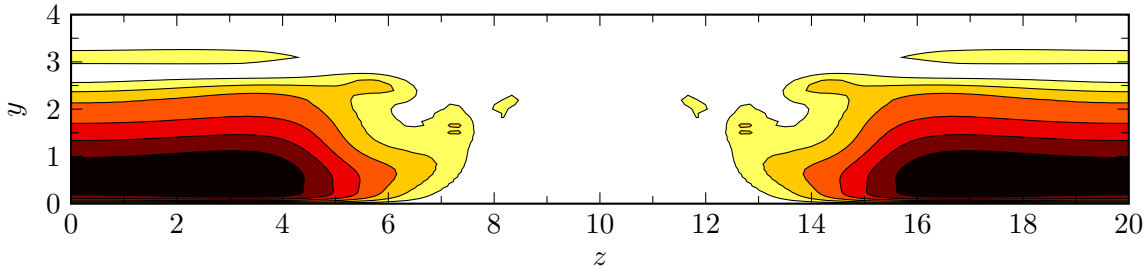

(a) Coarse grid

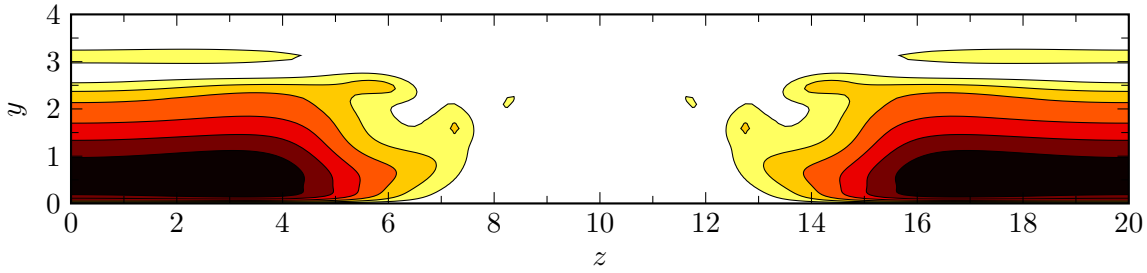

(b) Ref. grid

Figure 6.2. Mode shape of mode (1), visualised by contours of absolute u'-velocity, computed on the coarse and reference grid.

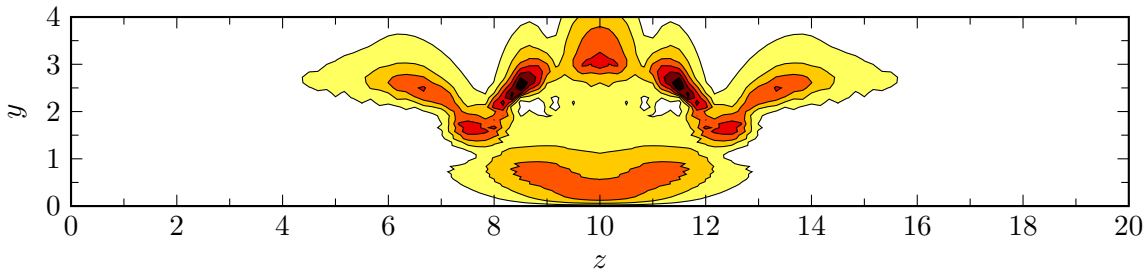

(a) Coarse grid

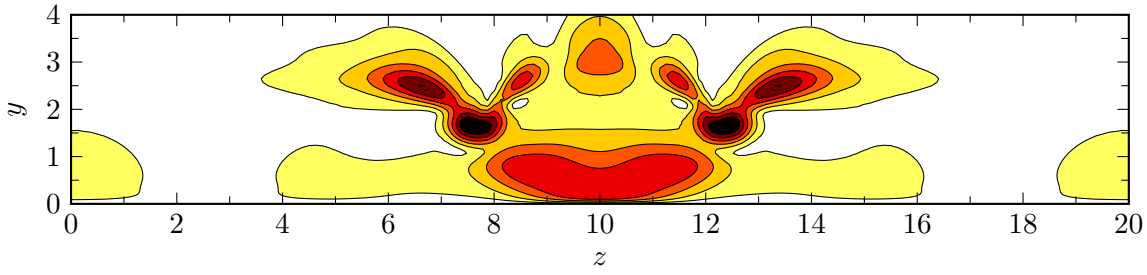

(b) Ref. grid

Figure 6.3. Mode shape of mode (3), visualised by contours of absolute u'-velocity, computed on the coarse and reference grid.

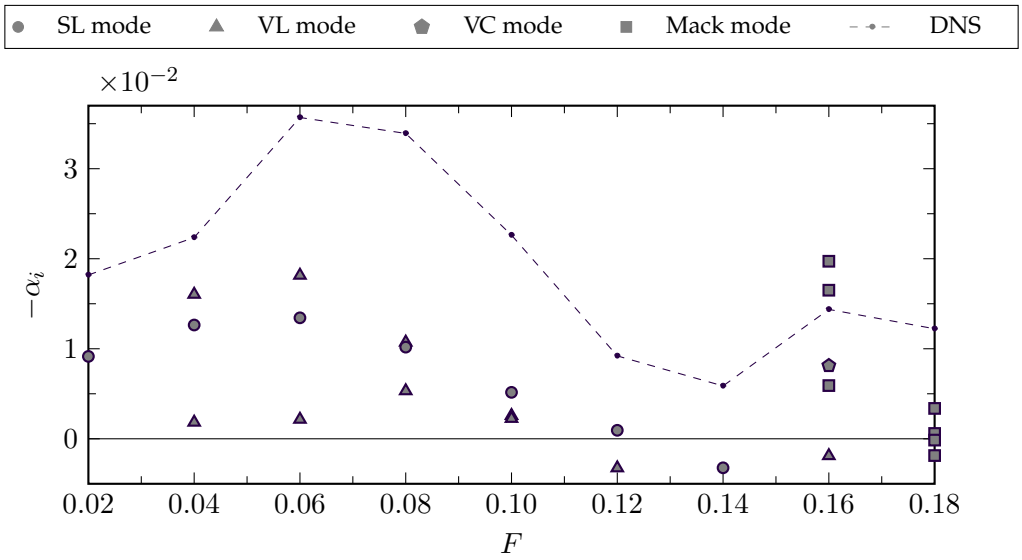

Figure 6.4. Unstable modes in the roughness wake, resulting from bi-local stability analysis, at $x = 96.4$ behind roughness case Cyl.

both sinuous and varicose wake modes are found, while Mack modes become the dominant modes at higher frequencies, i.e. $F \geq 0.16 - 0.18$. The general trend across the spectrum is that the growth rates are greatly underpredicted by the linear stability analysis. However, qualitatively the results seem to agree relatively well. From the DNS results the most unstable mode can be seen to have a frequency of $F = 0.06$ at $x = 96.4$. This peak at $F = 0.06$ is also captured by the bi-local stability analysis. Also the local peak in growth rate at $F = 0.16$ is captured by the stability analysis, although the linear stability analysis overpredicts the growth of these modes.

The mode shapes of the three most unstable modes resolved by the bi-local stability (BLS) analysis for $F = 0.06$ are shown in Figures 6.5a to 6.5c, and can be compared to the mode computed by the DNS, shown in Figure 6.5d. Figure 6.5a demonstrates the varicose-lateral (VL) nature of the most unstable mode (as was already shown in Figures 5.16 and 5.17) and shows that a fair agreement is found between the BLS and DNS results regarding the mode shape. The growth rate of the most unstable wake mode is approximately 49% lower for the stability analysis compared to the DNS results, i.e. $-\alpha_i = 0.01815$ compared to $\sigma_{\text{DNS}} = 0.03569$. The second most unstable mode is of a sinuous-lateral (SL) nature and has a growth rate that is roughly 25% lower than the dominant varicose mode, as indicated in Figure 6.5b. A second

unstable varicose-lateral mode has also been observed, shown in Figure 6.5c, that is mainly active in the lateral shear layers and much less in the top detached shear layer at the wake centreline. Its growth rate is almost one order of magnitude lower than the most unstable varicose mode, and would thus have essentially no contribution to the overall wake instability. It is therefore unlikely that the existence of this mode would have been observed in for example DNS results.

From Figure 6.4 it can be observed that the most unstable mode, computed by bi-local stability analysis, is not always of a varicose-lateral nature. For $F = 0.02$ only an unstable sinuous mode has been found, while for $F = 0.10 - 0.12$ both unstable varicose and sinuous modes have been observed, for which the sinuous-lateral mode has the largest growth rate. This does not agree with the DNS however, for which the most unstable mode is varicose-lateral, as shown in Figure 6.6d. Figures 6.6a to 6.6c show the three unstable modes, a single sinuous-lateral and two varicose-lateral modes, computed by the bi-local stability analysis for $F = 0.10$. At this frequency, the agreement between the DNS and the most unstable BLS mode, which is a sinuous-lateral mode, can be seen to be weaker. The DNS mode seems to correspond to a combination of both the SL and VL modes. The largest growth rate predicted by the stability analysis, corresponding to the sinuous-lateral mode, is roughly four times too low, i.e. $-\alpha_i = 0.005158$ compared to $\sigma_{\text{DNS}} = 0.02262$.

Figure 6.4 showed that there is another growth rate peak for a frequency of $F = 0.16$. The instabilities active at this higher frequencies correspond to Mack modes in the undisturbed boundary layer or varicose-centre wake modes, as was shown in Chapter 5 *(Roughness Receptivity & Wake Instability)*. In Figure 6.4 it was indicated that four unstable modes were found using bi-local stability analysis, and that the growth rate of the most unstable mode overpredicts the growth rate from the DNS. The mode shapes corresponding to these four unstable modes are shown in Figures 6.7 and 6.8.

It can be seen that the mode in Figures 6.7c and 6.8c is a varicose-centre (VC) mode active in the roughness wake, while the three other modes are active in the boundary layer at the side of the wake. The eigenfunctions of these modes are compared to the most unstable flat-plate boundary layer instability, i.e. a two-dimensional Mack mode, as computed by local linear stability theory (LST) in Figure 6.9. The wall-normal eigenfunctions are extracted at the spanwise positions where the amplitude is approximately largest, i.e. $z = 16.0$ for modes **(a)** and **(b)**, and $z = 20.0$ for mode **(d)**, and are normalised such that the maximum amplitude is unity and are rescaled

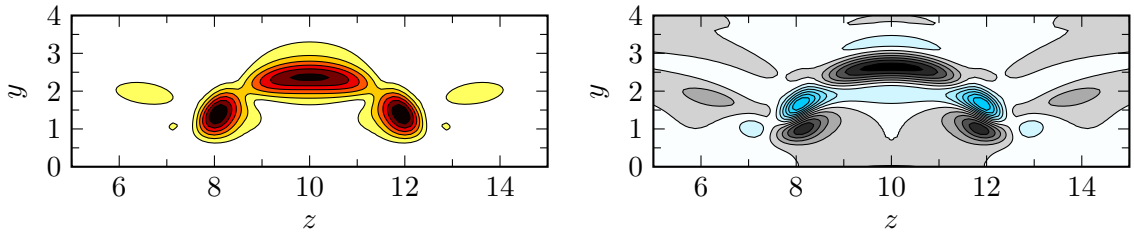

(a) VL mode, $(\alpha_r, \alpha_i) = (0.4193, -0.01815)$

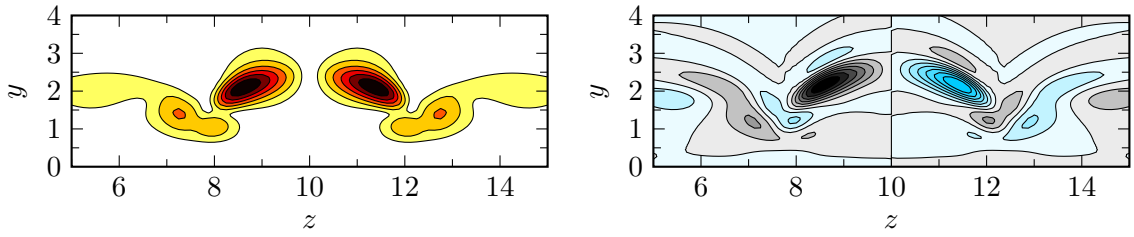

(b) SL mode, $(\alpha_r, \alpha_i) = (0.4181, -0.01344)$

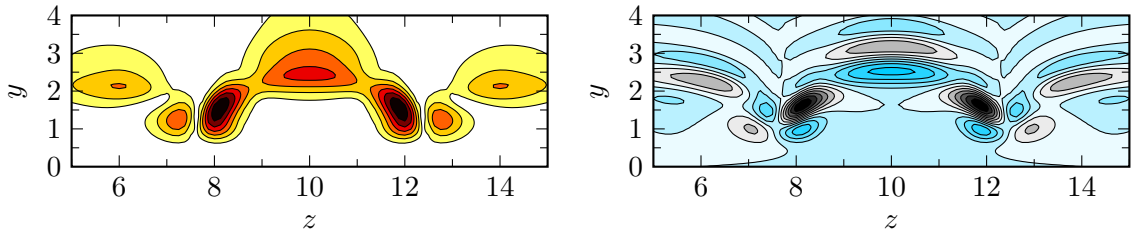

(c) VL mode, $(\alpha_r, \alpha_i) = (0.4195, -0.002153)$

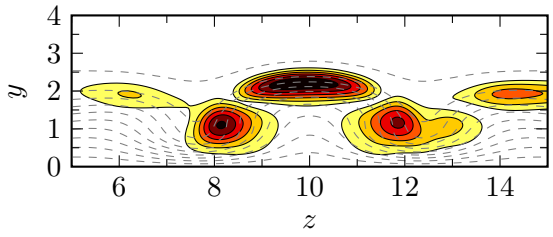

(d) DNS mode, $\sigma_{\mathrm{DNS}} = 0.03569$

Figure 6.5. Mode shape of the instability modes with $F = 0.06$ for case Cyl from BLS **(a-c)** and DNS **(d)** results. Mode shapes are visualised by contours of $|u'|$-velocity *(left)* and the real part of u'-velocity *(right)* at a streamwise location of $x = 96.4$.

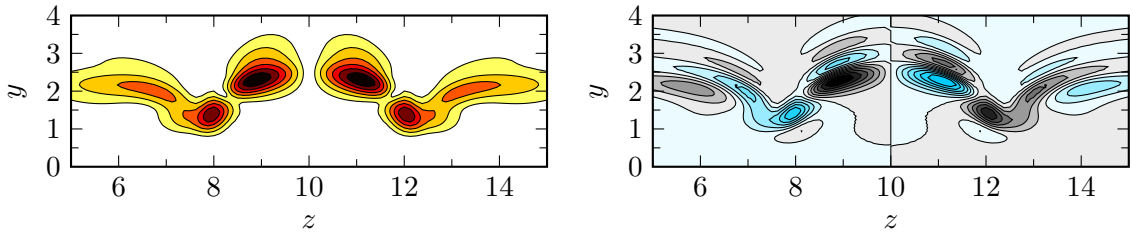

(a) SL mode, $(\alpha_r, \alpha_i) = (0.6850, -0.005158)$

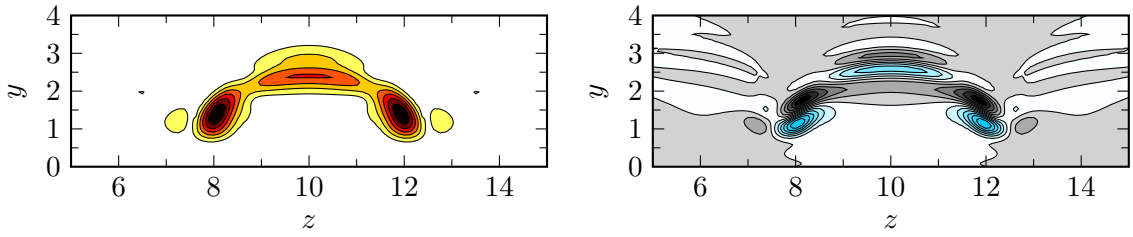

(b) VL mode, $(\alpha_r, \alpha_i) = (0.7104, -0.002568)$

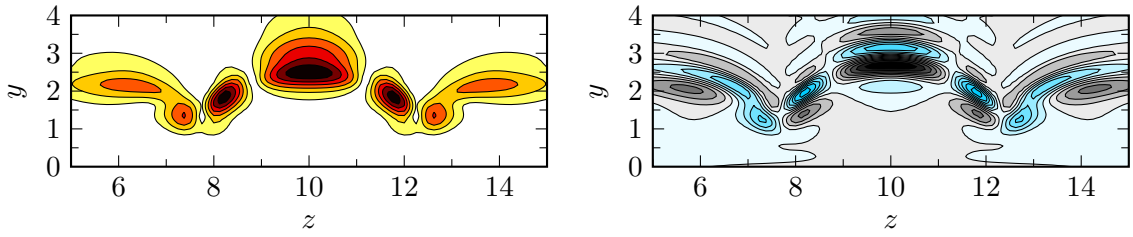

(c) VL mode, $(\alpha_r, \alpha_i) = (0.6850, -0.002250)$

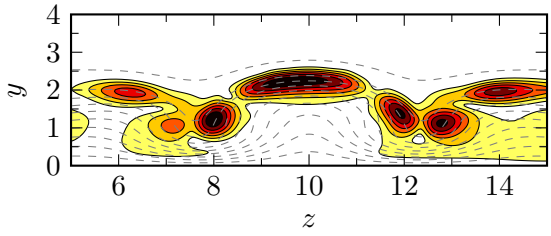

(d) DNS mode, $\sigma_{\text{DNS}} = 0.02262$

Figure 6.6. Mode shape of the instability modes with $F = 0.10$ for case CYL from BLS **(a-b)** and DNS **(c)** results. Mode shapes are visualised by contours of $|u'|$-velocity *(left)* and the real part of u'-velocity *(right)* at a streamwise location of $x = 96.4$.

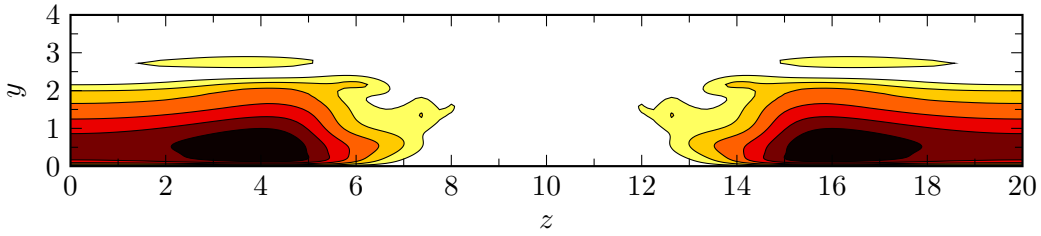

(a) Mack mode, $(\alpha_r, \alpha_i) = (1.0734, -0.01972)$

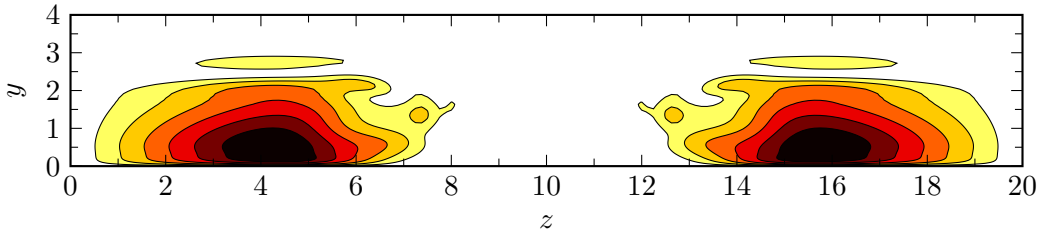

(b) Mack mode, $(\alpha_r, \alpha_i) = (1.0731, -0.01650)$

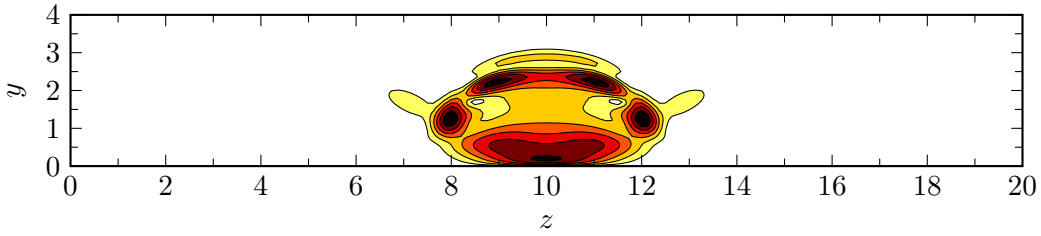

(c) VC mode, $(\alpha_r, \alpha_i) = (1.1150, -0.008125)$

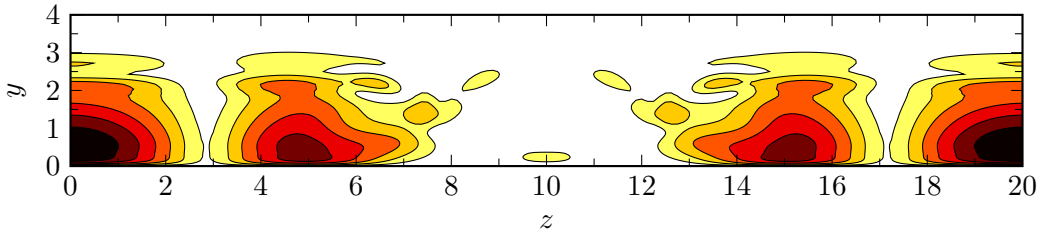

(d) Mack mode, $(\alpha_r, \alpha_i) = (1.0639, -0.005910)$

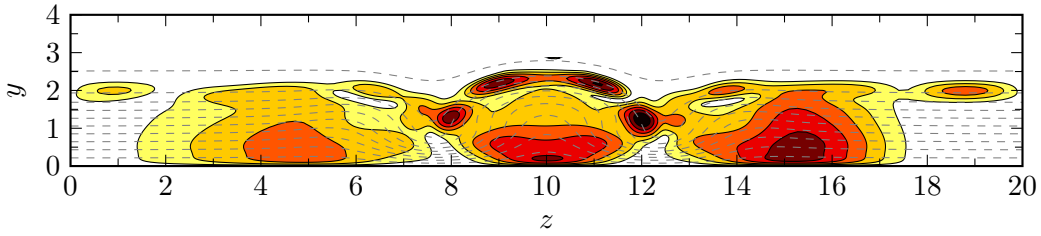

(e) DNS mode, $\sigma_{\text{DNS}} = 0.01437$

Figure 6.7. Mode shape of the instability modes with $F = 0.16$ for case Cyl from BLS **(a-d)** and DNS **(e)** results. Mode shapes are visualised by contours of $|u'|$-velocity at a streamwise location of $x = 96.4$.

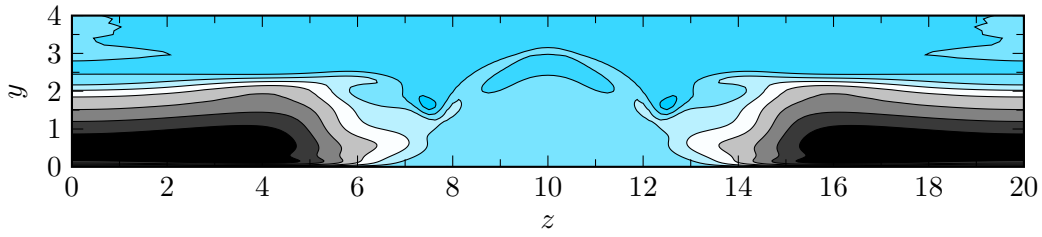

(a) Mack mode, $(\alpha_r, \alpha_i) = (1.0734, -0.01972)$

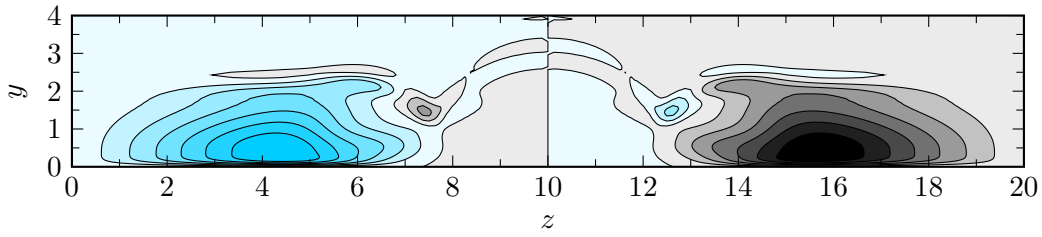

(b) Mack mode, $(\alpha_r, \alpha_i) = (1.0731, -0.01650)$

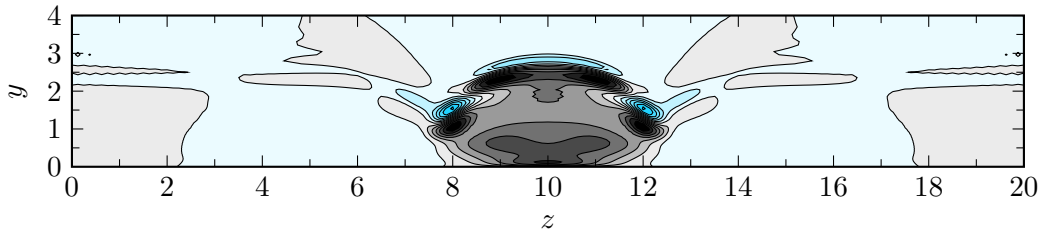

(c) VC mode, $(\alpha_r, \alpha_i) = (1.1150, -0.008125)$

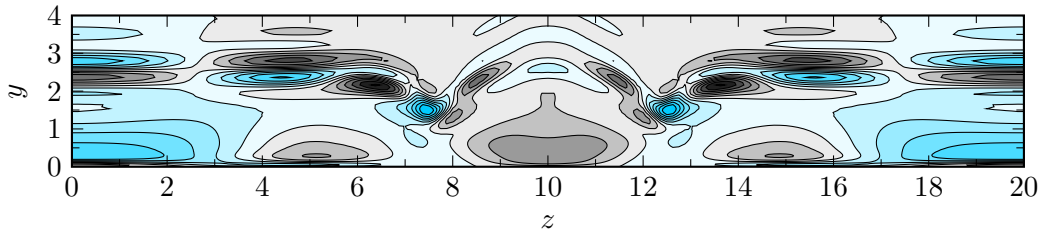

(d) Mack mode, $(\alpha_r, \alpha_i) = (1.0639, -0.005910)$

Figure 6.8. Mode shape of the instability modes with $F = 0.16$ for case CYL from BLS results, visualised by contours of the real part of u'-velocity at a streamwise location of $x = 96.4$.

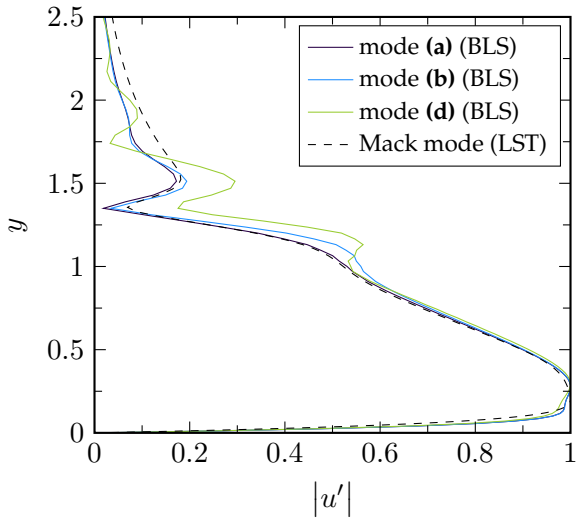

Figure 6.9. Comparison of the eigenfunctions of the BLS modes with $F = 0.16$ (as shown in Figure 6.7) with the eigenfunction of the most two-dimensional Mack mode computed by local LST.

in the wall-normal direction to match the wall-normal location of the modes. The main features of the BLS eigenfunctions are very well aligned with the Mack mode computed by the LST, indicating that the modes shown in Figures 6.7a, 6.7b and 6.7d are in fact two-dimensional and three-dimensional Mack modes in the undisturbed boundary layer.

The most unstable BLS mode is the two-dimensional Mack mode ($-\alpha_i = 0.01972$, $c_{ph} = 0.9366$), closely followed by a three-dimensional Mack mode ($-\alpha_i = 0.01650$, $c_{ph} = 0.9368$) that is asymmetric across the roughness wake and has a spanwise wavelength that is related or roughly equal to the spanwise extent of the domain, as demonstrated by Figure 6.8b. A much less unstable three-dimensional Mack mode, with a similar wavelength but symmetric across the wake, has also been observed ($-\alpha_i = 0.005910$, $c_{ph} = 0.9449$) and is shown in Figure 6.8d. As mentioned earlier, the results from the DNS show that the most unstable mode is a combination of a Mack mode and a varicose-centre mode in the wake (see Figure 6.7e). This varicose-centre mode was found by the bi-local stability analysis, as shown by Figures 6.7c and 6.8c, and strongly resembles the VC mode from the DNS, but is not predicted to be the most unstable. The growth of the VC mode as predicted by the BLS is $-\alpha_i = 0.008125$, which is approximately 57% of the DNS growth rate ($\sigma_{\text{DNS}} = 0.01437$).

The overall comparison of the growth rates is better for the Mack modes in the

undisturbed boundary layer than for the wakes modes at lower frequencies, which might be due to the non-parallel effects that are less significant for a boundary layer than for a roughness wake. This raises the question how the comparison between bi-local stability and DNS behaves further away from the roughness element near-wake.

6.2.2 Influence of streamwise distance

While in the previous section a comparison was made between linear stability analysis and the DNS results at a single streamwise position ($x = 96.4$), the growth of the instability modes along the domain is studied here for a selected number of frequencies. Figure 6.10 shows the growth rate of the instabilities with frequencies $F = 0.02$, $F = 0.06$, $F = 0.14$ and $F = 0.18$ along the domain for case CYL, both from the DNS results *(dashed lines)* and computed using bi-local stability analysis *(markers and solid lines)*.

From this figure and the discussion in Chapter 5 *(Roughness Receptivity & Wake Instability)*, it is clear that the DNS growth rate is not constant along the domain and varies highly with the streamwise distance. The growth rate of the instabilities with frequency $F = 0.02$ increases up to $x \approx 80$ after which it monotonically decreases and reaches a quasi-steady value for $x \gtrapprox 105$. The instabilities with frequencies $F = 0.06$, $F = 0.14$ and $F = 0.18$ experience a growth rate trend of decay, growth and subsequent monotonic decay. The growth rate peak occurs at different streamwise locations: $x \approx 90$ for $F = 0.06$, $x \approx 110$ for $F = 0.14$ and $x \approx 70$ for $F = 0.18$. While the instabilities with $F = 0.06$ and $F = 0.14$ have a decaying growth rate throughout the streamwise extent of the domain, a quasi-steady growth rate is reached for the instabilities with $F = 0.18$ for $x \gtrapprox 110$.

This strong streamwise-dependent behaviour of the disturbance growth is not accurately captured by the bi-local stability analysis, as can be seen in Figure 6.10. Except for the instabilities with $F = 0.14$, the bi-local stability results predict a monotonic decrease going downstream and consistently underpredicts the growth rates. While the growth rates of the DNS results for $F = 0.02$ and $F = 0.06$ is reduced more than half from their peaks to the end of the domain, the difference between the maximum and minimum BLS growth rates is considerably smaller. For $F = 0.14$ the bi-local stability analysis qualitatively predicts the behaviour, but underpredicts the growth rate rate at $x < 125$ and overpredicts it at $x > 125$. Also for $F = 0.18$ the qualitative behaviour is captured by the stability analysis, but the actual growth

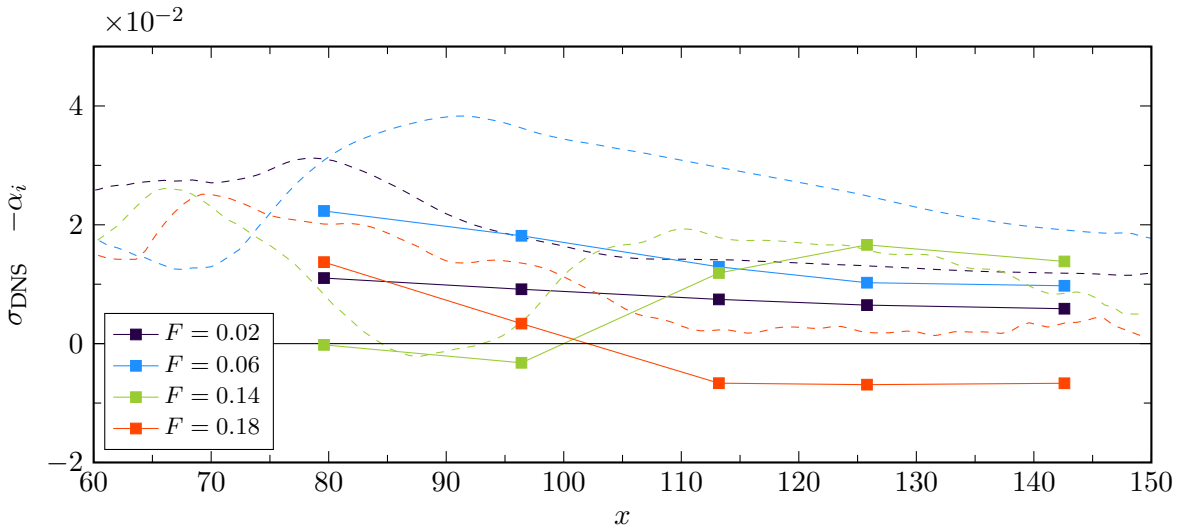

Figure 6.10. Comparison of instability growth rates between DNS *(dashed lines)* and bi-local stability *(markers and solid lines)* along the domain for case Cyl.

rate is severely underpredicted. The bi-local stability analysis even predicts these instabilities to be stable, while they are uniformly unstable in the DNS. Near the end of the domain at $x = 142.6$, the instability with $F = 0.06$ has the largest DNS growth rate, i.e. $\sigma_{\text{DNS}} = 0.01906$. The linear stability growth rate is approximately 49% lower, i.e. $-\alpha_i = -0.009738$. This relative difference is the same as the difference upstream at $x = 96.4$, as discussed in the previous section. The mode shapes of the BLS modes and the DNS are shown in Figure 6.11, which demonstrates that there is a fair agreement between the mode shape of the most unstable mode (Figure 6.11a) and the DNS (Figure 6.11d).

In general the agreement between the DNS and the bi-local stability analysis does not greatly improve further downstream, where non-parallel effects are expected to be reduced. Although some of the mode shapes are in fair agreement between the stability analysis results and DNS, the growth rates computed using the stability analysis are inaccurate. It can thus be said that bi-local stability may not be the appropriate tool to quantitatively predict the disturbance growth in the wake of roughness elements, where non-parallel effects are not negligible. Stability analysis tools that do not neglect the streamwise dependency and non-parallel flow, such as three-dimensional PSE or tri-global stability analysis, could give better results. The improved quantitative agreement that three-dimensional PSE can give, has earlier been shown by De Tullio et al. (2013).

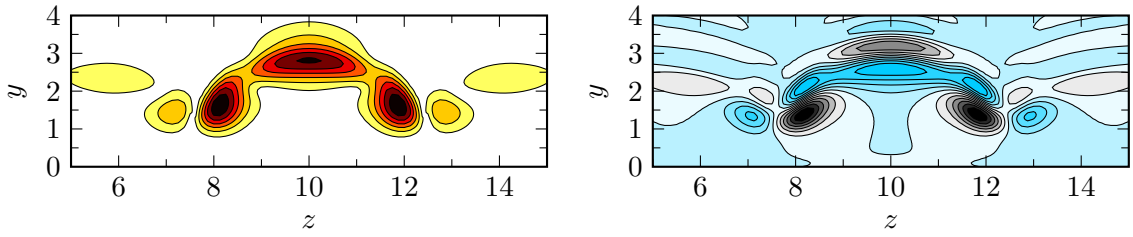

(a) VL mode, $(\alpha_r, \alpha_i) = (0.4202, -0.009738)$

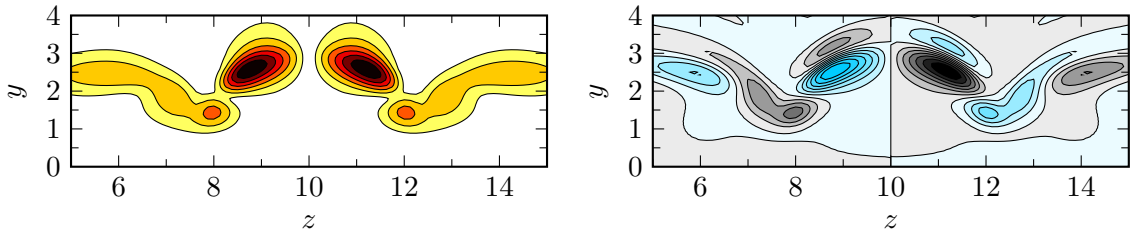

(b) SL mode, $(\alpha_r, \alpha_i) = (0.4084, -0.008296)$

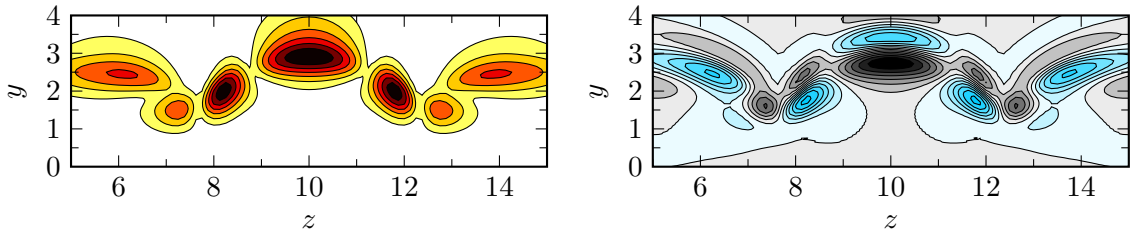

(c) VL mode, $(\alpha_r, \alpha_i) = (0.4070, -0.006578)$

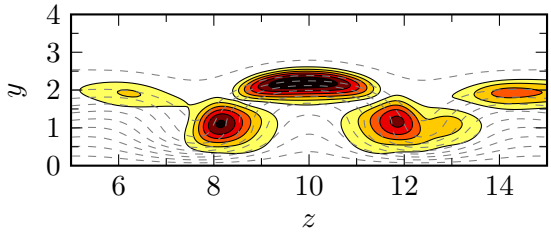

(d) DNS mode, $\sigma_{\text{DNS}} = 0.01906$

Figure 6.11. Mode shape of the instability modes with $F = 0.06$ for case CYL from BLS **(a-c)** and DNS **(d)** results. Mode shapes are visualised by contours of $|u'|$-velocity *(left)* and the real part of u'-velocity *(right)* at a streamwise location of $x = 142.6$.

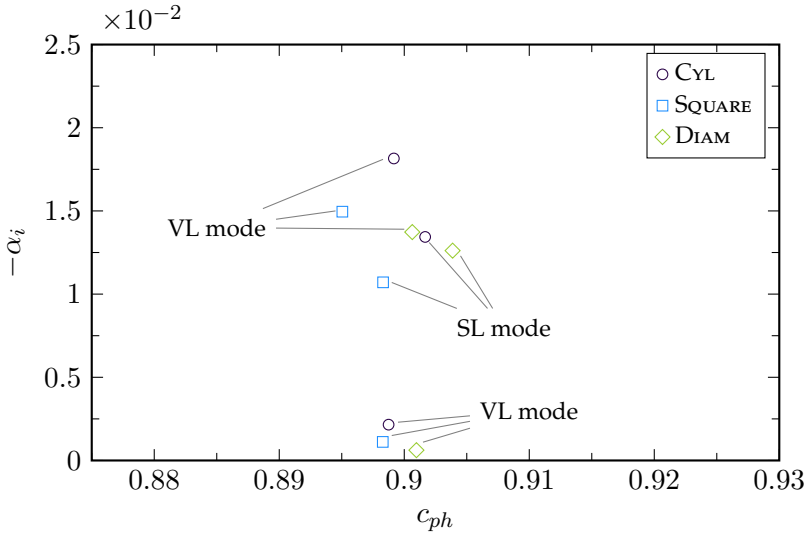

Figure 6.12. Comparison of the spectrum of the instability with $F = 0.06$ at $x = 96.4$ behind the different roughness elements.

6.2.3 Dependency on roughness element

The results presented so far in this chapter are only for the cylindrical flat-top case Cyl. In order to investigate whether bi-local stability analysis can predict the relative instability of the different flat-top roughness element cases, the wake instability behind cases Cyl, Square and Diam is discussed in this section. The bi-local stability analysis has been performed at a single downstream position ($x = 96.4$) and for the frequency at which the largest instability growth was observed, i.e. $F = 0.06$.

The spectrum of the unstable SL and VL wake modes found behind the various cases is shown in Figure 6.12. In this figure the different modes are annotated with their respective types. Two families of varicose-lateral modes and a sinuous-lateral mode can be seen to be found behind the flat-top roughness elements by the bi-local stability analysis. These unstable modes, i.e. two VL and one SL mode, have already been shown behind the cylindrical flat-top element in Figure 6.5. The most dominant mode at this frequency is a varicose-lateral mode for all the cases, followed by the sinuous-lateral mode. The secondary VL mode has a growth rate that is almost an order of magnitude smaller than the most unstable VL mode.

The mode shapes of the most unstable VL mode are given in Figure 6.13 for the three flat-top roughness elements. It can be seen that the structure of this VL mode is very similar for the roughness elements with the different planform shapes. This

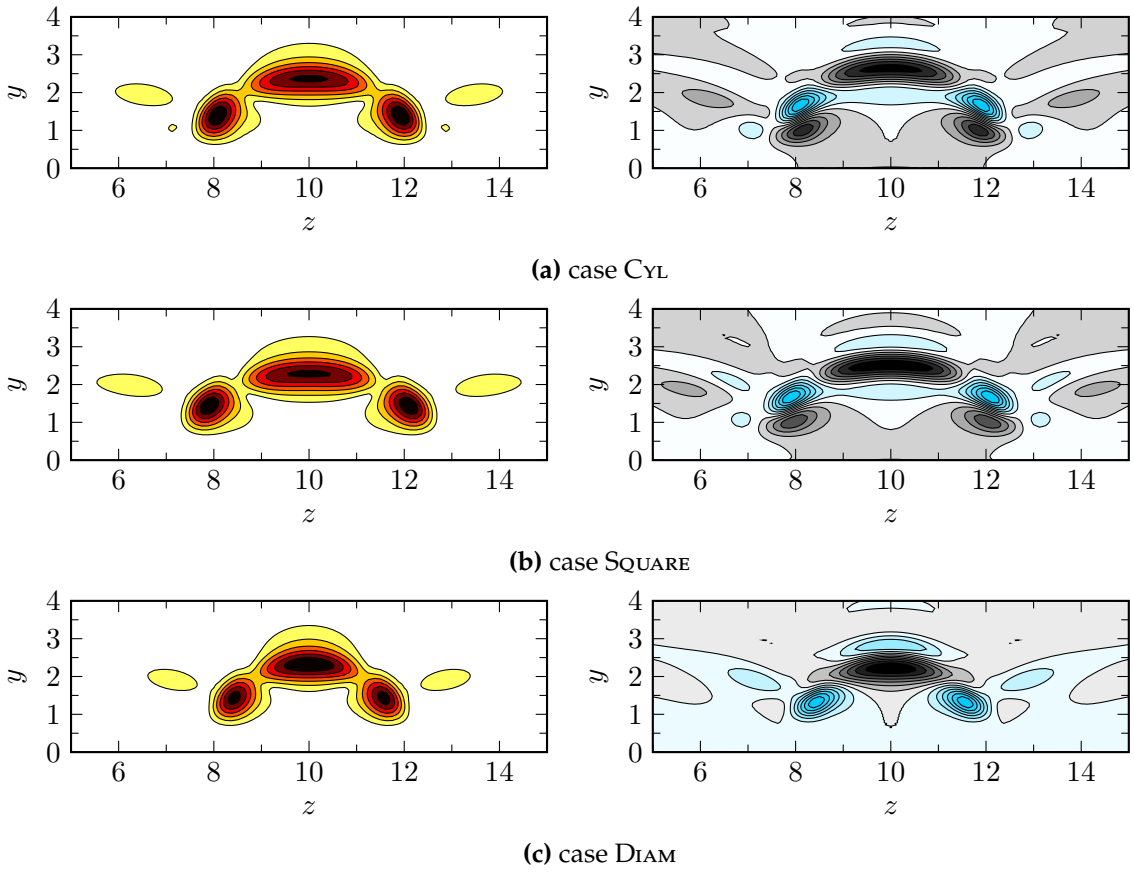

(a) case CYL

(b) case SQUARE

(c) case DIAM

Figure 6.13. Mode shape of the instability modes with $F = 0.06$ for cases CYL, SQUARE and DIAM. Mode shapes are visualised by contours of $|u'|$-velocity *(left)* and the real part of u'-velocity *(right)* at a streamwise location of $x = 96.4$.

behaviour was already observed in the DNS results presented in Chapter 5 *(Roughness Receptivity & Wake Instability)*.

It is interesting to note that the cylindrical flat-top element is predicted to be the most unstable among the roughness elements, which agrees with the results from the DNS. According to the BLS results, the square flat-top is more unstable than the diamond-shaped roughness element at this frequency, which is contrary to the DNS. However, near the streamwise position where the bi-local stability analysis is performed, i.e. $x = 96.4$, the DNS growth rates for $F = 0.06$ are rapidly decreasing and very streamwise-dependent. This results in the wake behind the square flat-top element becoming more unstable shortly further downstream, i.e. at $x \gtrapprox 105$, as was shown by Figure 5.19b. Figure 6.14 shows the growth rate of the most unstable mode,

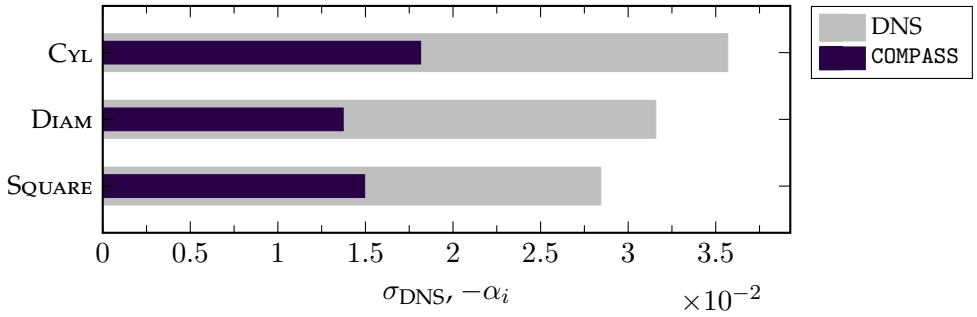

Figure 6.14. Comparison of the largest growth rate of the instabilities with $F = 0.06$ at $x = 96.4$ behind the different roughness elements.

obtained from the DNS and BLS results, for the different roughness elements, ranked by most unstable according to the DNS results. It gives an immediate overview of the discrepancy between the DNS and BLS growth rate of the most unstable wake mode.

6.3 Summary of results

A new linear stability analysis code (`COMPASS`) has been developed and validated in Chapter 3 *(COMPASS: Compressible Stability Analysis)*. In this chapter, the applicability of bi-local stability analysis on roughness wakes has been investigated by comparison with DNS.

It was found that the bi-local stability analysis is able to predict the most unstable instability mode and its frequency active in the roughness wake. Also the mode shapes can be accurately resolved in some cases. However, the growth rate predicted by the stability theory is found to be inaccurate. For example, the largest growth rate of the instabilities in the wake of a cylindrical flat-top roughness element, obtained using DNS, is twice as large as the growth rate predicted by the stability analysis. The comparison has been found to be better with boundary layer modes, e.g. Mack modes, than with wake modes, hinting that the non-parallel effects, neglected by the linear stability theory, are of great importance in the growth of instability modes. Therefore, tri-global instability analysis or three-dimensional PSE could be needed to give improved quantitative predictions of the instability of roughness wakes.

Chapter 7

Roughness-induced Transition

Part of the work in this chapter has appeared in:
Van den Eynde & Sandham, '**Numerical Simulations of Transition due to Isolated Roughness Elements at Mach 6**', *AIAA Journal*, 2015 (accepted), doi:10.2514/1.J054139

In this chapter the transition from a laminar to a turbulent boundary layer due to the presence of an isolated roughness element is investigated. It deals with the (non-linear) growth of instabilities in the roughness wake and the subsequent breakdown to transition, making it a logical follow-up to Chapter 5 *(Roughness Receptivity & Wake Instability)*, in which the excitation and evolution of linear instabilities in the roughness wake was studied.

7.1 Case details

In total ten different simulations have been run, looking at the roughness element height, shape, and the amplitude of the freestream disturbance environment. The set-up of the simulations is very similar to the cases in Chapter 5 *(Roughness Receptivity & Wake Instability)*, e.g. the same roughness elements, Mach number, wall temperature. Note that two additional roughness elements are investigated in this chapter: a cylindrical flat-top element with a smaller height, and a square roughness element with a smaller width. The domain size was increased in the streamwise direction to resolve a sufficiently large portion of the transition process, in the wall-normal direction to avoid any shock reflection from the top boundary onto the boundary layer, and in the spanwise direction to accommodate for the generation and growth of a turbulent wedge. Also the number of grid points was increased in all directions to accurately resolve the developing turbulence. Details of the domain and grid size

Table 7.1. Case details of the simulations of roughness-induced transition study of the current chapter.

Case	M	Re	T_w	k	Dist. ampl.	Geometry
H-⊗-1.0-Ae5	6.0	14 000	7.02	1.0	6×10^{-5}	smooth bump
H-⊗-1.0-Ae4	6.0	14 000	7.02	1.0	6×10^{-4}	smooth bump
H-○-1.0-Ae5	6.0	14 000	7.02	1.0	6×10^{-5}	flat-top (cyl.)
H-○-1.0-Ae4	6.0	14 000	7.02	1.0	6×10^{-4}	flat-top (cyl.)
H-□-1.0-Ae5	6.0	14 000	7.02	1.0	6×10^{-5}	flat-top (square)
H-◇-1.0-Ae5	6.0	14 000	7.02	1.0	6×10^{-5}	flat-top (diamond)
H-△-1.0-Ae5	6.0	14 000	7.02	1.0	6×10^{-5}	ramp-up
H-▽-1.0-Ae5	6.0	14 000	7.02	1.0	6×10^{-5}	ramp-down
H-●-0.5-Ae5	6.0	14 000	7.02	0.5	6×10^{-5}	flat-top (cyl.)
H-⬠-1.0-Ae5	6.0	14 000	7.02	1.0	6×10^{-5}	flat-top (sq.) ($W = 3.0$)

have been introduced in Chapter 4 *(Problem Definition & Numerical Set-up)* (Domain A). In order to promote the transition process and resolve it without increasing the length of the computational domain too much, the simulation Reynolds number, still based on the displacement thickness of the laminar boundary layer at the inflow, was increased from $Re = 8200$ to $Re = 14000$. Flow parameters and details of the different cases in this chapter are given in Table 7.1.

The naming of the roughness cases is done according to the following convention. The first letter signifies the wall temperature. It should be noted that in this chapter only hot (H) wall cases are studied and that the wall temperature T_w is set to the adiabatic wall temperature. The symbol after this first letter indicates the roughness shape: smooth bump (⊗), cylindrical (○), square (□) or diamond-shaped (◇) flat-top roughness elements, and the ramp-up and ramp-down elements are indicated by △ and ▽ respectively. The flat-top roughness element with height $k = 0.5$ is indicated with the symbol ● and the flat-top with width $W = 3.0$ with the symbol ⬠. Note that these symbols are also used as markers in the figures of this chapter, to allow for an easy distinction between results of different cases. The number that follows the roughness shape designation indicates the roughness height k. Except for the case with small ($k = 0.5$) flat-top roughness element H-●-0.5-Ae5, all cases have a roughness height of $k = 1.0$. The last part of the naming represents the amplitude of imposed acoustic forcing introduced in Equation (4.7): Ae5 for an amplitude $a = 6 \times 10^{-5}$ and Ae4 for $a = 6 \times 10^{-4}$.

7.2 Roughness-induced base flow modifications

Similarly to Chapter 5 *(Roughness Receptivity & Wake Instability)*, the main flow characteristics and base flow modifications due to the presence of the roughness element will be investigated first. Although the geometry of the roughness elements and some of the main flow variables (e.g. Mach number, wall temperature) for the simulations of this chapter are the same as for the cases in Chapter 5, the simulation Reynolds number (and thus roughness Reynolds number) has been increased significantly. The flow around the roughness element, and thus the roughness wake further downstream, will be affected by the increased local Reynolds number. Since it has been observed that relatively small differences in the base flow can affect the wake stability characteristics, it is important to gauge the differences between the cases to better understand the transition behaviour and processes.

7.2.1 Shear layers & recirculation regions

From Chapter 5 *(Roughness Receptivity & Wake Instability)*, it is known that the roughness elements generate wakes that consist of a low-speed streak flanked by a pair of high-speed streaks, resulting in increased levels of shear stress between the streaks, and a detached shear layer generated over the top of the roughness elements. It is these shear layers that sustain the growth of instabilities and are of primary importance to the wake instability and thus the subsequent transition process.

Figure 7.1 shows how the roughness shape and planform change the shear layers around and behind the roughness element, using contours of wall-normal shear $\partial u/\partial y$ (*left*) and shear magnitude u_s (*right*), defined as

$$u_s \coloneqq \sqrt{\left(\frac{\partial u}{\partial y}\right)^2 + \left(\frac{\partial u}{\partial z}\right)^2} \quad . \tag{7.1}$$

The recirculation regions around the roughness elements are indicated in Figure 7.1 using dashed red contour lines of small negative velocity, i.e. $u = -1 \times 10^{-5}$. The length of these recirculation regions, at the front and aft section of the roughness elements, is summarised in Table 7.2. Note that the results presented in this section are time-averaged over a single period of the imposed acoustic forcing function, introduced in Chapter 4 *(Problem Definition & Numerical Set-up)*.

Effect of frontal profile Figures 7.1a and 7.1b show the shear layers around the smooth bump and cylindrical flat-top roughness elements respectively. It can be seen

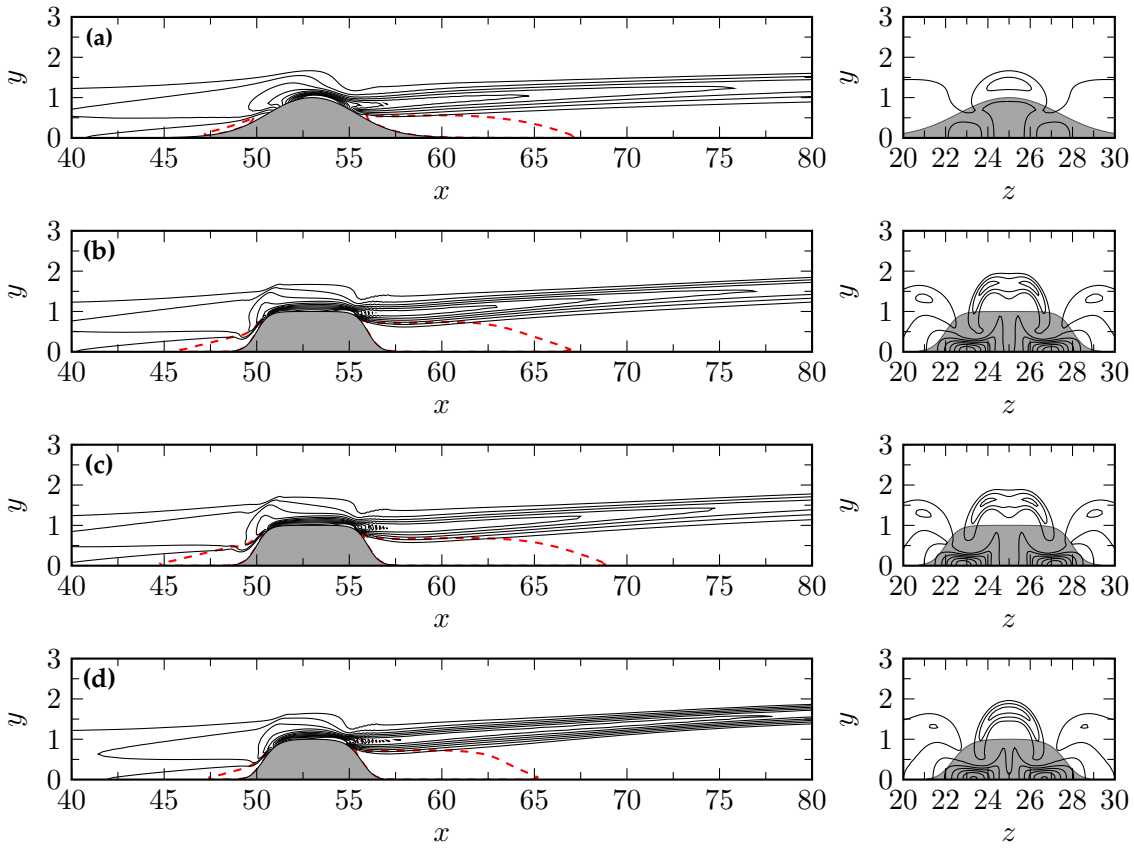

Figure 7.1. Wall-normal shear $\partial u/\partial y$ (*left*) at the domain centreline. Recirculation bubbles are visualised by dashed red contour lines of infinitesimally small negative streamwise velocity. Contours of shear magnitude u_s at $x = 85.0$ (*right*), with the roughness shape superimposed as a shaded contour. **(a)** H-⊗-1.0-Ae5; **(b)** H-○-1.0-Ae5; **(c)** H-□-1.0-Ae5; **(d)** H-◇-1.0-Ae5. (*Continued on next page*)

that the recirculation region upstream of the flat-top is larger, while the recirculation region downstream is of the same length. This is different to the simulations at a lower Reynolds number ($Re = 8200$) in Chapter 5, for which the aft recirculation region was observed to be considerably smaller for the smooth bump. The increase in in Reynolds number has also an effect on the shear layers. The value of the wall-normal shear stress downstream of the roughness elements, e.g. at $x = 80$, is similar between the smooth bump and flat-top, albeit thinner and further away from the wall behind the flat-top. For the lower Reynolds number simulations, the detached shear layer was much weaker behind the smooth bump element. The shear stress away from the roughness centreline is still heavily dependent on the roughness frontal shape, as can be seen in the right hand figures of Figures 7.1a

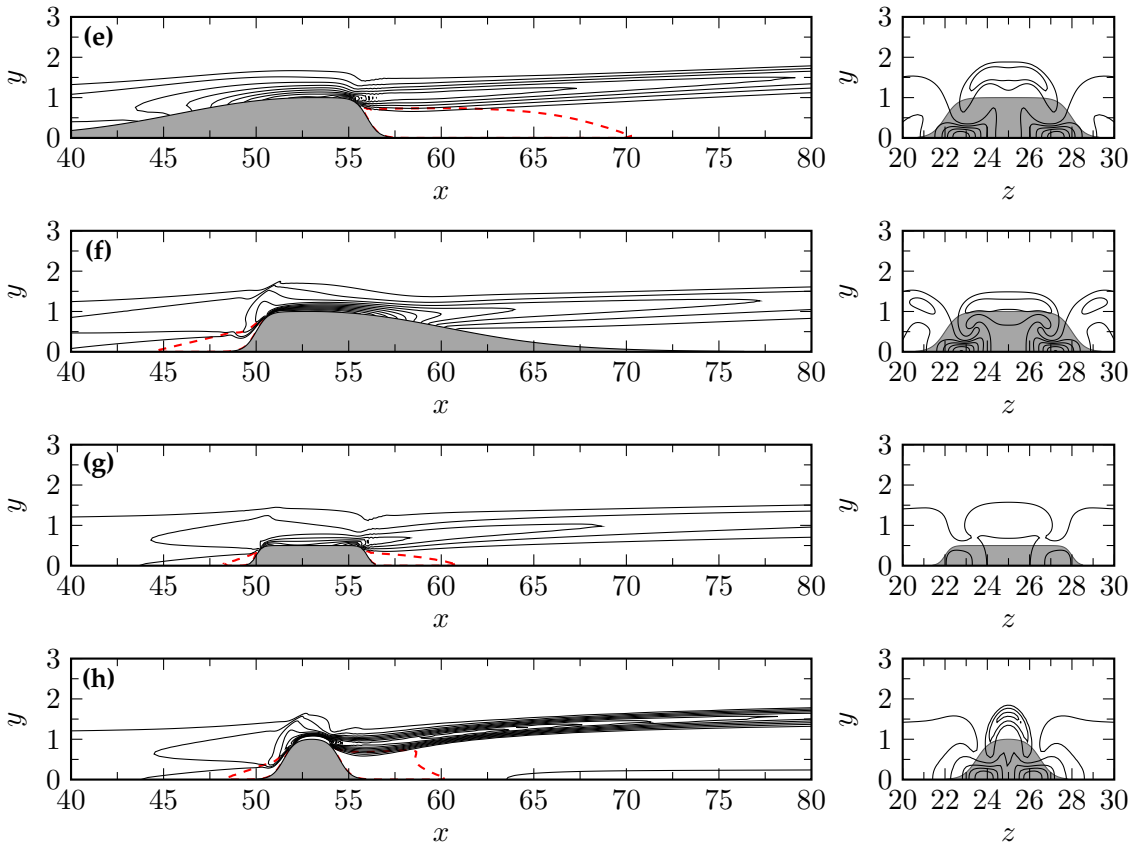

Figure 7.1 (cont.). Wall-normal shear $\partial u/\partial y$ (*left*) at the domain centreline. Recirculation bubbles are visualised by dashed red contour lines of infinitesimally small negative streamwise velocity. Contours of shear magnitude u_s at $x = 85.0$ (*right*), with the roughness shape superimposed as a shaded contour. **(e)** H-△-1.0-Ae5; **(g)** H-▽-1.0-Ae5; **(g)** H-●-0.5-Ae5; **(h)** H-⬠-1.0-Ae5

and 7.1b. The structure of the detached shear layer behind the flat-top can be seen to be more curved and concentrated, and the high-shear regions close to the wall (at $z \approx 23$ and $z \approx 25$), generated by streamwise vorticity induced by the roughness elements, are considerably weaker behind the smooth bump.

Effect of planform shape The effect of the planform of the roughness element can be observed by looking at Figures 7.1b to 7.1d, which shows the shear layers for the cylindrical, square and diamond-shaped flat-top roughness elements respectively. From these figures it can be seen that the difference between the cylindrical and square roughness element is small, while the diamond-shaped flat-top generates a slightly more curved detached shear layer and stronger wall-normal shear at the

roughness centreline. The recirculation regions downstream of the roughness elements can be seen to be dependent on the roughness planform: the diamond-shaped roughness element has the shortest recirculation region, followed by the cylindrical and finally the square flat-top roughness element. The separation lengths around the cylindrical and square elements are respectively 42% and 87% larger upstream and 15% and 37% larger downstream compared to the diamond-shaped roughness element. Very similar behaviour, qualitatively, was observed at a lower Reynolds number in Chapter 5.

Effect of ramps The effect of ramping up or ramping down the roughness element is shown by Figures 7.1e and 7.1f, which should be compared with the square flat-top case of Figure 7.1c. It can be seen that ramping up does not greatly modify the shear layers downstream. The strength and wall-normal location of the wall-normal shear at the centreline is roughly the same, although the shear regions off-centre and near the wall are slightly weaker. The recirculation region downstream of the ramp-up element is slightly larger, while upstream no recirculation region is present due to the more gentle change in geometry.

In the case of the ramp-down element, the flow upstream of the roughness behaves the same as the square flat-top element, while a large effect downstream can be observed. The downstream recirculation region has disappeared completely, which allows the detached shear layer to spread out and be brought closer to the wall, resulting in lower levels of wall-normal shear. The off-centre near-wall high-shear regions do not seem to be affected by the ramping up or down, which would indicate that the streamwise vorticity generated by the roughness element is not weakened by the ramped-down aft section of the roughness element.

Effect of roughness height The small flat-top roughness element (with $k = 0.5$) of case H-$\bullet$-0.5-Ae5 yields very weak shear layers compared to the flat-top element with height $k = 1.0$, as can be seen by comparing Figures 7.1b and 7.1g. The strength and structure of the detached shear layer is more similar to the smooth bump (with $k = 1.0$), shown in Figure 7.1a, and therefore the effect of these two roughness elements on the transition behavior is expected to be similar.

Effect of roughness width The effect of the roughness width or aspect ratio can be seen Figure 7.1h, which shows the case with $W = 3.0$ and can be compared to square flat-top element with $W = 6.0$ in Figure 7.1c. The detached shear layer at the

Table 7.2. Lengths of the recirculation regions upstream and downstream of the roughness elements.

Case	$L_{\text{sep}}^{\text{front}}$	$L_{\text{sep}}^{\text{aft}}$
H-⊗-1.0-Ae5	2.7	11.2
H-○-1.0-Ae5	4.4	11.3
H-□-1.0-Ae5	5.8	13.4
H-◇-1.0-Ae5	3.1	9.8
H-●-0.5-Ae5	1.7	4.8
H-△-1.0-Ae5	–	14.6
H-▽-1.0-Ae5	5.8	–
H-⬠-1.0-Ae5	3.3	5.7

centreline downstream of the narrower roughness element is stronger, more concentrated and more curved in the cross-flow plane. The high-shear regions off-centre and near the wall are weaker for the narrow roughness element, indicating that the streamwise vorticity generated by this element is not as strong. The recirculation regions around the $W = 3.0$ element are approximately 43% (upstream) and 57% (downstream) shorter than those around the flat-top with $W = 6.0$.

7.2.2 Vortical structures

The vortical flow structures generated around the roughness elements are shown in Figures 7.2 and 7.2, visualised by isosurfaces of second invariant of the velocity gradient tensor, i.e. the Q-criterion (Hunt et al., 1988), defined for compressible flow as

$$Q = \frac{1}{2}\left[\left(\frac{\partial u_i}{\partial x_i}\right)^2 - \frac{\partial u_i}{\partial x_j}\frac{\partial u_j}{\partial x_i}\right], \tag{7.2}$$

and coloured by the local streamwise velocity. The recirculation regions are shown using black isosurfaces, which gives a better understanding of the three-dimensional shape of the separation around the roughness elements.

From Figure 7.2a it can be seen that the smooth bump does not produce strong vortical structures downstream of the roughness. This is consistent with the relatively low spanwise shear stress in its wake, as observed in the previous section. A relatively large high-speed structure can be seen on top of the smooth bump, but this does not seem to have much influence on the downstream flow structures.

The planform does not seem to have a dramatic effect on the structures around the

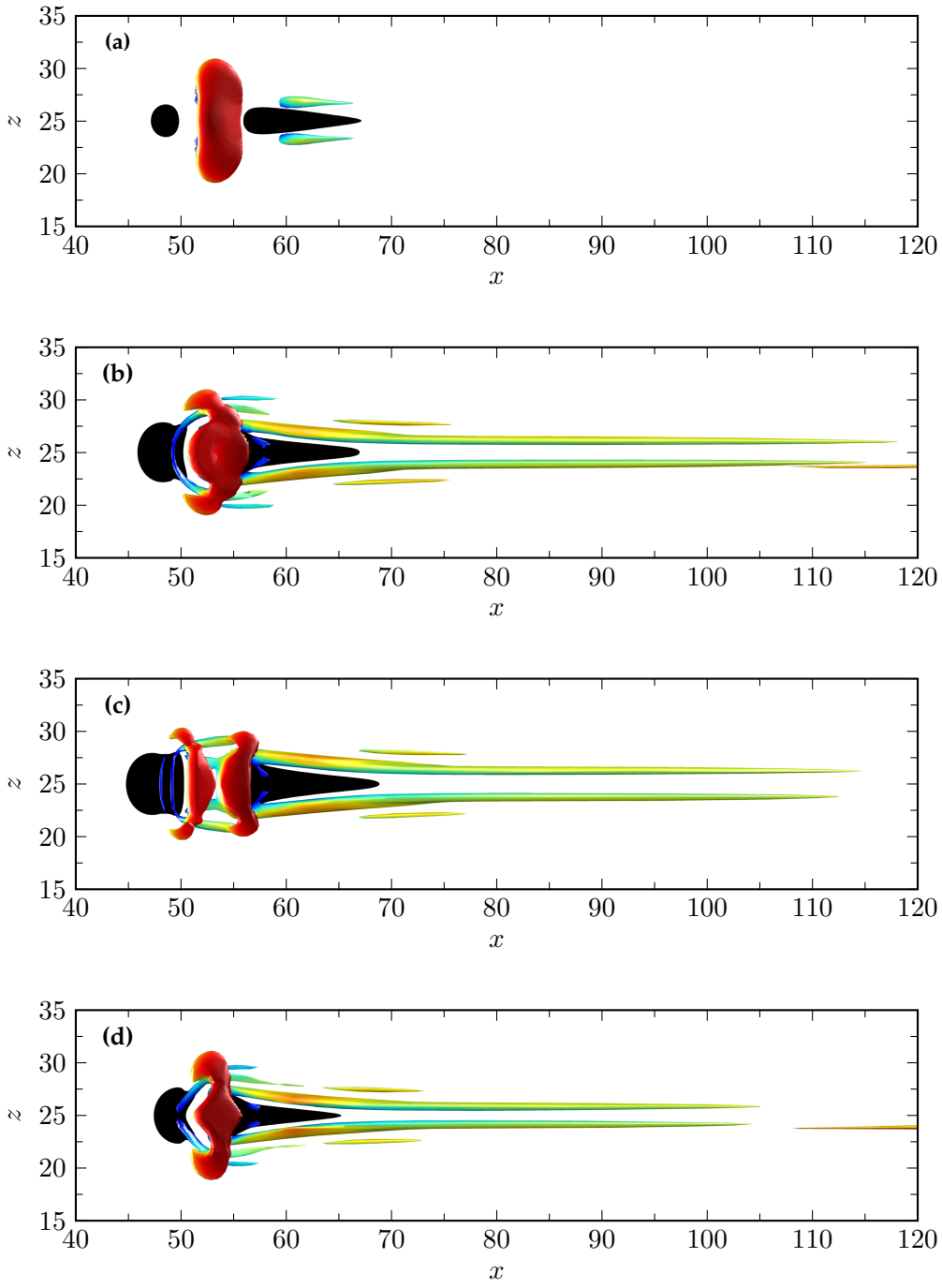

Figure 7.2. Top view of the flow structures around the roughness elements. Structures are shown by isosurfaces of $Q = 0.003$ coloured using the local streamwise velocity. Black isosurfaces indicate the recirculation regions. **(a)** H-⊗-1.0-Ae5; **(b)** H-○-1.0-Ae5; **(c)** H-□-1.0-Ae5; **(d)** H-◇-1.0-Ae5. (*Continued on next page*)

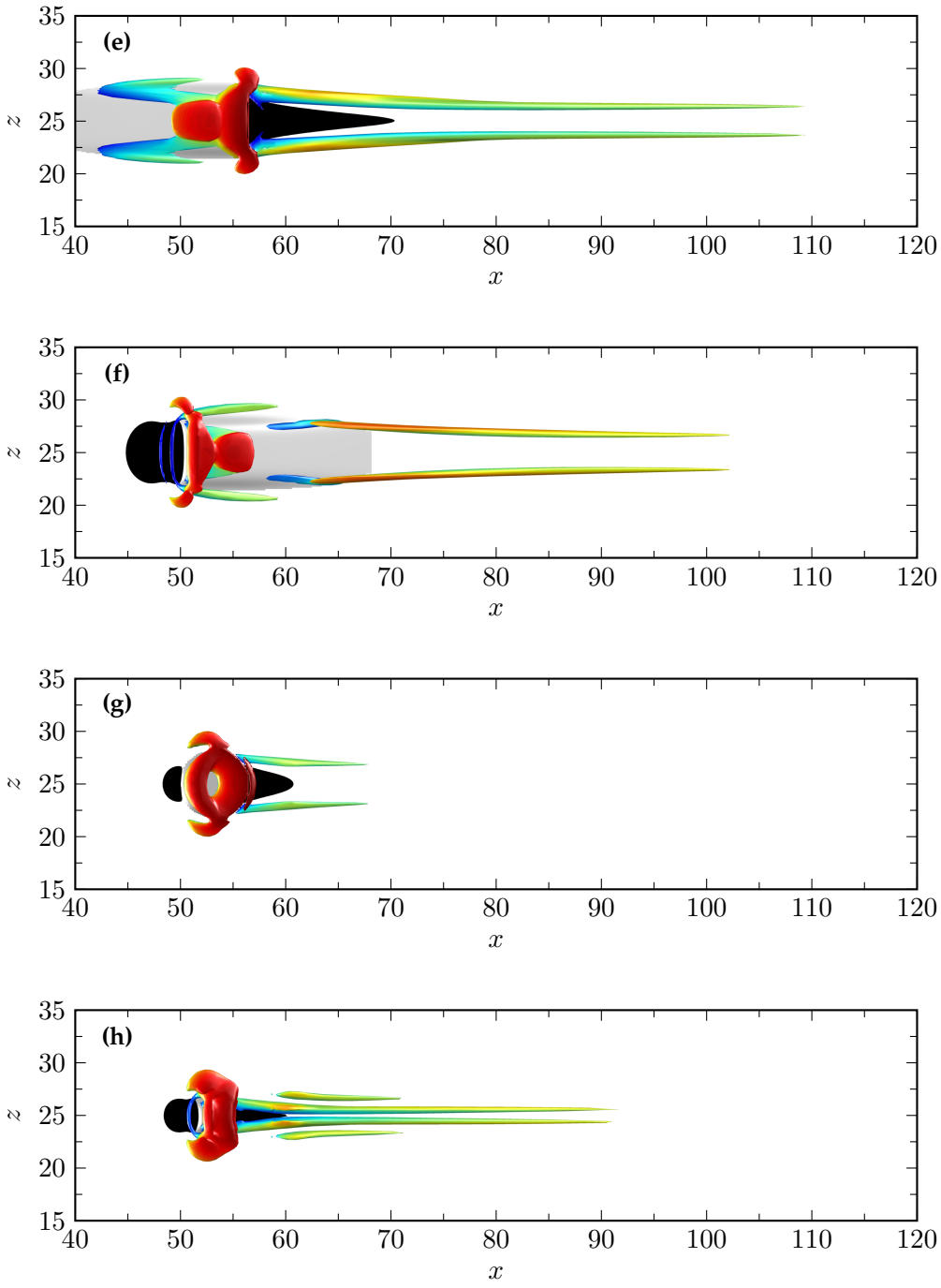

Figure 7.2 (cont.). Top view of the flow structures around the roughness elements. Structures are shown by isosurfaces of $Q = 0.003$ coloured using the local streamwise velocity. Black isosurfaces indicate the recirculation regions. **(e)** H-△-1.0-Ae5; **(f)** H-▽-1.0-Ae5; **(g)** H-●-0.5-Ae5; **(h)** H-⬠-1.0-Ae5

flat-top roughness elements, as shown in Figures 7.2b to 7.2d. Upstream of the roughness, a low-speed horseshoe vortex can be seen to wrap itself around the elements. Stronger vortices are generated at the aft section of the elements in a high speed flow region. These structures initially follow the shape of the downstream recirculation regions and become aligned in the streamwise direction further downstream. Because of the much narrower recirculation region behind the diamond-shaped roughness elements, this pair of streamwise-aligned vortices are located closer together than in the case of the cylindrical or square flat-top roughness element. The high-speed rollers generated on top, shown as red in Figures 7.2b to 7.2d, have a shape that is planform-dependent, but this structure does not seem to have an effect on the downstream flow structures.

In the case of the ramp-up element, shown in Figure 7.2e, no horseshoe vortex is generated. Similarly to the flat-top element without a ramp, a strong streamwise-aligned vortex pair is generated downstream with similar strength and spanwise position. Therefore, the flow structures downstream do not seem to be affected very much by the upstream ramp-up, and it is mainly the geometry of the roughness aft section that governs the flow structures in the roughness wake. This is confirmed by looking at the ramp-down element in Figure 7.2f. The flow structures at the front of the ramp-down roughness (i.e. horseshoe vortex, high-speed roller on top) are almost identical to the square flat-top element without a ramp, as shown in Figure 7.2c. However, the structures downstream of the ramp-down are considerably affected. The streamwise-aligned vortex pair seems to be thinner and have a higher local streamwise velocity, indicating that the streamwise velocity deficit behind the ramp-down roughness element is much lower than the flat-top element without downward ramp.

The small roughness element of case H-●-0.5-Ae5 does not generate strong vorticity downstream, as shown in Figure 7.2g. In that regard, the flow around the flat-top roughness element with $k = 0.5$ is not very different from the flow around the smooth bump element. For the case with a square flat-top element with $k = 1.0$ but a width $W = 3.0$ (H-⬠-1.0-Ae5) the flow structures are very similar to the full-width case H-□-1.0-Ae5, but the generated streamwise-aligned structures are located closer to the centreline.

7.3 Roughness effect on transition

Although it is known that surface roughness can promote early transition to turbulence, the exact behaviour of the flow and the characteristics of the transition process downstream of an isolated roughness element are hard to predict.

7.3.1 Prediction of roughness-induced transition

Traditionally a transition criterion based on roughness height has been used to separate the transitional and non-transitional cases. One of the most commonly-used roughness-induced transition criteria is the roughness Reynolds number Re_{kk} (Reda, 2002) defined as

$$Re_{kk} \coloneqq \frac{u_k \rho_k k}{\mu_k} \tag{7.3}$$

where u_k, ρ_k and μ_k are respectively the streamwise velocity, density and dynamic viscosity at the location and height k of the roughness in an unperturbed boundary layer. This approach does not take into account the shape, planform or background noise levels, yielding a range of critical Reynolds numbers Re_{kk} reported in the literature. Variations of Re_{kk}, where variables are taken at different locations (either at the wall or the roughness height) are occasionally used, such as

$$Re_{kw} \coloneqq \frac{u_k \rho_k k}{\mu_w} \tag{7.4}$$

(Bernardini et al., 2012a), but neither of these solve the inherent limitations of this type of transition criterion. More recently Bernardini et al. (2012b) proposed a new transition criterion based on momentum deficit due to the roughness element, Re_Q, defined as

$$Re_Q \coloneqq \frac{Q S_{yz}^{-1/2}}{\mu_w} \tag{7.5}$$

for which they found the critical value for bypass transition to occur at $Re_Q > 200 - 280$ for a wide range of roughness shapes. In this formula

$$Q \approx \rho_k \, k \, D \, u_k \, F(\text{shape}) \tag{7.6}$$

is the estimated momentum deficit, where

$$F(\text{shape}) = \int_0^1 \eta \, w^*(\eta) \, d\eta, \tag{7.7}$$

with $\eta = y/k$, and $w^*(\eta) = w(y)/D$. In these equations S_{yz} is the projected frontal area, $w(y)$ is the local width of the roughness element and D is the diameter of the

Table 7.3. Computed roughness Reynolds numbers Re_{kk}, Re_{kw}, Re_Q of the different cases.

Case	$\boldsymbol{Re_{kk}}$	$\boldsymbol{Re_{kw}}$	$\boldsymbol{Re_Q}$
H-⊗-1.0-Ae5	984	728	618
H-○-1.0-Ae5	984	728	793
H-□-1.0-Ae5	984	728	793
H-◇-1.0-Ae5	984	728	758
H-△-1.0-Ae5	984	728	793
H-▽-1.0-Ae5	984	728	793
H-●-0.5-Ae5	127	119	135
H-⬠-1.0-Ae5	984	728	516

roughness element. Equation (7.5) can also be expressed as

$$Re_Q = Re_{kw}\ (D/k)^{1/2}\ F(\text{shape})\,, \tag{7.8}$$

which is the equation used to compute Re_Q in the current work. This criterion, being based on the (estimated) momentum deficit, takes into account to some degree the frontal shape of the roughness element.

The values of Re_{kk} , Re_{kw} and Re_Q for the cases currently under investigation are given in Table 7.3. The values of Re_{kk} and Re_Q are also placed in the transition maps in Figure 7.3, proposed by Redford et al. (2010) and Bernardini et al. (2012b). Note that the shaded region in these maps are the proposed supercritical regions, i.e. the cases that lie in this region are expected to go through transition, while the others do not. It can be seen that all cases, except the flat-top roughness element with smaller height $k = 0.5$, are expected to trip the boundary layer and induce transition.

7.3.2 Transition onset location

The location at which transition is said to occur is not unambiguous. Different parameters can be looked at to determine the location of the point where the transition process starts, such as the boundary layer intermittency or the skin friction coefficient c_f. It is commonly said that an abrupt rise in skin friction signifies the start of the transition from a laminar to a turbulent boundary layer. However, how to quantify this rise and how to set an appropriate threshold is not straightforward and changing these parameters could result in significantly different computed transition onset locations.

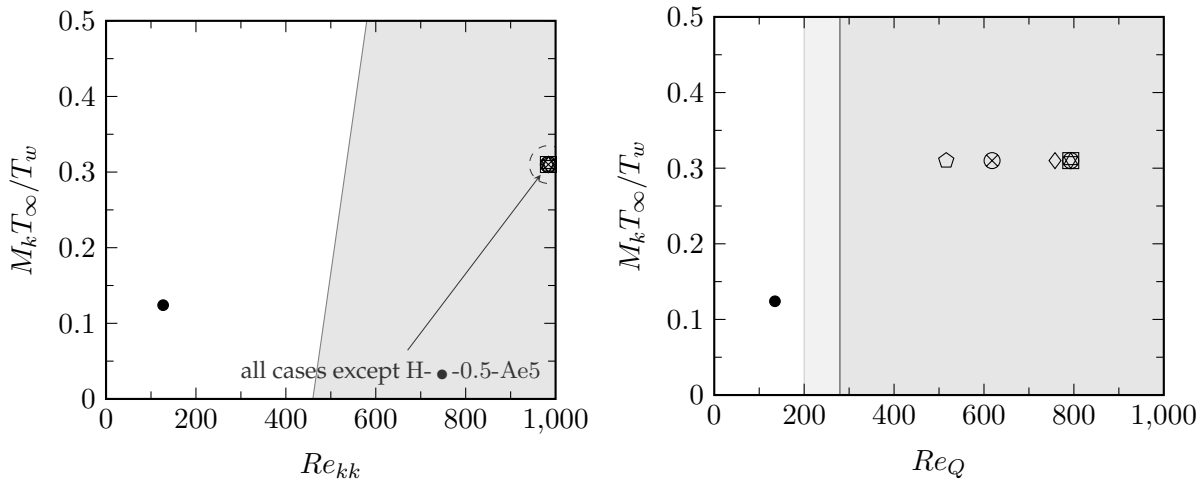

(a) (Redford et al., 2010) **(b)** (Bernardini et al., 2012b)

Figure 7.3. Transition maps proposed by Redford et al. (2010) and Bernardini et al. (2012b). The symbols in the maps denote the cases investigated in the current chapter.

In the current work, the transition onset location x_{tr} is defined as the first streamwise coordinate downstream of the roughness element such that the rate of increase of the skin friction coefficient, $c_f'(x) = \mathrm{d}\left(c_f\right)/\mathrm{d}x$, is larger than (or equal to) 2% of the value of the local skin friction coefficient $c_f(x)$, i.e.

$$x_{tr} \coloneqq x \left| \frac{c_f'(x)}{c_f(x)} \geq 0.02 \right. , \tag{7.9}$$

for which the values are computed at the roughness centreline. This definition is chosen because it consistently gives a reasonable estimates for the start of the skin friction rise, determined visually by the skin friction plots in this section. This criterion does break down near the edges of flow reversal regions, where $c_f = 0$, however.

The skin friction coefficient along the domain centreline is plotted in Figure 7.4 for all cases with low (*quiet*) freestream disturbances (cases Ae5). The dashed line in this figure shows the skin friction for a flat plate without a roughness element, and the red diamond symbols indicate the transition onset location detected by the criterion in Equation (7.9). From Figure 7.4 it can be seen that only cases H-○-1.0-Ae5, H-□-1.0-Ae5, H-◇-1.0-Ae5, H-△-1.0-Ae5 and H-⬠-1.0-Ae5 trigger a clear transition to turbulence, while cases H-⊗-1.0-Ae5, H-▽-1.0-Ae5 and H-●-0.5-Ae5 remain laminar within the computational domain. This is unexpected, since only roughness with

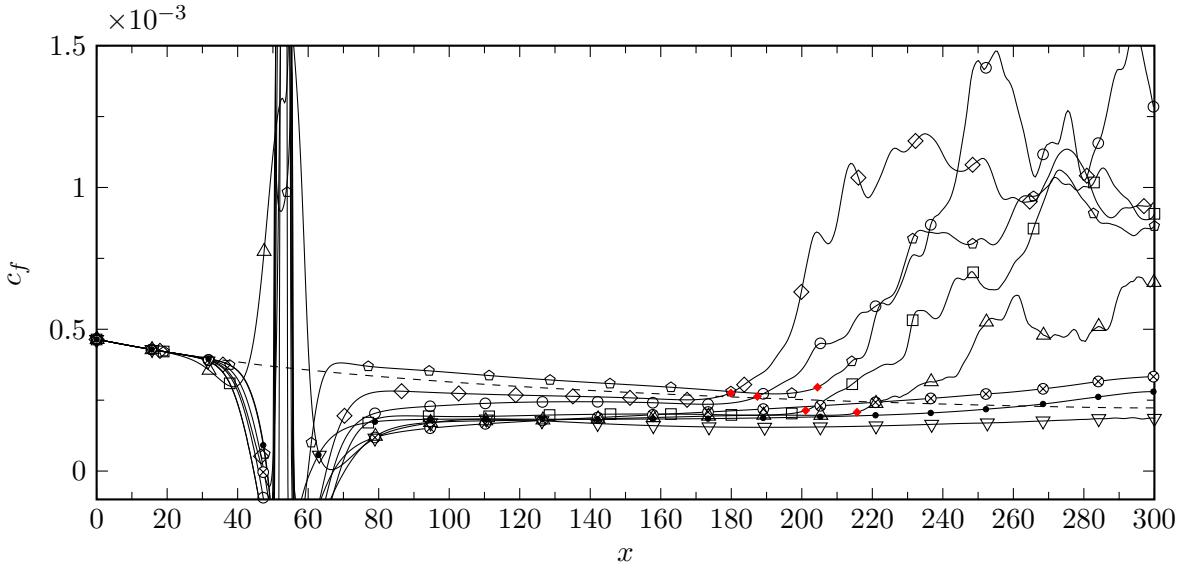

Figure 7.4. Skin friction coefficient along the domain centreline. Dashed line indicates the skin friction coefficient of a flat plate without roughness.

$k = 0.5$ (case H-●-0.5-Ae5) would be laminar according to the predictions based on Re_{kk} , Re_{kw} and Re_Q.

The transition to turbulence, or lack thereof, is also evident in Figure 7.5, which shows contours of the instantaneous temperature field (increasing temperature from yellow to red) at a location of $y = 1.0$ above the wall for all the *quiet* cases. From these contours, the generation of a hot low-speed streak flanked by colder high-speed streaks can be observed. Except for cases H-⊗-1.0-Ae5and H-●-0.5-Ae5, the streaks can be seen to become unstable and modulated at a certain location downstream of the roughness elements. Eventually the streaks break down and a turbulent wedge can be observed for the cases that go through transition. By comparing Figure 7.4 and Figure 7.5, it can be seen that the detected transition onset locations correspond to the locations where large streak modulations are visible, shortly before the breakdown to turbulence.

For the cases that go through transition, the transition onset location lies at approximately $x_{tr} = 180 - 215$, corresponding to $127 - 162$ inflow displacement thicknesses downstream of the roughness. The computed transition onset locations for all cases are summarised in Table 7.4. Although the difference between the different planform shapes is small, the diamond-shaped roughness element seems to be the most effective at inducing early transition, closely followed by the cylindrical flat-top

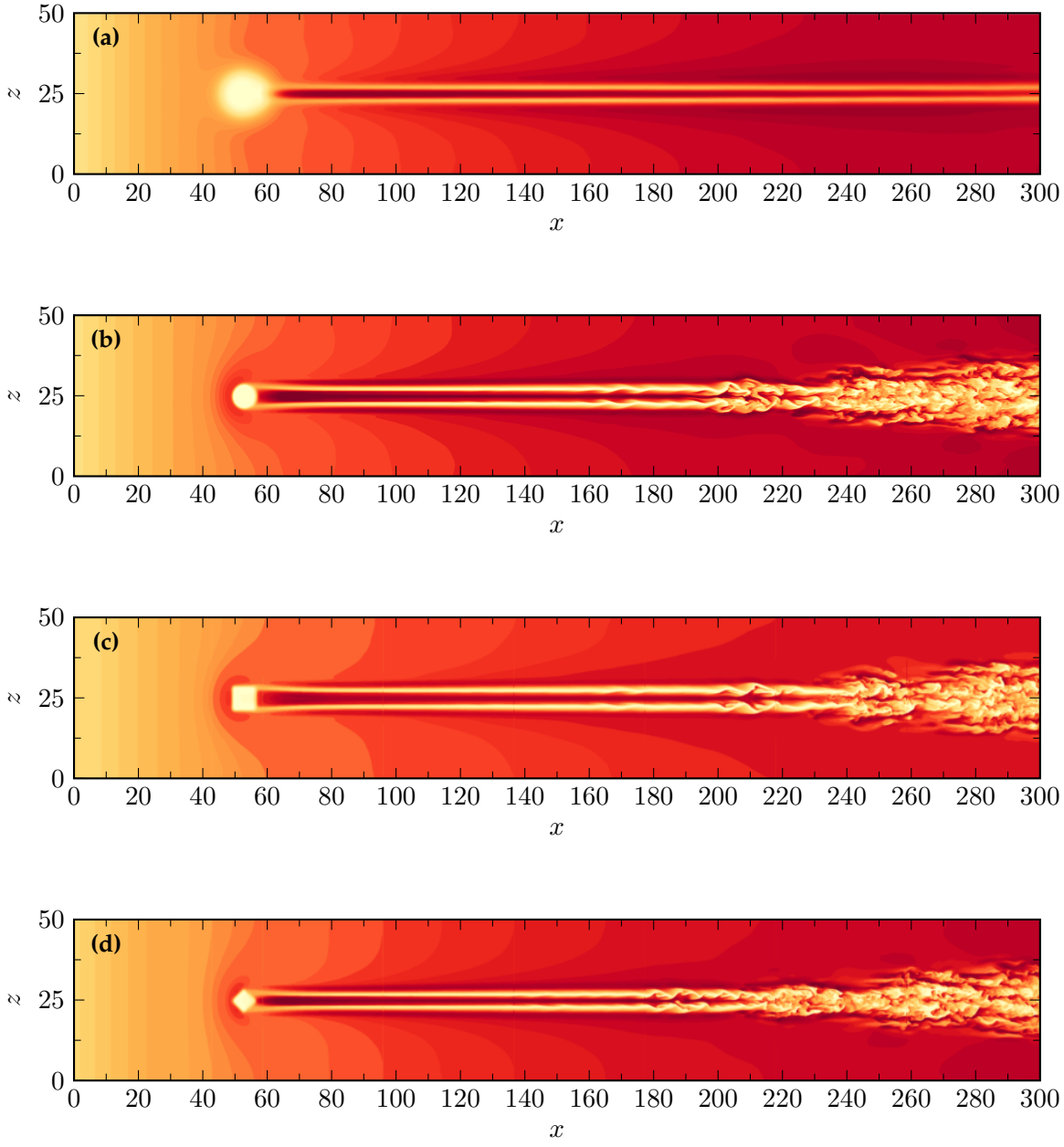

Figure 7.5. Contours of the instantaneous temperature field at a wall-normal location of $y = 1.0$. **(a)** H-⊗-1.0-Ae5; **(b)** H-○-1.0-Ae5; **(c)** H-□-1.0-Ae5; **(d)** H-◇-1.0-Ae5. (*Continued on next page*)

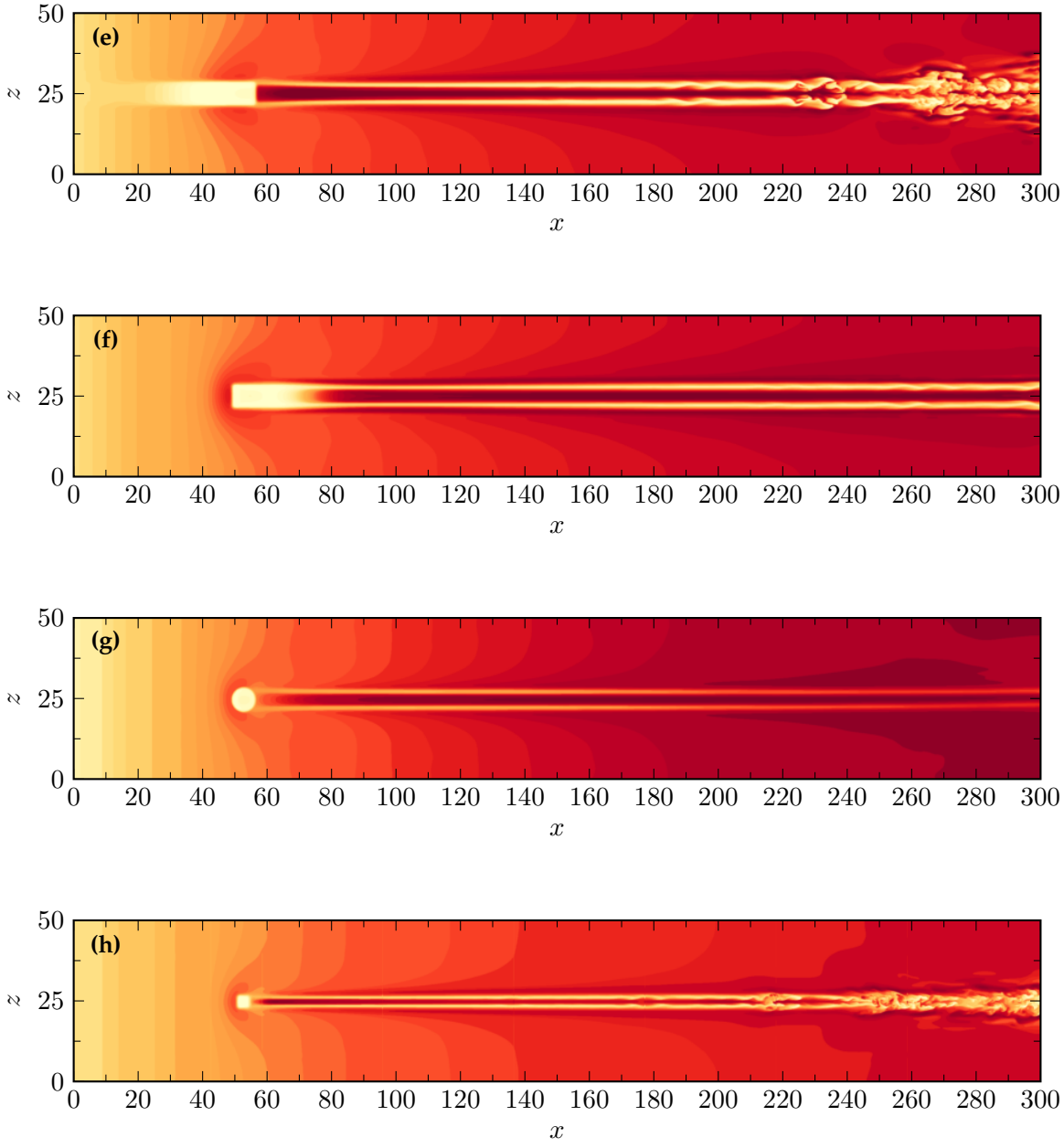

Figure 7.5 (cont.). Contours of the instantaneous temperature field at a wall-normal location of $y = 1.0$. **(e)** H-△-1.0-Ae5; **(f)** H-▽-1.0-Ae5; **(g)** H-●-0.5-Ae5; **(h)** H-⬠-1.0-Ae5

element. This seems to contradict the linear instability results presented in Chapter 5 *(Roughness Receptivity & Wake Instability)*, where it was shown that the instability growth rate behind the cylindrical roughness element was slightly larger than behind the diamond-shaped element. This apparent discrepancy will be explained in Section 7.4 further in this chapter. From Figure 7.4 it can be seen that the square flat-top element is less effective than the cylindrical or diamond-shaped elements at inducing early transition, which is in agreement with the linear instability results from Chapter 5. It is interesting to note that between these three cases, the case with the smallest aft recirculation region has the earliest transition point, while the case with the largest aft recirculation region has the transition onset point furthest downstream. The aspect ratio does not seem to have a large effect on transition, since the difference between transition onset locations of cases H-□-1.0-Ae5 and H-⬠-1.0-Ae5 is $\Delta x_{tr} \approx 3.3$. This is a very small difference, considering the method used for the transition detection. Ramping-up the square flat-top roughness element, i.e. as in case H-△-1.0-Ae5, does not seem to promote earlier transition but shows a small transition delay. However, even though the roughness element in case H-△-1.0-Ae5 is ramped-up, the recirculation region upstream of the square flat-top acts as an effective ramp. The recirculation actually has a steeper effective ramp angle, as can be deduced from Figure 7.1. Therefore, a ramped-up roughness element might still be more effective at promoting transition, but the effect would be very dependent on the actual shape and angle of the ramp.

As mentioned before, based on the transition criteria Re_{kk} and Re_Q, the smooth bump and ramp-down roughness elements were not expected to remain laminar. Even though the smooth bump has the same height and frontal projected area as the flat-top roughness elements, the less abrupt change in geometry and the absence of large recirculation regions yields a less unstable roughness wake and early transition is not induced. This seems in slight contradiction to the Mach 6 smooth bump simulations of Redford et al. (2010), who did see transition at a comparable Reynolds number. However, the acoustic disturbances they introduced in the freestream had an amplitude approximately 26 times larger than those in the current work. Since they also found a slight dependency of the transition onset location on the disturbance amplitude, the smooth bump in the current work might still induce transition within the computational domain in the presence of disturbances with higher amplitude. The effect of the freestream disturbance environment is investigated in the next section.

Table 7.4. Computed transition onset location x_{tr}, maximum streak amplitude A_{st}^{max} and growth rate σ downstream of the roughness elements.

Case	x_{tr}	A_{st}^{max}	$\sigma_{100<x<140}$
H-⊗-1.0-Ae5	–	0.315	0.045
H-⊗-1.0-Ae4	267.3	0.314	0.043
H-○-1.0-Ae5	187.4	0.585	0.111
H-○-1.0-Ae4	142.1	0.575	0.108
H-□-1.0-Ae5	201.1	0.546	0.101
H-◇-1.0-Ae5	179.9	0.561	0.106
H-●-0.5-Ae5	–	0.225	0.045
H-△-1.0-Ae5	215.6	0.548	0.092
H-▽-1.0-Ae5	–	0.437	0.048
H-⬠-1.0-Ae5	204.4	0.474	0.071

Especially the aft part of the roughness seems to be of great importance, demonstrated by the ramp-down case. The frontal profiles and the flow around the front part of the ramp-down and square flat-top roughness elements are the same, as demonstrated by Figures 7.1 and 7.2. However, the ramp-down at the aft section promotes attached flow and allows for the detached shear layer to spread and weaken, resulting in very different behavior of the roughness wake and subsequent transition. This observation suggests that the streamwise profile, and in particular the geometry of the aft section, is of significant importance in the prediction of roughness-induced transition. However, this characteristic is not taken into consideration in any of the commonly used engineering correlations.

7.3.3 Freestream disturbance environment

So far the effect of the freestream disturbance environment has not been discussed. Cases H-⊗-1.0-Ae4 and H-○-1.0-Ae4 have respectively a smooth bump and cylindrical flat-top roughness element, but have higher amplitude disturbances imposed in the freestream, i.e. a *noisier* freestream. The amplitude in these cases is one order of magnitude greater than the reference cases H-⊗-1.0-Ae5and H-○-1.0-Ae5.

By increasing the disturbance level in the freestream, the smooth bump does start transition near the end of the numerical domain, as can be seen in Figure 7.6. In the case of the flat-top roughness element, the transition onset location moves forward approximately 45 inflow displacement thicknesses to $x_{tr} = 142.1$. The amplitude of the disturbances in the noisy cases is still small enough to yield initially linear dis-

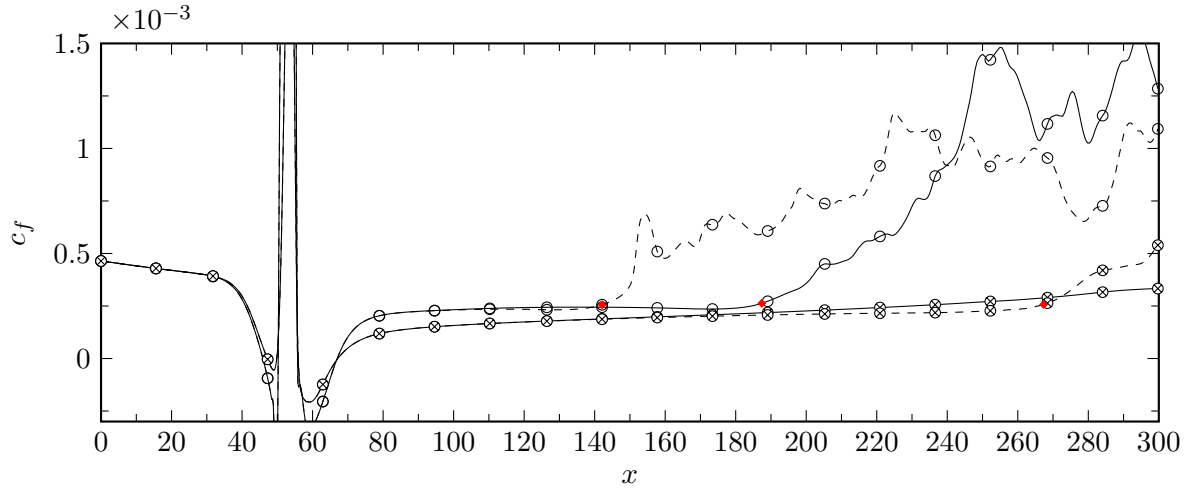

Figure 7.6. The effect of freestream disturbance level on the skin friction coefficient. Solid lines: *quiet* (Ae5); dashed lines: *noisy* (Ae4).

turbances. The receptivity process is also linear, such that an increase of disturbance amplitude in the freestream of one order of magnitude translates into an increase of disturbance amplitude in the boundary layer of one order magnitude larger. This can be seen in Figure 7.7, which shows the disturbance energy, defined as

$$e = \overline{u'u'} + \overline{v'v'} + \overline{w'w'}\,, \tag{7.10}$$

integrated over the boundary layer 99% thickness, evaluated at the roughness centre-line. Figure 7.7 shows that the growth rates of disturbances inside the boundary layer are not greatly affected by the increased freestream amplitude. The disturbances can be seen to grow exponentially and their growth rate is not greatly dependent on the freestream disturbance environment. The growth of instabilities is however very dependent on the roughness element, as the wake generated by the flat-top roughness element is clearly more unstable than the wake behind the smooth bump. After the region of exponential disturbance growth, the disturbance energy can be seen to reach a saturation limit for the cases going through transition. This saturation signifies the occurrence of non-linear interactions (De Tullio, 2013) which precede the breakdown to turbulence. It can thus be said that the transition onset location is shifted forward due to the linear receptivity process, and not due to a structurally modified transition process.

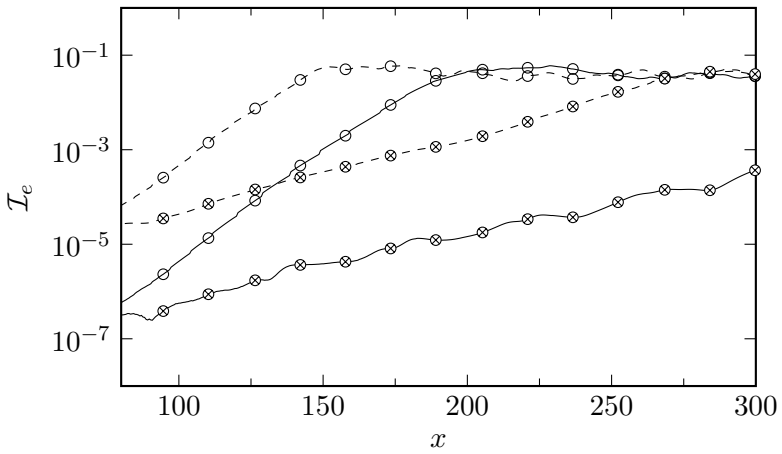

Figure 7.7. The effect of freestream disturbance level on the disturbance energy growth. Solid lines: *quiet* (Ae5); dashed lines: *noisy* (Ae4).

7.4 Instability growth in the wake

In order to develop better predictions of roughness-induced transition, the mechanisms governing the transition need to be better understood. A mechanism-based approach would need to take into account the freestream flow conditions, disturbance environment, and roughness shape. Since it has been shown here that the streamwise roughness profile, and in particular the aft section, can have a large influence on the transition process, the full three-dimensional roughness shape needs to be considered, a characteristic not regarded in the commonly-used transition prediction correlations. In this section the correlation of instability growth rate with several measures of the lift-up effect due to the roughness elements are considered.

7.4.1 Instability growth rate

Table 7.4 lists the exponential growth rates σ of the integrated disturbance energy $\mathcal{I}_e$. It should be noted that the computation of the growth rate is sensitive to the choice of evaluation location. The growth rate σ in Table 7.4 is computed as the average growth rate in the range $100 < x < 140$ in order to minimise this uncertainty.

It can be seen that the growth rates are highly dependent on the type of roughness element, and that even roughness elements with the same frontal profile (and thus the same values of Re_{kk}, Re_{kw} and Re_Q) can have significantly different growth rates. These roughness Reynolds numbers have been able to separate laminar and turbulent cases for simplified roughness geometries with various degrees of success,

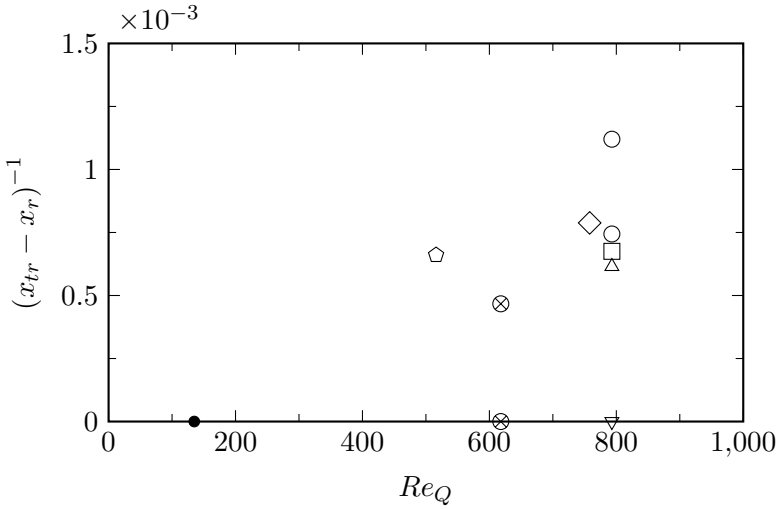

Figure 7.8. Inverse of the transition onset location plotted against the Reynolds number based on momentum deficit Re_Q.

but have a very limited applicability for general fully three-dimensional roughness shapes and cannot be used to predict the wake instability or subsequent location of transition. This is also evidenced by Figure 7.8, which shows the inverse of the transition length against Re_Q, and gives no clear indication of a useful correlation between the two.

From Table 7.4 it can be seen that the instability growth rate behind the cylindrical flat-top element is slightly greater than behind the diamond-shaped element. This confirms the linear instability growth results presented in Chapter 5 *(Roughness Receptivity & Wake Instability)*. The observation earlier in this chapter that the diamond-shaped roughness element has an earlier transition onset location than the cylindrical flat-top is explained by the fact that in the near-field of the diamond-shaped roughness element, instabilities are more amplified than near the cylindrical element.

7.4.2 Prediction of growth rate and transition

An important step in the development of a better roughness-induced transition prediction tool would be if a relation could be found between the disturbance growth rate and a macroscopic feature of the roughness element or the flow in the vicinity of the roughness. All the empirical roughness Reynolds numbers fail this test, since it has been shown that cases with the same value of Re_{kk}, Re_{kw} and Re_Q can have

entirely different instability growth rates and transition onset locations.

If a transient growth scenario is considered as the initial mechanism behind the transition induced by a three-dimensional isolated roughness element, a relation between the disturbance growth rate and transient growth characteristics is expected. Counter-rotating vortices generated behind the roughness element transport low-momentum fluid away from the wall at the centre and high-momentum fluid towards the wall at the sides of the roughness wake. This lift-up mechanism, proposed by Landahl (1980), generates streamwise streaks that initially grow algebraically in strength followed by a slow decay due to viscous dissipation. This process is transient growth, and has been studied extensively in the context of optimal growth and bypass transition, as reviewed by Reshotko (2001).

The generation of low- and high-momentum streaks has been observed behind the roughness elements for all the cases presented in the current work. Figure 7.9a shows the exponential disturbance growth rate plotted against the peak streamwise vorticity downstream of the roughness centre, and shows that stronger streamwise vorticity generated by the roughness element leads to a stronger lift-up effect and subsequently a larger disturbance growth rate. The horizontal line separating the shaded region in this figure indicates the linear growth rate for a flat plate boundary layer without a roughness element. The effect of counter-rotating streamwise vortices on lift-up is clearly dependent on the vorticity magnitude, but may also depend on the distance between the vortices, which is linked to the roughness element width. In contrast, the amplitude of the streak results directly from the lift-up mechanism and therefore is a metric that might give a trend independent of the roughness element geometry.

The amplitude of a streak may be defined, using the formulation of Andersson et al. (2001), as

$$A_{st} \coloneqq \frac{1}{2}\left[\max_{y,z}\{u-u_b\} - \min_{y,z}\{u-u_b\}\right], \tag{7.11}$$

where u_b is the undisturbed laminar base flow. An alternative integral-based streak amplitude definition can be used, similar to the definition by Shahinfar et al. (2013), i.e.

$$A_{st}^{\text{int}} \coloneqq \frac{1}{W}\int_{z=0}^{L_z}\int_{y=0}^{L_y} |u-u_b| \,\mathrm{d}y\,\mathrm{d}z\,. \tag{7.12}$$

Shahinfar et al. (2013) studied spanwise periodic streaks generated by an array of vortex generators. In their original definition, the integrated streak amplitude was normalised by the spanwise wavelength such that the spanwise extent of the streaks

has an effect on the integral streak amplitude. The notion behind this normalisation is that the integral streak amplitude becomes related to the spanwise shear stress between the streaks. By normalising the current integral streak amplitude definition in (7.12) by the roughness width W, a distinction can be made between cases with different roughness element widths.

It has been found that the latter definition does not work well for the non-periodic roughness wakes in the current work. Due to the increasing spanwise extent of the roughness wake going downstream, the integral streak amplitude increases monotonically up to the point of streak breakdown, even when the velocity difference of the streaks (and the spanwise shear stress) decreases. Therefore, the streak amplitude definition of Andersson et al. (2001) has been used.

Andersson et al. (2001) investigated secondary instabilities of streaks in an incompressible boundary layer and found that streak instability occurs above a critical streak amplitude. They also showed a direct relationship between streak amplitude and growth rate of the streak instabilities (with non-zero streamwise wavenumber). Table 7.4 lists the maximum streak amplitudes that are reached behind the roughness elements for all cases, and the computed growth rates are plotted against these values in Figure 7.9b. From this figure, it is clear that a direct relationship between maximum streak amplitude and averaged growth rate σ can be observed, and that this correlation (at streak amplitudes greater than 0.4) seems to be stronger than the trend between streamwise vorticity and growth rate. A linear regression line of the data points with $A_{st} > 0.4$ is plotted in Figure 7.9b, and is defined as

$$\sigma = 0.416\, A_{st}^{max} - 0.130\,. \tag{7.13}$$

A minor dependency of the peak streak amplitude on the freestream disturbance level is apparent in Table 7.4 for cases H-○-1.0-Ae4 and H-○-1.0-Ae5. It can be observed that the disturbance energy for *noisy* case H-○-1.0-Ae4 reaches relatively high levels, i.e. $\mathcal{O}\,(1\%)$, at the location of peak streak amplitude in the corresponding *quiet* case H-○-1.0-Ae5. Non-linearities arise at these high levels and case the streak to break down before the peak streak amplitude, obtained in the *quiet* case, is reached.

If the trend between peak streak amplitude and average growth rate holds for a large range of roughness shapes and freestream parameters, the exponential growth rate downstream of the roughness element could be predicted by accurately determining the base flow and the resulting streak amplitude downstream. The transition onset

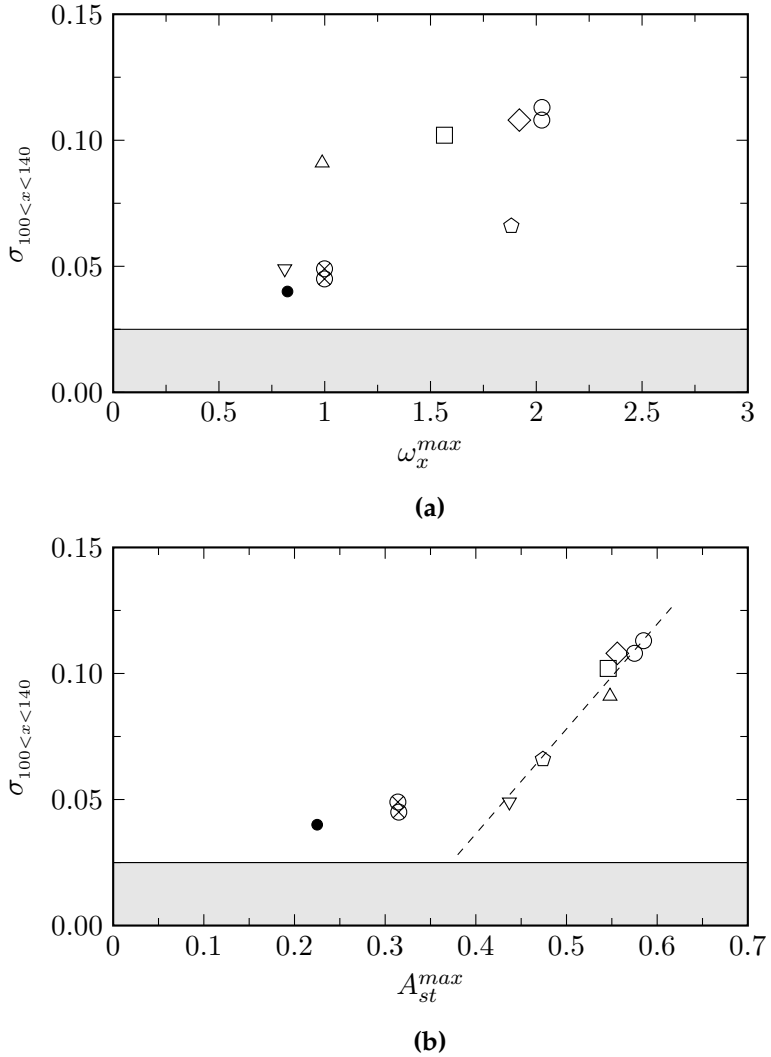

Figure 7.9. Growth rate of integrated disturbance energy plotted against **(a)** the peak streamwise vorticity and **(b)** the maximum streak amplitude reached downstream of the roughness elements.

location would then be able to be predicted using an N-factor-type estimation — similar to the N-factor prediction of boundary layer transition based on stability analysis. An accurate description of this relation would then provide a mechanism-based prediction of roughness-induced transition without the need for stability analysis.

7.5 Summary of results

In this chapter the full transition process from a laminar to a turbulent boundary layer due to the presence of an isolated roughness element has been investigated. The effects of the different roughness shapes on the linear instability of the wake, as discussed in Chapter 5 *(Roughness Receptivity & Wake Instability)*, have been found to extend to the non-linear instability growth and subsequent transition onset. The frontal roughness profile has a large influence on the transition onset: the flat-top elements induce transition while the smooth bump does not. The planform shape has a weak effect however, and the location of transition does not differ greatly between the cylindrical, square and diamond-shaped elements. The upward ramp has a slight stabilising effect, similarly to the result in Chapter 5, but this might be very dependent on the actual ramp angle. The downward ramp greatly stabilises the transition process and no transition has been observed behind this roughness element. It was found that the roughness width (or aspect ratio) has an insignificant effect on the transition onset location for the case studied here.

The amplitude of the freestream disturbance environment has been varied to examine its effect on the transition onset. The disturbance amplitude for the *noisy* environment has been taken one order of magnitude greater than the corresponding baseline *quiet* environment. The amplitude is still small enough to yield initially linear instabilities however. Due to the linear receptivity process it has been found that an increase of the disturbance amplitude in the freestream of one order of magnitude translates into an increase of the disturbance amplitude in the boundary layer of one order magnitude. An upstream shift of the transition onset location has been observed due to the *noisy* freestream, although the growth rate of the boundary layer instabilities is not greatly affected by the change in freestream disturbance amplitude. It can thus be said that the transition is promoted due to the linear receptivity process, and not due to a structurally modified transition process.

The engineering correlations commonly used to predict whether or not a roughness element induces transition are mainly based on the roughness height and, only

recently, the frontal profile. However, they do not take into account the full three-dimensional roughness shape. As we have observed that transition can be delayed or even suppressed by a downward ramp or slowly-varying aft geometry, the full three-dimensional shape, including the streamwise profile, needs to be considered. Also the disturbance environment needs to be taken into account if one wants to define a solid transition criterion. In this chapter, a direct relation has been found between the peak amplitude of the streamwise streaks generated behind the roughness element and the averaged exponential growth rate of the disturbances in the wake, which could be a first step towards a mechanism-based approach of roughness-induced transition.

Chapter 8

Conclusions & Future Work

8.1 Conclusions of the current work

In the current work the effects of isolated roughness elements on the instability and subsequent transition behaviour of a Mach 6.0 boundary layer has been studied. The principal focus has been on quantifying the influence of the three-dimensional roughness shape, i.e. frontal profile, planform shape, upward/downward ramps, and the external forcing on the stability of the roughness wake and the onset of transition to turbulence. It is therefore a logical extension to the dissertation of De Tullio (2013), who studied the transition induced by a single square roughness element at the same Mach number. The investigations have been performed numerically with direct numerical simulations, using the in-house DNS code `SBLI`, and linear stability analysis. For this purpose and in the scope of this dissertation, a new code (`COMPASS` - ***Comp****ressible* ***A****nalysis-of-****S****tability* ***S****uite*) has been developed that is able to perform local, bi-local and tri-global stability analysis of the compressible linearised Navier-Stokes equations. The code has been validated extensively (for local and bi-local stability analysis) from subsonic to hypersonic velocities.

This work comprises of three main results chapters: the receptivity of a boundary layer near roughness elements and the instability of roughness wakes has been discussed in Chapter 5 *(Roughness Receptivity & Wake Instability)*; the applicability of linear stability theory to roughness wakes has been examined in Chapter 6 *(Stability Analysis of Roughness Wakes)*; the full non-linear transition process, induced by different roughness elements, has been investigated in Chapter 7 *(Roughness-induced Transition)*.

Receptivity to different forcing types From the results on the receptivity study near a cylindrical flat-top roughness element, it has been found that acoustic disturbances are the most effective at exciting unstable boundary layer and wake modes. The instability behaviour of the wake has been shown to be qualitatively the same when imposing entropy fluctuations instead of acoustic forcing, but the amplitude of the disturbances are one order of magnitude smaller. By introducing vortical disturbances, the boundary layer instabilities were found to grow more slowly. A different receptivity mechanism seems to be active for this type of forcing. De Tullio (2013) reported similar results for a sharp-edged square roughness element, demonstrating that the interaction between the different disturbances and the roughness wake is independent of the structure of the wake, and in extension the shape of the roughness element. In the other studies of this dissertation, acoustic disturbances were chosen as forcing because of the enhanced receptivity compared to entropy and vorticity fluctuations.

Roughness wake generation and instability The flow encountering a roughness element is characterised by strong streamwise vorticity. The counter-rotating vortices behind the roughness element transport low-momentum fluid away from the wall at the roughness centreline and high-momentum fluid towards the wall away from the roughness centreline. This process results in a low-velocity streak at the roughness centreline flanked by high-velocity streaks, which comprise the roughness wake. High shear stress is present between and on top of these streaks, which can sustain convective wake instabilities.

The frontal profile of the roughness element has a large influence on this process and the resulting wake instability. While a large spectrum of unstable wake modes have been found in the wake of a flat-top element, a smooth bump (with the same maximum height) was found to act mainly as a disturbance amplifier without significantly increasing the growth rate of disturbances in the wake. The structure and strength of the roughness wake was found to be only weakly affected by the roughness planform shape. Both cylindrical, square and diamond-shaped roughness elements were studied. It was concluded that the most unstable wake mode is the same for all three cases, with similar growth rates. The most unstable wake mode was observed to be of a varicose-lateral nature (using the terminology of De Tullio and Sandham (2015), i.e. most active in the lateral and top shear layers between the streamwise streaks. The cylindrical roughness element was found to have the largest overall disturbance growth near the end of the domain, closely followed by

the diamond-shaped and finally the square element. In order to study the effect of the streamwise roughness profile, an upward or downward ramp was attached to the square roughness element. The presence of the upward ramp was found to have a relatively small effect on the roughness wake. The main effect of the upward ramp is the prolonged instability region of the varicose-centre mode, a mode active near the wall at the roughness centreline with strong similarities to the Mack mode. However, only a small decrease in overall disturbance growth of approximately 10% has been observed, due to the fact that the most unstable varicose-lateral mode is only slightly damped. The downward ramp at the aft section of the roughness element has a crucial effect on the resulting wake instability however. The slowly-varying geometry of the ramp completely avoids downstream separation, which allows the detached shear layer, generated over the top of the roughness element, to spread out and weaken significantly. Even though the frontal profile shape and roughness height are the same, the presence of the downward ramp results in a much less unstable wake. The overall disturbance amplitude at the end of the domain is approximately 30% lower than in the case without the downward ramp.

Applicability of linear stability theory The direct numerical simulations that were performed for this wake instability study are very computationally expensive and are impossible to run without access to a supercomputing facility. The applicability of linear stability analysis to predict the wake instability behaviour has been investigated, since it would allow for much less expensive computations. The stability analysis of a roughness wake has been performed using `COMPASS` by running bi-local stability computations of cross-flow planes taken in the wake of a roughness element from the direct numerical simulations. It was found that bi-local stability analysis is able to predict the frequency at which the most unstable mode is active, and also the instability mode shapes can be accurately resolved in most cases. However, the growth rate of these instability modes is incorrectly computed and generally strongly underpredicted. Therefore, bi-local stability analysis on its own might not be the appropriate tool to estimate the instability of the roughness wake. The results of the stability analysis demonstrate that non-parallel effects, which are neglected by the bi-local stability analysis, are of crucial importance in the accurate determination of the instability growth. It is therefore suggested that tools such as tri-global stability analysis and/or three-dimensional PSE could give an improved quantitative prediction of the wake instability.

Effect of roughness shape on transition onset The full non-linear transition process from a laminar to a turbulent boundary layer induced by roughness elements has been studied using direct numerical simulations, with a main focus on the effect of the three-dimensional roughness shape on the transition onset. Also the influence of freestream disturbance environment, i.e. a *quiet* or *noisy* environment, on the transition has been investigated. It has been found that the effects of the different roughness shapes on the linear instability of the wake extend to the non-linear instability growth and subsequent transition onset. The frontal profile has a large influence on the transition onset. The smooth bump does not induce transition while the cylindrical flat-top element with the same maximum height does. The planform shape has a weak effect, but the streamwise roughness profile is of great importance. While the upward ramp slightly delays the transition onset, behaviour which might be dependent on the actual ramp angle, the downward ramp highly stabilises the transition process and no transition is observed behind the ramp-down roughness element. The amplitude of the freestream disturbance environment has been found to have a significant effect on the transition onset location, with a *noisy* freestream promoting early transition. It has been found that the upstream shift in transition onset is due to the linear receptivity process, resulting in a higher initial amplitude of the boundary layer disturbances for stronger freestream disturbances, and not due to a structurally modified transition process.

Mechanism-based transition prediction Transition criteria based on simple engineering correlations are commonly used to determine a priori whether or not a roughness element will induce transition to turbulence. The commonly used criteria are mainly based on the roughness height, but do not take into account the full three-dimensional roughness shape or the freestream environment. Because it has been shown that the three-dimensional shape and the freestream disturbance environment can significantly influence the transition behaviour — promoting, delaying or even suppressing — it needs to be considered in an exhaustive transition criterion. However, such a criterion would still be based on correlations and have no background in the actual physical mechanisms of transition. Therefore a mechanism-based theory of roughness-induced transition is highly desirable.

A direct relationship has been observed between the peak amplitude of the streamwise streaks generated behind the roughness elements and the averaged exponential growth rate of the disturbances in the wake. Such a relationship has not been observed with any of the transition criteria, roughness parameters or streamwise

vorticity magnitude. Although this relationship, if confirmed for a larger number of cases, does not provide an a priori tool to predict the transition behaviour, since it needs the determination of the streak amplitude, it could prove to be an important first step towards a mechanism-based approach.

8.2 Suggestions for future work

The current work has touched upon some of the important factors in the stability of roughness wakes and subsequent roughness-induced transition, but some aspects remain unanswered. An extension and/or continuation of this work can be performed in the following ways:

(i) Since it has been suggested that non-parallel effects are not negligible in the instability of roughness wakes, the stability code `COMPASS` can be extended to include (three-dimensional) PSE. Tri-global stability analysis is technically already possible, but requires the implementation of suitable boundary conditions in the streamwise direction. It would then be possible to perform the stability analysis of roughness wakes without neglecting the non-parallel effects and assess its accuracy and/or applicability.

(ii) An extensive assessment of the observed relationship between the peak streak amplitude and the exponential growth rate of wake disturbances should be performed to validate and/or correct it for a larger number of roughness cases and flow parameters.

(iii) A mechanism-based approach of roughness-induced instability and transition, for example based on the observed relation, which takes into account three-dimensional roughness shape and freestream disturbance environment, is highly desirable .

(iv) The effects of compressibility and wall temperature of the instability of streamwise streaks could be investigated. Streak instability studies have been performed for incompressible flow (Andersson et al., 2001; Brandt et al., 2003, among others), but to the author's knowledge no such studies exist for compressible flows. This could support the development of such an approach.

(v) The global response of compressible boundary layers could be studied in the framework of optimal growth, to investigate the effects of compressibility and wall temperature on the generation of streamwise streaks by a transient growth process. This could be performed with `COMPASS` by analysis of the linearised Navier-Stokes equations.

Appendix A

Linearised Compressible Navier-Stokes Equations

The linearised form of the full three-dimensional compressible Navier-Stokes expressed in primitive variables, following the small amplitude *ansatz* of (3.2) discussed in Chapter 3 *(COMPASS: Compressible Stability Analysis)*, are given in this chapter.

For brevity and clarity, the variable arguments (x, y, z) and (x, y, z, t) are omitted in the following equations, i.e.

$$\begin{aligned}\tilde{\bullet} &:= \tilde{\bullet}(x, y, z, t) \\ \bar{\bullet} &:= \bar{\bullet}(x, y, z) \quad .\end{aligned}$$

Continuity equation

$$\begin{aligned}\frac{\partial\tilde{\rho}}{\partial t} + \bar{\rho}\frac{\partial\tilde{u}}{\partial x} + \tilde{u}\frac{\partial\bar{\rho}}{\partial x} + \bar{u}\frac{\partial\tilde{\rho}}{\partial x} + \tilde{\rho}\frac{\partial\bar{u}}{\partial x} + \bar{\rho}\frac{\partial\tilde{v}}{\partial y} + \tilde{v}\frac{\partial\bar{\rho}}{\partial y} + \bar{v}\frac{\partial\tilde{\rho}}{\partial y} + \tilde{\rho}\frac{\partial\bar{v}}{\partial y} \\ + \bar{\rho}\frac{\partial\tilde{w}}{\partial z} + \tilde{w}\frac{\partial\bar{\rho}}{\partial z} + \bar{w}\frac{\partial\tilde{\rho}}{\partial z} + \tilde{\rho}\frac{\partial\bar{w}}{\partial z} = 0 \qquad \text{(A.1)}\end{aligned}$$

Streamwise momentum conservation

$$\begin{aligned}&\tilde{\rho}\frac{\partial\bar{u}}{\partial t} + \bar{\rho}\frac{\partial\tilde{u}}{\partial t} + \tilde{\rho}\bar{u}\frac{\partial\bar{u}}{\partial x} + \bar{\rho}\tilde{u}\frac{\partial\bar{u}}{\partial x} + \bar{\rho}\bar{u}\frac{\partial\tilde{u}}{\partial x} + \tilde{\rho}\bar{v}\frac{\partial\bar{u}}{\partial y} + \bar{\rho}\tilde{v}\frac{\partial\bar{u}}{\partial y} + \bar{\rho}\bar{v}\frac{\partial\tilde{u}}{\partial y} + \tilde{\rho}\bar{w}\frac{\partial\bar{u}}{\partial z} + \bar{\rho}\tilde{w}\frac{\partial\bar{u}}{\partial z} + \bar{\rho}\bar{w}\frac{\partial\tilde{u}}{\partial z} \\ &= -\frac{1}{\gamma M^2}\left(\bar{\rho}\frac{\partial\tilde{T}}{\partial x} + \tilde{\rho}\frac{\partial\bar{T}}{\partial x}\right) + \frac{\bar{\mu}}{Re}\left[\frac{4}{3}\frac{\partial^2\tilde{u}}{\partial x^2} + \frac{\partial^2\tilde{u}}{\partial y^2} + \frac{\partial^2\tilde{u}}{\partial z^2} + \frac{1}{3}\frac{\partial^2\tilde{v}}{\partial x\partial y} + \frac{1}{3}\frac{\partial^2\tilde{w}}{\partial x\partial z}\right]\end{aligned}$$

$$
\begin{aligned}
&+\frac{1}{Re}\frac{\mathrm{d}\bar{\mu}}{\mathrm{d}\bar{T}}\tilde{T}\left[\frac{4}{3}\frac{\partial^2\bar{u}}{\partial x^2}+\frac{\partial^2\bar{u}}{\partial y^2}+\frac{\partial^2\bar{u}}{\partial z^2}+\frac{1}{3}\frac{\partial^2\bar{v}}{\partial x\partial y}+\frac{1}{3}\frac{\partial^2\bar{w}}{\partial x\partial z}\right]\\
&+\frac{1}{Re}\frac{\mathrm{d}\bar{\mu}}{\mathrm{d}\bar{T}}\frac{\partial\bar{T}}{\partial x}\left[\frac{4}{3}\frac{\partial\tilde{u}}{\partial x}-\frac{2}{3}\frac{\partial\tilde{v}}{\partial y}-\frac{2}{3}\frac{\partial\tilde{w}}{\partial z}\right]+\frac{1}{Re}\frac{\mathrm{d}\bar{\mu}}{\mathrm{d}\bar{T}}\frac{\partial\bar{T}}{\partial y}\left[\frac{\partial\tilde{v}}{\partial x}+\frac{\partial\tilde{u}}{\partial y}\right]+\frac{1}{Re}\frac{\mathrm{d}\bar{\mu}}{\mathrm{d}\bar{T}}\frac{\partial\bar{T}}{\partial z}\left[\frac{\partial\tilde{w}}{\partial x}+\frac{\partial\tilde{u}}{\partial z}\right]\\
&+\frac{1}{Re}\left(\frac{\mathrm{d}\bar{\mu}}{\mathrm{d}\bar{T}}\frac{\partial\tilde{T}}{\partial x}+\left(\frac{\mathrm{d}^2\bar{\mu}}{\mathrm{d}\bar{T}^2}\frac{\partial\bar{T}}{\partial x}+\frac{\mathrm{d}\bar{\mu}}{\mathrm{d}\bar{T}}\right)\tilde{T}\right)\left[\frac{4}{3}\frac{\partial\bar{u}}{\partial x}-\frac{2}{3}\frac{\partial\bar{v}}{\partial y}-\frac{2}{3}\frac{\partial\bar{w}}{\partial z}\right]\\
&+\frac{1}{Re}\left(\frac{\mathrm{d}\bar{\mu}}{\mathrm{d}\bar{T}}\frac{\partial\tilde{T}}{\partial y}+\left(\frac{\mathrm{d}^2\bar{\mu}}{\mathrm{d}\bar{T}^2}\frac{\partial\bar{T}}{\partial y}+\frac{\mathrm{d}\bar{\mu}}{\mathrm{d}\bar{T}}\right)\tilde{T}\right)\left[\frac{\partial\bar{v}}{\partial x}+\frac{\partial\bar{u}}{\partial y}\right]\\
&+\frac{1}{Re}\left(\frac{\mathrm{d}\bar{\mu}}{\mathrm{d}\bar{T}}\frac{\partial\tilde{T}}{\partial z}+\left(\frac{\mathrm{d}^2\bar{\mu}}{\mathrm{d}\bar{T}^2}\frac{\partial\bar{T}}{\partial z}+\frac{\mathrm{d}\bar{\mu}}{\mathrm{d}\bar{T}}\right)\tilde{T}\right)\left[\frac{\partial\bar{w}}{\partial x}+\frac{\partial\bar{u}}{\partial z}\right]
\end{aligned}
\tag{A.2}
$$

Wall-normal momentum conservation

$$
\begin{aligned}
&\tilde{\rho}\frac{\partial\bar{v}}{\partial t}+\bar{\rho}\frac{\partial\tilde{v}}{\partial t}+\tilde{\rho}\bar{u}\frac{\partial\bar{v}}{\partial x}+\bar{\rho}\tilde{u}\frac{\partial\bar{v}}{\partial x}+\bar{\rho}\bar{u}\frac{\partial\tilde{v}}{\partial x}+\tilde{\rho}\bar{v}\frac{\partial\bar{v}}{\partial y}+\bar{\rho}\tilde{v}\frac{\partial\bar{v}}{\partial y}+\bar{\rho}\bar{v}\frac{\partial\tilde{v}}{\partial y}+\tilde{\rho}\bar{w}\frac{\partial\bar{v}}{\partial z}+\bar{\rho}\tilde{w}\frac{\partial\bar{v}}{\partial z}+\bar{\rho}\bar{w}\frac{\partial\tilde{v}}{\partial z}\\
&=-\frac{1}{\gamma M^2}\left(\bar{\rho}\frac{\partial\tilde{T}}{\partial y}+\tilde{\rho}\frac{\partial\bar{T}}{\partial y}\right)+\frac{\bar{\mu}}{Re}\left[\frac{4}{3}\frac{\partial^2\tilde{v}}{\partial y^2}+\frac{\partial^2\tilde{v}}{\partial x^2}+\frac{\partial^2\tilde{v}}{\partial z^2}+\frac{1}{3}\frac{\partial^2\tilde{u}}{\partial x\partial y}+\frac{1}{3}\frac{\partial^2\tilde{w}}{\partial y\partial z}\right]\\
&+\frac{1}{Re}\frac{\mathrm{d}\bar{\mu}}{\mathrm{d}\bar{T}}\tilde{T}\left[\frac{4}{3}\frac{\partial^2\bar{v}}{\partial y^2}+\frac{\partial^2\bar{v}}{\partial x^2}+\frac{\partial^2\bar{v}}{\partial z^2}+\frac{1}{3}\frac{\partial^2\bar{u}}{\partial x\partial y}+\frac{1}{3}\frac{\partial^2\bar{w}}{\partial y\partial z}\right]\\
&+\frac{1}{Re}\frac{\mathrm{d}\bar{\mu}}{\mathrm{d}\bar{T}}\frac{\partial\bar{T}}{\partial x}\left[\frac{\partial\tilde{v}}{\partial x}+\frac{\partial\tilde{u}}{\partial y}\right]+\frac{1}{Re}\frac{\mathrm{d}\bar{\mu}}{\mathrm{d}\bar{T}}\frac{\partial\bar{T}}{\partial y}\left[\frac{4}{3}\frac{\partial\tilde{v}}{\partial y}-\frac{2}{3}\frac{\partial\tilde{u}}{\partial x}-\frac{2}{3}\frac{\partial\tilde{w}}{\partial z}\right]+\frac{1}{Re}\frac{\mathrm{d}\bar{\mu}}{\mathrm{d}\bar{T}}\frac{\partial\bar{T}}{\partial z}\left[\frac{\partial\tilde{w}}{\partial y}+\frac{\partial\tilde{v}}{\partial z}\right]\\
&+\frac{1}{Re}\left(\frac{\mathrm{d}\bar{\mu}}{\mathrm{d}\bar{T}}\frac{\partial\tilde{T}}{\partial x}+\left(\frac{\mathrm{d}^2\bar{\mu}}{\mathrm{d}\bar{T}^2}\frac{\partial\bar{T}}{\partial x}+\frac{\mathrm{d}\bar{\mu}}{\mathrm{d}\bar{T}}\right)\tilde{T}\right)\left[\frac{\partial\bar{v}}{\partial x}+\frac{\partial\bar{u}}{\partial y}\right]\\
&+\frac{1}{Re}\left(\frac{\mathrm{d}\bar{\mu}}{\mathrm{d}\bar{T}}\frac{\partial\tilde{T}}{\partial y}+\left(\frac{\mathrm{d}^2\bar{\mu}}{\mathrm{d}\bar{T}^2}\frac{\partial\bar{T}}{\partial y}+\frac{\mathrm{d}\bar{\mu}}{\mathrm{d}\bar{T}}\right)\tilde{T}\right)\left[\frac{4}{3}\frac{\partial\bar{v}}{\partial y}-\frac{2}{3}\frac{\partial\bar{u}}{\partial x}-\frac{2}{3}\frac{\partial\bar{w}}{\partial z}\right]\\
&+\frac{1}{Re}\left(\frac{\mathrm{d}\bar{\mu}}{\mathrm{d}\bar{T}}\frac{\partial\tilde{T}}{\partial z}+\left(\frac{\mathrm{d}^2\bar{\mu}}{\mathrm{d}\bar{T}^2}\frac{\partial\bar{T}}{\partial z}+\frac{\mathrm{d}\bar{\mu}}{\mathrm{d}\bar{T}}\right)\tilde{T}\right)\left[\frac{\partial\bar{w}}{\partial y}+\frac{\partial\bar{v}}{\partial z}\right]
\end{aligned}
\tag{A.3}
$$

Spanwise momentum conservation

$$
\begin{aligned}
&\tilde{\rho}\frac{\partial\bar{w}}{\partial t}+\bar{\rho}\frac{\partial\tilde{w}}{\partial t}+\tilde{\rho}\bar{u}\frac{\partial\bar{w}}{\partial x}+\bar{\rho}\tilde{u}\frac{\partial\bar{w}}{\partial x}+\bar{\rho}\bar{u}\frac{\partial\tilde{w}}{\partial x}+\tilde{\rho}\bar{v}\frac{\partial\bar{w}}{\partial y}+\bar{\rho}\tilde{v}\frac{\partial\bar{w}}{\partial y}+\bar{\rho}\bar{v}\frac{\partial\tilde{w}}{\partial y}+\tilde{\rho}\bar{w}\frac{\partial\bar{w}}{\partial z}+\bar{\rho}\tilde{w}\frac{\partial\bar{w}}{\partial z}+\bar{\rho}\bar{w}\frac{\partial\tilde{w}}{\partial z}\\
&=-\frac{1}{\gamma M^2}\left(\bar{\rho}\frac{\partial\tilde{T}}{\partial z}+\tilde{\rho}\frac{\partial\bar{T}}{\partial z}\right)+\frac{\bar{\mu}}{Re}\left[\frac{4}{3}\frac{\partial^2\tilde{v}}{\partial y^2}+\frac{\partial^2\tilde{v}}{\partial x^2}+\frac{\partial^2\tilde{v}}{\partial z^2}+\frac{1}{3}\frac{\partial^2\tilde{u}}{\partial x\partial y}+\frac{1}{3}\frac{\partial^2\tilde{w}}{\partial y\partial z}\right]\\
&+\frac{1}{Re}\frac{\mathrm{d}\bar{\mu}}{\mathrm{d}\bar{T}}\tilde{T}\left[\frac{4}{3}\frac{\partial^2\bar{v}}{\partial y^2}+\frac{\partial^2\bar{v}}{\partial x^2}+\frac{\partial^2\bar{v}}{\partial z^2}+\frac{1}{3}\frac{\partial^2\bar{u}}{\partial x\partial y}+\frac{1}{3}\frac{\partial^2\bar{w}}{\partial y\partial z}\right]
\end{aligned}
$$

$$+\frac{1}{Re}\frac{\mathrm{d}\bar{\mu}}{\mathrm{d}\bar{T}}\frac{\partial\bar{T}}{\partial x}\left[\frac{\partial\tilde{u}}{\partial z}+\frac{\partial\tilde{w}}{\partial x}\right]+\frac{1}{Re}\frac{\mathrm{d}\bar{\mu}}{\mathrm{d}\bar{T}}\frac{\partial\bar{T}}{\partial y}\left[\frac{\partial\tilde{w}}{\partial y}+\frac{\partial\tilde{v}}{\partial z}\right]+\frac{1}{Re}\frac{\mathrm{d}\bar{\mu}}{\mathrm{d}\bar{T}}\frac{\partial\bar{T}}{\partial z}\left[\frac{4}{3}\frac{\partial\tilde{w}}{\partial z}-\frac{2}{3}\frac{\partial\tilde{u}}{\partial x}-\frac{2}{3}\frac{\partial\tilde{v}}{\partial y}\right]$$
$$+\frac{1}{Re}\left(\frac{\mathrm{d}\bar{\mu}}{\mathrm{d}\bar{T}}\frac{\partial\tilde{T}}{\partial x}+\left(\frac{\mathrm{d}^2\bar{\mu}}{\mathrm{d}\bar{T}^2}\frac{\partial\bar{T}}{\partial x}+\frac{\mathrm{d}\bar{\mu}}{\mathrm{d}\bar{T}}\right)\tilde{T}\right)\left[\frac{\partial\bar{u}}{\partial z}+\frac{\partial\bar{w}}{\partial x}\right]$$
$$+\frac{1}{Re}\left(\frac{\mathrm{d}\bar{\mu}}{\mathrm{d}\bar{T}}\frac{\partial\tilde{T}}{\partial y}+\left(\frac{\mathrm{d}^2\bar{\mu}}{\mathrm{d}\bar{T}^2}\frac{\partial\bar{T}}{\partial y}+\frac{\mathrm{d}\bar{\mu}}{\mathrm{d}\bar{T}}\right)\tilde{T}\right)\left[\frac{\partial\bar{w}}{\partial y}+\frac{\partial\bar{v}}{\partial z}\right]$$
$$+\frac{1}{Re}\left(\frac{\mathrm{d}\bar{\mu}}{\mathrm{d}\bar{T}}\frac{\partial\tilde{T}}{\partial z}+\left(\frac{\mathrm{d}^2\bar{\mu}}{\mathrm{d}\bar{T}^2}\frac{\partial\bar{T}}{\partial z}+\frac{\mathrm{d}\bar{\mu}}{\mathrm{d}\bar{T}}\right)\tilde{T}\right)\left[\frac{4}{3}\frac{\partial\bar{w}}{\partial z}-\frac{2}{3}\frac{\partial\bar{u}}{\partial x}-\frac{2}{3}\frac{\partial\bar{v}}{\partial y}\right] \tag{A.4}$$

Energy equation

$$\bar{\rho}\frac{\partial\tilde{T}}{\partial t}+\bar{\rho}\bar{u}\frac{\partial\tilde{T}}{\partial x}+\left(\bar{\rho}\tilde{u}+\tilde{\rho}\bar{u}\right)\frac{\partial\bar{T}}{\partial x}+\bar{\rho}\bar{v}\frac{\partial\tilde{T}}{\partial y}+\left(\bar{\rho}\tilde{v}+\tilde{\rho}\bar{v}\right)\frac{\partial\bar{T}}{\partial y}+\bar{\rho}\bar{w}\frac{\partial\tilde{T}}{\partial z}+\left(\bar{\rho}\tilde{w}+\tilde{\rho}\bar{w}\right)\frac{\partial\bar{T}}{\partial z}$$
$$+(\gamma-1)\left[\left(\frac{\partial\bar{u}}{\partial x}+\frac{\partial\bar{v}}{\partial y}+\frac{\partial\bar{w}}{\partial z}\right)\bar{\rho}\tilde{T}+\left(\bar{\rho}\left(\frac{\partial\tilde{u}}{\partial x}+\frac{\partial\tilde{v}}{\partial y}+\frac{\partial\tilde{w}}{\partial z}\right)+\tilde{\rho}\frac{\partial\bar{u}}{\partial x}+\tilde{\rho}\frac{\partial\bar{v}}{\partial y}+\tilde{\rho}\frac{\partial\bar{w}}{\partial z}\right)\bar{T}\right]$$
$$=\frac{\gamma}{Re\,Pr}\left[\bar{\mu}\frac{\partial^2\tilde{T}}{\partial x^2}+2\frac{\mathrm{d}\bar{\mu}}{\mathrm{d}\bar{T}}\frac{\partial\bar{T}}{\partial x}\frac{\partial\tilde{T}}{\partial x}+\left(\frac{\mathrm{d}\bar{\mu}}{\mathrm{d}\bar{T}}\frac{\partial^2\bar{T}}{\partial x^2}+\frac{\mathrm{d}^2\bar{\mu}}{\mathrm{d}\bar{T}^2}\left(\frac{\partial\bar{T}}{\partial x}\right)^2+\frac{\mathrm{d}\bar{\mu}}{\mathrm{d}\bar{T}}\frac{\partial\bar{T}}{\partial x}\right)\tilde{T}\right.$$
$$+\bar{\mu}\frac{\partial^2\tilde{T}}{\partial y^2}+2\frac{\mathrm{d}\bar{\mu}}{\mathrm{d}\bar{T}}\frac{\partial\bar{T}}{\partial y}\frac{\partial\tilde{T}}{\partial y}+\left(\frac{\mathrm{d}\bar{\mu}}{\mathrm{d}\bar{T}}\frac{\partial^2\bar{T}}{\partial y^2}+\frac{\mathrm{d}^2\bar{\mu}}{\mathrm{d}\bar{T}^2}\left(\frac{\partial\bar{T}}{\partial y}\right)^2+\frac{\mathrm{d}\bar{\mu}}{\mathrm{d}\bar{T}}\frac{\partial\bar{T}}{\partial y}\right)\tilde{T}$$
$$\left.+\bar{\mu}\frac{\partial^2\tilde{T}}{\partial z^2}+2\frac{\mathrm{d}\bar{\mu}}{\mathrm{d}\bar{T}}\frac{\partial\bar{T}}{\partial z}\frac{\partial\tilde{T}}{\partial z}+\left(\frac{\mathrm{d}\bar{\mu}}{\mathrm{d}\bar{T}}\frac{\partial^2\bar{T}}{\partial z^2}+\frac{\mathrm{d}^2\bar{\mu}}{\mathrm{d}\bar{T}^2}\left(\frac{\partial\bar{T}}{\partial z}\right)^2+\frac{\mathrm{d}\bar{\mu}}{\mathrm{d}\bar{T}}\frac{\partial\bar{T}}{\partial z}\right)\tilde{T}\right]$$
$$+\gamma\left(\gamma-1\right)\frac{M^2}{Re}\left[\frac{8}{3}\bar{\mu}\frac{\partial\bar{u}}{\partial x}\frac{\partial\tilde{u}}{\partial x}-\frac{2}{3}\bar{\mu}\left(\frac{\partial\bar{v}}{\partial y}\frac{\partial\tilde{u}}{\partial x}+\frac{\partial\tilde{v}}{\partial y}\frac{\partial\bar{u}}{\partial x}+\frac{\partial\bar{w}}{\partial z}\frac{\partial\tilde{u}}{\partial x}+\frac{\partial\tilde{w}}{\partial z}\frac{\partial\bar{u}}{\partial x}\right)\right.$$
$$+\bar{\mu}\left(2\frac{\partial\bar{v}}{\partial x}\frac{\partial\tilde{v}}{\partial x}+\frac{\partial\bar{u}}{\partial y}\frac{\partial\tilde{v}}{\partial x}+\frac{\partial\tilde{u}}{\partial y}\frac{\partial\bar{v}}{\partial x}\right)+\bar{\mu}\left(2\frac{\partial\bar{w}}{\partial x}\frac{\partial\tilde{w}}{\partial x}+\frac{\partial\bar{u}}{\partial z}\frac{\partial\tilde{w}}{\partial x}+\frac{\partial\tilde{u}}{\partial z}\frac{\partial\bar{w}}{\partial x}\right)$$
$$+\bar{\mu}\left(2\frac{\partial\bar{u}}{\partial y}\frac{\partial\tilde{u}}{\partial y}+\frac{\partial\bar{v}}{\partial x}\frac{\partial\tilde{u}}{\partial y}+\frac{\partial\tilde{v}}{\partial x}\frac{\partial\bar{u}}{\partial y}\right)+\frac{8}{3}\bar{\mu}\frac{\partial\bar{v}}{\partial y}\frac{\partial\tilde{v}}{\partial y}$$
$$-\frac{2}{3}\bar{\mu}\left(\frac{\partial\bar{u}}{\partial x}\frac{\partial\tilde{v}}{\partial y}+\frac{\partial\tilde{u}}{\partial x}\frac{\partial\bar{v}}{\partial y}+\frac{\partial\bar{w}}{\partial z}\frac{\partial\tilde{v}}{\partial y}+\frac{\partial\tilde{w}}{\partial z}\frac{\partial\bar{v}}{\partial y}\right)+\bar{\mu}\left(2\frac{\partial\bar{w}}{\partial y}\frac{\partial\tilde{w}}{\partial y}+\frac{\partial\bar{v}}{\partial z}\frac{\partial\tilde{w}}{\partial y}+\frac{\partial\tilde{v}}{\partial z}\frac{\partial\bar{w}}{\partial y}\right)$$
$$+\bar{\mu}\left(2\frac{\partial\bar{u}}{\partial z}\frac{\partial\tilde{u}}{\partial z}+\frac{\partial\bar{w}}{\partial x}\frac{\partial\tilde{u}}{\partial z}+\frac{\partial\tilde{w}}{\partial x}\frac{\partial\bar{u}}{\partial z}\right)+\bar{\mu}\left(2\frac{\partial\bar{v}}{\partial z}\frac{\partial\tilde{v}}{\partial z}+\frac{\partial\bar{w}}{\partial y}\frac{\partial\tilde{v}}{\partial z}+\frac{\partial\tilde{w}}{\partial y}\frac{\partial\bar{v}}{\partial z}\right)$$
$$+\frac{8}{3}\bar{\mu}\frac{\partial\bar{w}}{\partial z}\frac{\partial\tilde{w}}{\partial z}-\frac{2}{3}\bar{\mu}\left(\frac{\partial\bar{u}}{\partial x}\frac{\partial\tilde{w}}{\partial z}+\frac{\partial\tilde{u}}{\partial x}\frac{\partial\bar{w}}{\partial z}+\frac{\partial\bar{v}}{\partial y}\frac{\partial\tilde{w}}{\partial z}+\frac{\partial\tilde{v}}{\partial y}\frac{\partial\bar{v}}{\partial z}\right)$$
$$+\left(\frac{4}{3}\left[\left(\frac{\partial\bar{u}}{\partial x}\right)^2+\left(\frac{\partial\bar{v}}{\partial y}\right)^2+\left(\frac{\partial\bar{w}}{\partial z}\right)^2\right]+\left(\frac{\partial\bar{v}}{\partial x}\right)^2+\left(\frac{\partial\bar{w}}{\partial x}\right)^2+\left(\frac{\partial\bar{u}}{\partial y}\right)^2+\left(\frac{\partial\bar{w}}{\partial y}\right)^2$$

$$+\left(\frac{\partial\bar{u}}{\partial z}\right)^2+\left(\frac{\partial\bar{v}}{\partial z}\right)^2-\frac{2}{3}\left(\frac{\partial\bar{v}}{\partial y}\frac{\partial\bar{u}}{\partial x}+\frac{\partial\bar{w}}{\partial z}\frac{\partial\bar{u}}{\partial x}+\frac{\partial\bar{u}}{\partial x}\frac{\partial\bar{v}}{\partial y}+\frac{\partial\bar{w}}{\partial z}\frac{\partial\bar{v}}{\partial y}+\frac{\partial\bar{u}}{\partial x}\frac{\partial\bar{w}}{\partial z}+\frac{\partial\bar{v}}{\partial y}\frac{\partial\bar{w}}{\partial z}\right)$$
$$+\frac{\partial\bar{u}}{\partial y}\frac{\partial\bar{v}}{\partial x}+\frac{\partial\bar{u}}{\partial z}\frac{\partial\bar{w}}{\partial x}+\frac{\partial\bar{v}}{\partial x}\frac{\partial\bar{u}}{\partial y}+\frac{\partial\bar{v}}{\partial z}\frac{\partial\bar{w}}{\partial y}+\frac{\partial\bar{w}}{\partial x}\frac{\partial\bar{u}}{\partial z}+\frac{\partial\bar{w}}{\partial y}\frac{\partial\bar{v}}{\partial z}\Bigg)\frac{\mathrm{d}\bar{\mu}}{\mathrm{d}\bar{T}}\tilde{T}\Bigg] \quad \text{(A.5)}$$

Appendix B

DNS Database

The raw data that was generated by the direct numerical simulation presented in this work has been archived and made publicly available. This makes it possible for the results presented here to be reproduced and allows for further and deeper analysis of the data by the global research community. This chapter describes the structure of the database, the nature of the data, and the specifications of the data file formats.

When using any of this data or publishing results derived from analysis of this database, please use the following citation

> Van den Eynde, J. P. J. P. & Sandham, N. D. (2015), **DNS Database of Roughness-induced Instability & Transition at Mach 6**

and the corresponding paper discussing the transition results:

> Van den Eynde, J.P.J.P. & Sandham, N.D. (2015), **Numerical Simulations of Transition due to Isolated Roughness Elements at Mach 6.** *AIAA Journal*, (accepted), doi:10.2514/1.J054139

Or use the following as BibTeX entries:

```
@misc{vandeneynde-2015-database,
 author = {{Van den Eynde}, J. P. J. P. and Sandham, N. D.},
 title  = {DNS Database of Roughness-induced Instability
           \& Transition at Mach 6},
 year   = {2015}
}
```

```
@article{vandeneynde-2015,
 author  = {{Van den Eynde}, J. P. J. P. and Sandham, N. D.},
 title   = {Numerical Simulations of Transition due to
              Isolated Roughness Elements at Mach 6},
 journal = {AIAA Journal},
 year    = {2015},
 doi     = {10.2514/1.J054139}
}
```

B.1 Access to the database

Access to the database is open to the public but needs to be requested to the University of Southampton. Please contact Prof. Neil Sandham (`n.sandham@soton.ac.uk`) to request access.

B.2 Structure of the database

The database contains the raw DNS data sets in two main directories, corresponding to the data used in Chapter 5 *(Roughness Receptivity & Wake Instability)* and Chapter 7 *(Roughness-induced Transition)*. These two main directories are respectively named:

- `/Van-den-Eynde_2015_M6_Re8200/` (Data from Chapter 5)
- `/Van-den-Eynde_2015_M6_Re14000/` (Data from Chapter 7)

Each of those directories contain sub-directories for the different roughness element cases. For the results of the receptivity and linear instability growth study in Chapter 5, the naming of these sub-directories are given in Table B.1. The data used for the roughness-induced transition study in Chapter 7 can be found in the sub-directories given in Table B.2.

Each of these sub-directories contain another two sub-directories,

- `./grid/` holding the grid-file,
- `./data/` containing the result files from the DNS code `SBLI`.

B.3 Data file formats

The directories described here contain a variety of different files, i.e. grid files, instantaneous data files, and time-averaged statistics files. It is important to note that each of these files are in a

- little-endian
- binary

format. In this section the binary file format specifications of the different file formats is described, such that the data in these files can be correctly read.

B.3.1 Grid files

The grid files, included in the 🗀`./grid/` directories, are named `[casename].xyz` and contain the coordinates of the fully three-dimensional grids $x(i,j,k)$, $y(i,j,k)$, $z(i,j,k)$, with $i = 1, 2, \ldots, N_x$, $j = 1, 2, \ldots, N_y$ and $k = 1, 2, \ldots, N_z$. The full specifications of the file format are given in Table B.3.

B.3.2 Instantaneous flow fields

Instantaneous flow fields in terms of the conservative variables $(\rho, \rho u, \rho v, \rho w, \rho E)^\top$ are written out in (single precision) multi-block `plot3d` files. These files are consistently named `plot3d_q#.####`, in which `#` signifies the block number and `####` signifies the simulation iteration number at which the flow variables are written out.

The data files for the results in Chapter 5 *(Roughness Receptivity & Wake Instability)*, i.e. in directory 🗀 `/Van-den-Eynde_2015_M6_Re8200/`, use single-block flow fields. Multi-block flow fields have been used in Chapter 7 *(Roughness-induced Transition)*, i.e. the data files in 🗀 `/Van-den-Eynde_2015_M6_Re14000/`. These flow fields in this directory have been divided in a number of blocks in the streamwise direction, such that the complete flow field can be obtained by simply appending the different block files in the streamwise direction.

Table B.1. Directories for the roughness cases in Chapter 5.

Case	Directory
Bump	🗀 `/Van-den-Eynde_2015_M6_Re8200/Smooth_Bump/`
Cyl (-A)	🗀 `/Van-den-Eynde_2015_M6_Re8200/Flat_Cyl_A/`
Cyl-V	🗀 `/Van-den-Eynde_2015_M6_Re8200/Flat_Cyl_V/`
Cyl-Æ	🗀 `/Van-den-Eynde_2015_M6_Re8200/Flat_Cyl_E/`
Cyl-T0.5	🗀 `/Van-den-Eynde_2015_M6_Re8200/Flat_Cyl_T05/`
Square	🗀 `/Van-den-Eynde_2015_M6_Re8200/Flat_Square/`
Diam	🗀 `/Van-den-Eynde_2015_M6_Re8200/Flat_Diamond/`
R-Up	🗀 `/Van-den-Eynde_2015_M6_Re8200/Ramp_Up/`
R-Down	🗀 `/Van-den-Eynde_2015_M6_Re8200/Ramp_Down/`

Table B.2. Directories for the roughness cases in Chapter 7.

Case	Directory
H-⊗-1.0-Ae5	🗀 `/Van-den-Eynde_2015_M6_Re14000/Smooth_Bump_Ae5/`
H-⊗-1.0-Ae4	🗀 `/Van-den-Eynde_2015_M6_Re14000/Smooth_Bump_Ae4/`
H-○-1.0-Ae5	🗀 `/Van-den-Eynde_2015_M6_Re14000/Flat_Cyl_Ae5/`
H-○-1.0-Ae4	🗀 `/Van-den-Eynde_2015_M6_Re14000/Flat_Cyl_Ae4/`
H-□-1.0-Ae5	🗀 `/Van-den-Eynde_2015_M6_Re14000/Flat_Square_Ae5/`
H-◇-1.0-Ae5	🗀 `/Van-den-Eynde_2015_M6_Re14000/Flat_Diamond_Ae5/`
H-△-1.0-Ae5	🗀 `/Van-den-Eynde_2015_M6_Re14000/Ramp_Up_Ae5/`
H-▽-1.0-Ae5	🗀 `/Van-den-Eynde_2015_M6_Re14000/Ramp_Down_Ae5/`
H-●-0.5-Ae5	🗀 `/Van-den-Eynde_2015_M6_Re14000/Flat_Cyl_H05/`
H-⬠-1.0-Ae5	🗀 `/Van-den-Eynde_2015_M6_Re14000/Flat_Square_W3/`

Table B.3. Specification of the binary grid file format.

Size (Bytes)	Data Type	Description
8	`integer`	number of grid points in x-direction `nx`
8	`integer`	number of grid points in y-direction `ny`
8	`integer`	number of grid points in z-direction `nz`
8	`null`	
8	`float`	x-coordinate $x(1,1,1)$
8	`float`	x-coordinate $x(2,1,1)$
⋮	⋮	⋮
8	`float`	x-coordinate $x(\texttt{nx},1,1)$
8	`float`	x-coordinate $x(1,2,1)$
⋮	⋮	⋮
8	`float`	x-coordinate $x(\texttt{nx},\texttt{ny},1)$
8	`float`	x-coordinate $x(1,1,2)$
⋮	⋮	⋮
8	`float`	x-coordinate $x(\texttt{nx},\texttt{ny},\texttt{nz})$
8	`float`	y-coordinate $y(1,1,1)$
⋮	⋮	⋮
8	`float`	y-coordinate $y(\texttt{nx},\texttt{ny},\texttt{nz})$
8	`float`	z-coordinate $z(1,1,1)$
⋮	⋮	⋮
8	`float`	z-coordinate $z(\texttt{nx},\texttt{ny},\texttt{nz})$

The file format specification of the individual `plot3d` files is given in Table B.4.

B.3.3 Time-averaged flow field statistics

Time-averaged flow field statistics are written out in `Statistics#.####` files, which have a format similar to the `plot3d` file format but contain 27 statistical quantities instead of the conservative flow variables. The exact specifications of the `Statistics` files are given in Table B.5. The statistical quantities contained in these files are given in Table B.6.

Table B.4. Specification of the binary (single precision) plot3d format containing instantaneous flow fields in conservative flow variables.

Size (Bytes)	Data Type	Description
4	integer	number of grid points in x-direction nx
4	integer	number of grid points in y-direction ny
4	integer	number of grid points in z-direction nz
4	float	Mach number M
4	float	0 (not in use)
4	float	Reynolds number Re
4	float	Time t
4	float	density $\rho(1,1,1)$
4	float	density $\rho(2,1,1)$
⋮	⋮	⋮
4	float	density $\rho(\mathtt{nx},\mathtt{ny},\mathtt{nz})$
4	float	streamwise momentum $\rho u(1,1,1)$
⋮	⋮	⋮
4	float	streamwise momentum $\rho u(\mathtt{nx},\mathtt{ny},\mathtt{nz})$
4	float	wall-normal momentum $\rho v(1,1,1)$
⋮	⋮	⋮
4	float	wall-normal momentum $\rho v(\mathtt{nx},\mathtt{ny},\mathtt{nz})$
4	float	spanwise momentum $\rho w(1,1,1)$
⋮	⋮	⋮
4	float	spanwise momentum $\rho w(\mathtt{nx},\mathtt{ny},\mathtt{nz})$
4	float	total energy $\rho E(1,1,1)$
⋮	⋮	⋮
4	float	total energy $\rho E(\mathtt{nx},\mathtt{ny},\mathtt{nz})$

Table B.5. Specification of the binary file format containing time-averaged flow field statistics.

Size (Bytes)	Data Type	Description
4	integer	number of grid points in x-direction nx
4	integer	number of grid points in y-direction ny
4	integer	number of grid points in z-direction nz
4	float	Mach number M
4	float	0 (not in use)
4	float	Reynolds number Re
4	float	Time t
4	float	statistical quantity 1, $q_1(1,1,1)$
4	float	statistical quantity 1, $q_1(2,1,1)$
⋮	⋮	⋮
4	float	statistical quantity 1, $q_1(\mathtt{nx},\mathtt{ny},\mathtt{nz})$
4	float	statistical quantity 2, $q_2(1,1,1)$
⋮	⋮	⋮
4	float	statistical quantity 2, $q_2(\mathtt{nx},\mathtt{ny},\mathtt{nz})$
⋮	⋮	⋮
4	float	statistical quantity 27, $q_{27}(1,1,1)$
⋮	⋮	⋮
4	float	statistical quantity 27, $q_{27}(\mathtt{nx},\mathtt{ny},\mathtt{nz})$

Table B.6. Statistical quantities contained in the statistics files.

	1	2	3	4	5	6	7	8	9	10
$\boldsymbol{q}_{\#}$	$\overline{\rho\rho}$	$\overline{\rho u}$	$\overline{\rho v}$	$\overline{\rho w}$	$\overline{\rho\rho\rho}$	$\overline{\rho uu}$	$\overline{\rho uv}$	$\overline{\rho uw}$	$\overline{\rho vv}$	$\overline{\rho vw}$

	11	12	13	14	15	16	17	18	19	20
$\boldsymbol{q}_{\#}$	$\overline{\rho ww}$	$\overline{\rho u}$	$\overline{\rho v}$	$\overline{\rho w}$	$\overline{uu}$	$\overline{uv}$	$\overline{uw}$	$\overline{vv}$	$\overline{vw}$	$\overline{ww}$

	21	22	23	24	25	26	27
$\boldsymbol{q}_{\#}$	$\overline{p}$	$\overline{T}$	$\overline{pp}$	$\overline{TT}$	$\overline{T_0}$	$\overline{T_0T_0}$	$\overline{\rho T}$

Bibliography

Adamson, T.C.J. and Messiter, A.F. 'Analysis of two-dimensional interactions between shock waves and boundary layers'. *Annual Review of Fluid Mechanics*, 12(1):pp. 103–138 (1980).

Andersson, P., Brandt, L., Bottaro, A., and Henningson, D.S. 'On the Breakdown of Boundary Layer Streaks'. *Journal of Fluid Mechanics*, 428:pp. 29–60 (2001).

Balay, S., Abhyankar, S., Adams, M.F., Brown, J., Brune, P., Buschelman, K., Eijkhout, V., Gropp, W.D., Kaushik, D., Knepley, M.G., McInnes, L.C., Rupp, K., Smith, B.F., and Zhang, H. 'PETSc Web page'. http://www.mcs.anl.gov/petsc (2014).

Bernardini, M., Pirozzoli, S., and Orlandi, P. 'Compressibility Effects on Roughness-Induced Boundary Layer Transition'. *International Journal of Heat and Fluid Flow*, 35:pp. 45–51 (2012a).

Bernardini, M., Pirozzoli, S., Orlandi, P., and Lele, S.K. 'Compressible Boundary Layer Transition Induced by Isolated Roughness Elements'. In 'Center of Turbulence Research, Proceedings of the Summer Program', pp. 15–24. Published at http://ctr.stanford.edu/Summer/SP08/ (2012b).

Bernardini, M., Pirozzoli, S., Orlandi, P., and Lele, S.K. 'Parameterization of Boundary-Layer Transition Induced by Isolated Roughness Elements'. *AIAA Journal*, 52(10):pp. 2261–2269 (2014).

Berry, S.A. and Hamilton, H.H. 'Discrete roughness effects on shuttle orbiter at Mach 6'. In 'Proceedings of the 32nd AIAA Fluid Dynamics Conference', AIAA Paper 2002-2744 (2002).

Brandt, L., Cossu, C., Chomaz, J.M., Huerre, P., and Henningson, D.S. 'On the convectively unstable nature of optimal streaks in boundary layers'. *Journal of Fluid Mechanics*, 485:pp. 221–242 (2003).

Carpenter, M., Nordström, J., and Gottlieb, D. 'A Stable and Conservative Interface Treatment of Arbitrary Spatial Accuracy'. *Journal of Computational Physics*, 148(2):pp. 341–365 (1999).

Choudhari, M. 'Boundary-layer receptivity due to distributed surface imperfections of a deterministic or random nature'. *Theoretical and Computational Fluid Dynamics*, pp. 101–117 (1993).

Choudhari, M., Li, F., Wu, M., Chang, C., Edwards, J., Kegerise, M., and King, R. 'Laminar-Turbulent Transition behind Discrete Roughness Elements in a High-Speed Boundary Layer'. In '48th AIAA Aerospace Sciences Meeting Including the New Horizons Forum and Aerospace Exposition', AIAA Paper 2010-1575 (2010).

Choudhari, M., Norris, A., Li, F., Chang, C.L., and Edwards, J. 'Wake Instabilities behind Discrete Roughness Elements in High Speed Boundary Layers'. In '51st AIAA Aerospace Sciences Meeting', pp. 1–17. American Institute of Aeronautics and Astronautics, Reston, Virigina (2013).

Choudhari, M. and Streett, C. 'Boundary layer receptivity phenomena in three-dimensional and high-speed boundary layers'. *AIAA Journal*, 90 (1990).

Danabasoglu, G. and Biringen, S. 'A Chebyshev matrix method for the spatial modes of the Orr-Sommerfeld equation'. *International Journal for Numerical Methods in Fluids*, 11(January):pp. 1033–1037 (1990).

De Tullio, N. *Receptivity and Transition to Turbulence of Supersonic Boundary Layers with Surface Roughness*. Ph.D. thesis, University of Southampton (2013).

De Tullio, N., Paredes, P., Sandham, N.D., and Theofilis, V. 'Laminar-turbulent transition induced by a discrete roughness element in a supersonic boundary layer'. *Journal of Fluid Mechanics*, 735:pp. 613–646 (2013).

De Tullio, N. and Sandham, N.D. 'Direct Numerical Simulations of Roughness Receptivity and Transitional Shock-Wave/Boundary-Layer Interactions'. *Technical report*, NATO RTO-MP-AVT-200 (2012).

De Tullio, N. and Sandham, N.D. 'Influence of Boundary-Layer Disturbances on the Instability of a Roughness Wake in a High-Speed Boundary Layer'. *Journal of Fluid Mechanics*, 763:pp. 136–165 (2015).

Don, W. and Solomonoff, A. 'Accuracy enhancement for higher derivatives using Chebyshev collocation and a mapping technique'. *SIAM Journal on Scientific Computing* (1997).

Ducros, F., Ferrand, V., Nicoud, F., Weber, C., Darracq, D., Gacherieu, C., and Poinsot, T. 'Large-Eddy Simulation of the Shock/Turbulence Interaction'. *Journal of Computational Physics*, 152(2):pp. 517–549 (1999).

Fedorov, A.V. 'Receptivity of a high-speed boundary layer to acoustic disturbances'. *Journal of Fluid Mechanics*, 491:pp. 101–129 (2003).

Fedorov, A.V. 'Transition and Stability of High-Speed Boundary Layers'. *Annual Review of Fluid Mechanics*, 43(1):pp. 79–95 (2011).

Fedorov, A.V. and Khokhlov, A.P. 'Excitation of unstable modes in a supersonic boundary layer by acoustic waves'. *Fluid Dynamics*, (4):pp. 531–537 (1991).

Fedorov, A.V. and Khokhlov, A.P. 'Sensitivity of a supersonic boundary layer to acoustic disturbances'. *Fluid Dynamics*, 27(1):pp. 29–34 (1992).

Fedorov, A.V. and Khokhlov, A.P. 'Receptivity of hypersonic boundary layer to wall disturbances'. *Theoretical and Computational Fluid Dynamics*, 15:pp. 231–254 (2002).

Gaponenko, V.R., Ivanov, A.V., Kachanov, Y.S., and Crouch, J.D. 'Swept-wing boundary-layer receptivity to surface non-uniformities'. *Journal of Fluid Mechanics*, 461:pp. 93–126 (2002).

Gaponov, S. 'On the interaction of a supersonic boundary layer with acoustic waves'. *Thermophysics and Aeromechanics*, 3:pp. 181–189 (1995).

Gaster, M. 'A note on the relation between temporally-increasing and spatially-increasing disturbances in hydrodynamic stability'. *Journal of Fluid Mechanics*, 14(02):p. 222 (1962).

Groskopf, G., Kloker, M.J., and Marxen, O. 'Bi-Global Secondary Stability Theory for High-Speed Boundary-Layer Flows'. In 'Center of Turbulence Research,

Proceedings of the Summer Program', pp. 1–18. Published at http://ctr.stanford.edu/Summer/SP08/ (2008).

Harten, A. 'The artificial compression method for computation of shocks and contact discontinuities. III. Self-adjusting hybrid schemes.' *Mathematics of Computation*, 32(142):pp. 363–389 (1979).

Hermanns, M. and Hernández, J.A. 'Stable high-order finite-difference methods based on non-uniform grid point distributions'. *International Journal for Numerical Methods in Fluids*, 56:pp. 233–255 (2008).

Hernandez, V., Roman, J.E., and Vidal, V. 'SLEPc: A Scalable and Flexible Toolkit for the Solution of Eigenvalue Problems'. *ACM Trans. Math. Software*, 31(3):pp. 351–362 (2005).

Horvath, T.J., Zalameda, J.N., Wood, W.A., Berry, S.A., Schwartz, R.J., Dantowitz, R.F., Spisz, T.S., and Taylor, J.C. 'Global Infrared Observations of Roughness Induced Transition on the Space Shuttle Orbiter'. *Technical report*, NASA Langley Research Center, Hampton, VA, United States (2012).

Hultgren, L. and Gustavsson, L. 'Algebraic growth of disturbances in a laminar boundary layer'. *Physics of Fluids*, 24:pp. 1000–1004 (1981).

Hunt, J.C.R., Wray, A.A., and Moin, P. 'Eddies, Streams, and Convergence Zones in Turbulent Flows'. In 'Center of Turbulence Research, Proceedings of the Summer Program', pp. 193–208 (1988).

Kachanov, Y. 'Physical mechanisms of laminar-boundary-layer transition'. *Annual Review of Fluid Mechanics*, 26:pp. 411–482 (1994).

Kendall, J. 'Wind tunnel experiments relating to supersonic and hypersonic boundary layer transition'. *AIAA Journal*, 13(3):pp. 290–299 (1975).

Kerschen, E.J. 'Boundary Layer Receptivity Theory'. *Technical report* (1993).

Kimmel, R.L. and Poggie, J. 'Effect of total temperature on boundary-layer stability at Mach 6'. *AIAA Journal*, 38(9):pp. 1754–1755 (2000).

Kovasznay, L. 'Turbulence in supersonic flow'. *J. Aero. Sci.*, 20:pp. 657–682 (1953).

Landahl, M.T. 'A Note on an Algebraic Instability of Inviscid Parallel Shear Flows'. *Journal of Fluid Mechanics*, 98:pp. 243–251 (1980).

Lees, L. and Reshotko, E. 'Stability of the compressible laminar boundary layer'. *Journal of Fluid Mechanics*, 12(4):pp. 555–590 (1962).

Lele, S.K. 'Compressibility effects on turbulence'. *Annual Review of Fluid Mechanics*, 26:pp. 211–54 (1994).

Ma, Y. and Zhong, X. 'Receptivity of a supersonic boundary layer over a flat plate. Part 1. Wave structures and interactions'. *Journal of Fluid Mechanics*, 488:pp. 31–78 (2003).

Ma, Y. and Zhong, X. 'Receptivity of a supersonic boundary layer over a flat plate. Part 3. Effects of different types of free-stream disturbances'. *Journal of Fluid Mechanics*, 532:pp. 63–109 (2005).

Macaraeg, M.G. 'A spectral collocation solution to the compressible stability Eigenvalue problem'. *Technical report*, NASA Technical Paper 2858 (1988).

Mack, L. 'Linear stability theory and the problem of supersonic boundary-layer transition'. *AIAA Journal*, 13(3):pp. 278–289 (1975).

Mack, L. 'Boundary-layer linear stability theory'. In 'AGARD Spec. Course on Stability and Transition of Laminar Flow', NASA Jet Propulsion Laboratory (1984).

Malik, M.R. 'Numerical methods for hypersonic boundary layer stability'. *Journal of Computational Physics*, 86(2):pp. 376–413 (1990).

Marxen, O. and Iaccarino, G. 'Numerical Simulation of the Effect of a Roughness Element on High-Speed Boundary-Layer Instability'. In '38th AIAA Fluid Dynamics Conference', AIAA Paper 2008-4400, pp. 1–17 (2008).

Maslov, A., Shiplyuk, A., Sidorenko, A., and Arnal, D. 'Leading-edge receptivity of a hypersonic boundary layer on a flat plate'. *Journal of Fluid Mechanics*, 426:pp. 73–94 (2001).

McKenzie, J.F. and Westphal, K. 'Interaction of Linear Waves with Oblique Shock Waves'. *Physics of Fluids*, 11(11):p. 2350 (1968).

Morkovin, M. 'On the many faces of transition'. In 'Viscous Drag Reduction', Plenum Press (1969).

Morkovin, M. 'Transition in open flow systems – A reassessment'. *Bull. Am. Phys. Soc*, 39:pp. 1–31 (1994).

Orr, W. 'The stability or instability of the steady motions of a perfect liquid and of a viscous liquid. Part II: A viscous liquid'. In 'Proceedings of the Royal Irish Academy. Section A', (1907).

Platte, R.B., Trefethen, L.N., and Kuijlaars, A.B.J. 'Impossibility of Fast Stable Approximation of Analytic Functions from Equispaced Samples'. *SIAM Review*, 53:pp. 308–318 (2011).

Pook, D.A. *The Origin and Effects of Free-Stream Vortical Disturbances on Boundary Layer Transition in Wind Tunnels*. Ph.D. thesis, RMIT University (2013).

Reda, D.C. 'Review and Synthesis of Roughness-Dominated Transition Correlations for Reentry Applications'. *Journal of Spacecraft and Rockets*, 39(2):pp. 161–167 (2002).

Reddy, S.C., Schmid, P.J., Baggett, J.S., and Henningson, D.S. 'On stability of streamwise streaks and transition thresholds in plane channel flows'. *Journal of Fluid Mechanics*, 365:pp. 269–303 (1998).

Redford, J.A., Sandham, N.D., and Roberts, G.T. 'Compressibility Effects on Boundary-Layer Transition Induced by an Isolated Roughness Element'. *AIAA Journal*, 48(12):pp. 2818–2830 (2010).

Reed, H., Saric, W., and Arnal, D. 'Linear stability theory applied to boundary layers'. *Annual Review of Fluid Mechanics*, 28:pp. 389–428 (1996).

Reshotko, E. 'Boundary-Layer Stability and Transition'. *Annual Review of Fluid Mechanics*, 8:pp. 311–349 (1976).

Reshotko, E. 'Transient Growth: A Factor in Bypass Transition'. *Physics of Fluids*, 13(5):p. 1067 (2001).

Reshotko, E. 'Transition Issues for Atmospheric Entry'. *Journal of Spacecraft and Rockets*, 45(2):pp. 161–164 (2008a).

Reshotko, E. 'Transition Prediction: Supersonic and Hypersonic Flows'. *Technical report*, NATO EN-AVT-151-16 (2008b).

Reynolds, O. 'Experimental investigation of the circumstances which determine whether the motion of water shall be direct or sinuous, and of the law of resistance in parallel'. *Proceedings of the Royal Society of London*, pp. 84–99 (1883).

Sandham, N.D., Li, Q., and Yee, H.C. 'Entropy Splitting for High-Order Numerical Simulation of Compressible Turbulence'. *Journal of Computational Physics*, 178(2):pp. 307–322 (2002).

Sandham, N.D. and Lüdeke, H. 'Numerical Study of Mach 6 Boundary-Layer Stabilization by Means of a Porous Surface'. *AIAA Journal*, 47(9):pp. 2243–2252 (2009).

Sandhu, H.S. and Sandham, N.D. 'Boundary conditions for spatially growing compressible shear layers'. *Rept. QMW-EP-1100, Faculty of Engineering, Queen Mary and Westfield College* (1994).

Saric, W.S., Reed, H.L., and White, E.B. 'Stability and Transition of Three-Dimensional Boundary Layers'. *Annual Review of Fluid Mechanics*, 35(1):pp. 413–440 (2003).

Schmid, P.J. and Henningson, D.S. *Stability and Transition in Shear Flows*. Springer (2001).

Schneider, S.P. 'Hypersonic laminarturbulent transition on circular cones and scramjet forebodies'. *Progress in Aerospace Sciences*, 40(1-2):pp. 1–50 (2004).

Schneider, S.P. 'Effects of Roughness on Hypersonic Boundary-Layer Transition'. *Journal of Spacecraft and Rockets*, 45(2):pp. 193–209 (2008).

Shahinfar, S., Fransson, J.H.M., Sattarzadeh, S.S., and Talamelli, a. 'Scaling of streamwise boundary layer streaks and their ability to reduce skin-friction drag'. *Journal of Fluid Mechanics*, 733:pp. 1–32 (2013).

Sommerfeld, A. 'Ein Beitrag zur hydrodynamischen Erklärung der turbulenten Flüssigkeitsbewegungen'. In 'Proceedings of the 4th International Congress of Mathematicians', pp. 116–124. Rome (1908).

Squire, H.B. 'On the Stability for Three-Dimensional Disturbances of Viscous Fluid Flow between Parallel Walls'. *Proceedings of the Royal Society A: Mathematical, Physical and Engineering Sciences*, 142(847):pp. 621–628 (1933).

Stetson, K., Kimmel, R., Donaldson, J., Siler, L., and Thompson, E. 'A comparison of planar and conical boundary layer stability and transition at a Mach number of 8'. In 'AIAA, Plasma Dynamics and Lasers Conference', pp. 24–26. Honolulu, HI (1991).

Stewart, G.W. 'A Krylov-Schur Algorithm for Large Eigenproblems'. *SIAM Journal on Matrix Analysis and Applications*, 23(3):pp. 601–614 (2002).

Stokes, G. 'On some cases of fluid motion'. *Trans. Camb. Phil. Soc*, VIII(1):pp. 105–137 (1843).

Subbareddy, P., Bartkowicz, M., and Candler, G. 'Direct numerical simulation of high-speed transition due to an isolated roughness element'. *Journal of Fluid Mechanics*, 748:pp. 848–878 (2014).

Tani, I. 'Boundary-layer transition'. *Annual Review of Fluid Mechanics*, 1:pp. 169–196 (1969).

Touber, E. and Sandham, N.D. 'Low-order Stochastic Modelling of Low-Frequency Motions in Reflected Shock-Wave/Boundary-Layer Interactions'. *Journal of Fluid Mechanics*, 671:pp. 417–465 (2011).

Van den Eynde, J.P.J.P. and Sandham, N.D. 'Numerical Simulations of Transition due to Isolated Roughness Elements at Mach 6'. *AIAA Journal*, (accepted) (2015).

Wheaton, B.M. and Schneider, S.P. 'Roughness-Induced Instability in a Hypersonic Laminar Boundary Layer'. *AIAA Journal*, 50(6):pp. 1245–1256 (2012).

Wheaton, B.M. and Schneider, S.P. 'Hypersonic Boundary-Layer Instabilities due to Near-Critical Roughness'. *Journal of Spacecraft and Rockets*, 51(1):pp. 327–342 (2014).

White, F.M. *Viscous fluid flow*. McGraw-Hill, 2nd edition (1991).

Wray, A.A. 'Very Low Storage Time-Advancement Schemes'. *Technical report*, NASA Ames Research Center (1986).

Yee, H.C., Sandham, N.D., and Djomehri, M.J. 'Low-Dissipative High-Order Shock-Capturing Methods using Characteristic-Based Filters'. *Journal of Computational Physics*, 150(1):pp. 199–238 (1999).

Zhong, X. and Wang, X. 'Direct Numerical Simulation on the Receptivity, Instability, and Transition of Hypersonic Boundary Layers'. *Annual Review of Fluid Mechanics*, 44(1):pp. 527–561 (2012).